

ACCRETION MODES, AGN FEEDBACK AND STAR FORMATION

A THESIS SUBMITTED TO THE UNIVERSITY OF HERTFORDSHIRE
IN PARTIAL FULFILLMENT OF THE REQUIREMENTS OF THE DEGREE OF
DOCTOR OF PHILOSOPHY
CENTRE FOR ASTROPHYSICS RESEARCH

July, 2016

By
Gülay Gürkan Uygun
School of Physics, Astronomy and Mathematics
Centre for Astrophysics Research
The University of Hertfordshire

Contents

Abbreviations	13
Abstract	19
Declaration	21
Copyright	22
Acknowledgements	23
Publications	25
1 Introduction	29
1.1 A brief history	29
1.2 Properties of active galactic nuclei	31
1.2.1 Central source and accretion disc	31
1.2.2 X-ray emitting corona	34
1.2.3 Emission line regions	35
1.2.4 Torus	36
1.3 Classification of active galactic nuclei	38
1.3.1 Radio galaxies	38
1.3.2 Seyfert galaxies	45
1.3.3 Quasars	47
1.3.4 The unification model	47
1.4 AGN and galaxy evolution	50
1.4.1 AGN activity, star formation and environments	50
1.4.2 AGN Feedback	53
1.5 Far-IR/radio correlation	55
1.6 Objectives and thesis outline	57

2	Data	60
2.1	Introduction	60
2.2	Near- and mid-infrared data	62
2.3	Far-infrared data	64
2.3.1	The <i>Herschel</i> telescope	64
2.3.2	<i>Herschel</i> -ATLAS survey	66
2.4	Optical data	70
2.4.1	Related catalogue data	70
2.5	Radio data	71
2.6	Radio Interferometry	71
2.6.1	The FIRST survey	75
2.6.2	The NVSS survey	78
2.6.3	The LOFAR survey of the H-ATLAS/NGP field	78
3	The <i>WISE</i> properties of radio-loud AGN	80
3.1	Abstract	80
3.2	Introduction	81
3.3	Data and Analysis	84
3.3.1	Samples	84
3.3.2	<i>WISE</i> magnitudes	86
3.3.3	Consistency between <i>WISE</i> and <i>Spitzer</i>	89
3.3.4	<i>WISE</i> luminosities	89
3.4	Results	91
3.4.1	Colour–colour diagrams	91
3.4.2	Investigation of the old stellar population	93
3.4.3	The possibility of a starburst contribution?	97
3.4.4	Quasar-radio galaxy unification	97
3.4.5	Dichotomy for LERGs and HERGs	102
3.5	Summary and Conclusions	109
4	RL vs. RQ: AGN activity and SFR	111
4.1	Abstract	111
4.2	Introduction	112
4.3	Data	115
4.3.1	Sample and classification	115
4.3.2	Far-infrared data, star formation and specific star formation rates	123

4.3.3	Near- and mid-infrared data	125
4.3.4	AGN power indicators	127
4.4	Results	134
4.4.1	Stacking SFR: Radio-loud and radio-quiet comparison	134
4.4.2	Correlation between black hole accretion rate and star formation rate	150
4.4.3	Stacking SFR: HERG and LERG comparison	151
4.5	Discussion	155
4.5.1	Interpretation of the correlation between SFR and AGN power	155
4.5.2	Probable reasons for the difference between SFR/SSFR of radio-loud and radio-quiet AGN	158
4.5.3	The differences between SFR/SSFR in HERGs and LERGs	159
4.6	Summary and Conclusions	160
5	LOFAR survey of the H-ATLAS/NGP field	162
5.1	Introduction	162
5.2	LOFAR	163
5.3	LOFAR Observations	169
5.4	LOFAR Data Reduction, Calibration and Imaging	170
5.4.1	Direction-independent Calibration	170
5.4.2	Direction-dependent Calibration ('Facet' Calibration)	176
5.5	Evaluation of the image quality	181
5.6	The LOFAR catalogue of the H-ATLAS NGP field	183
5.6.1	The raw catalogue	183
5.6.2	The final catalogue	185
5.7	Source associations and optical identifications	186
5.7.1	Initial cross-matching	186
5.7.2	Source associations	186
5.7.3	Optical identification of sources	188
5.7.4	Spectroscopic/photometric redshifts and optical magnitudes	196
5.7.5	Secondary review of the optical identification	198
5.8	Summary and conclusions	199
6	The radio luminosity/SFR relation	201
6.1	Abstract	201
6.2	Introduction	202

6.3	DATA	204
6.3.1	Sample and emission line classification	204
6.3.2	Radio data	205
6.3.3	Far-IR data	206
6.3.4	Star formation rates	208
6.4	Analysis and results	213
6.4.1	The low-frequency radio luminosity–SFR relation	213
6.4.2	The far-IR–radio correlation	220
6.5	Interpretation	228
6.5.1	The L_{150} /SFR relation	228
6.5.2	The far-IR/radio correlation of SFGs	233
6.6	Conclusions and future work	235
7	Conclusions and future prospects	238
7.1	Probing radio-loud AGN at high-redshifts with <i>WISE</i>	239
7.2	AGN–star-formation relation	241
7.2.1	Future Prospects	242
7.3	<i>LOFAR</i> survey of the H-ATLAS-NGP field	243
7.3.1	Future Prospects	243
7.4	Low-frequency radio luminosity/SFR relation	244
7.4.1	Future Prospects	246
A	Extended LOFAR radio sources	247

List of Tables

2.1	Details of the <i>Herschel</i> -ATLAS fields.	66
3.1	<i>WISE</i> detection summary for each sample.	88
3.2	ASURV median estimates of <i>WISE</i> luminosities of sources in the sample.	100
3.3	Results of partial correlation analyses.	107
4.1	Summary of the sample galaxies.	117
4.2	The mean temperature values for different populations.	124
4.3	AGN power definitions for different type of objects.	131
4.4	Results of the stacking analysis regarding the full samples	143
4.5	Results of the stacking analysis of the sample where the composite objects are not included.	144
4.6	The stacking analysis results of radio-loud (HERGs and LERGs) and radio-quiet AGN samples matched in their stellar masses.	149
4.7	SFR/ \dot{M}_{BH} ratios for radio-loud and radio-quiet AGN.	152
4.8	The stacking analysis results for HERGs and LERGs.	154
5.1	Low-frequency radio surveys.	164
5.2	The LOFAR project tasks.	165
5.3	LOFAR observations of the NGP field.	170
5.4	Spectral windows of the LOFAR/NGP observations used.	177
5.5	Details of the LOFAR pointings.	182
5.6	Correction factors applied per field.	184
5.7	Classification statistics.	190
5.8	Redshift statistics of sources with optical identifications.	198
6.1	Counts of galaxies in the sample and their detection rates.	205
6.2	Parameterisations that were used for regression analyses.	217
6.3	Stacking L_{150} of SFG in SFR bins.	220

6.4	Stacking L_{150} of SFGs in L_{250} bins.	225
6.5	Stacking L_{150} and $L_{1.4}$ of SFGs in L_{250} bins.	228

List of Figures

1.1	Example of an optical emission-line diagnostic diagram.	37
1.2	Radio images of FRI-I type radio source and FR II type of radio galaxy.	43
1.3	An example sketch of radiatively inefficient accretion.	46
1.4	Example of the spectral energy distribution of an AGN.	47
1.5	A graphic of the expected structures of radiatively efficient AGN.	49
1.6	Various properties of AGN population.	55
2.1	View of the <i>WISE</i> telescope.	62
2.2	Example <i>WISE</i> images.	63
2.3	View of the <i>Herschel</i> telescope.	65
2.4	The <i>Herschel</i> -ATLAS fields.	67
2.5	<i>Herschel</i> -ATLAS images.	69
2.6	View of the SDSS telescope.	71
2.7	Example SDSS <i>r</i> -band image.	72
2.8	A schematic illustration of a two-element radio interferometer.	74
2.9	View of the VLA.	76
2.10	Example of a FIRST image.	77
2.11	Example of a NVSS image.	79
3.1	The 151 MHz radio luminosity distribution of the samples.	85
3.2	Comparison of <i>WISE</i> and <i>Spitzer</i> measurements.	90
3.3	<i>WISE</i> colour-colour diagrams of all objects in the combined sample.	92
3.4	Plot of 3.4 μm magnitudes versus redshift.	94
3.5	Plot of 3.4 μm luminosity (left) and 4.6 μm luminosity (right) versus redshift.	96
3.6	The 12 μm and 22 μm luminosity distributions of sample sources.	101
3.7	Plot of 12 μm luminosity (right) and 22 μm luminosity (left) versus 151 MHz radio luminosity.	105

3.8	Plot of 22 μm luminosity versus 151 MHz radio luminosity.	106
3.9	Plot of 22 μm luminosity versus 5 GHz core luminosity.	107
3.10	Histogram of the distribution of 22 μm luminosity over 3.4 μm luminosity.	108
4.1	Optical emission-line classification of the sample sources.	120
4.2	Mass and redshift distribution of sources.	121
4.3	The distribution of the radio-loudness parameter for radio-quiet AGN and HERGs.	122
4.4	Plot of 250 μm luminosity versus SFRs of star-forming galaxies.	126
4.5	The relation between L_{22} and L_{250} for star-forming objects and the sample sources that are detected in <i>WISE-22 μm</i> band.	128
4.6	The distribution of the residual luminosities of the star-forming objects (left) and AGN in the sample detected at 22 μm (right) as a function of L_{22}	129
4.7	The relation between $L_{[\text{OIII}]}$ and L_{250} for star-forming objects and the sample sources that are significantly (3σ) detected in their [OIII] emission-lines.	132
4.8	The distribution of the residual luminosities of the star-forming objects (left) and detected AGN in the sample (right) as a function of $L_{[\text{OIII}]}$	133
4.9	The comparison of density maps of the residuals both for the composites and radio-quiet AGN.	134
4.10	The distributions of SFRs of the sources in the sample.	136
4.11	Plot of the stacking analysis of radio-loud and radio-quiet AGN.	138
4.12	Plot of stacking analysis of radio-loud and radio-quiet AGN where the intrinsic relation between z and SSFR is taken into account.	139
4.13	The distribution of AGN power/SFR versus redshift for radio-quiet AGN, HERGs and LERGs.	140
4.14	Plot of stacking analysis of radio-loud and -quiet AGN where composite objects are not included.	142
4.15	Stellar mass distribution of each AGN sample before and after the matching process.	146
4.16	Plot of the SFR stacking analysis of radio-loud and radio-quiet AGN using mass-matched samples.	147
4.17	The relation between the rate of black hole growth and the rate of galaxy growth for the AGN samples.	151

4.18	Result of stacking analysis of radio-loud AGN sample.	153
5.1	The LOFAR stations.	167
5.2	The median averaged spectrum for the LBA and HBA antennas.	168
5.3	<i>UV</i> coverage.	171
5.4	The phase offsets between XX and YY phases.	173
5.5	The fitted clock and TEC differences.	174
5.6	The LOFAR map with facets and tessellations.	178
5.7	The LOFAR/NGP SW pointing map.	179
5.8	Zoomed region of the LOFAR/NGP SW pointing map.	180
5.9	The r.m.s. map of the four pointings.	184
5.10	Cumulative histogram of the area below a given r.m.s. value.	185
5.11	Example images of extended sources.	187
5.12	Classification:single source case.	191
5.13	Classification:multiple source case.	192
5.14	Classification:artefact case.	193
5.15	Classification: quasar counterpart case.	194
5.16	Classification: 3C284.	195
5.17	Redshift distribution of sources with optical IDs.	197
5.18	Redshift distribution of radio quasars.	199
6.1	The distribution of the luminosity at 150 MHz of all galaxies in the sample as a function of their redshifts.	207
6.2	Stellar mass–SFR plot of all galaxies in the sample.	209
6.3	Comparison of SFRs which are derived by different methods for SFGs and other galaxies in the sample.	212
6.4	L_{150} distribution of SFG as a function of SFR.	215
6.5	Redshift and mass dependence of the L_{150} /SFR relation.	218
6.6	Redshift and mass dependence of the L_{150} /SFR relation.	219
6.7	Mass and SFR dependence of the L_{150} /SFR relation.	221
6.8	L_{150} distribution of different class of galaxies as a function of SFR.	222
6.9	L_{150} distribution of different class of galaxies as a function of SFR.	223
6.10	L_{150} distribution of SFGs as a function of L_{250}	225
6.11	L_{150} distribution of different class of galaxies as a function of L_{250}	226
6.12	L_{150} distribution of limits of the sample galaxies.	227
6.13	L_{250} distribution of SFGs as a function of L_{150}	229

A.1	Postage stamps of the optically identified objects.	248
A.2	Continued.	249
A.3	Continued.	250
A.4	Continued.	251
A.5	Continued.	252
A.6	Continued.	253
A.7	Continued.	254
A.8	Continued.	255
A.9	Continued.	256
A.10	Continued.	257

Abbreviations

ADAF: Advection-Dominated Accretion Flow

ADIOS: Adiabatic Inflow-Outflow Solution

AGN: Active Galactic Nuclei

ASTRON: The Netherlands Institute for Radio Astronomy

ATLAS: The Astrophysical Terahertz Large Area Survey

BCG: Bright Cluster Galaxy

BBS: BlackBoard Selfcal

BH12: Best & Heckman 2012

BLR: Broad Line Region

BLRG: Broad Line Radio Galaxy

BL Lac: BL Lacertae

BPT: Baldwin, Phillips & Terlevich

CDAF: Convection-Dominated Accretion Flow

CEP: CEntral Processing

COBALT: The COrrelator and Beam-forming Application platform for the LOFAR Telescope

CPU: Central Processing Unit

DDDP: Default Pre-Processing Pipeline

DEC: Declination

ESA: European Space Agency

EVLA: The Extended Very Large Array

FIR: Far-infrared

FIRC: Far-infrared—Radio Correlation

FIRST: The Faint Images of the Radio Sky at Twenty-cm

FOV: Field of View

FR I: Fanaroff & Riley I

FR II: Fanaroff & Riley II

HBA: High Band Array

HERG: High-Excitation Radio Galaxy

HIFI: Heterodyne Instrument for the Far Infrared

HMQ: The Half Million Quasars catalogue

GAMA: The Galaxy And Mass Assembly redshift survey

GLEAM: The GaLactic and Extragalactic All-sky MWA survey

GMRT: The Giant Meterwave Radio Telescope

GPU: Graphic Processing Units

GSM: Global Sky Model

GZ2: Galaxy Zoo 2

IC: Inverse-Compton

ICM: Intercluster Medium

ID: Identification

IGM: Intergalactic Medium

IPAC: The Infrared Processing and Analysis Center

IR: Infrared

KS: KolmogorovSmirnov test

LBA: Low Band Array

LERG: Low-Excitation Radio Galaxy

LINERs: Low-Ionisation Nuclear Emission-line Regions

LOFAR: The LOw Frequency ARray

LTA: Long-Term Archive

MAGPHYS: The Multi-wavelength Analysis of Galaxy Physical Properties

MCMC: Markov-Chain Monte Carlo methods

MFIR: Mid-Far Infrared

MPA-JHU: The Max Planck Institute for Astrophysics and John Hopkins University

MWA: The Murchison Widefield Array

MSSS: The LOFAR Multifrequency Snapshot Sky Survey

NASA: The National Aeronautics and Space Administration

NGP: The North Galactic Plane field

NLR: Narrow Line Region

NLRG: Narrow Line Radio Galaxy

NVSS: The NRAO V1a Sky Survey

NRAO: The National Radio Astronomy Observatory

PACS: Photodetector Array Camera and Spectrometer

PSF: Point Spread Function

PYBDSM: The Python Blob Detection and Source Measurement software

RA: Right Ascension

RFI: Radio Frequency Interference

RIAF: Radiatively Inefficient Accretion Flow

SDSS: Sloan Digital Sky Survey

SED: Spectral Energy Distribution

SFG: Star-forming Galaxy

SFR: Star Formation Rate

Sgr A*: Sagittarius A*

SGP: The South Galactic pole field

SKA: The Square Kilometer Array

SKSP: The Surveys Key Science Project

SMBH: Super Massive Black Hole

SNR: Signal to Noise Ratio

SPIRE: Spectral and Photometric Imaging Receiver

SSFR: Specific Star Formation Rate

STILTS: Starlink Tables Infrastructure Library Tool Set

TEC: The Total Electron Content

TIFR: The Tata Institute of Fundamental Research

XMM: The X-ray Multi-Mirror Mission

ULIRG: Ultra Luminous Infrared Galaxy

UV: Ultra-Violet

VLA: Very Large Array

VLSS: The VLA Low-Frequency Sky Survey

WENNS: The Westerbork Northern Sky Survey

WISE: The Wide-field Infrared Survey

WSRT: The Westerbork Synthesis Radio Telescope

Abstract

I study mid-infrared and star formation properties of AGN samples using infrared observations, and star-forming galaxies using radio observations in order to investigate the link between star formation, AGN activity and radio luminosity. I present the results of these investigations in this thesis.

I carried out an analysis of four complete samples of radio-loud AGN (3CRR, 2Jy, 6CE and 7CE) using near- and mid-IR data taken by the *Wide-Field Infrared Survey Explorer (WISE)*. The combined sample consists of quasars and radio galaxies, and covers a redshift range $0.003 < z < 3.395$. The dichotomy in the mid-IR properties of low- and high-excitation radio galaxies (LERGs - HERGs) is analysed using large complete samples. The results show that a division in the accretion modes of powerful LERGs and HERGs clearly stands out in the mid-IR radio plane. Evaluation of the positions of the sample objects in *WISE* colour-colour diagrams shows that widely used *WISE* colour cuts are not completely reliable in selecting AGN.

I examined the link between AGN activity and star formation by constructing matched samples of local ($0 < z < 0.6$) radio-loud and radio-quiet AGN in the *Herschel*-ATLAS fields. AGN accretion and jet powers in these active galaxies are traced by [OIII] emission-line and radio luminosity, respectively. Star formation properties were derived using *Herschel* 250- μm and stellar mass measurements are taken from the SDSS–MPA-JHU catalogue. The stacking analyses show that star formation rates (SFRs) and specific star formation rate (SSFRs) of both radio-loud and radio-quiet AGN increase with increasing AGN power but that radio-loud AGN tend to have lower SFR. Additionally, radio-quiet AGN are found to have approximately an order of magnitude higher SSFRs than radio-loud AGN for a given level of AGN power. The difference between the star formation properties of radio-loud and -quiet AGN is also seen in samples matched in stellar mass.

I also investigated the relationship between SFR and low-frequency radio luminosity observed in star-forming galaxies. I used a sample of star-forming galaxies in the

local Universe selected from the SDSS–MPA–JHU catalogue. *LOFAR* observations of the *Herschel*-ATLAS North Galactic Pole field (NGP) were carried out as part of the *LOFAR* surveys Key Science Project at an effective frequency of 150 MHz, which provided low-frequency radio luminosity of sample galaxies. SFRs of galaxies in the sample were derived using MAGPHYS spectral energy distribution (SED) fitting. The results of this study show that the slope of L_{150}/SFR is less than unity and not universal for all star-forming galaxies (SFGs) in the local Universe ($0 < z < 0.3$). The slope of the L_{150}/SFR relation is also found to be steeper than the $L_{1.4}/\text{SFR}$ relation, probably due to the contribution from thermal radio emission at 1.4 GHz. If the L_{150}/SFR relation for strongly star-forming objects is explained naively by electron calorimetry, I conclude that low luminosity sources are not ideal calorimeters and differ from the main locus of SFGs at low redshifts. The different gradients we obtain for the far-IR/radio correlation using samples selected at different frequencies reveal the selection effects on relations derived in this thesis.

Declaration

No portion of the work referred to in this thesis has been submitted in support of an application for another degree or qualification of this or any other university or other institution of learning.

Copyright

Copyright in text of this thesis rests with the Author. Copies (by any process) either in full, or of extracts, may be made **only** in accordance with instructions given by the Author. This page must form part of any such copies made. Further copies (by any process) of copies made in accordance with such instructions may not be made without the permission (in writing) of the Author.

The ownership of any intellectual property rights which may be described in this thesis is vested in the University of Hertfordshire, subject to any prior agreement to the contrary, and may not be made available for use by third parties without the written permission of the University, which will prescribe the terms and conditions of any such agreement.

Further information on the conditions under which disclosures and exploitation may take place is available from the Head of the School of Physics, Astronomy and Mathematics.

Centre for Astrophysics Research
The University of Hertfordshire.

Acknowledgements

The final part of an academic education is about to be completed. It has been a long and very tough journey since the age of six. I can safely call this journey an outlier; far far away from the average stories :). Therefore, the right thing would be to thank each individual or event that was part of this success (either by hindering that taught me to be stronger or contributing positively that taught me to appreciate support). However, this would lead me to write a book as long as this thesis so I will try to keep it brief here. :)

First and foremost, I would like to express my heartfelt thanks to my supervisor Prof. Martin J. Hardcastle, not because I am obliged to here, but because I really want to! A large part of getting a PhD is team work and Martin has been the most incredible team partner I could ever have hoped for. Throughout this PhD he showed admirable patience and his guidance has led me to become an independent researcher. Martin is one of the most diligent yet caring scientists I have ever met. I feel privileged to have worked with him and he will always be my mentor.

I also would like to thank to Dr Daniel Smith, Dr Nicky Brassington and Dr Nick Wright for kindly answering my silly questions and in particular Daniel for all his support.

Special thanks to Dr Eleni Kalfountzou, Dr Wendy Williams and Dr Beatriz Mingo for patiently reading parts of my thesis and helping me to improve it.

Eleni and Wendy I wish I met both of you much earlier and had a chance to spend more time together as you both made the last period of my PhD special. It is so great to know that there are sincere people like you in this community.

I also thank to my PhD fellows with whom I had great times. Especially I thank Dr Hywel Farnhill and Dr Federico Morocco for throwing Horsa Garden parties for any sort of excuse – unforgettable times :)

My dear Dr Stefania Maccalli, your existence in my life makes me so happy and feel special, thanks for being there with me all the time.

My dear parents Orhan and Emine Gürkan! You provided the opportunity for me to study what I am passionate about against all kinds of hard circumstances and it is only with your courage that I have been able to reach this point. I am indebted to both of you for all your contributions. My dear sister Gülbahar Gürkan thanks for providing support when I needed it. My love Emrah Uygun, you have been with me since the last years of my undergraduate studies. You have showed endless courage and supported me no matter what! If you were not there with me perhaps I would not be able to accomplish this. Thanks very much for your exhaustless patience over the period of this PhD, in particular when I ended up with only one usable arm after the unfortunate accident towards the end of my PhD. I honestly cannot pay you back for your help and support. Love you all!

I would also like to express my appreciation for the financial support provided by the University of Hertfordshire.

Finally, a word of thanks to radio AGN for providing with me a PhD souvenir: a twitching eye! :)

I apologise in case I have forgotten to acknowledge anyone. I believe that every single person and every single piece of the environment where I have been has contributed to my achievement in higher education that I cannot pay back.

Gülay Gürkan Uygun
Hatfield , July 2016

Publications

Gürkan G., Hardcastle, M.J., Jarvis, M.J., LOFAR & H-ATLAS Collab.,
The low–frequency radio luminosity–star formation rate relation, 2016, MNRAS, in prep.

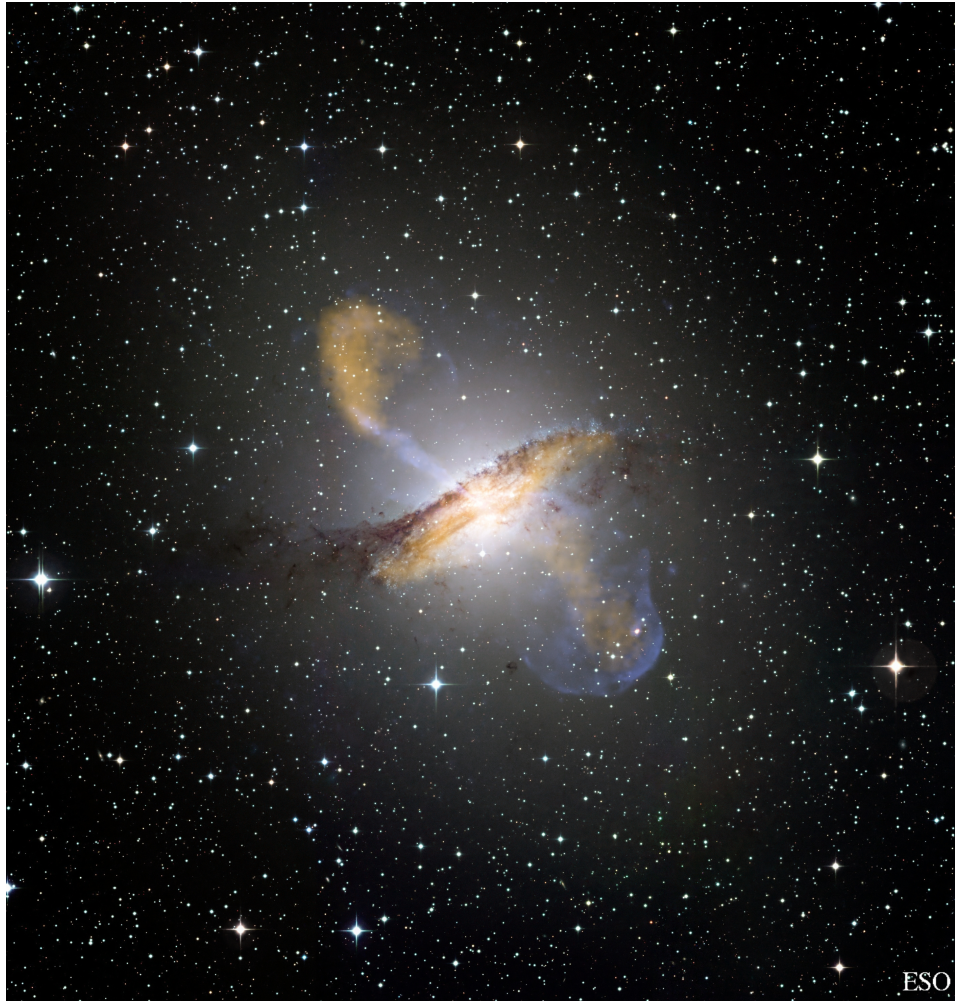
Hardcastle M.J., **Gürkan G.**, van Weeren, R.J., Williams, W.L., Best, P.N., de Gasperin, F., Rafferty, D.A., Read, S.C., Sabater, J., Shimwell, T.W., Smith, D.J.B., Tasse, C., Bourne, B., Brienza, M., Brügger, M., Brunetti, G., Chyzy, K.T., Conway, J., Dunne, L., Eales, S.A., Maddox, S.J., Jarvis, M.J., Mahony, E.K., Morganti, R., Prandoni, I., Röttgering, H.J.A., Valiante, E. and White, G.J.,
LOFAR/H-ATLAS: A deep low-frequency survey of the Herschel-ATLAS North Galactic Pole field, 2016, MNRAS, accepted, ([arXiv:1606.09437](#)).

Gürkan G., Hardcastle, M.J., Jarvis, M.J., Smith, D.J.B., Bourne, N., Dunne, L., Maddox, S., Ivison, R.J., Fritz, J.,
Herschel-ATLAS: The connection between star formation and AGN activity in radio-loud and radio-quiet active galaxies, 2015, MNRAS, 452, 3776 ([arXiv:1507.01552](#))

Gürkan G., Hardcastle, M.J., Jarvis, M.J.,
The WISE properties of complete samples of radio-loud AGN, 2014, MNRAS, 438, 1149 ([arXiv:1308.4843](#))

Gürkan G., Jackson, N., Browne, I. W. A., Koopmans, L.V.E., Fassnacht, C. D., Berciano Alba, A.,
Measuring gravitational lens time delays using low-resolution radio monitoring observations, 2014, MNRAS, 441, 127 ([arXiv:1403.4986](#)).

*Dedicated to a little girl,
who always wished to understand the Universe.*



$$\begin{aligned}\nabla \times E &= -\frac{\partial B}{\partial t} \\ \nabla \cdot E &= 0 \\ \nabla \times B &= \mu_0 \varepsilon_0 \frac{\partial E}{\partial t} \\ \nabla \cdot B &= 0\end{aligned}$$

Chapter 1

Introduction

“The best thing for being sad,” replied Merlin, beginning to puff and blow, “is to learn something. That’s the only thing that never fails. You may grow old and trembling in your anatomies, you may lie awake at night listening to the disorder of your veins, you may miss your only love, you may see the world about you devastated by evil lunatics, or know your honour trampled in the sewers of baser minds. There is only one thing for it then – to learn. Learn why the world wags and what wags it. That is the only thing which the mind can never exhaust, never alienate, never be tortured by, never fear or distrust, and never dream of regretting. Learning is the only thing for you. Look what a lot of things there are to learn.”

Terence H. White, *The Once and Future King*

1.1 A brief history

Although the emission lines of active galactic nuclei (AGN) have been known since the early 20th century (e.g. Fath 1909) AGN did not arouse interest as a research subject until Carl Seyfert noticed that a few galaxies have bright nuclei producing broad emission lines in their spectra, and carried out the first systematic study of such galaxies (Seyfert 1943). These galaxies have since been called “Seyfert galaxies” and they are categorised into sub-groups according to their emission-line properties (Section 1.2).

After the first detection of cosmic radio waves by Jansky (1933), Reber (1944) provided a detailed map of the sky at 160 MHz showing most of the notable features of the Galactic radiation (such as the concentration of the radiation towards the plane of the Milky Way and the peak at the Galactic centre). Since the end of World War II radio astronomy has strongly evolved. Hey et al. (1946) made the discovery of a discrete source in Cygnus while surveying the Milky Way at 60 MHz and the first optical identifications of discrete sources were presented by Bolton et al. (1949). All these investigations were followed by radio surveys. The first radio survey (1C survey) was carried out by Ryle et al. (1950). This was followed by the 2C survey (Shakeshaft et al. 1955) that mapped around 2000 sources, most of which were thought to be Galactic objects. It was suspected by radio astronomers that the detections in the 2C survey were dominated by spurious sources due to low-resolution of the radio interferometer: Mills & Slee (1957) carried out a survey of radio sources in a limited region of the sky which had overlap with the 2C survey area and comparison of the catalogues of these surveys showed that actually both 1C and 2C surveys were confusion-limited. This was followed by other successful radio surveys such as the third Cambridge survey (Edge et al. 1959, 3C), the third Cambridge revision survey (Bennett & Smith 1961, 3CR), the fourth Cambridge survey (Gower et al. 1967, 4C), the Parkes radio survey (Ekers 1969, PKS) and the Ohio radio survey (Ehman et al. 1970). The 3C survey was probably the first successful radio survey to deal with the discrepancies found between the earlier surveys.

Optical identifications of some of the radio sources found in the surveys confused scientists, as they looked like stars on optical images. However, their spectra had broad emission lines at wavelengths where lines had not been identified before (Matthews & Sandage 1963). In fact, the four lines (H_γ , H_β , H_σ and H_ϵ) identified in the spectrum of 3C 273 agreed well with a redshift of $z \sim 0.15$. This allowed Schmidt to identify the hydrogen Balmer-series emission lines and Mg II $\lambda 2798$ in the spectrum of 3C 273 (Schmidt 1963). This motivated the spectral analyses of other radio sources.

Since the nature of these sources was not understood at the time, they were called ‘quasi-stellar radio sources (quasars)’. The most intriguing fact about these objects was that they had enormous luminosities at large distances. The physics behind the extreme luminosities of these objects then gained attention. For instance, accretion onto a super-massive black hole (SMBH) was proposed to be the power source of quasars (e.g. Zel’dovich & Rees 1964; Salpeter 1964). Their role in galaxy formation and evolution was also foreseen; for example Burbidge et al. (1963) discussed the fact

that activity of galaxy nuclei may affect the structure and evolution of galaxies. Considering their large distances, quasars also became popular cosmological probes. All these results motivated the search for new quasars. With subsequent surveys numerous quasars and active galaxies were discovered at different redshifts and these samples of galaxies have allowed astronomers to investigate various properties of these objects such as the energy source, the nature of their structures etc.

1.2 Properties of active galactic nuclei

Active galactic nuclei (AGN) can be loosely defined as the active central regions of massive galaxies which manifest themselves by substantial energy release leading to observable radiation. In commonly accepted models, the enormous power required to produce the observed emission is generated by accretion of material on to black holes in the centre of these galaxies (Kormendy & Richstone 1995; Magorrian et al. 1998; Ferrarese & Merritt 2000). In time, observations showed that AGN can be found in many ways! In the next section, I will introduce our current understanding of the structures of these objects and their observational signatures. The structures explained below may not be components of all types of AGN; these particular types of object will be discussed in Section 1.3.1.

1.2.1 Central source and accretion disc

As mentioned in the previous section, in the current view of AGN, every active galaxy contains a SMBH. The effective size of the black hole is defined by its Schwarzschild radius according to General Relativity. The position of the event horizon of a black hole is defined by the Schwarzschild radius and below this radius no light escapes. The masses of massive black holes at the centre of galaxies are expected to be in the range of $10^6 - 10^{10} M_{\odot}$ (e.g. Gültekin et al. 2009; McConnell & Ma 2013).

According to current models black hole seeds can be formed either by a direct collapse of massive gas regions and form massive seeds (e.g. Bromm et al. 2002) or by the death of the very first stars forming low-mass seeds (e.g. Haehnelt & Rees 1993). These black hole seeds then grow to massive black holes (Rees 1984). The growth of black holes is suggested to be through mass accretion (e.g. Shakura & Sunyaev 1973; Rees 1984) and the energy source of active galaxies is the accretion of mass (gas, dust and stellar matter). When the matter does not have sufficient energy to escape from the

gravitational influence of the black hole it will sit on a stable orbit around the SMBH. By a continuous process of particle interaction (viscous drag) orbiting matter at large radii will move to smaller radii transferring angular momentum outwards and mass inwards. Therefore, instead of a direct fall of matter into the SMBH the matter will form a disk around it. The scale size of an accretion disk depends on the mass of a black hole and the rate of accretion (Frank et al. 2002).

The luminosity produced due to accretion can be defined as:

$$L_{acc} = \eta \dot{M} c^2, \quad (1.1)$$

where η (a dimensionless quantity) is the efficiency of the conversion of mass to energy, \dot{M} is the accretion rate and c is the speed of light. The theoretical maximum value of η depends on the position of the inner edge (correspondingly spin) and can range between 0.05 (for non-spinning black hole) and $\simeq 0.4$ (for a spinning black hole at its maximum, e.g. Frank et al. 2002; Middleton 2015; Tchekhovskoy 2015). For a typical AGN, it is roughly $\eta \approx 0.1$ (e.g. Frank et al. 2002). It can be seen that the energy generation by a SMBH does not directly depend on the mass of the black hole (although the accretion rate and η are related to the black hole mass). However, the radiation pressure generated by the emitting matter regulates the accretion onto the SMBH: for a given mass there will be an upper limit on the luminosity (or accretion rate) at which the radiation pressure overcomes the gravity and stops accretion (Eddington 1925). This is called the Eddington luminosity and is given by:

$$L_{edd} = \frac{4\pi G M_{BH} m_p c}{\sigma_T}, \quad (1.2)$$

where M_{BH} is the mass of the black hole, m_p is the mass of the proton, σ_T is the cross-section of the electron and c is the speed of light. Here it is assumed that accretion is spherically symmetric (e.g. Bondi accretion, Bondi 1952) at a steady rate. At small accretion rates the accretion luminosity will be smaller than the Eddington luminosity. Thin-disk accretion occurs whenever the luminosity of the accretion is between 1% and a few times 10% of the Eddington luminosity (e.g. Tchekhovskoy 2015).

The characteristic temperature of the inner parts of the accretion disk, where most of the thermal energy is radiated, is around 10^5 K. If the disk is Keplerian, optically thick and geometrically thin with $H/R \ll 1$ ($\approx c_s/\nu$; c_s is the sound speed and ν is the rotational speed, H :the thickness of the disk, R :the radius of the disk), the radiation from the thin disk accretion can be modelled by a sum of black bodies of different

temperatures depending on radius. The radiation from the inner region peaks at the ultra-violet (UV) and optical emission mainly arise from the outer regions of the disk (Frank et al. 2002).

Radiatively inefficient accretion

There are also accretion mechanisms which differ from the standard thin disk accretion and I briefly discuss these in this section.

An advection-dominated accretion flow (ADAF; Narayan & Yi 1994, 1995a,b) is one of the mechanisms that differ from the standard thin disk accretion. ADAFs can show variations based on the roles of convection and outflows: adiabatic inflow-outflow solution (ADIOS; Blandford & Begelman 1999) and convection-dominated accretion flow (CDAF; Narayan et al. 2000). According to the ADAF model, once the accretion rate ($\dot{m} \equiv \dot{M}/\dot{M}_{Edd}$ where \dot{M} is the black hole accretion rate and \dot{M}_{Edd} is the Eddington accretion rate) drops to significantly low levels an ADAF solution is expected. At low accretion rates the density of inflowing matter will be low (as the cooling time scale is inversely proportional to density) so the accretion flow does not have enough time to cool and form a thin disk and the gravitational potential energy released due to accretion will not be radiated immediately. Instead, the energy is trapped into the accretion flow and advected into the SMBH with only a little radiation being emitted (i.e radiatively inefficient). In that case, the flow has a different accretion temperature: the temperature of the accretion is expected to be almost virial (that is, much larger than the thin disk accretion). The high temperature of the gas causes the disk to puff up and become geometrically thick ($H/R \sim 0.5$) and optically thin. The radiative efficiency from Eq. 1.1 can be derived as:

$$\eta \equiv \frac{L_{acc}}{\dot{M}c^2} \quad (1.3)$$

which is expected to be lower than 0.01 for radiatively inefficient accretion. The ADAF model (e.g. Narayan et al. 1995) and its updated versions (radiatively inefficient accretion flow-RIAF) have been applied to Sagittarius A* (Sgr A*) and the findings explain most of the features of this source (e.g. Yuan et al. 2003, 2004).

In the CDAF model the outward transport by viscous stress is equal to the inward angular momentum transport by convection and the net accretion rate is very small (Narayan et al. 2000; Quataert & Gruzinov 2000; Igumenshchev 2002). The

main assumption is that a hot accretion flow is considered to be convectively unstable (Narayan & Yi 1994). Whether the CDAF model can be applied to the numerical magneto-hydrodynamic (MHD) simulations is still a matter of debate (e.g. Stone & Pringle 2001; Narayan et al. 2002).

In the ADIOS model mass loss in a wind is considered to be a reason for the inward decrease of the accretion rate (Yuan & Narayan 2014). However, in this model how the wind is produced is not explained. Furthermore, the mass-loss index is used as a free parameter ranging between 0 and 1. In his most recent work Begelman (2012) uses a version of the ADIOS model in which the mass-loss index was found to be close to unity which is much different than what simulations find. A recent review on hot accretion flows around black holes can be found in Yuan & Narayan (2014).

At lower accretion rates the radial velocity is expected to be larger than that found in a thin disk. Since the gas close to the black hole has high temperatures with large radial velocities, the emitted radiation is expected to be dominated by synchrotron (hybrid thermal–non-thermal; e.g. Özel et al. 2000), inverse-Compton and bremsstrahlung (e.g. Narayan & Raymond 1999), modified by Comptonisation instead of a blackbody (Yuan & Narayan 2014). The observed synchrotron emission from Sgr A* supports this picture of the expected radiation processes (e.g. Yuan et al. 2003).

Super-Eddington accretion

There may also be an accretion state at which the accretion luminosity can be above the Eddington luminosity ($L_{acc} > L_{Edd}$). In this case, with increasing accretion rate the thickness, density and radial velocity of the disk increase. In this state of accretion the disk is optically thick. The time scale for the photons to diffuse out of the disk becomes large and the photons cannot leave the accretion flow. Therefore, this type of accretion state (super-Eddington accretion state) also ends up with very little radiation (i.e. radiatively-inefficient; Tchekhovskoy 2015).

1.2.2 X-ray emitting corona

Rapid variability of the X-ray emission of AGN indicates that X-ray photons are produced in the inner, compact region of the AGN. In most models, it is thought that a disk ‘corona’ is generated by electrons near their virial temperature. The X-ray and γ -ray photons are generated by inverse-Compton scattering of the optical/UV continuum photons from the disk (or photons from a jet) by the hot ($kT \approx 10^9$ K) corona. The

geometry of the corona is unknown; however, it is often assumed to be spherical (e.g. Haardt 1993). The coupling between the disk and corona is also not well understood (Haardt & Maraschi 1991).

1.2.3 Emission line regions

Spectral observations of AGN showed that they can present highly ionised emission lines in their optical spectra. There are two different types of transition lines that can be observed: permitted lines (e.g. H_α , H_β , Mg II) which occur due to photoionisation of atoms in the clouds of broad emission-line region (BLR) by the AGN radiation, and forbidden lines (e.g. [OIII] $\lambda\lambda$ 4959, 5007, [OII] λ 3727, [NII] λ 6717), which occur because the low density nature of the clouds in the narrow emission-line region (NLR) does not allow collisional de-excitation (Peterson 1997). Detailed analysis of the emission lines provides useful information about the central engine and the ionised gas in the central region, such as the density, geometry of the gas and the pressure of the medium (Robson 1996).

In the BLR, hot (with T_{eff} order of $\sim 10^4$ K) gas clouds move with high velocities of up to $10,000 \text{ km s}^{-1}$. Among the emission-line regions the BLR is the closest to the central core (within ~ 1 pc of the central region). The size and shape of the region is not clearly known although its geometry and size can be understood by studies of the emission-line response to the AGN continuum variability (AGN reverberation mapping, e.g. Peterson 1993). The density of the clouds in this region can be as high as $\sim 10^{16} \text{ m}^{-3}$, so almost all forbidden lines are collisionally de-excited and we do not observe forbidden lines (Osterbrock 1989; Rees et al. 1989). The emission lines that are generated in the BLR are intrinsically narrow and are broadened due to the Doppler effect.

On the other hand, the NLR is situated further away from the central engine, at around 10-100 pc, and in this region gas clouds can have cooler temperatures ($\sim 5,000$ K) although the electron temperature is expected to change with the changing density of electrons. They also have a broad range of densities and velocities, up to $\sim 900 \text{ km s}^{-1}$. Emission lines in the NLR are also very important for AGN studies because the gas in this region is extended to large distances and can be spatially resolved in the optical, which allows us to gain information about the distribution and kinematics of the emission-line gas.

Narrow emission-line flux ratios have been widely used to diagnose the photo-ionising source in galaxies. The ‘‘Baldwin, Phillips & Terlevich’’ (BPT) diagram was

the first emission-line diagnostic diagram, proposed by Baldwin et al. (1981). Commonly used narrow emission lines in BPT type diagnostic diagrams are [OIII] λ 5007, H_{α} , H_{β} , [NII] λ 6584 (Fig. 1.1 shows an example of a typical BPT diagram). There are three main excitation mechanisms that can cause these emission lines: (i) photoionisation by O and B stars, (ii) photoionisation by AGN and (iii) shock-wave heating. Since AGN are capable of producing more energetic photons than stars they occupy the upper right part of the diagram, whereas star-forming galaxies populate a sequence from the upper left to the lower centre as a consequence of having lower ionisation parameters.

Emission lines can be observed in the X-ray spectra of AGN. The main processes that cause these lines are fluorescence in the inner part of the cold accretion disk (which corresponds to thermal emission up to 2keV) and photoionisation (corresponding to the Fe-K $n=2-1$ transition of iron at energy 6.4 keV, Matt et al. 1997).

1.2.4 Torus

In 1985, spectropolarimetric studies of the typical Seyfert 2 active galaxy NGC 1068 revealed broad emission lines in polarised light (Antonucci & Miller 1985). Being able to see broad emission lines only in polarised light means that the direct view of the BLR is blocked by a structure. This structure was thought to be composed of dust as it obscures almost all direct emission from the BLR; free-free electron scattering outside the torus allows us to see a small fraction of the BLR, polarized as a result of the scattering. This study provided the first observational evidence for an optically thick, gas and dust structure in active galaxies which is now commonly called the “AGN torus” (Fig. 1.5). Models that try to unify different observational properties of AGN make use of the presence of a torus and the viewing angle of the AGN (e.g. Barthel 1989; Antonucci 1993; Urry & Padovani 1995). This will be discussed in Section 1.3.4.

The AGN torus surrounds the central region and the BLR at pc scales but the NLR can still be observed from any direction as it is extended. The bulk of material in the torus is warm ($T \sim 1000 - 2000\text{K}$) and dust sublimation defines the inner edge of the torus (to be able to form a dusty structure close to the central engine which emits at around $2 \mu\text{m}$ it should be close to the sublimation temperature) as well as the outer boundary of BLR. Near-IR reverberation mapping of AGN also supports this picture (Kishimoto et al. 2011). NGC 1068 and Circinus are Seyfert 2 active galaxies and have detailed mid-IR interferometric studies (e.g. Jaffe et al. 2004; Tristram et al.

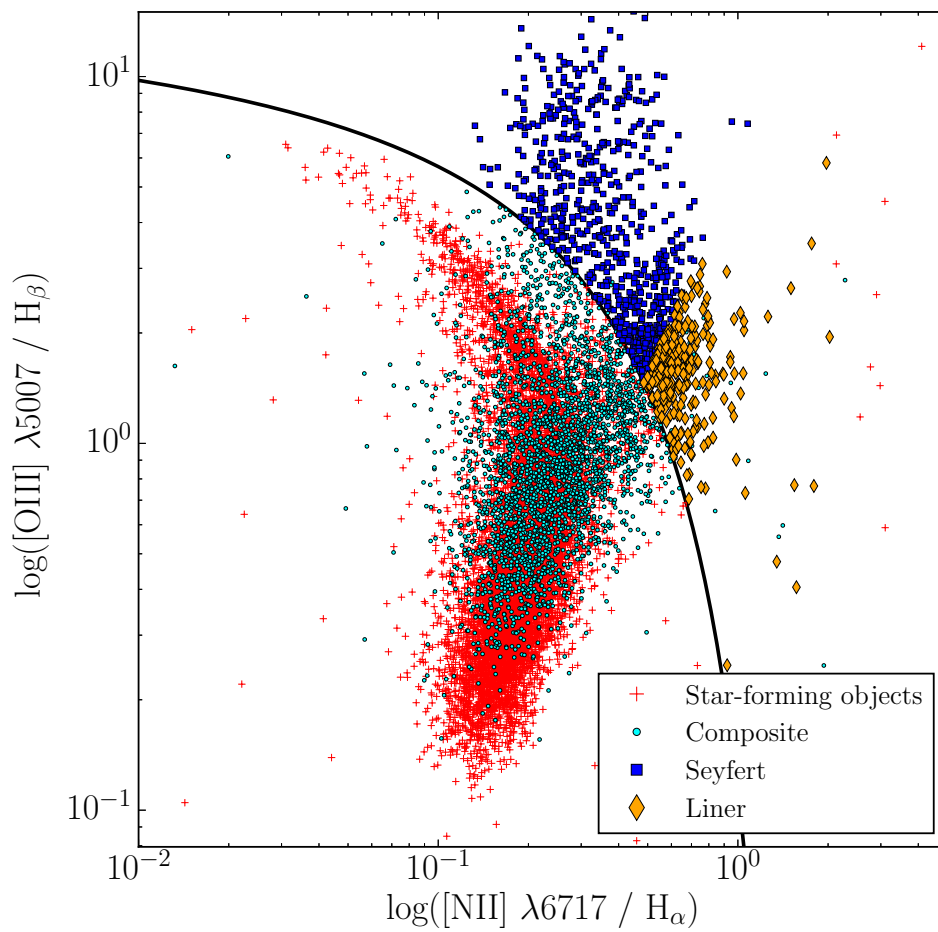


Figure 1.1: Example of an emission-line diagnostic diagram using the ratio of emission-lines $[\text{NII}]/[\text{H}\alpha]$ and $[\text{OIII}]/[\text{H}\beta]$ (Chapter 4).

2007). Investigations of the torus structure in these galaxies showed that the torus can be modelled as a two-component dust distribution: the inner component is 0.5 pc, thick, hot ($T > 800\text{K}$) and present an elongation; the other component is 3-4 pc, colder ($T \sim 300\text{K}$) and present less elongation (e.g. Jaffe et al. 2004; Tristram et al. 2007). The broad range of the mid-IR SED of AGN has been explained by a clumpy torus structure in which the clouds have a range of temperatures (e.g. Nenkova et al. 2002, 2008a). The torus is stabilised mainly by the velocity dispersion of these clouds, through thermal and radiation pressure. The geometry of the torus (a thick doughnut shape) is due to the frictional heating between the clouds (with rotational speeds $> 100 \text{ km s}^{-1}$) as well as turbulence induced by supernovae and nuclear stellar winds (e.g. Hönig et al. 2006). Most of the continuum emission produced by the central engine will be intercepted if the torus is on the observer's line of sight and the bulk of this emission will re-radiate in the mid-IR. However, we may still expect to see some contribution from the torus in the near- and far-IR (e.g. Riffel et al. 2009). Figure 1.4 shows an example of SED of an AGN with and without strong radio emission.

1.3 Classification of active galactic nuclei

In order to provide an overall picture of AGN, models were proposed to unify these various observational properties (e.g. Antonucci 1993; Urry & Padovani 1995). Different classification schemes have been proposed based on the observed properties of active galaxies at different wavelengths. Although all these classifications and models help us to understand AGN, there is no single model/scheme that can unify all the different observational features of these sources. This is because several parameters (such as evolution, environment and the properties of the central engine) are involved. I will only briefly describe AGN classes as the detailed properties of different classes of objects are not within the scope of this work.

1.3.1 Radio galaxies

Radio galaxies are active galaxies with characteristic extended features, observed mostly in the radio. These structures are briefly described in the next section. They are typically identified with elliptical galaxies (e.g. Donzelli et al. 2007) although there are exceptions (e.g. Croston et al. 2007; Mingo et al. 2011). They can show emission lines

in their spectra, and they can be classified with respect to their emission lines as high-excitation radio galaxies (HERGs) and low-excitation radio galaxies (LERGs). Details of the emission-line classification are given in the following section.

Observational radio properties and morphologies of powerful radio sources also vary. Fanaroff & Riley (1974) classified radio sources as FR I and FR II with respect to the surface brightness of radio jets and lobes. Radio objects that are bright in the core and dimmer at the extended parts are identified as FR I. On the other hand, FR II sources have brighter radio lobes and fainter radio cores. The FR I/II classification is correlated with radio luminosity. Although it is primarily a morphological classification, two types of radio galaxies were found to be divided by radio luminosity ($L_{178\text{-MHz}} \sim 2 \times 10^{25} \text{W Hz sr}^{-1}$, Fanaroff & Riley 1974; Owen & Ledlow 1994).

The jet properties of the FR II and FR I sources are different. FR II objects have well-collimated, narrow angle jets which can extend to very high distances (e.g. Mullin et al. 2006). On the other hand, the jets associated with FR I objects cannot reach these large distances while maintaining relativistic speeds due to entrainment which cause them to decelerate in kiloparsec scales (e.g. Reynolds et al. 1996; Wykes et al. 2013). Fig. 1.2 shows some examples of these sources. The terminology used to describe to diverse observed radio structures is explained in the next section.

Large scale structures of strong radio sources: Jets, Hotspots and Lobes

If an active galaxy is a strong radio source (a radio galaxy or a radio quasar) we may expect to see large scale, extended structures at radio wavelengths. About 10% of AGN are known to present these features and I will briefly explain these structures of radio galaxies in this Section.

- **Jets:** A jet can be defined as a well-collimated relativistic flow that can extend to distances from kpc to Mpc. The formation of jets occurs in the vicinity of the central engine, although the launching mechanism is not clear. Magnetic field is often involved in theories of jet production (e.g. McKinney & Blandford 2009); for a review see Donzelli et al. (2007). Jets can be observed at optical, radio and X-ray wavelengths, and synchrotron and inverse-Compton (IC) are the main processes responsible for this radiation.

The full derivation of the synchrotron theory is outside the scope of this work so I will provide a brief summary of it. For a comprehensive treatment, I refer to Rybicki & Lightman (1979); Hughes (1991); Longair (2011); Hardcastle (2015).

Synchrotron radiation originates from the interactions of relativistic electrons (and/or positrons) with a magnetic field. Electrons orbit helically in the magnetic field and the characteristic frequency of the electromagnetic radiation is given by (Rybicki & Lightman 1979):

$$\nu \approx \gamma^2 \frac{eB}{2\pi m_e} \quad (1.4)$$

where B is the strength of the magnetic field, e and m_e are the charge of the electron and the mass of the electron, respectively, and γ is the Lorentz factor of the electron.

Since the particle is radiating it will be losing its energy (i.e. cooling). The mean rate of energy loss of a synchrotron-radiating electron is then given by:

$$\frac{dE}{dt} = \frac{4}{3} \sigma_T c U_B \gamma^2 \quad (1.5)$$

where σ_T is the Thompson cross-section. U_B is the energy density in the magnetic field that is given as $U_B = B^2/2\mu_0$ where B is the magnetic field and μ_0 is the permeability of a vacuum. The time scale for energy loss will be equal to

$$\tau = \frac{E}{dE/dt} = \frac{3mc}{4\sigma_T U_B \gamma} \quad (1.6)$$

This means that at higher frequencies (correspondingly at higher energies) emitting electrons have shorter lifetimes. These characteristics of synchrotron radiation have important implications for the relation investigated in Chapter 6.

The power emitted by a single electron peaks around its characteristic frequency. Summing these quantities for an ensemble of relativistic electrons with differing energies gives us the total synchrotron radiation intensity. If we assume that the electron energy spectrum follows a power law:

$$N(E) \propto N_0 E^{-s} dE \quad (1.7)$$

where s is the index of the electron power law distribution, then synchrotron emissivity of an ensemble of electrons in terms of frequency per volume of space can be derived by integrating over a range of electron energies assuming a uniform magnetic field (Rybicki & Lightman 1979):

$$J(\nu) = \int_{E_{min}}^{E_{max}} j_{(\nu)}(\nu) N(E) dE \quad (1.8)$$

where j_{ν} stands for the emissivity of an individual electron. Substituting Eq. 1.7 in Eq. 1.8 provides the following:

$$J(\nu) = \int_{E_{min}}^{E_{max}} j_{(\nu)}(\nu) N_0 E^{-s} dE \quad (1.9)$$

Here we are considering a simple model where the emissivity of an electron peaks around a critical frequency (ν) and we know that $\nu \propto E^2 B$, thus it can be shown that $j(\nu)$ is given by:

$$J_{\nu}(\nu) \propto N_0 B^{\frac{1-s}{2}} \nu^{\frac{1+s}{2}} \quad (1.10)$$

Here the logarithmic slope of the electron energy spectrum, $\alpha = \frac{s+1}{2}$. This relation relates the index of the electron energy distribution and the spectral index of the emitted synchrotron radiation energy spectrum. All these derivations were done by assuming the emission is optically thin. At lower frequencies we may expect to see some of photons being scattered by the plasma on their way out of the synchrotron emitting source (i.e. synchrotron self-absorption). This may have important consequences for the relation between star formation rate (SFR) and the low-frequency radio luminosity derived in Chapter 6.

Observations have shown that jets are mostly one-sided (e.g. Bridle & Perley 1984; Hardcastle et al. 1997); the explanation is the relative orientation of the source and relativistic bulk motions giving rise to Doppler boosting. Observations show that the apparent speed of FR II jets can vary between ~ 0.55 and $0.75c$ (e.g. Hardcastle et al. 1999; Mullin & Hardcastle 2009). The particle content of jets is still debated. The favoured models suggest that the major component is an electron-positron plasma (e.g. Dunn et al. 2006). On the other hand, normal matter is expected to be entrained when a jet interacts with the medium.

Another source of continuum emission is inverse-Compton scattering. When a charged particle with high energy interacts with a photon, the photon energy is boosted by the energy gained from the relativistic particle. A full derivation of the inverse-Compton scattering is outside the scope of this work: what follows is a brief summary. The energy loss rate of a relativistic electron that is exposed

to an isotropic photon field (e.g. the cosmic microwave background) is given by (Rybicki & Lightman 1979):

$$\frac{dE}{dt} = \frac{4}{3}\sigma_T c \gamma^2 U_{\text{photon}} \quad (1.11)$$

where σ_T is the Thompson intersection, c is the speed of light, γ is the Lorentz factor and U_{photon} is the energy density of the photon field. This equation also shows the close link between synchrotron emission and inverse-Compton emission, as inverse-Compton emission is the case of a relativistic electron interacting with a photon field, instead of a magnetic field, which is the case in synchrotron emission. We observe emission due to inverse-Compton scattering in hotspots, lobes and the corona (Haardt 1993; Celotti et al. 2001; Croston et al. 2005).

There is also thermal bremsstrahlung (free-free emission or braking radiation) emission which occurs when a free charged particle is accelerated due to another charged particle. This radiation is typically emitted from an optically thin gas although it may become optically thick and self-absorbed at longer wavelengths.

- **Hotspots:** When the collimated powerful jets from radio sources meet the ambient medium they decelerate through terminal shocks and form bright compact regions emitting at radio and X-ray wavelengths (e.g. Blandford & Rees 1974). These regions are known as “hotspots” (see Jenkins & McEllin 1977, Laing 1989 and Bridle et al. 1994 for different approaches to define a hotspot). This is a location of particle acceleration and magnetic field magnification by plasma instabilities (e.g. Hardcastle et al. 2007a; Tregillis et al. 2002). Hotspots are mainly associated with FR II type radio sources. Although hotspots are known as the jet termination point, the jets can terminate at different regions such as in the plumes, mainly observed in FR I type objects (e.g. Hardcastle & Sakelliou 2004). Studies of hotspots can provide important information about the jet-lobe plasma interactions (e.g. Leahy et al. 1997; Hardcastle 1999) and the physics of high energy particle acceleration, as FR II hotspots and FR I jets are the only locations that show direct evidence for particle acceleration¹ (e.g. Meisenheimer et al. 1989; Worrall et al. 2001; Hardcastle et al. 2007a). The spectral indices of these structures are less steep than those of radio lobes and this also indicates that hotspots have undergone less energy loss (i.e. younger) than the extended

¹See also Croston et al. (2009) for high-energy particle acceleration at radio-lobe shocks.

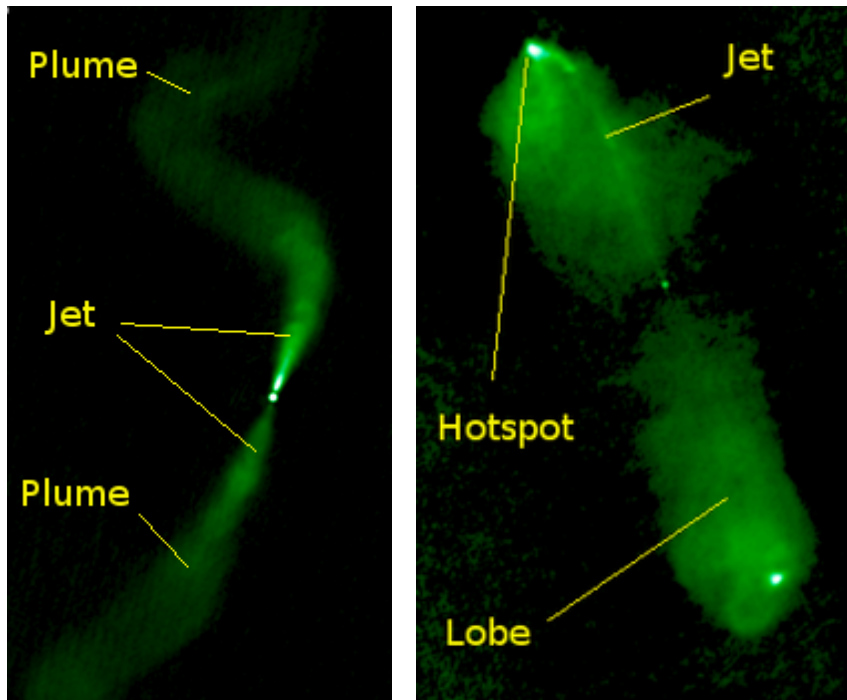


Figure 1.2: Radio images of FRI-I type radio source 3C31 (left) and FR II type of radio galaxy 3C98 (right). Credit:3C31&3C98/M.J.Hardcastle

radio emitting structures.

- **Lobes:** The accelerated plasma, after leaving the hotspots, is constrained by the medium to form the extended regions known as “lobes” (e.g. Longair et al. 1973; Scheuer 1974). These are the extended regions of emitting plasma (cocoon like structures) at radio wavelengths associated with all FR IIs and some FR Is. Lobes can have complex morphologies such as classical FR II lobes, plumes, tails, bridges and haloes. Plumes are mostly observed in low power radio sources like FR Is.

Emission line classification of radio galaxies

As mentioned above, radio galaxies can be classified with respect to their emission lines in the observed spectra as HERGs and LERGs. We mainly observe narrow and broad emission lines in the spectra of AGN, and some types of objects also show absorption lines. The separation of radio sources has been done mainly by using the ratio of the forbidden lines [OIII] and [OII] (e.g. Heckman 1980).

- **High-excitation radio galaxies**

Radio galaxies with broad and narrow emission lines (broad line radio galaxies – BLRGs) and radio galaxies with narrow emission lines only (narrow line radio galaxies – NLRGs) are identified as HERGs. The ionising continuum is thought to be powered by accretion of cold matter via a geometrically thin and optically thick accretion disk. HERGs follow the conventional picture of AGN and observations show that they have an accretion disk, a mid-infrared emitting torus (e.g. Haas et al. 2004) and an X-ray emitting corona (e.g. Hardcastle & Worrall 1999). AGN that do not show strong radio cores or extended emission (radio faint quasars and Seyfert I/II galaxies) have the same properties as HERGs; namely radiatively efficient accretion, emission-line regions and dusty torus, but they lack strong radio jets. Host galaxies of HERGs are mostly less massive elliptical galaxies than their low-excitation counterparts (discussed below). They are found in less dense environments and have blue colours (e.g. Janssen et al. 2012; Tasse et al. 2008; Smolčić 2009; Ineson et al. 2015). Their SFRs are lower than those of normal galaxies but perhaps slightly higher than their low-excitation cousins (Hardcastle et al. 2013, and Chapter 4).

- **Low-excitation radio galaxies**

Hine & Longair (1979) pointed out the existence of a population of radio galaxies that do not present the strong emission lines conventionally seen in powerful radio AGN (HERGs). This class of objects, called LERGs (Fig. 1.3), are predominantly found at low radio luminosities (e.g. Hardcastle et al. 2006, 2009; Mingo et al. 2014, and Chapter 3). This population poses a problem for simple unification (as discussed in Section 1.3.4), falling outside the generic picture derived from AGN without strong radio emission. They do not exhibit any expected feature of unified AGN, lacking a radiatively efficient accretion disk, an X-ray emitting corona (Evans et al. 2006; Hardcastle et al. 2006) and an obscuring torus in the mid-IR (Whysong & Antonucci 2004; Ogle et al. 2006). They also show low accretion rates with comparison to HERGs (e.g. Best & Heckman 2012; Mingo et al. 2014). All these properties of the different emission-line classes show that the emission-line strength is not the only difference between them (e.g. Hardcastle et al. 2007b).

In contrast to HERGs, the host galaxies of LERGs are massive elliptical galaxies. They are found in gas-rich environments. They have redder colours and SFRs much lower than those of HERGs. Observations show that LERGs have low radio luminosities and are found mostly at low redshift, although observations are biased towards to high power sources at high redshifts so more sensitive and deeper observations are necessary to obtain a full complete samples of LERGs; e.g. Mingo et al. (2014) and Chapter 3. LERGs also show little cosmological evolution whereas HERGs evolve rapidly across cosmic time (e.g. Best et al. 2014; Williams & Röttgering 2015).

The equivalent radio faint counterparts of these objects may be galaxies with low-ionisation nuclear emission-line regions (LINERs) although, as the name itself implies, the relationship between LINERs and AGN is unclear. This is because the LINER-type spectra can be produced by other mechanisms such as starburst-driven winds, cooling flows and in shock-heated gas (e.g. Heckman 1987; Filippenko 1992).

- **BL Lacertae**

There is another group of radio sources whose optical spectra show weak (or no) emission lines, although they can have absorption lines. They are called “BL Lacertae objects (BL Lacs)”. These are thought to be LERGs observed close to the axis of the relativistic jet so that the jet component dominates the continuum emission (Fig. 1.3). BL Lacs can show dramatic variability because the emission from the jet is strongly beamed. They can be classified into two sub-groups, based on their observed peak frequency: low-frequency peaked BL Lacs and high-frequency peaked BL Lacs (e.g. Padovani & Giommi 1995).

1.3.2 Seyfert galaxies

Seyfert galaxies are mostly associated with spiral galaxies (e.g. de Vaucouleurs & de Vaucouleurs 1968). They do not present strong radio emission relative to their UV/optical emission. They can show emission lines in their spectra. They can be divided into subgroups based on the width of their emission lines: Seyfert I galaxies which show only narrow emission lines, and Seyfert II galaxies that are characterised by narrow as well as broad emission lines (very similar to quasar spectra).

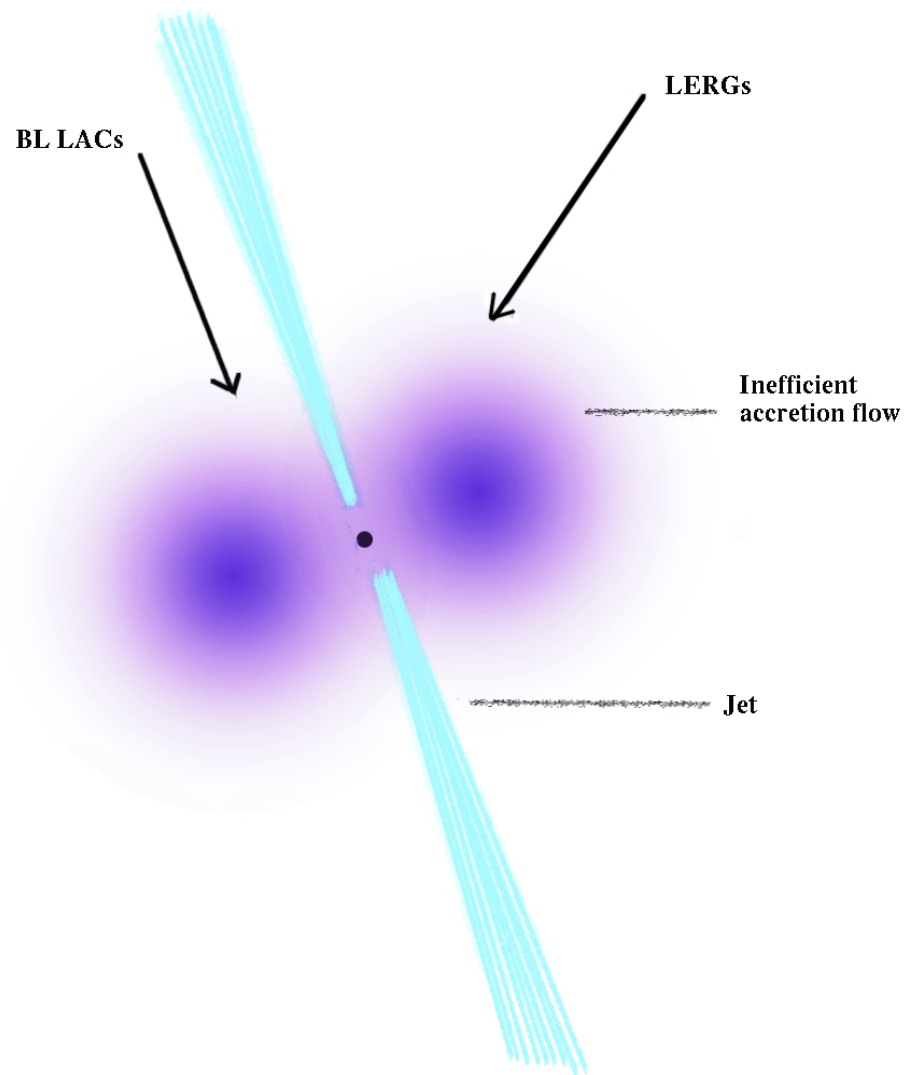


Figure 1.3: An example sketch of radiatively inefficient accretion and the classification based on a viewing angle are seen. The structure sizes are not to scale.

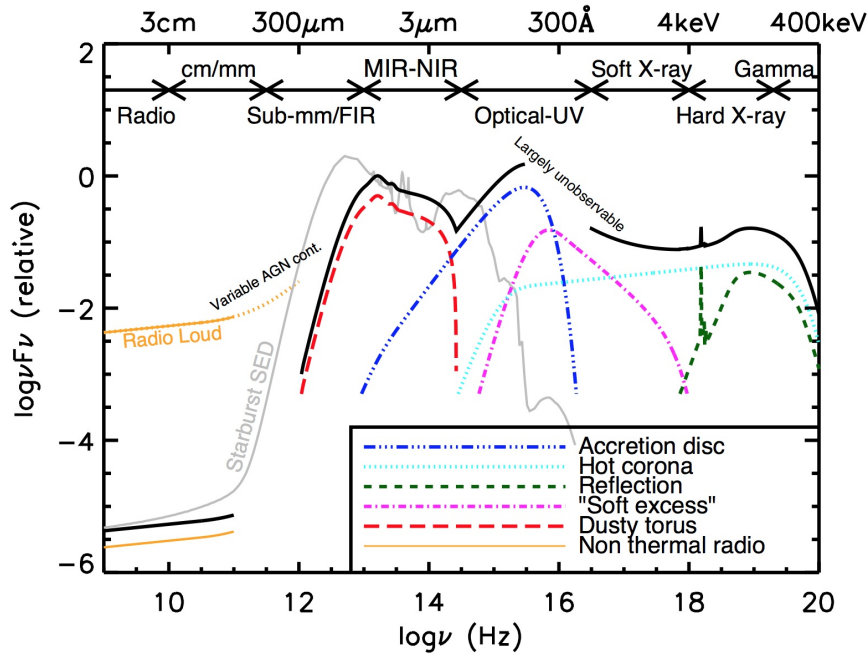


Figure 1.4: Example of the spectral energy distribution (SED) of an AGN with and without strong radio emission. The radio-loud/radio-quiet division was discussed in detail in Section 1.3.4. Credit:SED-AGN/C.Harrison

1.3.3 Quasars

In general, quasars have very high luminosities which outshine their host galaxies and they are observed as compact sources. Quasars also present emission lines in their spectra. Quasars can be classified as type I and type II quasars. In type II quasars the central region is obscured from the observer by large amount of gas and dust (e.g. Zakamska et al. 2005). They can also be divided into two groups based on their radio emission relative to the UV/optical emission: radio-loud quasars and radio-quiet quasars (e.g. Kellermann et al. 1989).

1.3.4 The unification model

The simple unification scheme of quasars and radio galaxies developed by Barthel (1989) is based on orientation dependent effects. According to this model, radio galaxies and quasars are the same objects seen at different angles. If a source is viewed within a cone of half-angle approximately 45° then the optical continuum emission can be observed and the object is called a quasar or a BLRG, if a source is seen edge-on, where the nucleus is blocked by the dusty torus, the source is then identified as

NLRG. The same model is also used to unify sources which do not have strong radio emission. In that case, sources seen face-on are called Seyfert I or radio-quiet quasars; sources observed edge-on are identified as Seyfert II galaxies or type II radio-quiet quasars. This simple unification model is also supported by various observation and is correct to some extent. However, LERGs do not show any feature of typical AGN and cannot be unified with quasars or NLRGs, as discussed in Section 1.3.1.

Classification of AGN

AGN with high radio luminosities form $\sim 10\%$ of all AGN population although the radio-loud phase may be intermittent (e.g. Best et al. 2005; Saikia et al. 2010). The remaining $\sim 90\%$ of AGN have also radio emission (Doi et al. 2013) but this is not as strong as we observe in radio galaxies and radio quasars (e.g. Condon 1992) and it may in some cases be due to entirely to star formation in the host galaxy (e.g. Zakamska et al. 2016). This difference revealed among observed AGN samples led to radio classification of these sources. There are various diagnostics using radio and optical measurements to classify sources as “radio-loud” or “radio-quiet” AGN (e.g. Kellermann 1964; Stocke et al. 1992). However, these diagnostics are based on using ratios of the radio flux (or luminosity) to the optical flux (or luminosity) where the optical flux is a combination of emission from the accretion, optical jet and stars. Therefore, these diagnostics cannot provide a clear information about the true nature of these sources; ideally we should classify these sources using their accretion and radio luminosities. Although I used classical terminology in my published works (Chapters 3 and 4), in this introduction I have avoided doing this.

“Why some AGN have strong radio jets and why some do not?” is a question that remains to be answered. There are different suggestions regarding this; for example, the black hole spin rate is one of the parameters that can affect the production of strong jets (Wilson & Colbert 1995, see also Reynolds 2015). Furthermore, the effects of magnetic fields cannot be neglected (e.g. Pudritz et al. 2012, references therein). It should also be noted that one of the biggest challenges in studies of radio sources is to estimate the total jet kinetic power. Various studies have shown that it is not straightforward to estimate the jet power and the effect of environment cannot be neglected (e.g. Hardcastle & Krause 2014; Godfrey & Shabala 2016).

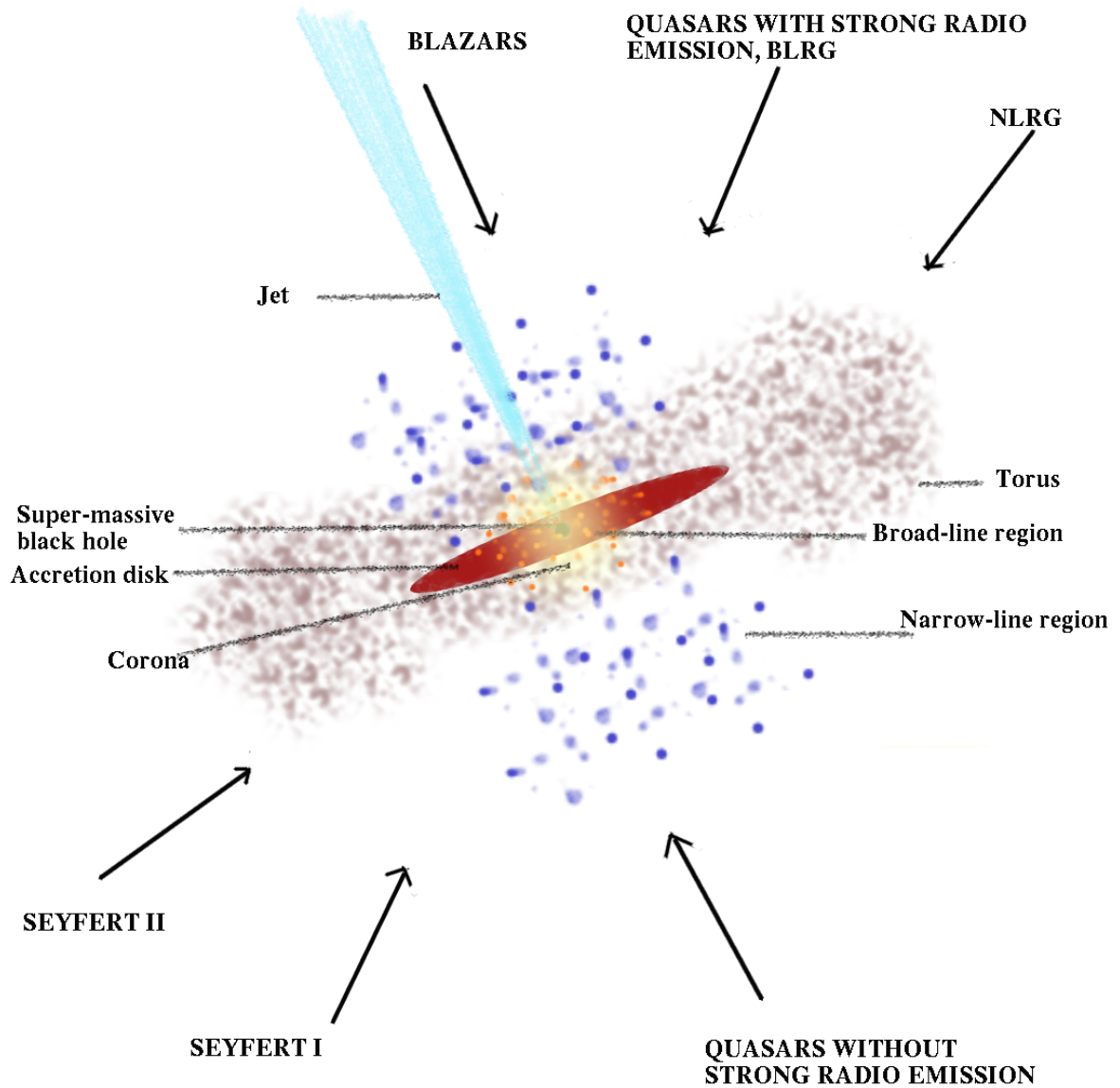


Figure 1.5: A graphic showing the expected structures of radiatively efficient AGN and the classification based on a viewing angle are seen, based on the illustration by Antonucci (1993) and Urry & Padovani (1995). The structure sizes are not to scale.

1.4 AGN and galaxy evolution

1.4.1 AGN activity, star formation and environments

As mentioned in Section 1.1.1 massive black holes grow via accretion of matter. The source of material accreted onto the massive black hole originates from scales much larger than the accretion disk, such as the host galaxy or intra-cluster medium (ICM). In order for matter to reach sub-parsec scales from larger scales some mechanisms that can cause the matter to lose its angular momentum and can transport it from large scales to smaller scales must be involved. These can be divided into secular processes (internal stellar processes, minor mergers or smooth accretion from the IGM and large-scale processes (galaxy interactions, major mergers etc., Hopkins et al. 2006, 2008). I will briefly discuss the results of studies in which AGN samples were evaluated in terms of the processes governing their growth, their host galaxy properties (star formation and morphology) and their environments. Recent reviews on the role of AGN in galaxy evolution and AGN feedback can be found in Alexander & Hickox (2012); Fabian (2012) and Heckman & Best (2014).

Different AGN samples have been studied to understand how massive black holes grow and what kind of mechanisms are involved. The results of some studies indicate that large scale interactions are not responsible for transporting the gas from AGN host galaxies to the sub-parsec scales (e.g. Wild et al. 2007; Reichard et al. 2009; Li et al. 2008) whereas there are studies with contrary findings (e.g. Ellison et al. 2011; Sabater et al. 2013; Ellison et al. 2013). The disagreement between these studies might be due to selection effects (such as using samples selected at different wavebands or using parameters derived in a different way etc.). In the case of radio AGN, it is hard to generate large samples of nearby HERGs (i.e. they are rare in the local Universe) as they are mostly found to have high luminosities. There are some investigations which find supporting evidence for merger interactions in the host galaxies of powerful HERGs (Heckman et al. 1986; Tasse et al. 2008; Tadhunter et al. 2011; Ramos Almeida et al. 2011). As I already noted above, low-luminosity radio AGN are common in the low redshift Universe and these objects are thought to have a different accretion mechanism (i.e. radiatively inefficient accretion). It is generally found that LERGs do not show any sign of mergers or strong tidal interactions in their host galaxies (e.g. Ellison et al. 2015). Secular processes are considered to be sufficient to move some of the available gas to the inner regions of galaxies to feed black holes (e.g. Ellison et al. 2011) in low accretion-rate systems at low redshifts. Some authors have compared the

star formation properties of radiatively efficient and inefficient radio AGN populations (Baldi & Capetti 2008; Herbert et al. 2010; Hardcastle et al. 2013). These works found different SFRs and SSFRs in the host galaxies of HERGs and LERGs. On the other hand, in Chapter 4, I show that there is only very tentative evidence for a difference between these types of sources when matched in AGN power.

The relation between star formation and AGN activity (luminosity or power) has gained much interest within the AGN community as it can provide important clues about the growth and evolution of galaxies. Investigations of this relation using samples from the local Universe have mixed results: some of these works find a correlation between star formation and AGN activity (e.g. Hao et al. 2005; Satyapal et al. 2005; Netzer 2009; Shi et al. 2009; Chen et al. 2013a, and Chapter 4) and some found no correlation (e.g. Harrison et al. 2012; Rosario et al. 2012; Rovilos et al. 2012; Mullaney et al. 2012; Bongiorno et al. 2012). The reasons for these differences are discussed in Chapter 4. Comparisons of AGN samples selected from different surveys show that they can have different host galaxy properties (e.g. Hickox et al. 2014). On the other hand, accumulating observational data on the distributions of cold gas and star formation show that the host galaxies of radiatively efficient AGN have a sufficient supply of cold gas on kiloparsec scales (e.g. Kauffmann et al. 2007; Hicks et al. 2013). Studies indicate that radiatively efficient AGN prefer less dense environments reinforcing the idea of different accretion modes (e.g. Kauffmann et al. 2004; Miller et al. 2003).

To summarise, it appears that the growth of radiatively efficient AGN in the local Universe does not require large scale interactions; instead secular processes (e.g. disk instabilities, minor mergers, recycled gas from dying stars, galaxy bars etc.) can efficiently drive the cold gas from host galaxies of radiatively active nuclei to the central regions. The same processes also seem to be responsible for the growth of LERGs which accrete in a radiatively inefficient manner. However, it should be noted that the source of accretion is most likely different for these sources as mentioned in the previous section. Hot gas in the IGM is thought to be accreted at a low level in LERGs through cooling (e.g. Best et al. 2005, 2006; Hardcastle et al. 2007b). Morphological studies of LERGs in the local Universe reinforce the idea of a different origin of the accreting gas as they are almost exclusively hosted by giant elliptical galaxies that sit in dense, hot gas-rich regions (e.g. Best et al. 2005; Ineson et al. 2015).

It is known that the prevalence of AGN is a strong function of stellar mass, although the slope of this function varies for different types of AGN (e.g. Best et al. 2005; Janssen et al. 2012). A comparison of the star formation properties of AGN samples

and local star-forming galaxies as a function of stellar mass clearly reveals that AGN have different SFRs/SSFRs from normal galaxies (e.g. Fig. 6 in Fumagalli et al. (2014), Fig. 2 in Heckman & Best (2014) and Fig. 4.10 in Chapter 4). A naive conclusion drawn from the observed differences in the SFRs/SSFRs of galaxy samples is that a typical galaxy evolves as a star-forming galaxy and the accretion of cold gas from its halo (or via mergers) increases its mass. When it reaches some critical mass, the supply of cold gas stops and the star formation is quenched. Afterwards, the galaxy continues to evolve and become a “red and dead” galaxy. The mass growth may continue through other processes such as subsequent mergers and interactions. A crucial point regarding this model is that theoretical models have had to invoke some processes to stop (or suppress) star formation and move the galaxy to the red and dead phase. I discuss the importance of these interactions for galaxy evolution in the next section.

The space density of low-luminosity AGN peaks around $z < 1$ and that of high-luminosity AGN peaks around $z \sim 2$ (e.g. Bongiorno et al. 2007; Rigby et al. 2011); this anti-hierarchical evolution of AGN is very similar to the cosmic downsizing of star forming galaxies (e.g. Cowie et al. 1996; Fontanot et al. 2009). Star formation studies of X-ray, IR or optical AGN also show that AGN host galaxies at high redshifts ($z \sim 2$) have star formation properties similar to normal star forming galaxies (e.g. Mainieri et al. 2011; Rosario et al. 2013). Large-scale processes may occur due to galaxy interactions or galaxy major mergers (e.g. Barnes & Hernquist 1992, 1996; García-Burillo et al. 2005). These strong gravitational torques may become important when we move to high redshifts. The morphologies of AGN samples at high redshifts often show signs of major mergers or interactions (e.g. Silverman et al. 2011; Kocevski et al. 2012) so the growth of massive black holes could be driven by these large scale interactions, although Mainieri et al. (2011) do not find evidence of mergers for the bulge-dominated galaxies in their sample. As we move to high redshifts we see that the number of radiatively efficient radio AGN increase but LERGs do not show the same evolution as the increase in the number density is less steep than that we observe for HERGs (e.g. Donoso et al. 2009; Simpson et al. 2012; Best et al. 2014). Since all radiatively efficient AGN (radio, IR, X-ray and optical) start dominating at higher redshifts and they prefer similar environments, we expect to observe comparable properties for the host galaxies of distant radiatively efficient AGN. It is worth noting that there is an indication of systematic differences among host galaxies of AGN selected at different wavelengths (e.g. Hickox et al. 2009; Juneau et al. 2013). The properties

of different classes of AGN population mentioned in this chapter are summarised in Figure 1.6, taken from Heckman & Best (2014).

1.4.2 AGN Feedback

How the central engine and the host galaxy relate to each other and bring about a strong relationship between the mass of SMBHs and their host galaxy properties (e.g. the galaxy luminosity, velocity and the galaxy bulge mass) has been an important question for galaxy formation and evolution research (e.g. Kormendy & Richstone 1995; Magorrian et al. 1998; Ferrarese & Merritt 2000; Gebhardt et al. 2000; Merritt & Ferrarese 2001; McLure & Dunlop 2002; Marconi & Hunt 2003; Gültekin et al. 2009). One way to model this interaction, which has been commonly invoked in the simulations to mirror the properties of massive galaxies observed in the local Universe, is a feedback mechanism from AGN (e.g. Springel et al. 2005; Bower et al. 2006; Croton et al. 2006). Two different feedback processes are invoked: ‘radiation dominated feedback’ and ‘kinetic feedback’. Although AGN feedback is mostly considered to be a negative effect (i.e. stopping or suppressing star formation) on the host galaxy the opposite may be the case for some systems. I provide further details about this in the following section where I separately discuss the two flavours of feedback processes.

- **Radiation dominated feedback**

Different names are used to describe this type of feedback such as ‘cold-mode’, ‘radiative-mode’ or ‘quasar-mode’. Accretion onto a galaxy is supposed to be halted by a quasar accreting at the Eddington limit (Silk & Rees 1998). In theory, this interaction can be achieved in two ways: radiation pressure on dusty gas or AGN wind. The interaction by either method has to be strong in order to be able to move the gas or dust out of the galaxy and stop (or suppress) star formation. In the case of radiation pressure it is thought that it works on dust embedded in the gas and drives galactic winds or outflows through momentum deposition which can expel the gas and affect the star formation at host galaxy scales (e.g. Fabian 1999; Murray et al. 2005). If the coupling is due to winds then this requires the winds to have high column densities, velocities and covering factors effective at large radius (e.g. King et al. 2011). The blue-shifted absorption lines observed in the ultraviolet (UV), optical and soft X-ray spectra of powerful quasars are the observational evidence of these outflows. However, since it is not straightforward to determine their physical properties (such as their column densities,

sizes etc.) the role of these outflows on the host galaxy scale remains uncertain. Although the dynamical and physical state of the ionised gas have been also considered as an observational indication of outflows, it is not certain whether these outflows were triggered by the small scale jets that were observed in radio faint sources (Veilleux et al. 2005; Rosario et al. 2010, references therein). We may expect to observe outflows in strong quasars and ultra-luminous infrared galaxies (ULIRGs; e.g. Fischer et al. 2010; Veilleux et al. 2013). However, it is uncertain whether the radiation produced by all types of radiatively efficient AGN can generate such outflows and define the fate of its host galaxy. Sources in which we may expect to see radiative feedback to occur are quasars and galaxies that are not strong radio sources as well as HERGs.

- **Kinetic feedback**

Other names used in the literature to describe this feedback are ‘hot-mode’, ‘radiatively inefficient’, ‘radio-mode’. In kinetic feedback, the production of jets through accretion of hot gas from the haloes of radio AGN or cooling is the dominant process restricting star formation in the host galaxy. Deposition of the energy from jets is expected to occur via radio bubbles rather than direct interaction of the jets with the medium. Indeed, the observed weak shocks or sound waves surrounding some radio bubbles can be considered as evidence for this type of feedback (e.g. Fabian et al. 2006). Cavities are inflated by the deposition of the jet energy through mechanical work and observations also show that in cavities and bubbles radio AGN can expel the hot gas either from their haloes or surrounding groups and clusters (e.g. McNamara et al. 2000; Fabian et al. 2006). This AGN activity in brightest cluster galaxies (BCGs) is suggested to be a solution to the ‘cooling flow problem’ as X-ray observations of cooling-flow clusters have revealed that the temperature of the central cores of these clusters do not fall to the predicted levels (e.g. David et al. 2001). Radio galaxies and radio-loud quasars are possible sources in which we may see this type of feedback as they can produce collimated jets. It is crucial to note that HERGs and radio-loud quasars also produce radiative output. Therefore, these objects can exhibit both types of feedback processes.

Hitherto, I have discussed the negative effect of AGN feedback. Some studies indicate that jets can affect their host environment in a positive way, in the sense that they can trigger star formation in the host galaxy rather than quenching it (e.g. Eales & Rawlings 1990; Best et al. 1998a; Jarvis et al. 2001b; Inskip et al.

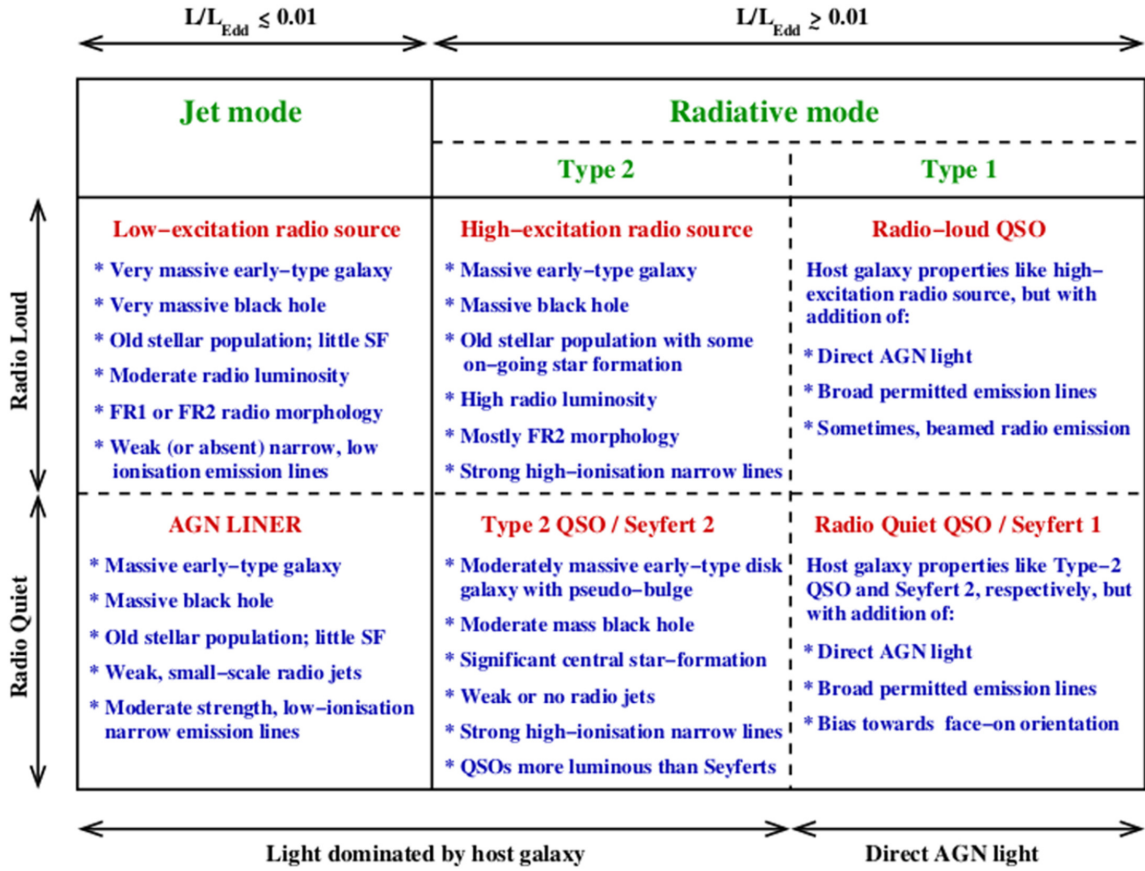


Figure 1.6: The schema presents different properties of AGN population (reproduced from Heckman & Best 2014).

2005). In this scenario, the radio jets drive shocks in the interstellar medium which enhance the star formation and cause a positive AGN feedback.

1.5 The correlation between far-IR and radio continuum in star-forming galaxies

As discussed in the previous sections, energy source for radio emission in active galaxies is connected to a super-massive black hole whereas in normal (non-active) galaxies radio emission is synchrotron radiation from relativistic electrons and free-free emission from HII regions. Both types of radiation are connected to star formation.

The star formation rate of a galaxy is a fundamental parameter of its evolutionary

state and various SFR indicators of galaxies have been used in the literature over the years. For recent reviews, see Kennicutt & Evans (2012) and Calzetti (2013). Two important SFR calibrations can be derived using the IR and radio continuum emission from galaxies. In the first of these, optical and ultraviolet emission from young stars (age ranges 0–100 Myr with masses up to several solar masses) is partially absorbed by larger dust grains (relative to grains whose emission peaks at shorter IR wavelengths) in the interstellar medium (ISM) of galaxies and re-emitted in the FIR. Therefore, the thermal FIR emission provides a probe of the energy released by star formation. On the other hand, radio emission from non-active galaxies is a combination of free-free emission from ionised gas due to massive stars and synchrotron emission which arises from charged particles accelerated by supernova explosions, the end products of massive stars. Therefore, radio emission (from non-active galaxies) can be used as an indirect probe of the recent number of massive stars and therefore of SFR.

In the early 1970s van der Kruit (1971, 1973) showed that a correlation exists between the FIR emission and radio emission from spiral galaxies. Since then this empirical relation (FIRC, hereafter) has been a topic of several studies aiming to understand the physical reasons behind the FIRC, its evolution (if it exists) and to explore what type of galaxies follow it (e.g. Harwit & Pacini 1975; Rickard & Harvey 1984; de Jong et al. 1985; Helou et al. 1985; Hummel et al. 1988; Condon 1992; Appleton et al. 2004; Jarvis et al. 2010; Ivison et al. 2010a,b; Bourne et al. 2011; Smith et al. 2014; Magnelli et al. 2015). Investigations of the FIRC showed that this correlation holds for galaxies ranging from dwarfs (e.g. Wu et al. 2008) to ultra-luminous infrared galaxies (ULIRGs; $L_{IR} \gtrsim 10^{12.5} L_{\odot}$; e.g. Yun et al. 2001) and is linear across this luminosity range. On the other hand, Bell (2003); Boyle et al. (2007) and Beswick et al. (2008) suggested that at low luminosities the FIRC may deviate from the tight well-known correlation. Although there are various factors which affect results obtained in these studies, one explanation for contradictory results might be the sensitivity limits of observations from which samples were derived.

The naive explanation of the linearity of this relation assumes that galaxies are electron *calorimeters* (all of the energy from the cosmic-ray electrons [CR e] is radiated away as radio synchrotron emission before these electrons escape the galaxies) and *UV calorimeters* [galaxies are optically thick in the UV light from young stars so that the intercepted UV emission is re-radiated in the far-IR: Voelk (1989)]. This latter assumption is probably not completely true, because the observed UV luminosities

and the observed far-IR luminosities from star-forming galaxies (SFGs) are similar to each other (e.g. Bell 2003; Martin et al. 2005). Furthermore, the electron calorimetry model might not hold either for our own galaxy or lower mass galaxies, as the typical synchrotron cooling time is expected to be longer than the inferred diffusion escape time of electron in these galaxies (e.g. Lisenfeld et al. 1996); non-thermal radio emission has been observed in the haloes of spiral galaxies (e.g. Heesen et al. 2009) which shows that the diffusion escape time of electrons is comparable to the typical energy loss time scale. Non-calorimeter theories have also been proposed (Helou & Bica 1993; Niklas & Beck 1997; Lacki et al. 2010). For example, Lacki et al. (2010) and Lacki & Thompson (2010) presented a non-calorimeter model taking into account different parameters (e.g. energy losses, the strength of magnetic field and gas density etc.) as a function of the gas surface density and argued that the correlation breaks down for low surface brightness dwarfs due to the escape of CR e . Such models imply that stellar mass (or galaxy size) has an effect in a non-calorimeter model. This is because the time scale for CR e to diffuse and escape the galaxy before they radiate all their energy in radio depends on the size of a galaxy.

As summarised above, since the 70's we have been observing this correlation between the IR flux densities, at 10–100 microns, and radio flux densities almost exclusively at GHz bands. Radio data used in these studies were at GHz bands because radio surveys were mostly carried out at these radio frequencies (e.g. Becker et al. 1995; Condon et al. 1998). In the far-IR, with *Herschel*, we have had a better understanding of the dust properties of galaxies (e.g. Hardcastle et al. 2010; Dunne et al. 2011; Smith et al. 2012a, 2013, 2014) as we are able to study large galaxy samples at larger far-IR wavelengths. In the radio, with new radio interferometer arrays such as the LOw-Frequency ARray (LOFAR) we are able to move toward lower radio frequencies, at which thermal radio emission becomes increasingly negligible. Therefore, one may expect to see variation in the FIRC at lower radio frequencies. This motivates another question to be answered: “Can the low-frequency radio luminosity be used to trace the SFR of local star-forming galaxies?” which has been investigated in Chapter 6.

1.6 Objectives and thesis outline

The main objective of this thesis is to study the properties of AGN and star-forming galaxies using multi-wavelength data to pursue answers to the following questions:

- Mid-IR studies of radio sources hitherto have been based on single sources or small or incomplete samples. In addition to this, due to the lack of complete mid-IR observations of radio samples, many investigations were carried out using incoherent data sets where the mid-IR observations were taken for a variety of purposes. In order to remove this deficit in radio-loud AGN research, I have provided a complete mid-IR study of a complete and relatively large sample by aiming to answer the following questions: Do the different emission-line classes of radio galaxies have characteristic mid-IR natures? How can we diagnose accretion modes in radio-loud AGN? How reliable are the infrared colour-colour diagrams to select AGN? What are their near- and mid-IR properties?
- In the past, star formation studies of AGN have mostly focused on high-redshift sources to observe the thermal dust emission that peaks in the far-infrared, which limited the samples to powerful objects. However, with *Herschel* we can expand this to low redshifts to provide insights into the following questions: What are the star formation properties of different types of AGN in the local Universe ($0 < z < 0.6$) as a function of their AGN activity? Do we see any differences in the star-formation properties of HERGs and LERGs in the local Universe? Whether any correlation exists or not, what can we learn about the growth of massive black holes in the contemporary Universe?
- Radio emission is a key indicator of star-formation activity in galaxies, but the relationship between star formation and radio luminosity has to date been studied almost exclusively at 1.4 GHz and above. At lower frequencies we would expect differences due to the reduced contribution from thermal emission. By utilising low-frequency radio data from LOFAR, the combination of *Herschel* and optical data provide excellent constraints on star-formation rates, I have carried out a detailed study of the low-frequency radio/star-formation relation in the nearby universe to answer questions such as “What can we learn from low-frequency radio observations with regard to the radio–FIR relation that we observe in local star-forming galaxies?”, “What is the relation between the low-frequency radio luminosity and star formation rate in these galaxies?”.

The analyses performed to study these issues can be divided into four main parts:

1. The near and mid-IR properties of radio-loud AGN and their accretion modes have been studied utilising Wide-field Infrared Survey Explorer (*WISE*) data.

For the project I used the 3CRR, 2Jy, 6CE and 7CE samples. The complete sample covers a redshift range $0 < z < 3.8$, which provides an opportunity to study radio sources both at low and high redshifts. Data from *WISE* allowed me to provide a complete mid-IR study of radio-loud AGN for the first time. For this reason, it has importance in radio-loud AGN research (Chapter 3).

2. The star formation properties of radio-loud and radio-quiet AGN as a function of their AGN activities have been explored. For this research I used the MPA-JHU sample which has galaxies at low redshifts ($0 < z < 0.6$) selected from the seventh data release of the Sloan Digital Sky Survey (SDSS). Their star formation properties were derived using data from *Herschel*. In order to take into account non-detections in *Herschel* bands I used a stacking analysis: I binned samples in AGN power and stacked their SFRs and specific star formation rates (SSFRs). The same process has been implemented for radio-loud and radio-quiet AGN samples as well as for HERGs and LERGs (Chapter 4).
3. A deep LOFAR survey of the *Herschel*-ATLAS North Galactic Pole (NGP) field has been carried out. In order to produce a catalogue of radio sources detected by LOFAR and to find their optical counterparts I developed software to look at images of all sources in the catalogue at radio and optical wavelengths. Image data were automatically obtained from FIRST, NVSS and SDSS. The catalogue I produced has been used to study AGN in the NGP field. Description of the data reduction, imaging and the cataloguing are presented in Chapter 5.
4. The relation between the low-frequency radio luminosity and star formation rate has been investigated using low-frequency radio data from LOFAR and star formation rates derived from SED fitting using MAGPHYS. In order to carry out this project I used a sample of local star-forming galaxies from the MPA-JHU catalogue. In my analysis I included non-detections and carried out a stacking analysis. I investigated the same relation for radio galaxies as well in order to evaluate emission-line diagnostics (Chapter 6).

Chapter 2

Data

“Any time scientists disagree, it’s because we have insufficient data. Then we can agree on what kind of data to get; we get the data; and the data solves the problem. Either I’m right, or you’re right, or we’re both wrong. And we move on. That kind of conflict resolution does not exist in politics or religion.”

Neil deGrasse Tyson

2.1 Introduction

In this chapter I will provide an overview of the telescopes and the data, used for my PhD projects. I will also summarise the catalogues that were utilised for the studies presented in this thesis. The following is a summary of the projects and the data used throughout my PhD:

1. **The infrared properties of complete samples of radio-loud AGN**

Near and mid-infrared data taken by the *Wide-Field Infrared Survey Explorer* (*WISE*, Wright et al. 2010a) telescope were used to carry out a complete infrared study of radio-loud AGN. Additionally, I utilised measurements taken with the *Spitzer* telescope (Werner et al. 2004), of the sample sources where available. Low-frequency radio flux densities were also available for two of my samples so these measurements were used for this project; these were the catalogues of

the 3CRR¹ (Bennett 1962; Laing et al. 1983) and 2Jy² samples (Wall & Peacock 1985; Tadhunter et al. 1993).

2. The connection between star formation and AGN activity in radio-loud and radio-quiet active galaxies

In order to study star formation properties of active galaxies, far-infrared flux densities of sources in the sample (star-forming objects and AGN), taken by the *Herschel* telescope were used. Other auxiliary data utilised for this project include mid-IR data taken by the *WISE* telescope, the Giant Meterwave Radio Telescope³ (GMRT) and the Faint Images of the Radio Sky at Twenty-cm (FIRST, Becker et al. 1995) measurements of sources in the sample (where available) and the Max Planck Institute for Astrophysics and John Hopkins University (MPA-JHU)⁴ catalogue containing optical emission line fluxes, SFRs derived using H α emission line (Brinchmann et al. 2004) and stellar masses (Kauffmann et al. 2003a; Salim et al. 2007) of the objects.

3. LOFAR survey of the *Herschel*-ATLAS North Galactic Pole (NGP) field

In an attempt to identify possible associations and optical counterparts of sources detected by the Low Frequency Array (LOFAR, van Haarlem et al. 2013), LOFAR maps were used (details of the data reduction are provided separately in Chapter 5). Auxiliary data used for this purpose are FIRST, the National Radio Astronomy Observatory (NRAO) VLA Sky Survey (NVSS Condon et al. 1998) and the seventh data release of Sloan Digital Sky Survey (DR7 SDSS, Abazajian et al. 2009) *r*-band images of the LOFAR sources, and the Half Million Quasar (HMQ, Flesch 2015) catalogue.

4. The low-frequency radio luminosity – star formation rate relation

LOFAR flux densities at 150 MHz of sources in the MPA-JHU catalogue (Chapter 5) and star formation rates from these objects derived using the Multi-wavelength Analysis of Galaxy Physical Properties code (MAGPHYS, da Cunha et al. 2008) were used for exploring the low-frequency radio luminosity – star formation rate relation in the low-redshift Universe ($z < 0.6$).

¹<http://3crr.extragalactic.info/>

²<http://2jy.extragalactic.info/>

³http://gmrt.ncra.tifr.res.in/gmrt_hpage/Users/Help/help.html

⁴<http://www.mpa-garching.mpg.de/SDSS/>

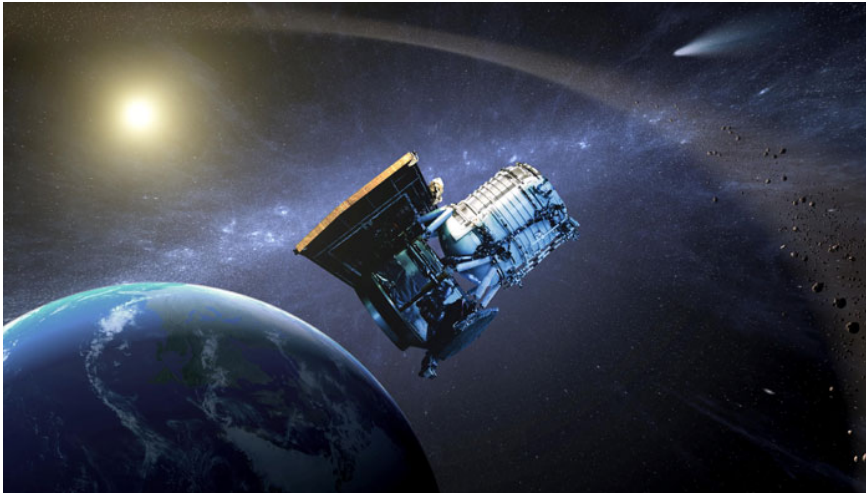


Figure 2.1: Artist's concept of the *WISE* telescope. Credit: NASA/JPL-Caltech

2.2 Near- and mid-infrared data

Near- and mid-infrared (IR) data taken by the *WISE* instrument were mainly used for the work given in the third chapter, and I also utilised the *WISE* data for the project presented in the fourth chapter.

WISE (Wright et al. 2010a) is a mission funded by NASA. It was launched in 2009 December 14 in order to map the whole sky by 2010 mid-July, taking overlapping snapshots, in four IR bands ($W1$ [$3.4 \mu\text{m}$], $W2$ [$4.6 \mu\text{m}$], $W3$ [$12 \mu\text{m}$], $W4$ [$22 \mu\text{m}$]) with an angular resolution of 6.1, 6.4, 6.5 and 12 arcsec, respectively. Fig. 2.2 shows the images of the same region on the sky at four *WISE* bands.

The *WISE* telescope is a four channel imager (Fig. 2.1) that operates in a single mode and has the following equipment:

- a 40-cm telescope with a 47 arcmin field of view and re-imaging optics
- a scan mirror to stabilise the line-of-sight while the spacecraft scans the sky
- detector arrays at 3.4, 4.6, 12, and 22 μm with a plate scale of 2.75 arcsec/pixel
- a two-stage solid-hydrogen cryostat to cool focal planes and optics

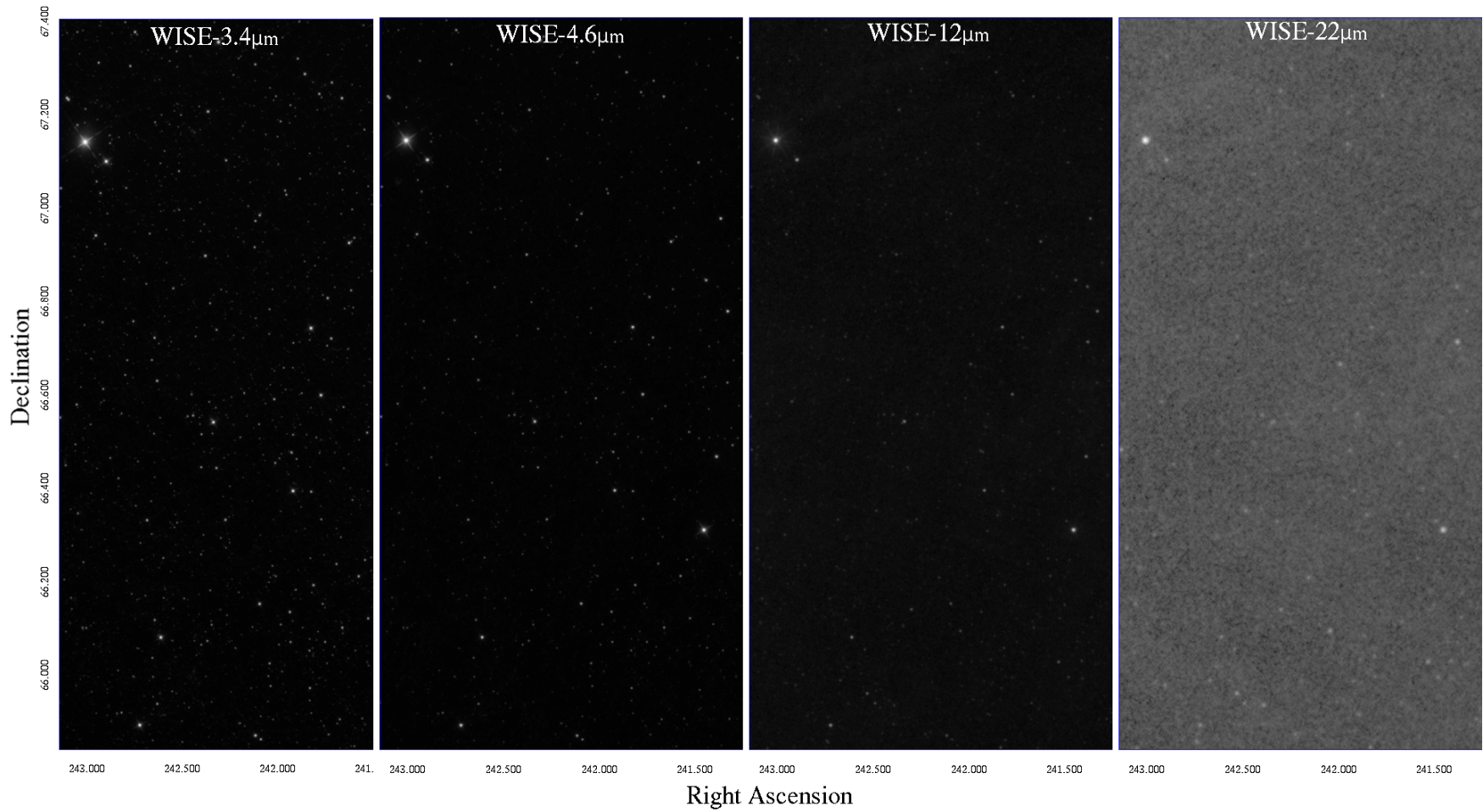


Figure 2.2: Example *WISE* images of the same region on the sky.

In order to measure near- and mid-IR flux densities of the radio-loud sample that was used in Chapter 3, the *WISE* all-sky catalogue was used. Using the NASA/Infrared Processing and Analysis Center (IPAC) infrared science archive⁵, the catalogue was searched for all objects in the sample within 10 arcsec. The expected number of sources within 10 arcsec is around 3.49×10^{-4} so that a source detected within the search region of a given position is very unlikely to be a false association: the total expected number of false detections is 0.12. Details of the catalogue search is given in Chapter 3.

As described in the next chapter, the *WISE* measurements are given in Vega magnitudes so the magnitudes of the sources were converted into Jy using the standard *WISE* zero-points⁶. Data from the *Spitzer* Space Telescope (Werner et al. 2004) were also utilised in order to explore the consistency between *WISE* and *Spitzer* measurements. Details of this comparison analysis and the derivation of the *WISE* luminosities in the four *WISE* bands are given in Chapter 3.

2.3 Far-infrared data

Far-IR data taken with the *Herschel* telescope for the *Herschel*-Astrophysical Terahertz Large Area Survey (H-ATLAS or *Herschel*-ATLAS Eales et al. 2010a) were used for the work presented in Chapter 4.

2.3.1 The *Herschel* telescope

The European Space Agency (ESA)'s *Herschel* Space Observatory (with participation from the National Aeronautics and Space Administration-NASA) is the largest infrared mission carried out to date and has the largest single mirror ever built for a space telescope. The telescope is a Cassegrain type telescope with a primary mirror diameter of 3.5 meters. Figure 2.3 shows the schematic view of the *Herschel* telescope and a size comparison to other space telescopes. The spacecraft was launched in 14 May 2009, with three-year lifetime, and was switched off in 17 June 2013⁷. The telescope has three scientific instruments:

- **Heterodyne Instrument for the Far Infrared (HIFI):** A high resolution heterodyne spectrometer with velocity resolutions better than 0.1 km s^{-1} (de Graauw

⁵<http://irsa.ipac.caltech.edu/frontpage/>

⁶The relation used for the conversion can be found at <http://wise2.ipac.caltech.edu/docs/release/allsky/expsup/>

⁷<http://sci.esa.int/herschel/34682-summary/>

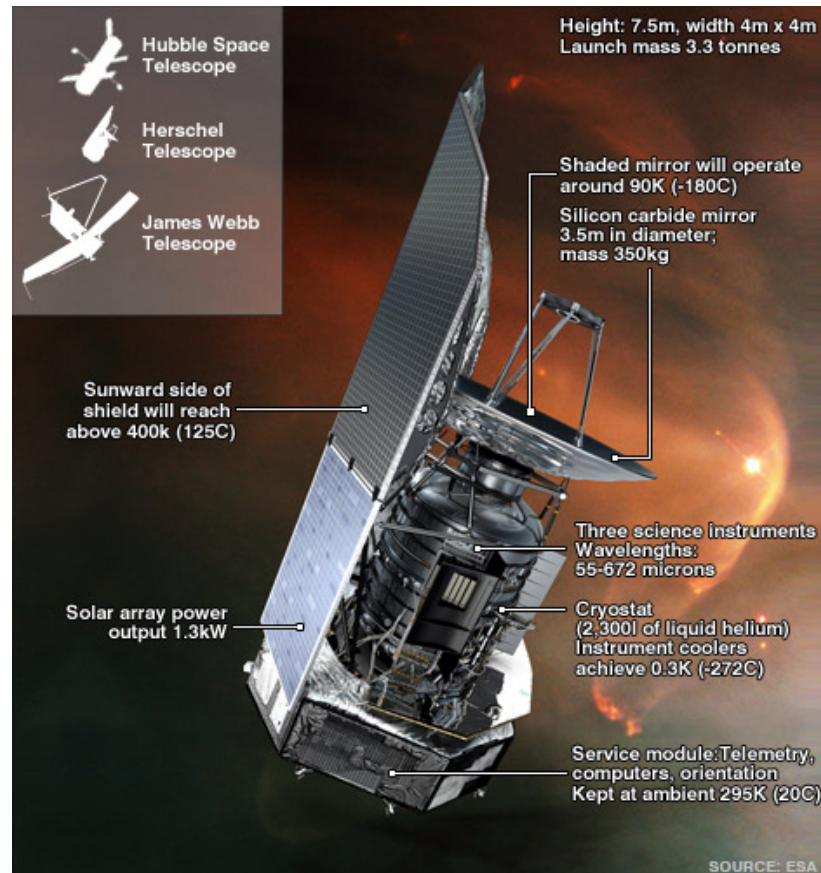


Figure 2.3: View of the *Herschel* telescope. Credit: ESA

et al. 2010). The frequency range of HIFI is from 480 to 1250 GHz and from 1410 to 1910 GHz, divided into six bands.

- **Photodetector Array Camera and Spectrometer (PACS):** An imaging photometer and a spectrometer that with a medium resolution, covering the wavelength range from $\sim 60 \mu\text{m}$ to $210 \mu\text{m}$ bands for spectroscopy and imaging at $70 \mu\text{m}$, $100 \mu\text{m}$ and $160 \mu\text{m}$ bands (Ibar et al. 2010; Poglitsch et al. 2010a).
- **Spectral and Photometric Imaging Receiver (SPIRE):** An imaging photometer and Fourier transform spectrometer, operating at $250 \mu\text{m}$, $350 \mu\text{m}$ and $500 \mu\text{m}$ bands. (Griffin et al. 2010a; Pascale et al. 2011, Valiante et. al. in prep.).

The data used for the work presented in Chapter 4 were collected at 100 , $160 \mu\text{m}$ PACS bands and at 250 , 350 and $500 \mu\text{m}$ SPIRE bands. The 3.5 m *Herschel* telescope is diffraction limited (Ibar et al. 2010) and the resolutions that can be reached

at *Herschel* bands are 3.2 arcsec (60-130 μm), 6.4 arcsec (130-210 μm) and, 18.2, 24.9 and 36.3 arcsec at 250 μm , 350 μm and 500 μm bands, respectively ⁸.

2.3.2 *Herschel*-ATLAS survey

The *Herschel*-ATLAS is a 570 deg² survey that was carried out by the the *Herschel* telescope from 2009 to 2010 (600 hours survey time in total). Details of the survey fields are the following (see also Table 2.1 for details):

- **The North Galactic Pole field (NGP):** A 150 deg² field close to the north Galactic pole (Fig. 2.4-top panel).
- **Three Galaxy And Mass Assembly redshift survey (GAMA) fields:** Three fields each of which is around 56 deg² in area, coinciding with the GAMA (Driver et al. 2011) fields (Fig. 2.4-top panel).
- **The South Galactic pole field (SGP):** two fields that are close to the south Galactic pole. A small rectangular block is 17 degrees by 6 degrees and a larger one is 26.7 \times 6 deg², in area (Fig. 2.4-bottom panel).

The *Herschel*-ATLAS data collected over the NGP and three GAMA fields were used for the study presented in Chapter 4 and the NGP field data was used for the work presented in Chapter 6.

Name	Center	RA width (deg)	DEC width (deg)
NGP	13 18 00, 29 00 00	15	10
GAMA A	09 00 00, 00 00 00	14	3
GAMA B	12 00 00, 00 00 00	14	3
GAMA C	14 30 00, 00 00 00	14	3
SGP A	02 09 00, -32 54 50	11	6
SGP B	23 15 36, -32 54 00	31	6

Table 2.1: Details of the *Herschel*-ATLAS fields, re-produced from Eales et al. (2010a). From left to right the columns are: the name of the field, the central coordinates of the field, the width of the field in right ascension and declination, respectively.

Details of the *Herschel* flux measurements were given by Hardcastle et al. (2010) and Hardcastle et al. (2013). I will briefly describe the process here. In order to measure flux densities of the sample sources over the NGP and GAMA fields, point spread

⁸<http://herschel.esac.esa.int/Docs/Herschel/html/ch03s02.html>

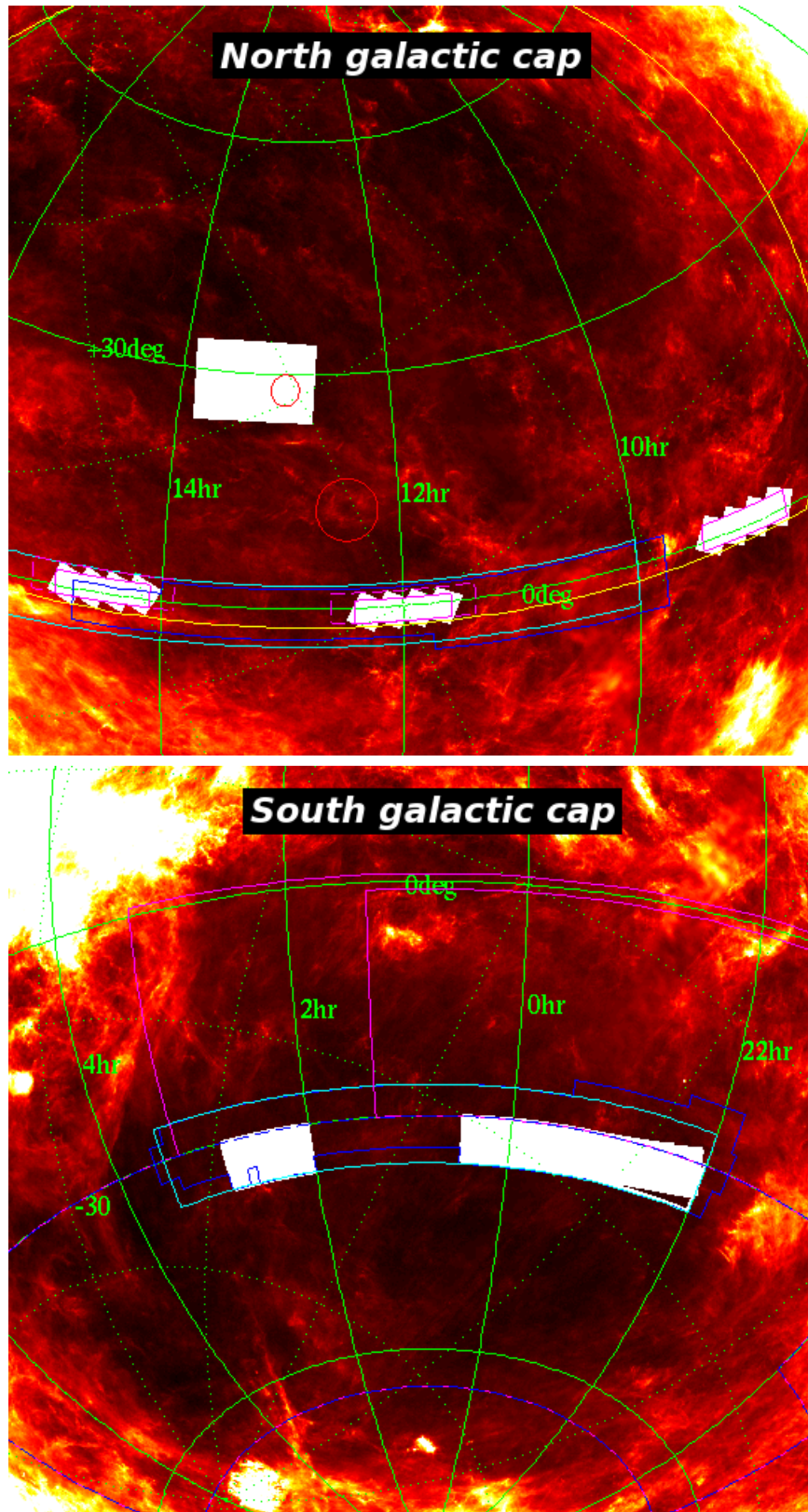


Figure 2.4: The top panel shows the NGP (a rectangular block centred on RA=199.5, Dec=29) and GAMA (the smaller white rectangles centred at at RA 9 hours, 12 hours and 14.5 hours in the image) fields. The bottom panel shows two the SGP fields (roughly rectangular blocks centred on RA=351.3, Dec=-32.8 and RA=36.7, Dec=-30.7, respectively. Credit:Herschel-ATLAS)

function (PSF) convolved, background subtracted images of these fields at SPIRE bands were obtained. The maximum-likelihood estimate of the flux densities at the positions of objects in these images together with the error on the fluxes were measured. Figure 2.5 shows images of the same region in the sky at PACS and SPIRE bands.

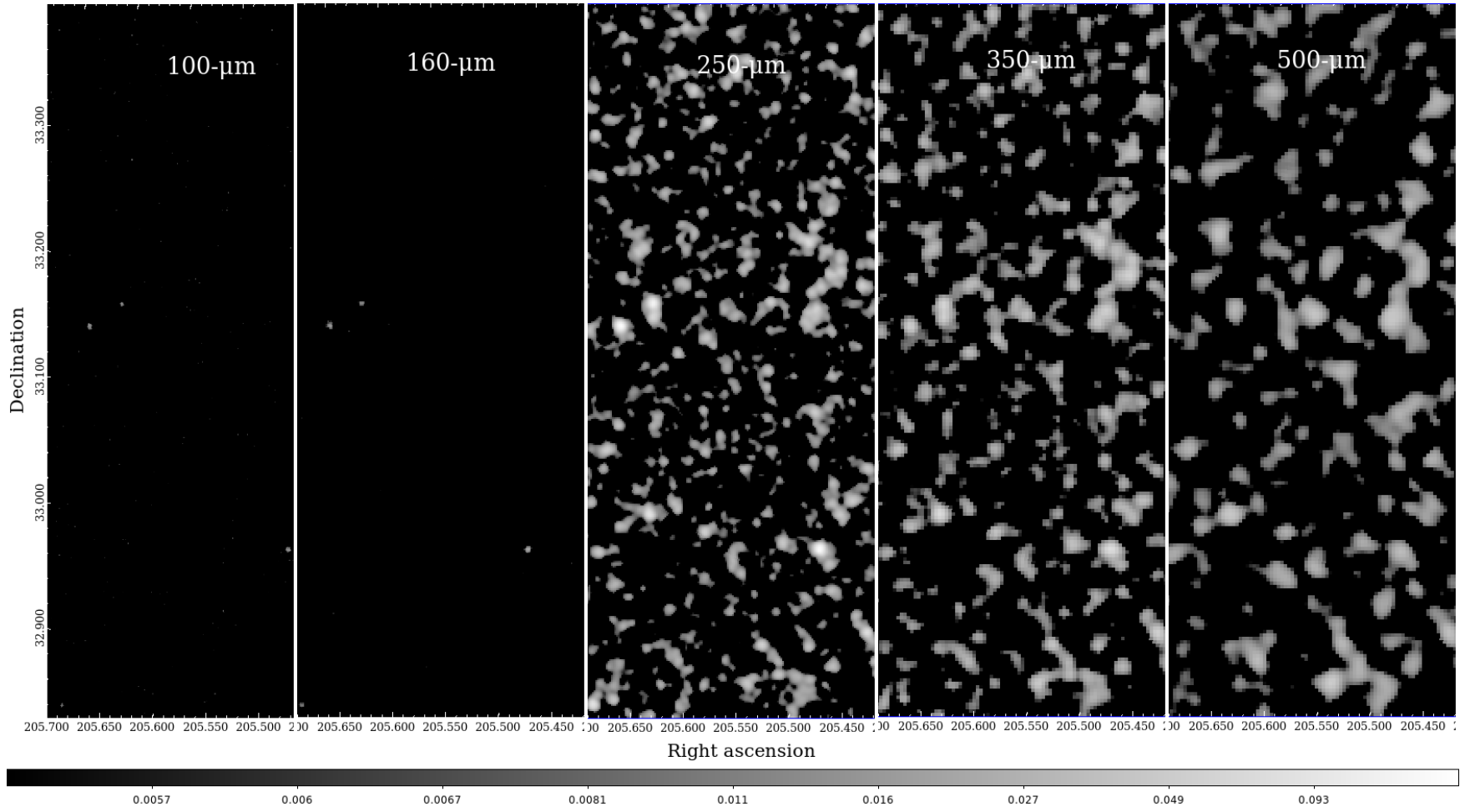


Figure 2.5: PACS and SPIRE band images of the same region of the sky.

2.4 Optical data

Data from SDSS were used for the work presented in Chapters 4 and 6.

SDSS is a photometric and spectroscopic survey that was carried out using a dedicated 2.5 m telescope (Fig. 2.6), having five imaging bands (u, g, r, i, z), at Apache Point Observatory in New Mexico. Details about the telescope are given by Gunn et al. (2006). To date, the survey has had 12 data releases and the total area of the imaging (including overlapping areas and excluding supernovae runs) is around 31,637 deg² (e.g. the final data release DR12, Alam et al. 2015).

I used SDSS DR7 r -band images for the work I detail in Chapter 6. An example of an r -band image is shown in Fig. 2.7. There are also two catalogues, which have optical measurements of galaxies and quasars, which were used for the studies given in this thesis: I will provide a summary of these in the next section.

2.4.1 Related catalogue data

- **MPA-JHU catalogue:** In 2000/2001 a group from the Max Planck Institute for Astrophysics, and the John Hopkins University (MPA-JHU⁹) carried out a project to re-analyse all SDSS spectra using an optimised pipeline. This work provided the MPA-JHU catalogue. The group derived improved stellar masses for the galaxies in the catalogue (Kauffmann et al. 2003a; Salim et al. 2007), SFRs (Brinchmann et al. 2004) and gas phase metallicities (Tremonti et al. 2004). The final release of the catalogue contains the derived galaxy properties from the emission line analysis of the SDSS DR7 data. This includes, for example, emission line equivalent widths of optical emission lines, emission line fluxes and errors on them etc. The MPA-JHU catalogue was used for the studies presented in Chapter 4 and 6. In particular, I utilised optical emission line measurements given in the catalogue in order to implement emission-line classification of sources in my sample. I additionally used SFRs of the sample sources derived from the H $_{\alpha}$ emission lines and stellar mass measurements provided in the catalogue.
- **HMQ catalogue:** The Half Million Quasars (HMQ) catalogue is the largest quasar catalogue published to date (Flesch 2015). The catalogue was produced by combining earlier releases of the SDSS quasar catalogues (e.g. Pâris et al.

⁹<http://www.mpa-garching.mpg.de/SDSS/>

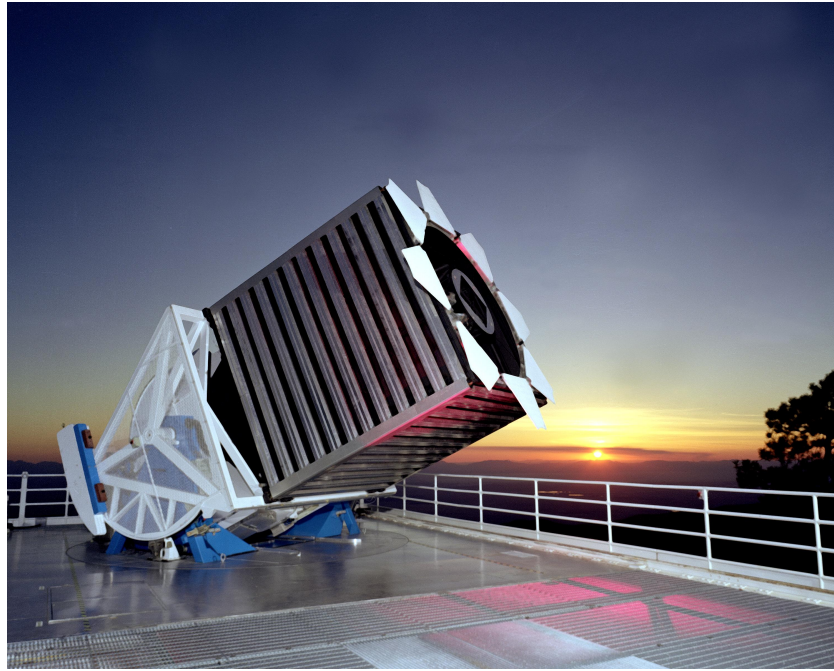


Figure 2.6: View of the 2.5-m SDSS telescope located at Apache Point Observatory (APO) in New Mexico. Credit: skyserver.sdss.org

2014) and has a total of 510,764 objects (including AGN and BL Lac objects). It contains high-confidence (≥ 99 per cent) photometric SDSS candidates and type-II AGN with radio/X-ray associations. SDSS names (if not available, other survey names) of the catalogued sources are provided. Optical band magnitudes (r and b bands) and available redshift measurements in the literature are also given in the catalogue. I only used this catalogue in order to obtain quasar counterparts of the sources detected in the LOFAR maps.

2.5 Radio data

For the works that were presented in the Chapters 5 and 6, I used radio image data from the following surveys:(i) FIRST, (ii) NVSS and (iii) LOFAR/NGP.

2.6 Radio Interferometry

The approximate angular resolution (θ) of a single dish is given by the following relation:

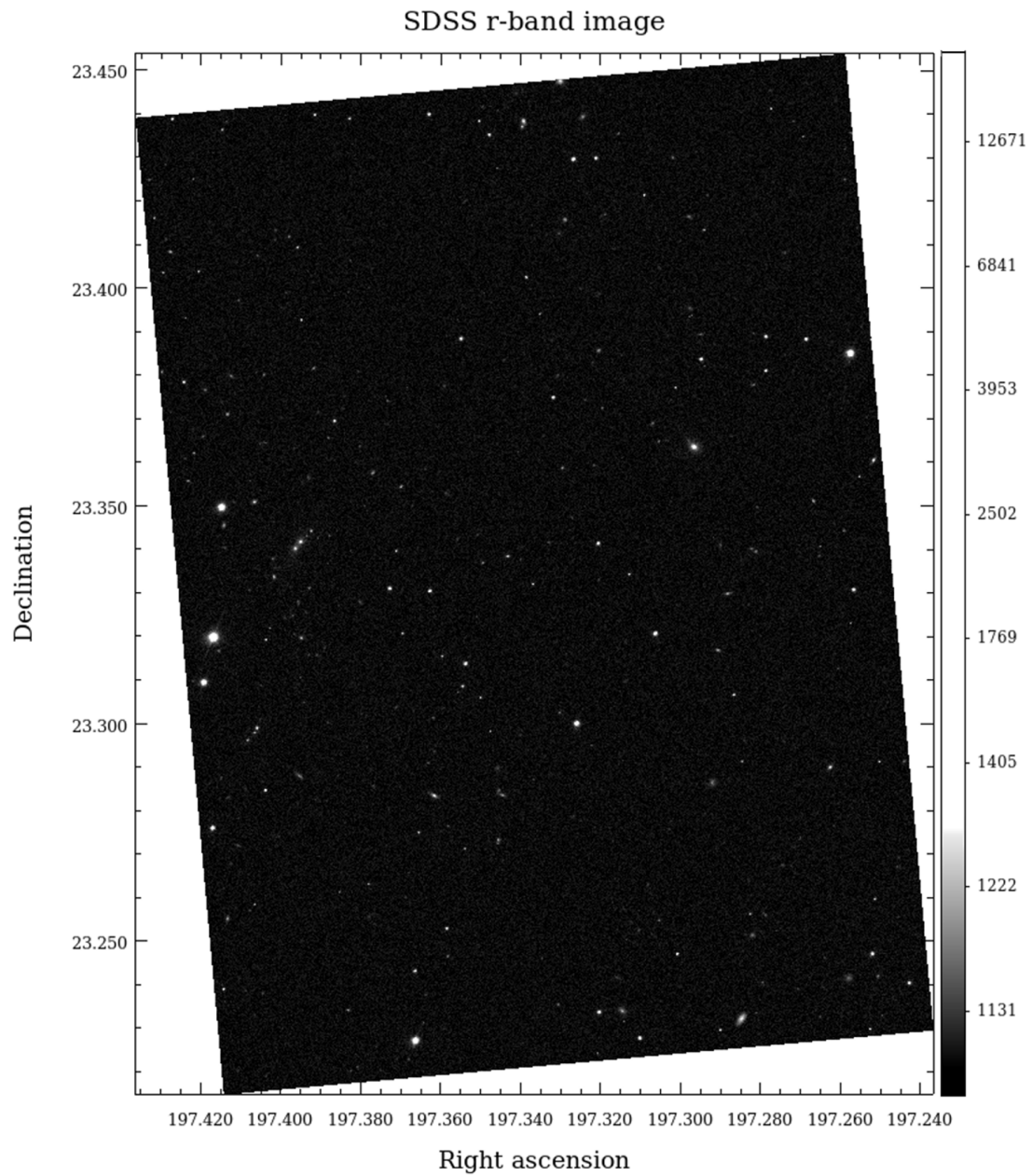


Figure 2.7: Example SDSS *r*-band image that was used for the study presented in this thesis.

$$\theta \approx 1.22 \frac{\lambda}{D}, \quad (2.1)$$

where λ is the electromagnetic wavelength and D refers to the diameter of the telescope's aperture. Relation (2.1) shows that the resolution θ , of a single dish is determined by the aperture diameter D of the dish. Since the maximum achievable diameter for a single dish is limited (currently the largest steerable single dish has a diameter of 100 meters) by engineering constraints, an aperture synthesis technique was developed by which a number of antennas can be combined to achieve the desired resolution (from arcsec to sub-arcsec). The simplest illustration of this technique is a two-element interferometer, which can be seen in Figure 2.8.

In Figure 2.8, B is the baseline between the two antennas. Since there is a geometric path difference between them, there is a time delay, τ_g , in the signals that reach the antennas. θ is the angle at which the telescope observes.

A two-element radio interferometer is constructed by multiplying (correlating) the signals received by the individual antennas and integrating over time (\sim a few seconds). The output of this correlation is known as a *complex visibility*, which is a component of the Fourier transform of the sky brightness distribution in the direction the telescope is pointing, and is expressed in terms of amplitude and phase (Ryle & Hewish 1960).

The maximum resolution (synthesis beam) limited by the achievable maximum baseline. However, as the number of antennas that can be used is limited, the (u, v) plane cannot be covered completely. To overcome this issue, it is possible to utilise the Earth's rotation. As the Earth rotates the projected baselines provide more (u, v) coverage. Although the sample of points in the (u, v) plane can be increased by means of this aperture synthesis, it still contains gaps (i.e it is not completely filled). The sampling of the Fourier plane at a discrete number of points is $S(u, v)$, the sampling function. The Fourier transform of this sampling function is known as the *dirty beam* (or point spread function). What we measure is the dirty map which is a convolution of the true source brightness and the dirty beam. The Fourier transform relationship between V and I means that the multiplication by $S(u, v)$ in the visibility plane is a convolution in the image plane. With a deconvolution method we can obtain a clean image.

In practice, there are many effects that affect the observed visibilities and can cause loss of true visibility information. In order to eliminate (or minimise) these effects, a number of processes are carried out. The first step in radio data reduction is to clean

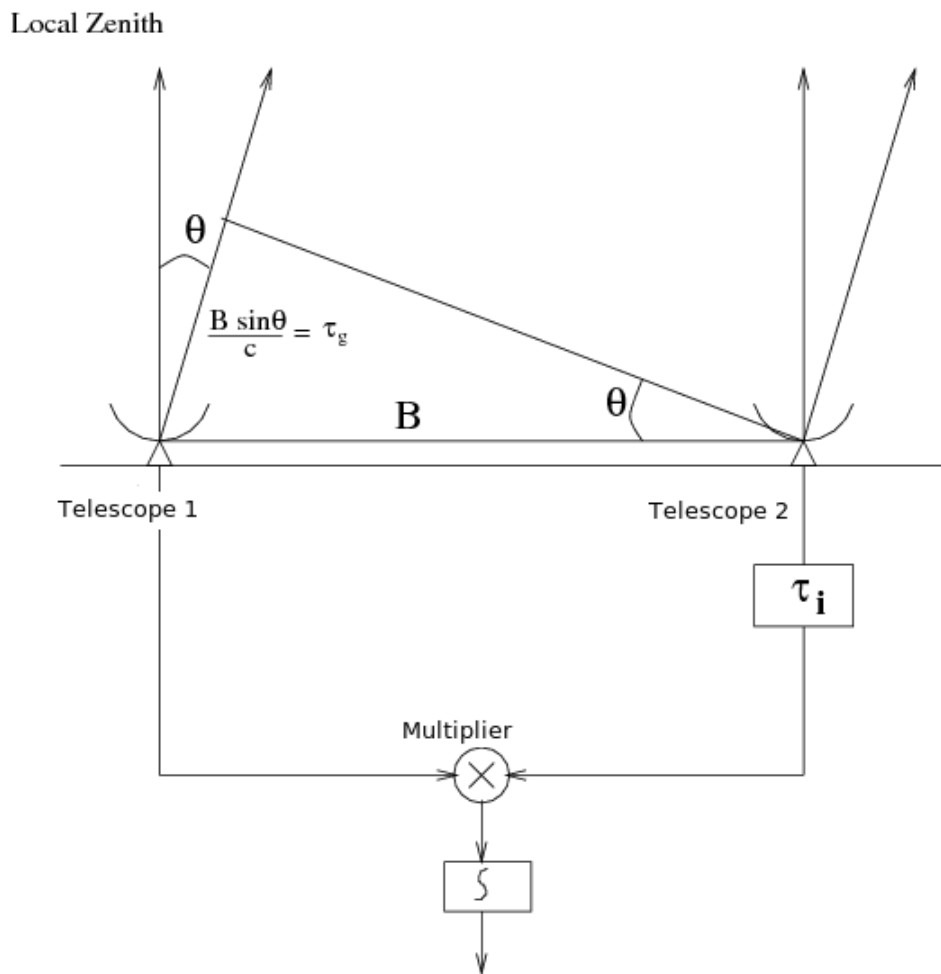


Figure 2.8: A simplified one dimensional block diagram of a two-element interferometer. A compensating delay τ_i is introduced into the path of one of the signals. The two signals are then multiplied and integrated to measure the complex visibility. Credit: Bhatnagar (2001).

data by removing discrepant and corrupted data introduced by radio interference. The next step is a range of calibrations that are carried out to correct the observed visibilities in order to make them as close as possible to the true visibilities by removing instrumental and ionospheric effects from the data. These calibrations include calibrations of the phases and/or amplitudes of the data either with respect to a reference source or with respect to the target itself ('self-calibration').

In order to measure the absolute flux of a target source on the sky, flux calibration is carried out using a well-known bright point source with constant flux which is normally unresolved by the instrument at the observed frequency (alternatively, a well-defined calibrator source model can also be used¹⁰). Phase calibration is then implemented in order to correct for phases in the direction of the target source. This is done by using a stable calibrator source that is positionally close to a target source. Self-calibration can also be implemented, if a target source has sufficient signal to noise ratio (SNR), in order to improve the dynamic range of radio images as there will still be residual phase errors remaining after initial calibration. In this process, after imaging the data, the clean components in the image are used as an input model in order to calibrate the original UV data. After self-calibration the noise in the image is checked to see if there is any improvement. The self-calibration process is re-iterated using clean components of the final image produced at a previous step until there is no change observed in dynamic range of the image.

The above information is only a generic overview of radio interferometric observations. The challenges and the atmospheric effects can vary based on the frequency range of radio observations and the types of antennas used. In the case for LOFAR (from which the data have been used for the work presented in Chapter 5), since the FOV of LOFAR is wide many bright sources are often present in the target field (this is discussed in Chapter 5) and removal of the effects of these sources is important. At low frequencies, the ionosphere is not uniform and can change within short time intervals (\sim minutes) across the sky. Therefore, direction-dependent calibration has a crucial role in LOFAR data reduction (details are given in Chapter 5).

2.6.1 The FIRST survey

FIRST is a radio survey that was carried out with the NRAO VLA (Fig. 2.9) in its B-configuration at 20-cm, mapping over 10,000 square degrees of the North Galactic

¹⁰<https://science.nrao.edu/facilities/vla/docs/manuals/oss2013a/performance/cal-fluxscale>



Figure 2.9: View of the VLA.

Cap and South Galactic Cap (Becker et al. 1995). The final FIRST survey products include radio images (which were edited, self-calibrated and CLEANed using automated pipeline) at 5 arcsec resolution with a typical r.m.s. noise of 0.15 mJy as well as a catalogue of sources (at the 1 mJy source detection threshold) including total and peak flux densities and source sizes. Fig. 2.10 shows an example of a FIRST image that was used for my work presented in Chapter 5. The FIRST survey was designed to cover the SDSS survey area and ~ 40 per cent of the FIRST sources have optical counterparts detected by SDSS ¹¹.

¹¹<http://sundog.stsci.edu/first/description.html>

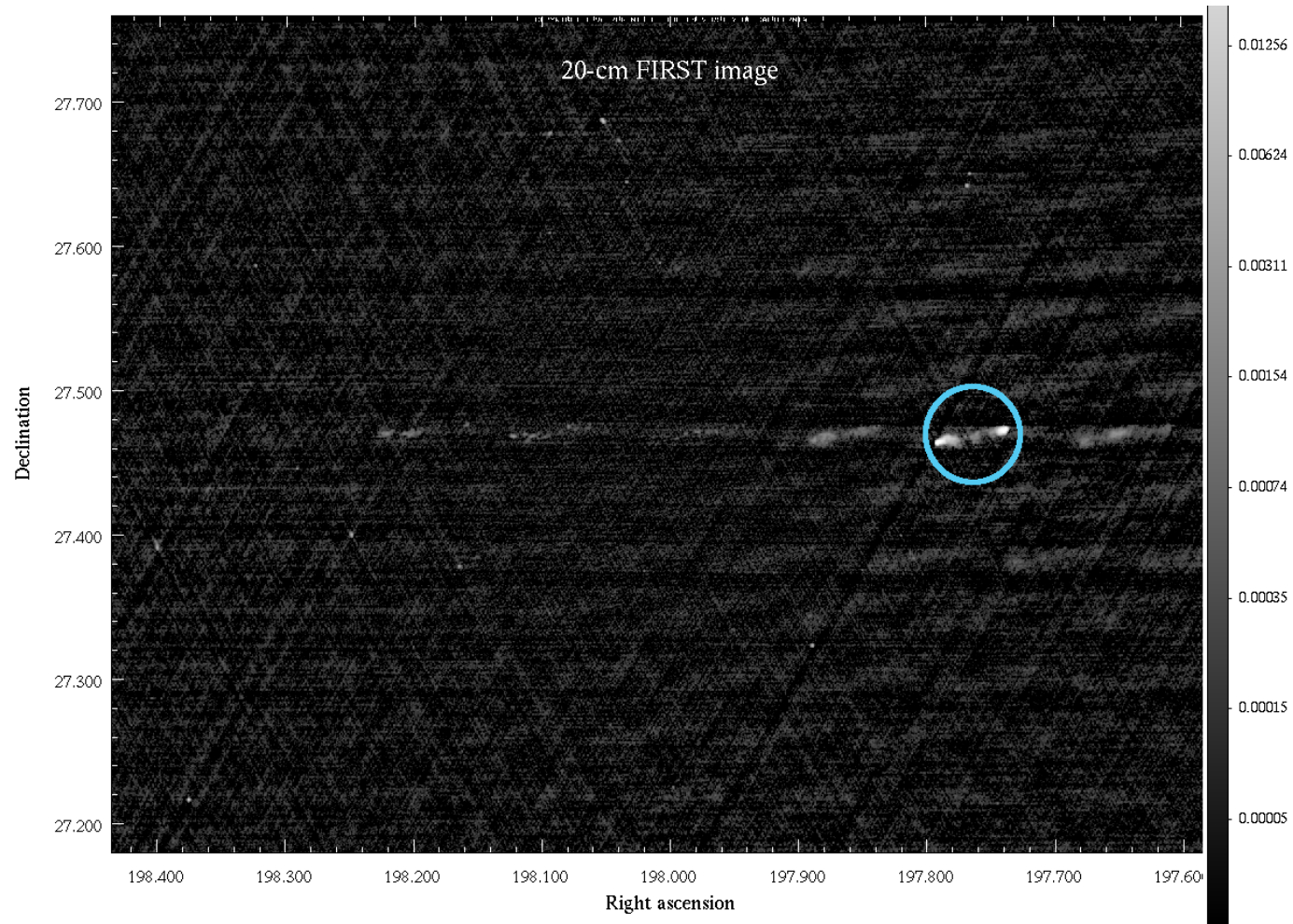


Figure 2.10: Example of a FIRST image which was used for the study presented in Chapter 5. The blue circle shows the radio galaxy 3C284, which is poorly imaged by FIRST.

Since FIRST is sensitive to compact, core regions of radio galaxies, FIRST maps were utilised in order to assist identifying possible associations and optical identifications of sources detected by the LOFAR survey . Details of this work are given in Chapter 5.

2.6.2 The NVSS survey

NVSS is a radio continuum survey carried out by the VLA in its D- and DnC-configuration at 1.4 GHz, covering the Northern sky at above -40 deg declination (Condon et al. 1998). The NVSS survey maps have a resolution of 45 arcsec, much larger than the FIRST survey, so it is more sensitive to extended emission of radio sources. The r.m.s. noise is ~ 0.45 mJy and the completeness limit is around 2.5 mJy. A catalogue of discrete sources on these maps (a total of around 1.8 million sources) was also provided by the survey.

As mentioned above, NVSS is sensitive to extended emission associated with active radio galaxies. In order to assist the work of identification of LOFAR sources I also used NVSS maps (an example of a NVSS image is shown in Fig. 2.11).

2.6.3 The LOFAR survey of the H-ATLAS/NGP field

The *Herschel*-ATLAS NGP field was observed with LOFAR (van Haarlem et al. 2013) in 2013 as a part of the LOFAR Key Science Project (KSP, Röttgering et al. 2006). Observations were carried out in four pointings. The effective frequency of the final maps is 150 MHz. The final maps of the pointings have roughly the same resolution ($\sim 10 \times 8$ arcsec). The catalogue produced from these maps has 15521 sources in total. Details of the observations, data reduction and catalogue production are given in Chapter 5. LOFAR 150 MHz flux densities of the sources in the MPA-JHU catalogue overlapping with the H-ATLAS/NGP field were used in Chapter 6.

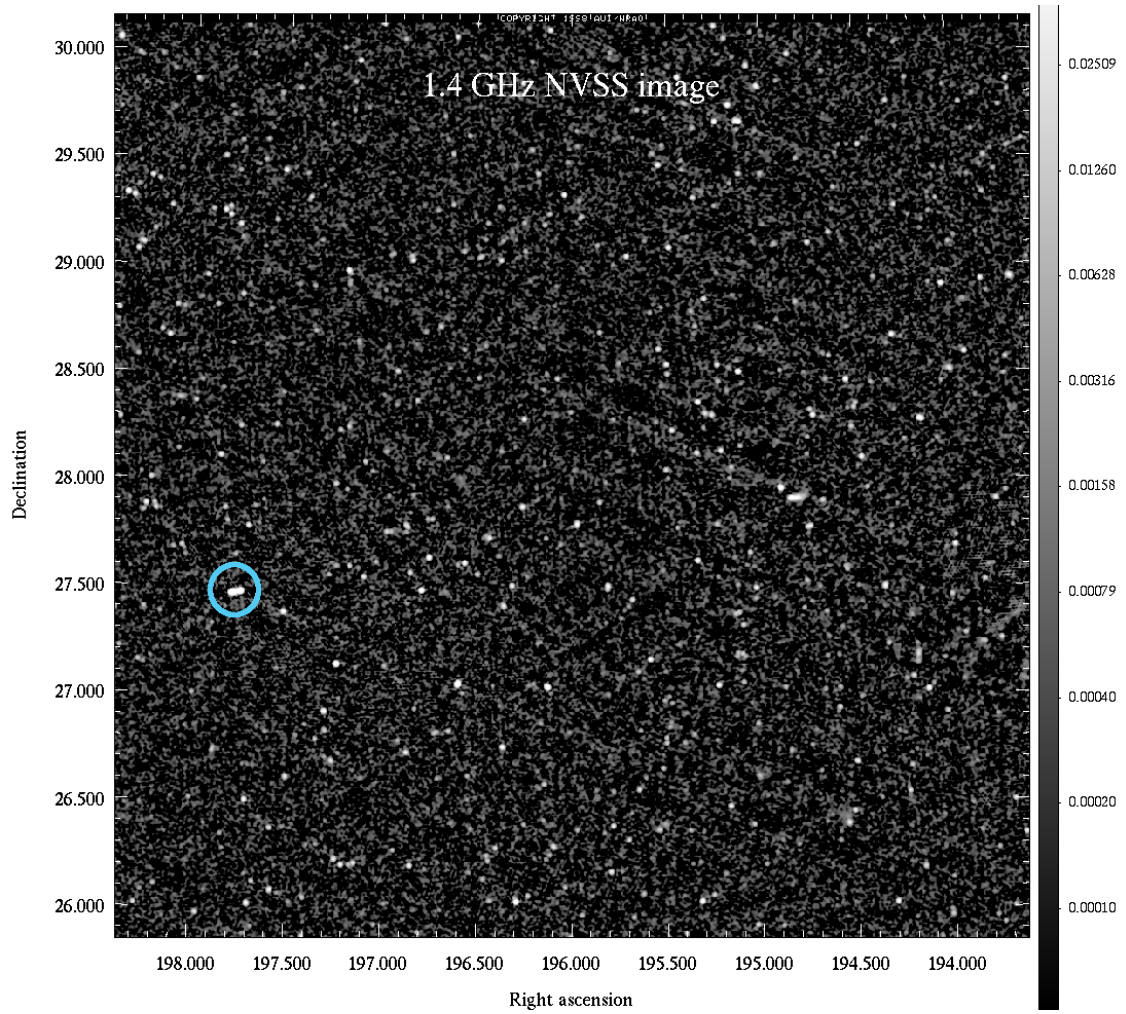


Figure 2.11: Example of a NVSS image used for the study presented in Chapter 5. The blue circle shows the radio galaxy 3C284.

Chapter 3

The *WISE* properties of complete samples of radio-loud AGN

“If you want to find the secrets of the universe, think in terms of energy, frequency and vibration”

Nikola Tesla

3.1 Abstract

I present an analysis of four complete samples of radio-loud AGN (3CRR, 2Jy, 6CE and 7CE) using near- and mid-IR data taken by the *WISE*. The combined sample consists of 79 quasars and 273 radio galaxies, and covers a redshift range $0.003 < z < 3.395$. The dichotomy in the mid-IR properties of LERGs and HERGs is analysed for the first time using large complete samples. The results demonstrate that a division in the accretion modes of LERGs and HERGs clearly stands out in the mid-IR–radio plane ($L_{22\mu\text{m}}=5\times 10^{43}$ erg s⁻¹). This means that *WISE* data can be effectively used to diagnose accretion modes in radio-loud AGN. The mid-IR properties of all objects were analysed to test the unification between quasars and radio galaxies, consistent with earlier work and I argue that smooth torus models best reproduce the observation. Quasars are found to have higher mid-IR luminosities than radio galaxies. I also studied all the sources in the near-IR to gain insights into evolution of AGN host galaxies. A relation found between the near-IR luminosity and redshift, well-known in the near-IR, is apparent in the two near-IR *WISE* bands, supporting the idea that radio sources

are hosted by massive elliptical galaxies that formed their stars at high redshifts and evolved passively thereafter. Evaluation of the positions of the sample objects in *WISE* colour-colour diagrams shows that widely used *WISE* colour cuts are not completely reliable in selecting AGN.

3.2 Introduction

The nature of the energy source in AGN has been a matter of debate for a long while. In commonly accepted models, the energy is generated by accretion of cold material onto black holes in the centre of active galaxies (Kormendy & Richstone 1995; Magorrian et al. 1998; Ferrarese & Merritt 2000). The accretion produces photoionising UV radiation, and gives rise to X-ray emission via Compton scattering. Hot, high-velocity gas clouds located within ~ 1 pc of the obscuring torus produce the broad emission lines that can be observed in their spectra while narrow emission lines are produced by the lower velocity gas clouds situated further away at ~ 10 -100 pc (Antonucci 1984; Urry & Padovani 1995). Different classes of AGN, however, present different observational features in optical, X-ray and radio bands. An orientation effect is the main ingredient of both optical and radio unification schemes: in the optical, radio-loud AGN are classified according to whether they have broad emission lines in their spectra, which can be obscured by dust and gas (torus) at certain angles (e.g. Antonucci & Miller 1985). In this case, the obscuring structure is expected to re-radiate strongly in the mid-infrared (Meisenheimer et al. 2001; Whysong & Antonucci 2004; Ogle et al. 2006).

The simple unification scheme of quasars and radio galaxies developed by Barthel (1989) is based on orientation dependent effects. According to this model, radio galaxies and quasars are the same objects seen at different angles. If a source is viewed within a cone of half-angle approximately 45° it is called a quasar or BLRG; if a source is viewed edge-on, where the nucleus is blocked by the dusty torus, the source is then identified as a radio galaxy NLRG. On the other hand, Hine & Longair (1979) pointed out the existence of a population of radio galaxies that do not present the strong emission lines conventionally seen in powerful AGN HERGs. This class of objects, called LERGs, are predominantly found to be at low-radio luminosities. This population poses a problem for simple unification, falling outside the generic view of radio-loud AGN. They do not exhibit any expected feature of unified AGN; radiatively efficient accretion disk, X-ray emitting corona (Evans et al. 2006; Hardcastle et al. 2006) and

obscuring torus in the mid-IR (Whysong & Antonucci 2004; Ogle et al. 2006).

Hardcastle et al. (2007b) suggested that a different source of fuel for the accretion process may be responsible for this difference. In this picture, HERGs (quasars, BLRGs and NLRGs) accrete in ‘cold mode’; in which accretion of cold matter onto a super-massive black hole via an optically thick geometrically thin accretion disk produce radiation efficiently, whereas LERGs (alternatively called weak-line radio galaxies, or WLRGs) are thought to be fuelled by the accretion of the hot gas in haloes of their host galaxies through advection dominated flows (Narayan & Yi 1995b; Best et al. 2006; Hardcastle et al. 2007b; Janssen et al. 2012) and release the accretion energy in the form of jets or winds (Chiaberge et al. 2002; Merloni & Heinz 2007) [see also McNamara et al. (2011); Martínez-Sansigre & Rawlings (2011)]. The relation between accretion rate and jet power was studied by Allen et al. (2006) and Bondi accretion rates have been evaluated for LERGs and HERGs by Hardcastle et al. (2007b). They showed that the majority of LERGs have jet powers comparable to the available Bondi power while many NLRGs have jet powers higher than Bondi accretion level, emphasising the possibility that LERGs are powered by accretion from the hot phase. Recently a similar conclusion was reached by Russell et al. (2013). It is worth noting that studies of AGN environments support the idea of a different origin of the accreting gas; LERGs occupy gas-rich environments and redder, lower star-formation galaxies in comparison to HERGs at comparable redshifts (e.g. Hardcastle 2004; Kraft et al. 2007; Tasse et al. 2008; Best & Heckman 2012; Hardcastle & Krause 2013). However, another hypothesis to explain the diversity in accretion-modes of AGN is that there is a limiting value of the Eddington-scaled accretion rate above which radiatively efficient accretion takes place (e.g. Narayan & Yi 1995b). It has recently been shown that LERGs and HERGs are plausibly separated at a critical value of the Eddington-scaled accretion rate (e.g. Best & Heckman 2012; Russell et al. 2013; Mingo et al. 2014). This model does not require a one-to-one correspondence between fuel source and accretion mode, but, since sources fuelled by accretion from the hot phase will tend to contain massive black holes being fuelled at a low rate, it retains many of the predictions from the Hardcastle et al. (2007b) model. Further discussion of the nature of LERGs and HERGs can be found in a recent review by Antonucci (2012).

Determining the radiative power of AGN, particularly obscured AGN, is observationally difficult. To date, many hidden AGN have been discovered using hard X-rays but this technique only works for Compton-thin AGN (Madejski et al. 2000; Eracleous & Halpern 2001). Spectropolarimetry is another way of confirming a hidden nucleus

(Miller & Antonucci 1983; Antonucci & Miller 1985; Ogle et al. 1997). However, it has limitations because in the case of lack of scattering material the results would yield false negatives. Mid-IR data is important in searching for radiatively efficient accretion in radio galaxies and testing the unification hypothesis, because in the presence of the putative dusty torus, optical-UV emission from quasar nucleus is intercepted by the torus and re-radiated in the mid-IR, which is only mildly sensitive to orientation (Whysong & Antonucci 2004; Shi et al. 2005; Hardcastle et al. 2009; Dicken et al. 2009; Fernandes et al. 2011).

Many previous authors have used the mid-IR properties of radio sources to test the unification hypothesis. Heckman et al. (1992, 1994) used the Infrared Astronomical Satellite (*IRAS*) measurements of 3CR radio galaxies and quasars at $z > 0.3$, and found that quasars were ≈ 4 times brighter than radio galaxies in their mid-IR and far-IR fluxes (at 25, 60 and 100 μm). They concluded that either mid-IR emission from radio-loud AGN is not isotropic or quasars are intrinsically different sources of mid-IR than radio galaxies with the same radio power, which would imply that the simple unification scheme needs to be revised. Similar results were also obtained in various subsequent studies using *Spitzer* (e.g. Cleary et al. 2007; Haas et al. 2008) and different reasons were suggested for the excess magnitudes seen in quasars in the mid-IR such as non-thermal emission and dust absorption. On the other hand, some other studies provided opposite results, suggesting that quasars and radio galaxies show identical mid-IR magnitudes (e.g. Meisenheimer et al. 2001; Haas et al. 2004, 2005; Siebenmorgen et al. 2005; Shi et al. 2005; Dicken et al. 2009).

Mid-IR studies of radio sources hitherto have been based on single sources or small or incomplete samples. In addition to this, due to the lack of complete mid-IR observations of radio samples, many investigations were carried out using incoherent data sets where the mid-IR observations were taken for a variety of purposes. One of the motivations of this work is to remove this deficit in radio-loud AGN research, providing a complete mid-IR study of the complete and relatively large sample. Here I present, for the first time, the mid-IR properties of four complete samples, namely 3CRR, 2Jy, 6CE and 7CE, which overall cover a wide redshift range ($0.0029 < z < 3.93$). For the analysis, the mid-IR data taken by *WISE* (Wright et al. 2010a) have been used. The objective of this work is to evaluate the utility of mid-IR data to investigate radiatively efficient/inefficient radio loud-AGN and the nature of HERGs and LERGs with *WISE* data. I also examine the mid-IR properties of these complete samples by addressing the quasar-radio galaxy unification and the near-IR properties by comparing these results

with previous studies.

This chapter is organised as follows: a description of the samples, the method of determination of *WISE* fluxes and luminosities and tests of the consistency between *WISE* and *Spitzer* data are given in Section 2. The key results are given in Section 3: *WISE* colour-colour diagrams of the sources are presented discussing the available colour cuts in the literature. An investigation of the old stellar population in the sample is presented and the unification of quasars and NLRGs is discussed. The dichotomy for LERGs and HERGs is re-evaluated in the light of these results. Finally, Section 4 presents a summary of the results and conclusions drawn.

The cosmological parameters used throughout the studies presented in this thesis and the subsequent chapters are as follows: $\Omega_m=0.3$, $\Omega_\Lambda=0.7$ and $H_0=70 \text{ km s}^{-1} \text{ Mpc}^{-1}$.

3.3 Data and Analysis

3.3.1 Samples

The 3CRR, 2Jy, 6CE and 7CE samples were chosen for this analysis. These complete samples are designed to include all radio sources brighter than the specified flux density limit in a particular area of sky at the selected frequency. Most of the samples have complete redshift measurements and emission-line classifications. Figure 3.1 shows the low-frequency radio luminosity and redshift distributions of the objects in the four samples which are described in more detail in the following subsections.

The 3CRR Sample:

I used the revised sub-sample of the 3CR catalogue of radio sources (Bennett 1962), which have flux densities greater than 10.9 Jy at 178 MHz (Laing et al. 1983). There are 172 sources with $0.0029 < z < 2.012$ including 37 LERGs, 82 NLRGs, 10 BLRGs and 43 quasars. 3C231 was excluded from the analysis as its radio emission is due to a starburst.

The 2Jy Sample:

Another complete radio sample chosen for the analysis is a sub-sample of the 2Jy objects which has homogeneous spectroscopic observations (Wall & Peacock 1985; Tadhunter et al. 1993). The complete sample was generated selecting radio objects with

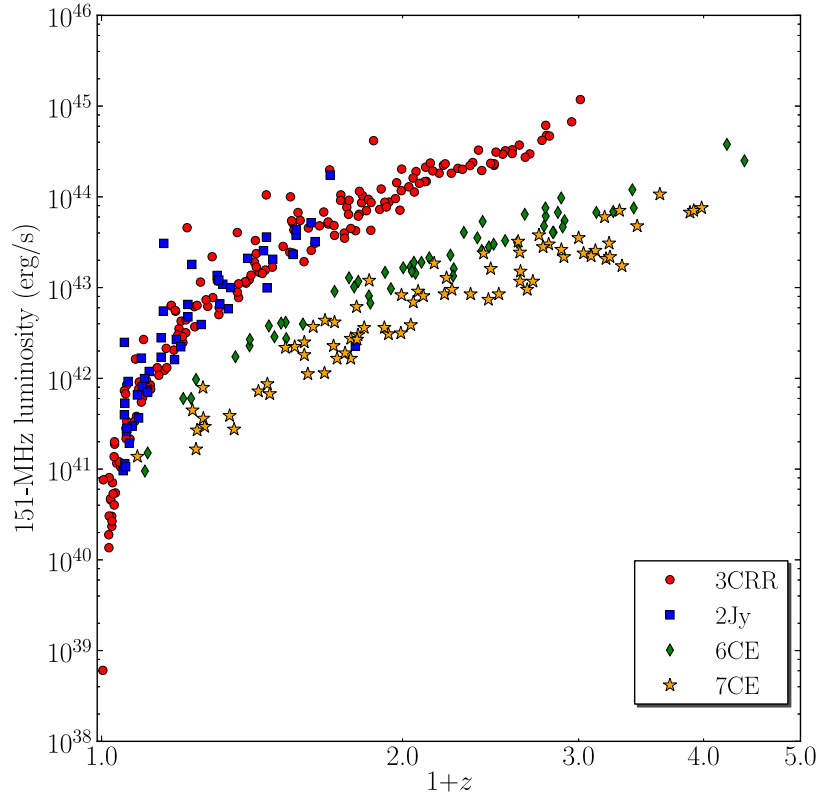


Figure 3.1: The 151 MHz radio luminosity distribution of the samples against redshift described in section 2.1. The 3CRR sample objects are plotted as red circles, the 2Jy sample as blue squares, the 7CE sample as orange stars and the 6CE sample as green diamonds.

flux densities above 2Jy at 2.7 GHz. The sub-sample consists of 48 steep-spectrum sources (objects dominated by emission from the beamed relativistic jet and core components are excluded so that this minimises the contamination from non-thermal emission) with $0.05 < z < 0.7$, which have mid-far infrared (MFIR) imaging and spectra taken by *Spitzer* (Dicken et al. 2008, 2009, 2012) as well as 98 percent complete *Chandra/XMM* X-ray imaging (Mingo et al. 2014). This sample has 10 LERGs, 20 NLRGs, 13 BLRGs and 5 quasars.

The 6CE Sample:

The 6CE sub-sample is drawn from the 6C survey (Baldwin et al. 1985) and was designed to select objects fainter than 3C objects, in order to investigate the cosmic evolution of radio galaxies (Eales 1985b; Eales et al. 1997). The flux density limit for the sample is $2 \leq S_{151} \leq 3.93$ Jy. It has virtually complete spectroscopic redshift measurements as well as infrared imaging (Eales et al. 1997; Rawlings et al. 2001). The 6CE sample has 58 sources including 19 LERGs, 28 HERGs and 9 quasars, whose redshift ranges between 0.105 and 3.395.

The 7CE Sample:

The 7CE sample, drawn from the 7C survey (Visser et al. 1995), is a complete sample having flux densities greater than 0.5 Jy at 151 MHz (Willott et al. 1998, 2002). This sample has 90 percent spectroscopic redshift completeness and 49 radio galaxies have near-infrared imaging (Willott et al. 2003). It comprises 74 radio sources covering redshift from 0.086 to 2.982: 4 LERGs, 46 NLRGs, 2 BLRGs and 22 quasars.

Radio sources in the 7CE sample are classified only as NLRGs, BLRGs and quasars. In order to distinguish LERGs from NLRGs, equivalent widths of the [OII] and [OIII] emission lines were collected from the literature (Willott et al. 1998, 2003). NLRGs were re-classified as LERGs considering the criteria suggested by Jackson & Rawlings (1997): sources with equivalent widths of $< 10 \text{ \AA}$ in [OIII] or [OII]/[OIII] ratios of > 1 or both. Many NLRGs do not have [OIII] detections in their spectra; this is mainly because at higher redshifts the [OIII] is redshifted beyond the visible spectral window. For this reason, I note that there may be more LERGs in the 7CE sample classified as NLRGs at $z > 0.8$.

3.3.2 WISE magnitudes

The *WISE* mission has observed the whole sky in four mid-IR bands (*W1* [$3.4 \mu\text{m}$], *W2* [$4.6 \mu\text{m}$], *W3* [$12 \mu\text{m}$], *W4* [$22 \mu\text{m}$]) with an angular resolution of 6.1, 6.4, 6.5 and 12 arcsec, respectively. The *WISE* all-sky catalogue was searched for all objects in the samples. This was done by searching the catalogue within 10 arcsec. The expected number of sources within 10 arcsec is around 0.349 so that a source detected within the search region of a given position is very unlikely to be a false association: the total expected number of false detections is ~ 120 . The sample sources are away from the Galactic plane, where the density of *WISE* sources is highest. Since powerful radio

galaxies tend to be the dominant objects in any group or clusters they inhabit, I do not expect any excess source density due to clustering to affect the results. In the search, I used the optical coordinates of the 6CE (Allington-Smith et al. 1982; Eales 1985a; Lilly 1989; Eales & Rawlings 1993) and 7CE samples (Willott et al. 1998, 2003), and radio coordinates of the 3CRR¹ and 2Jy samples² (radio core coordinates provide accurate positions of AGN but the 6CE and 7CE samples do not have high-resolution radio observations capable of resolving the radio cores of the objects). In the case of multiple matches per source, these objects were treated separately; *WISE* images of individual sources were obtained and checked against high-resolution radio images to make sure that the right source was detected. Matches for all of the 3CRR (172) and 2Jy (48) objects were found in the catalogue. However, only 47 sources in the 6CE sample out of 58 and 68 in the 7CE sample (74) had detections. Sources rejected from the *WISE* all-sky catalogue for various reasons (such as low flux signal-to-noise ratios, spurious detections of image artifacts, or duplicate entries of source detections) are stored in the *WISE* all-sky reject table. The *WISE* reject table was searched to get magnitudes of non-detected sources. In the case here, the sources found in the reject table have either upper limits or low flux signal-to-noise ratio. Among 17 non-detected sources 15 of them had matches or upper limit measurements in the reject table. *WISE* images of the remaining two sources were checked. Because of a very low SNR, I was not able to obtain their magnitudes, so these sources (6CE-1143+3703 and 6CE-1148+3638) were excluded from the analysis. Almost all of the sources in these samples had matches with $\text{SNR} > 2$ in the shorter *WISE* bands (3.4 and 4.6 μm). Most of the upper-limit measurements ($\text{SNR} < 2$) were obtained in the 12 and 22 μm *WISE* bands. Upper limits are indicated as arrows in the plots presented in the rest of the paper. The detections are summarised in Table 3.1, which also presents the quantity of upper-limit measurements grouped according to source classification. The *WISE* measurements are given in Vega magnitudes so the magnitudes of the sources were converted into Jy using the standard *WISE* zero-points³.

¹<http://3crr.extragalactic.info/>

²<http://2jy.extragalactic.info/>

³The relation used for the conversion can be found at <http://wise2.ipac.caltech.edu/docs/release/allsky/expsup/>

Samples	Class	Quantity	3.4 μm upper-limits	4.6 μm upper-limits	12 μm upper-limits	22 μm upper-limits
3CRR	Total	172	—	—	21	41
	LERG	37	—	—	6	12
	NLRG	82	—	—	14	26
	BLRG	10	—	—	—	—
	Quasar	43	—	—	1	2
2Jy	Total	48	—	—	—	3
	LERG	10	—	—	—	3
	NLRG	20	—	—	—	—
	BLRG	13	—	—	—	—
	Quasar	5	—	—	—	—
6CE	Total	58	—	—	23	38
	LERG	8	—	—	4	7
	LERG?	11	—	—	6	8
	HERG	24	—	—	11	16
	HERG?	4	—	—	2	3
	Quasar	9	—	—	—	—
7CE	Total	74	—	6	36	54
	LERG	4	—	—	2	3
	NLRG	46	—	6	29	38
	BLRG	2	—	—	1	1
	Quasar	22	—	—	4	12

Table 3.1: Table shows the detections for each sample in four *WISE* bands. LERG and HERG with question mark indicate that the classification is not certain. Many of the sources had upper-limit measurements in the longer *WISE* bands (12 and 22 μm). Among the samples, mostly NLRGs and LERGs have upper limits at long wavelengths.

3.3.3 Consistency between *WISE* and *Spitzer*

Many sources in the samples considered here have mid-IR imaging or spectroscopy, taken by the *Spitzer* Space Telescope (Werner et al. 2004), therefore, I am able to check the consistency between *WISE* and *Spitzer* data. In order to do this, I used *Spitzer* measurements of 3CRR and 2Jy sources. In the 3CRR sample, 92 sources have 15 μm rest-frame (Ogle et al. 2006; Cleary et al. 2007; Hardcastle et al. 2009) and 49 objects have 24 μm observed-frame, while all 2Jy objects (48) have 24 μm observed-frame *Spitzer* measurements. The results can be seen in Figure 3.2. A comparison of the 24 μm *Spitzer* and 22 μm *WISE* fluxes of both samples show excellent agreement between *Spitzer* and *WISE* data. There is also a good agreement between 15 μm (rest-frame) and 22 μm (lab-frame) fluxes although as expected, it shows a larger scatter in the correlation.

3.3.4 *WISE* luminosities

Before computing *WISE* luminosities in the four *WISE* bands, the 12 μm –22 μm spectral indices ($F_\nu \propto \nu^{-\alpha}$) were calculated. The mean index value (2.45, SD=0.88) corresponding to NLRGs, which should not be affected by contamination from direct quasar emission, of the 3CRR population where I have good detections in both bands was used for *K*-corrections of the whole sample. The luminosities of the objects in the 12 and 22 μm (observed) bands were then calculated. The same process has been implemented for computing the 3.4 and 4.6 μm luminosities of the sources using the 3.4 μm –4.6 μm spectral indices (the mean index value is 0.14). *K*-corrections were not derived using SED because different components (old stellar population, torus and non-thermal emission⁴) are included in the mid-IR. However, it should be noted that this method of calculating the *K*-correction in 3.4 μm band may not provide the best results because it does not take into account any curvature below 3.4 μm which is expected for radio galaxies; thus 3.4 μm luminosities should be treated with caution. 151 MHz luminosities were extrapolated for the 3CRR and 2Jy samples using the radio spectral indices and 178 MHz or 408 MHz flux density measurements from the catalogues. 5 GHz core flux densities regarding the 3CRR and 2Jy objects in the catalogues are used.

⁴Although the objects are steep-spectrum sources, a minimal effect of non-thermal contamination may still be observed.

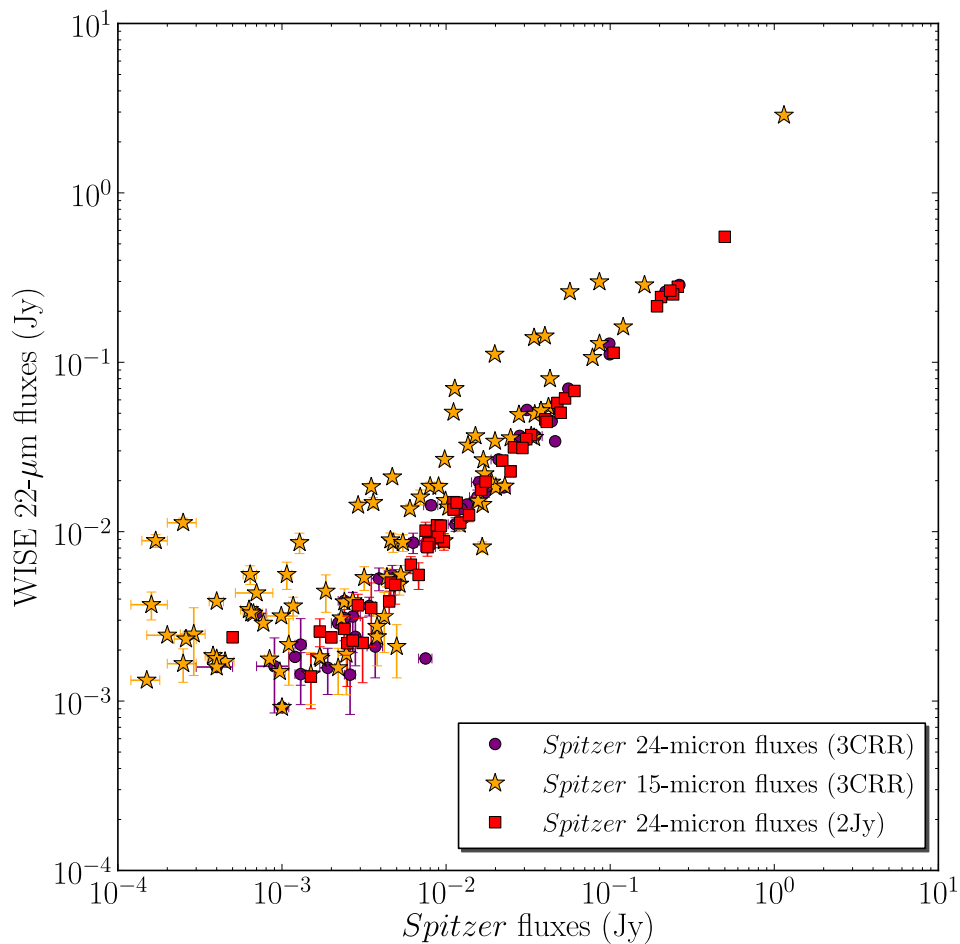


Figure 3.2: To show the consistency between *WISE* and *Spitzer* data I used sources in the 3CRR and 2Jy samples that have *Spitzer* measurements (Ogle et al. 2006; Cleary et al. 2007; Dicken et al. 2008; Hardcastle et al. 2009). Stars indicate 24 μm and circles 15 μm *Spitzer* fluxes of sources from the 3CRR sample, and squares indicate 24 μm *Spitzer* fluxes of the 2Jy sample sources. The 22 μm *WISE* magnitudes were plotted versus *Spitzer* magnitudes. A good agreement between the fluxes measured via *WISE* and *Spitzer* is clearly seen.

3.4 Results

3.4.1 Colour–colour diagrams

Various methods have been developed for separating AGN from normal galaxies in the mid-IR (e.g. Lacy et al. 2004; Stern et al. 2005). In particular, *WISE* colours have been utilised to select AGN (e.g. Assef et al. 2010; Jarrett et al. 2011; Mateos et al. 2012; Stern et al. 2012; Wu et al. 2012; Assef et al. 2013). Before carrying out the main quantitative analysis, I investigated the positions of the objects in *WISE* colour–colour diagrams. Figure 3.3 shows colour-colour plots produced by using *WISE* $W1$, $W2$, $W3$ ($3.4\ \mu\text{m}$, $4.6\ \mu\text{m}$, $12\ \mu\text{m}$ –Vega magnitudes) and *WISE* $W1$, $W2$, $W4$ ($3.4\ \mu\text{m}$, $4.6\ \mu\text{m}$, $22\ \mu\text{m}$ –Vega magnitudes). Upper limits are indicated as arrows in the plots.

The $W1$, $W2$ and $W3$ colours are widely used for selecting AGN (e.g. Mateos et al. 2012). For comparison in Figure 3.3 (left) I show the AGN wedge with the black solid box defined by Mateos et al. (2012). It can be seen in Figure 3.3 that these widely used colour cuts are not reliable for selecting all types of AGN. All LERGs and almost half of NLRGs are omitted if these colour cuts are used. This suggests that *WISE* colour cuts should be used with care for selecting AGN: in particular the fact that many NLRGs are not selected suggests that such colour cuts may be biased against heavily obscured type-2 AGN.

In both plots quasars and BLRGs have similar colours. NLRGs occupy a range of colours, which is suggestive of varying amounts of quasar contamination in the *WISE* near-IR bands. Using $W4$ instead of $W3$ leads to a better separation of LERGs and NLRGs.

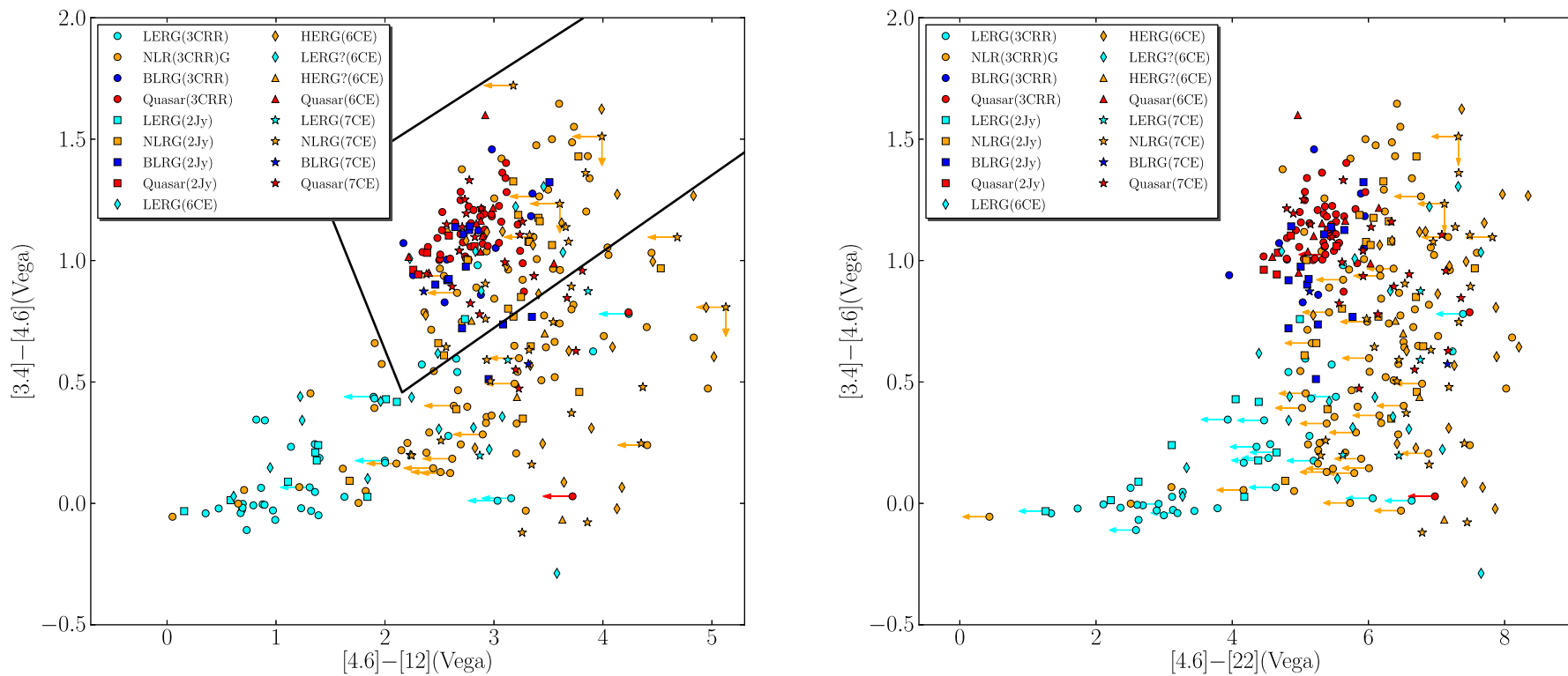


Figure 3.3: *WISE* colour-colour diagrams of all objects in the combined sample. In the left plot for comparison I also show the three-band AGN wedge ($W2 - W3 \geq 2.517$, $W1 - W2 > 0.315 \times (W2 - W3) - 0.222$ and $W1 - W2 < 0.315 \times (W2 - W3) + 0.796$) with black solid box defined by Mateos et al. (2012). Upper limits are indicated as arrows.

To determine the separation quantitatively, the best separation line was chosen at $W1 - W2 = 2$ and $W2 - W4 = 4.9$. The number of LERGs and NLRGs were counted in each side. For $W1 - W2 < 2$ the number of LERGs is 40 and of NLRGs is 16, and for $W1 - W2 > 2$ there are 30 LERGs and 159 NLRGs. For $W2 - W4 < 4.9$ there are 41 LERGs and 10 NLRGs, the number of LERGs is 29 and of NLRGs is 165 for $W2 - W4 > 4.9$. Thus, the $W2 - W4$ selection is slightly better at rejecting NLRGs from the LERG region. This shows that the effect of the torus is stronger in $22 \mu\text{m}$ band, as expected.

3.4.2 Investigation of the old stellar population

Since the near-IR emission from radio galaxies is dominated by the old stellar population of the host galaxies, studies of radio objects over a wide redshift range in the near-IR provide insights into the evolution of stellar components underlying such objects. The distribution of $3.4 \mu\text{m}$ magnitudes versus redshift is shown in Figure 3.4. In this figure a relationship between near-IR band and redshift; an increase in magnitude with redshift, which is identical to the $K - z$ relation of radio galaxies seen in previous studies of various radio samples (e.g Lilly & Longair 1982; Eales et al. 1997; Jarvis et al. 2001a; Willott et al. 2003; Inskip et al. 2010). The relation between $3.4 \mu\text{m}$ and redshift is modelled by fitting a second-order polynomial ($15.46 + 2.85 \log_{10} z - 0.13(\log_{10} z)^2$) which provided the best fit to the data. Only NLRGs and LERGs were used in the fits because quasars/BLRGs are contaminated by non-stellar quasar emission. A tight correlation between K magnitudes and redshift has been interpreted as showing that the radio galaxies are a homogeneous population associated with giant elliptical galaxies containing old stellar populations at lower redshifts. They formed the majority of their stars at high redshifts ($z \gtrsim 3$, but see Best et al. (1998b); van Breugel et al. (1999)) and evolved passively thereafter (e.g. Lilly 1989; McLure & Dunlop 2000; Jarvis et al. 2001a). The results provide no motivation for doubting this conclusion.

In Figure 3.5 I also show the $3.4 \mu\text{m}$ luminosity and $4.6 \mu\text{m}$ luminosity versus redshift of the sources. 3CRR and 2Jy sources display almost identical near-IR luminosities. On the other hand, 6CE and 7CE objects lie close to each other and they have fainter host galaxies than the 3CRR sample at high redshift ($z \gtrsim 0.7$). To quantify this, I calculated the ratio of median fluxes of the samples for different redshift bins. The ratio of median fluxes for the 3CRR and 2Jy samples' galaxies in the $3.4 \mu\text{m}$ waveband is 0.7 (0.08) for $z = 0 - 0.7$. This ratio for the 6CE and 7CE samples is 1.8 (0.8) for

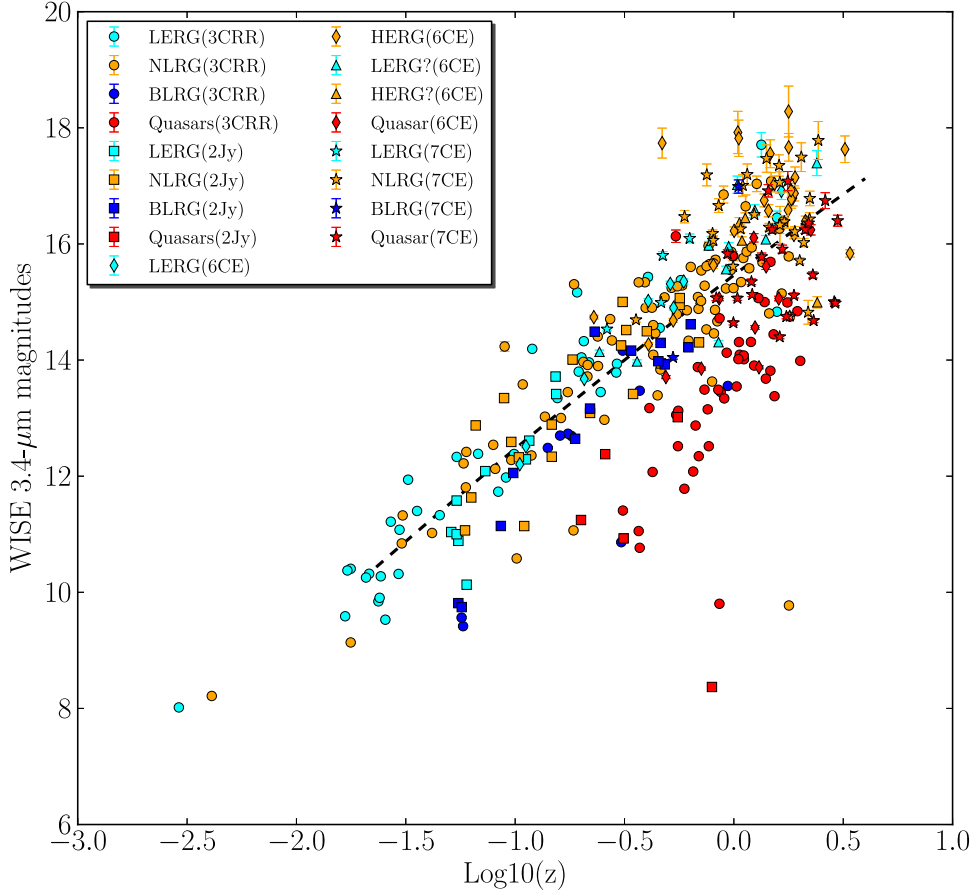


Figure 3.4: Plot of $3.4 \mu\text{m}$ magnitudes versus redshift. A black dash line shows the best fit.

$z = 1 - 1.517$. If the 3CRR and 6CE samples are considered the flux ratio is 1.7 (0.3) for the same redshift bin. A similar trend was seen in other studies (e.g. Eales et al. 1997; Best et al. 1998b; Jarvis et al. 2001a; Inskip et al. 2002; Willott et al. 2003; McLure et al. 2004).

A possible explanation for this is that 3CRR sources are hosted by more massive systems (and proportionally more luminous) compared to the 6CE and 7CE radio galaxies (e.g. Best et al. 1998b). The jet power of a radio source is expected to be determined by the mass of the black hole in the centre of the source, the matter that accretes on to it and the efficiency of the accretion. Thus, powerful radio sources are more likely to host high mass black holes. As many observational studies have shown (e.g. Kormendy & Richstone 1995; Magorrian et al. 1998; McLure & Dunlop 2001) that the central black hole masses are roughly in proportion with the mass of host galaxies,

3CRR and 2Jy galaxies would be expected to tend to reside in more massive galaxies which are brighter at $3.4 \mu\text{m}$ than the 6CE and 7CE galaxies.

Regarding different classes, we see that in each sample BLRGs have similar distributions to NLRGs in both near-IR bands. They could be either intrinsically weak AGN or reddened quasars. LERGs and NLRGs also show similar near-IR luminosities over the redshift range. The 6CE sample is classified mainly as LERGs and HERGs so HERGs will include some NLRGs and BLRGs. In both plots, we see that HERGs (6CE) mostly appear close to NLRGs (6CE) which is not surprising since they will most likely be narrow-line objects. Quasars are more luminous at both near-IR wavelengths in comparison with radio galaxies in each sample. This is most plausibly due to non-stellar quasar emission that contributes to the near-IR band.

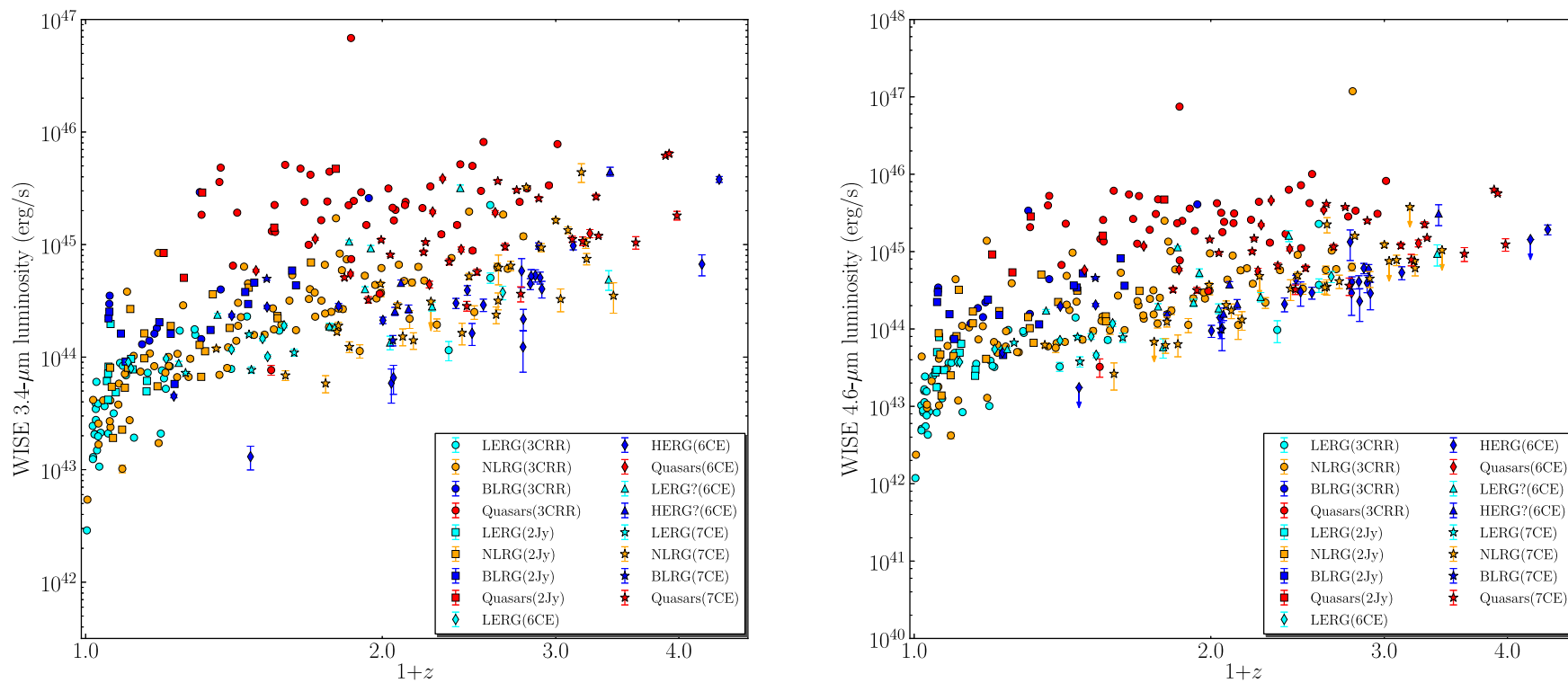


Figure 3.5: Plot of 3.4 μm luminosity (left) and 4.6 μm luminosity (right) versus redshift. Upper limits are indicated as arrows.

3.4.3 The possibility of a starburst contribution?

In Figure 3.6 I show the mid-IR luminosity distribution (observed frame 12 μm luminosity and 22 μm luminosity) of different class of sources as a function of redshift. It is important to consider whether any of this mid-IR emission could originate from warm dust heated by star formation. Therefore, I investigated any contribution of a starburst at the 22 μm waveband. In the most extreme case the integrated IR luminosity of a starburst is around 10^{46} erg s^{-1} (Elbaz et al. 2011). I used the relation $\log(L_{\text{IR}}) = 1.02 + 0.972 \times \log(L_{12\mu\text{m}})$ given by Takeuchi et al. (2005) to estimate the luminosity at 22 μm band. This value is around 10^{45} erg s^{-1} . Any object brighter than this cannot be a starburst. This allows me to rule out this possibility for most of the objects. Most of the remaining sources are LERGs and NLRGs, but these do not present starburst colours on the colour-colour diagrams of Figure 3.3. Starbursts would occupy the right bottom corner. LERGs have bluer colours and sit in the bottom left region on the plots. Furthermore, a continuum between the properties of sources above and below 10^{45} erg s^{-1} is apparent in the 12 and 22 μm luminosity versus redshift plots. We conclude that star-formation activity cannot contribute significantly to the observed mid-IR emission and continue on the assumption that it is related primarily to AGN activity.

3.4.4 Quasar-radio galaxy unification

In standard AGN models, optical/UV emission obscured by dusty structures around the accretion disc is re-radiated in the mid-IR. Thus, hidden quasars can be inferred by means of mid-IR observations. It can be clearly seen in Figure 3.6 that there is more scatter in the 12 μm luminosities than in the 22 μm luminosities. The old stellar population has a slight contribution at 12 μm , but possibly more importantly PAHs have a strong effect at this wavelength (e.g. Weedman et al. 2006, and references therein), thus the higher scatter may be attributed to this.

A comparison of the mid-IR properties of different classes of AGN reveals that quasars have higher mid-IR luminosities with respect to NLRGs. To quantify any excess in quasar mid-IR emission, median values of 12 μm and 22 μm luminosities in 4 redshift bins were obtained for both quasars and NLRGs. Since I have upper limits, to calculate median values I use survival-analysis statistics which are used for data sets with censored data. The median values were derived using the ASURV (Schmitt 1985; Feigelson & Nelson 1985; Isobe et al. 1986) computer package which uses the Kaplan-Meier estimator. Errors for the estimates of the median values were obtained using the

bootstrapping technique. The ratios of the median values then quantify this excess emission in quasars. Calculated median values with their errors, selected redshift bins and the ratios are given in Table 3.2. LERGs have lower mid-IR luminosities than the other class of objects, as seen in both plots. Although BLRGs tend to have higher mid-IR luminosities than NLRGs, an overlap between NLRGs and BLRGs is seen. To show this quantitatively median values of the $22 \mu\text{m}$ fluxes in 3 redshift bins for both BLRGs and NLRGs were obtained. These values were used to calculate the flux ratios. The ratios are 2.5 (0.4), 0.8 (0.07) and 1.0 (0.05) for the redshift bins $z = 0.05 - 0.75$, $z = 0.75 - 1.45$ and $z = 1.45 - 2.15$, respectively.

In all redshift bins, quasars exhibit stronger mid-IR emission than NLRGs. Since re-radiated UV-optical emission from AGN dominates the $22 \mu\text{m}$ flux, ratios of the median values regarding the objects for this waveband can give the best indication of the difference in the mid-IR emission between quasars and radio galaxies. In the first redshift bins quasars are about 10 times more luminous than radio galaxies. The ratio decreases towards higher redshifts although quasars still have stronger behaviour in their mid-IR luminosities (≈ 3 -2 times more luminous than radio galaxies). The decrease in the ratio towards high redshifts does not appear to be a simple effect of redshifting non-evolving SEDs of quasars and radio galaxies. Obtaining the distribution of SEDs as a function of luminosity and redshift would allow me to study this particular trend in more detail, but this is beyond the scope of this work.

A significant difference ($\gtrsim 2$) in the mid-IR magnitudes of quasars and radio galaxies was also reported by several studies (e.g. Heckman et al. 1992, 1994; Haas et al. 2005; Cleary et al. 2007; Hönig et al. 2011). Other authors (e.g. Meisenheimer et al. 2001; Haas et al. 2004) used small samples and found a slight difference between the properties of quasars and galaxies in the IR bands. Various interpretations (such as torus anisotropy, effects of the environments) were used to explain this. Dicken et al. (2009) obtained no difference between the mid-IR luminosities of the broad- and narrow-line objects from the 2Jy sample. However, although they used a complete sample, it is small in size. The work is the first to use large, complete samples with coherent mid-IR data and good coverage of the redshift range where quasars and radio galaxies coexist in large numbers.

Different torus models have been proposed to explain different properties of quasars and radio galaxies (e.g. Pier & Krolik 1992, 1993; Nenkova et al. 2002, 2008a,b; Schartmann et al. 2005; Lawrence 1991; Simpson 1998; Grimes et al. 2003) and anisotropic emission due to the torus is expected in all suggested models. In order

to evaluate these results in terms of different torus models I first calculated the critical angles (θ_{crit}) which is the angle to the line of sight separating quasars and radio galaxies. To do that, as described in Barthel (1989) I used the probability function of finding a source within an angle to the line of sight for a randomly distributed set of sources and the number of quasars and radio galaxies found in a given redshift bin. The characteristic angles (the expected angle to the line of sight) for quasars (θ_Q) and radio galaxies (θ_{RG}) were computed for each redshift bin. These results are also shown in Table 3.2.

I then examined the results with regard to the predictions of well-known torus models such as torus with smooth density distribution (Schartmann et al. 2005) and torus with clumps (Nenkova et al. 2008b). The results for both 12 μm and 22 μm wavebands are in agreement with the predictions of smooth torus models which show a relatively strong effect of anisotropy compared to clumpy torus models. For instance, there is a higher difference in the luminosities of quasars and radio galaxies at lower redshifts compared to the higher redshifts. Figure 8 in Schartmann et al. (2005) shows an inclination angle study for a range of wavelengths considering a smooth torus model; according to this figure, for the first two redshift bins, I expect to see a strong anisotropy in the mid-IR luminosity for calculated characteristic angles of quasars and radio galaxies at a corresponding wavelength (from the angles around 30° to 70° approximately a factor of four decrease is expected at 11 μm (rest-wavelength)). A similar study for clumpy torus models (Nenkova et al. 2008b, their Figure 10) shows only a slight difference in the mid-IR magnitudes for expected angles of quasars and radio galaxies (the difference in the mid-IR magnitudes between the angles around 30° and 70° is a factor of 1.2 at 12 μm (rest-wavelength)). As previously mentioned there are three components that contribute to the mid-IR: re-radiation from torus; emission from the old stellar population and non-thermal contamination that can be seen in quasars/BLRGs. Any effect from an old stellar population is expected to be the same for both quasars and NLRGs. In clumpy torus models, substantial non-thermal contamination in quasars/BLRGs would have to be present to explain the results obtained here.

Redshift bins	Class & Ratio	N	3.4 μm $\times 10^{45}$ erg/s	4.6 μm $\times 10^{45}$ erg/s	12 μm $\times 10^{45}$ erg/s	22 μm $\times 10^{45}$ erg/s	θ_{crit}	θ_Q	θ_{RG}
0.2<z<0.621	Quasars	15	1.365 (0.350)	1.531 (0.432)	2.983 (0.6285)	3.951 (0.913)		32.2	
	NLRGs	49	0.142 (0.017)	0.090 (0.015)	0.137 (0.0885)	0.239 (0.167)			70.4
	Ratio		9.612 (2.720)	17.011 (5.623)	21.773 (14.794)	16.531 (12.199)	49		
0.621<z<1.00	Quasars	20	1.645 (0.633)	1.913 (0.5325)	6.298 (1.329)	10.232 (2.538)		36	
	NLRGs	38	0.270 (0.042)	0.154 (0.0305)	0.437 (0.112)	1.433 (0.171)			73
	Ratio		6.092 (2.533)	12.422 (4.243)	14.411 (4.797)	7.140 (1.965)	55		
1.00<z<1.517	Quasars	23	1.566 (0.458)	1.738 (0.424)	8.852 (1.671)	17.077 (2.233)		45.4	
	NLRGs	25	0.264 (0.036)	0.288 (0.061)	1.553 (0.510)	4.951 (1.288)			80.1
	Ratio		5.931 (1.881)	6.034 (1.957)	5.699 (2.160)	3.449 (1.004)	70		
1.517<z<1.96	Quasars	11	2.782(0.397)	3.231 (0.374)	35.475 (3.866)	42.618 (8.610)		44.8	
	NLRGs	21	0.556(0.052)	0.431 (0.094)	2.826 (1.874)	16.106 (3.547)			79.6
	Ratio		5.003 (0.856)	7.496 (1.850)	12.553 (8.043)	2.646 (0.790)	69		

Table 3.2: Median values of the 3.4 μm , 4.6 μm , 22 μm and 12 μm luminosities were derived using the ASURV (Schmitt 1985; Feigelson & Nelson 1985; Isobe et al. 1986) computer package for four different redshift bins. Redshift bins are shown in column 1, N indicates number of sources included to calculate median values, shown in column 3. Classes and ratios computed are given in column 4, 5, 6, 7 for the 3.4 μm , 4.6 μm , 12 μm and 22 μm luminosities respectively. Errors in calculations are given in parentheses. Column 8 shows the critical angles calculated and characteristic angles found for quasars as well as radio galaxies are given column 9 and 10.

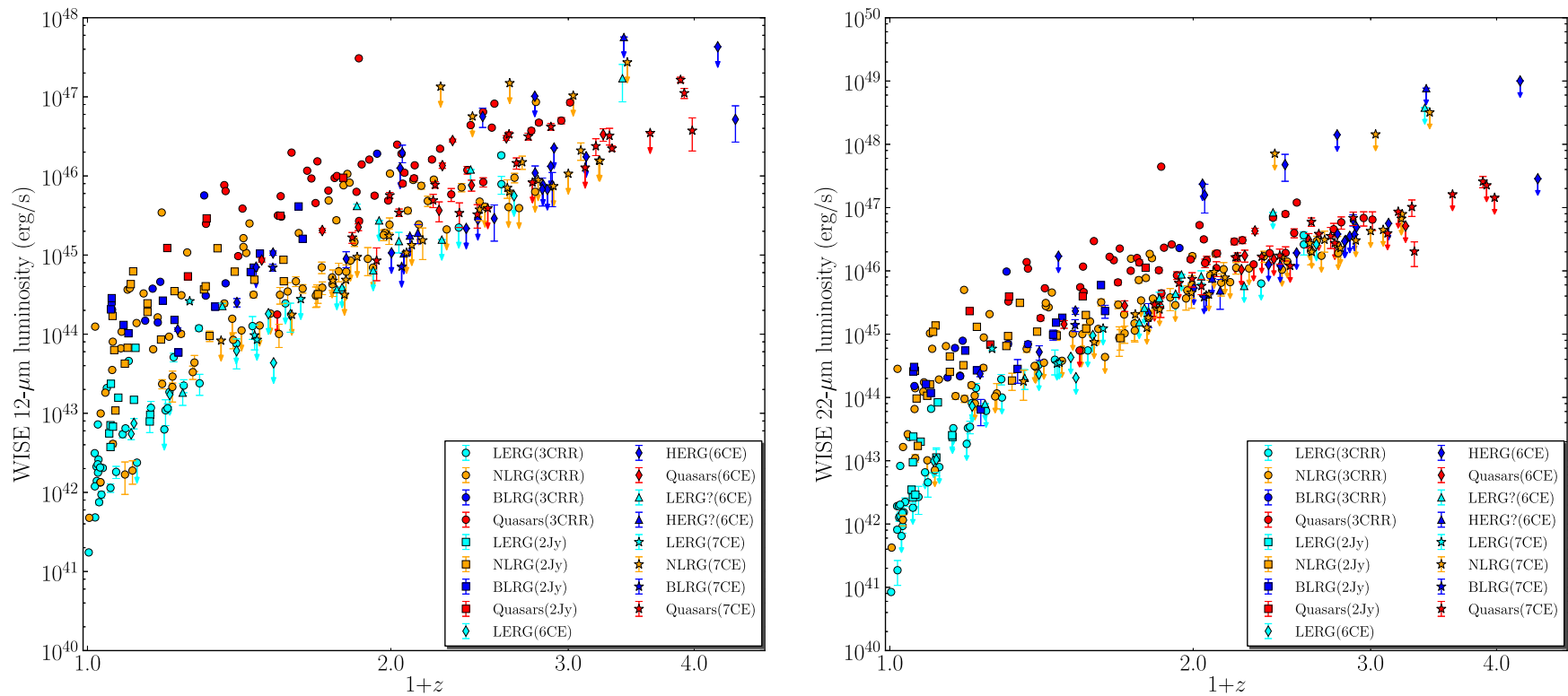


Figure 3.6: Plot of $12\mu\text{m}$ luminosity (left) and $22\mu\text{m}$ luminosity (right) versus redshift. Upper limits are indicated as arrows.

3.4.5 Dichotomy for LERGs and HERGs

The primary aim in this section is to investigate how LERGs can fit into unification models and to what level mid-IR radiation can aid us in classifying LERGs and HERGs. The low-frequency radio luminosity is related to the time-averaged jet kinetic power but also the age of the source and to the properties of the external environment (e.g. Hardcastle & Krause 2013). The mid-IR luminosity gives information about the torus emission (if it is present) and can be considered as a proxy for the intrinsic AGN luminosity (e.g. Fernandes et al. 2011). There may be some contamination, such as emission from the old stellar population and any possible anisotropy in the torus emission, as mentioned in the previous section. There can also be contributions from jet related non-thermal emission, Doppler boosted due to low inclinations (mainly in quasars and BLRGs).

In Figure 3.7 I present the mid-IR luminosity versus low-frequency radio luminosity (at 151 MHz) for the radio sources in the samples. In both plots I see a correlation between the 151 MHz and mid-IR luminosities. This is expected as presumably both luminosities are roughly isotropic indicators of AGN nuclear activity. The 12 μm plot has higher scatter than the 22 μm one; this is ascribable to strong PAH features and emission from an old stellar population which still contributes at 12 μm band. Further examination of each of the samples in both plots shows that there is a scatter in the correlation due to selection biases. The 3CRR/2Jy objects have high radio luminosities in comparison to 6CE/7CE objects for a given mid-IR luminosity. The 6CE/7CE objects exhibit lower jet powers in comparison to the 3CRR/2Jy sources for a chosen radiative power (For a given 22-micron luminosity ($L_{22\mu\text{m}} = 10^{45} \text{ erg s}^{-1}$) the corresponding 151 MHz luminosity for the 3CRR sample is $3 \times 10^{43} \text{ erg s}^{-1}$, this value is $4 \times 10^{42} \text{ erg s}^{-1}$ for the 6CE sample and $1 \times 10^{42} \text{ erg s}^{-1}$ for the 7CE sample.). This suggests that we may not necessarily see a one-to-one correlation between radiative power and jet power (Ogle et al. 2006; Punsly & Zhang 2011; Fernandes et al. 2011; Mingo et al. 2014). 3CRR and 2Jy objects, which are the most radio-luminous sources in the Universe in their redshift range, are selected to have highest radio luminosity for a given AGN power.

Considering the LERG/HERG division, the correlation between the low-frequency radio luminosity and mid-IR luminosity is very clear for HERGs. However, this correlation disappears for LERGs. I have used a quantitative test of partial correlation that takes into account censored data (Akritas & Siebert 1996). The results of this correlation analysis can be found in Table 3.3. I performed the correlation analysis between

22 μm and 151 MHz luminosity for all samples as well as for LERGs and HERGs separately. These results confirm the physical relationship between mid-IR and radio luminosities seen for HERGs (the strength of the correlation is given by $\tau/\sigma=6.08$). On the other hand, the relationship is not significant for LERGs ($\tau/\sigma=1.89$).

In order to highlight the separate positions of HERGs and LERGs in the radio–mid-IR plane, I re-plotted the 22 μm –, 22 μm –151 MHz luminosities using a different colour scheme. This can be seen in Figure 3.8 where HERGs are plotted with purple colours and LERGs with cyan colours. In this plot, an approximate empirical cutoff between LERGs and HERGs stands out, corresponding to a 22 μm luminosity around $5 \times 10^{43} \text{ erg s}^{-1}$ [$L_{\text{bol}} \approx 10^{45} \text{ erg s}^{-1}$, assuming that the bolometric correction is ~ 20 (Runnoe et al. 2012b)]. A similar dividing luminosity was also found by Ogle et al. (2006) using a much smaller sample. The objects lying below this line are almost exclusively LERGs. Some overlap between LERGs and NLRGs appears in this plot. Classifications of some sources (especially in the 6CE sample, those labelled with question mark) are not clear which may cause this overlap. Furthermore, as argued by (e.g. Mingo et al. 2014) some low-power objects classified as NLRGs should actually be classified as LERGs. However, it is important to note that almost all LERGs above this cutoff are upper limits. An object that is detected and has a luminosity higher than $5 \times 10^{43} \text{ erg s}^{-1}$ is almost certainly a HERG.

The partial correlation test has also been carried out for all objects and each class in the 3CRR and 2Jy samples using the 5 GHz luminosity– 22 μm luminosity (Figure 3.9) to see if there is any significant correlation between these luminosities. Since only the 3CRR and 2Jy samples have radio core observations, the 6CE and 7CE samples were not used for the analysis. The results of this correlation analysis are also shown in Table 3.3. In Figure 3.9 NLRGs and BLRGs almost overlap, but quasars have higher luminosities at both wavelengths which can be attributed to some other (non-thermal or emission from the disk) contamination seen in the mid-IR for BLRGs and quasars. Despite the correlation seen for all sources, owing to the effect of redshift dependency, we do not see a significant correlation for each population apart from the LERGs. The results support the findings of the similar analysis of Hardcastle et al. (2009). The radio-core luminosity of AGN is an indicator of instantaneous jet power (e.g. Blandford & Königl 1979). The significant correlation between radio-core emission and mid-IR emission seen in LERGs strengthens the idea that the mid-IR power in LERGs can originate in jets instead of the standard accretion mechanism (e.g. Chiaberge et al. 2002).

As seen in Figure 3.8, LERGs exhibit very weak mid-IR emission and some have only upper limits. This can obviously be attributed to lack of obscuring structures. The results also reinforce the prediction that different accretion modes govern HERGs and LERGs. What drives these different modes is a crucial question.

As discussed in Section 1, one of the hypotheses for the difference between HERGs and LERGs is that there is a limiting value of the Eddington-scaled accretion rate above which radiatively efficient accretion takes place. In order to test this hypothesis I use available *WISE* data; using $22\ \mu\text{m}$ luminosity as a proxy for the total radiative luminosity of AGN and the $3.6\ \mu\text{m}$ luminosity for stellar luminosity (\sim stellar mass), which is correlated with black-hole mass and thus with the Eddington luminosity for LERGs and NLRGs. Quasars and BLRGs can be contaminated by non-thermal emission in both bands. Moreover, the nuclear quasar emission can overwhelm the stellar light measured at $3.4\ \mu\text{m}$. For these reasons, quasars and BLRGs are excluded from the plots. The ratio of $22\ \mu\text{m}$ to $3.6\ \mu\text{m}$ then should provide a proxy of the Eddington-scaled accretion rate for NLRGs and LERGs. The results of this test can be seen in Figure 3.10. In Figure 3.10 (left) all NLRGs and LERGs are used, independent of upper limits. In order to see the effect of upper limits, I also show the distribution of the ratio excluding upper limits (Figure 3.10-right). Although the result does not change, the overlap between NLRGs and LERGs is reduced in the plot. It is clear that while NLRGs show high values of this ratio (~ 0.3 -10) LERGs have much lower values (~ 0.01 -0.3). Similarly, different accretion rates for HERGs and LERGs were obtained in recent studies (Best & Heckman 2012; Russell et al. 2013; Mingo et al. 2014). It is worth noting that in both histograms there are some overlaps but since I am only using rough estimators for calculation of the accretion rates this is expected. Furthermore, the classifications of some sources are not clear (such as some sources in the 6CE sample) and this can also lead to some overlap. Nevertheless, this suggests that the $22\ \mu\text{m}/3.6\ \mu\text{m}$ luminosity ratio can give a good empirical NLRG/LERG classification. A more detailed discussion of the Eddington-scaled accretion rate in radio galaxies is given by (Mingo et al. 2014; Fernandes et al. 2015).

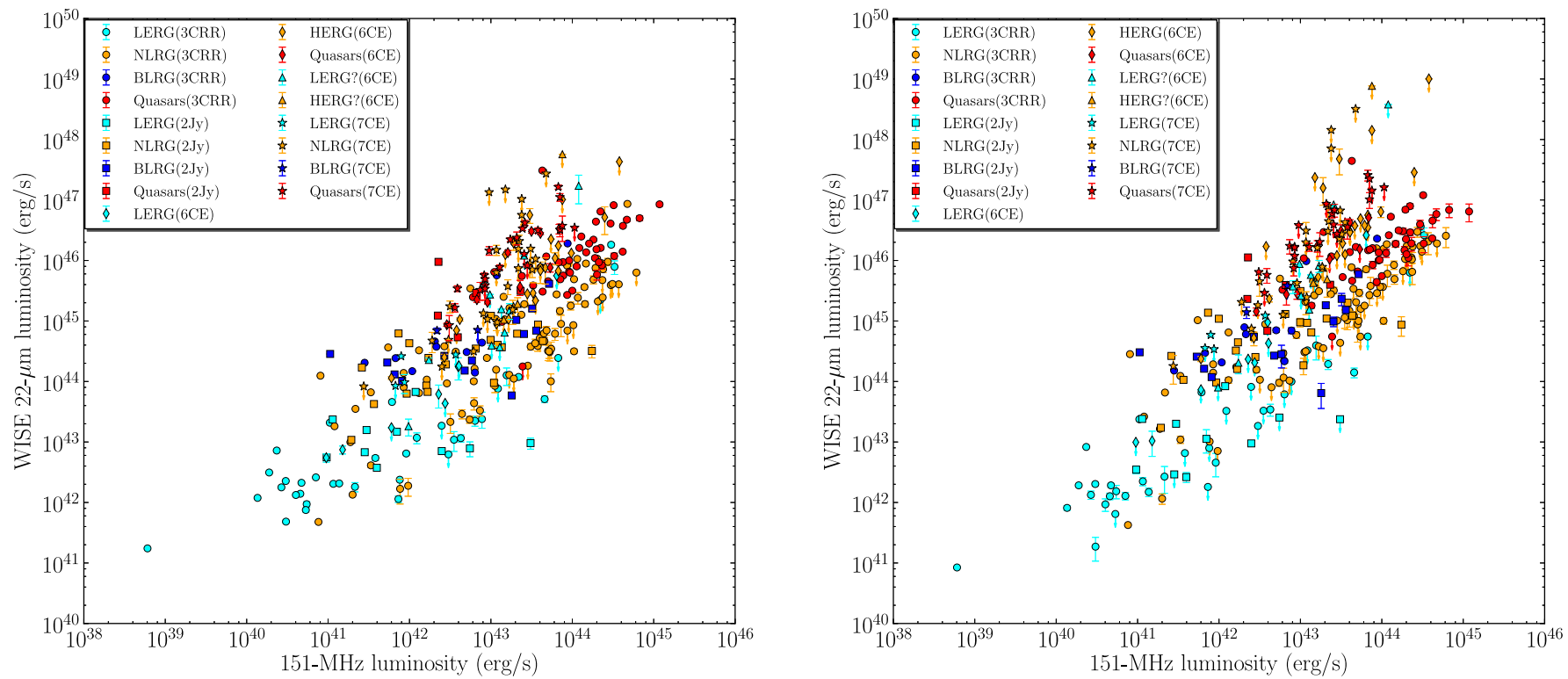


Figure 3.7: Plot of 12 μ m luminosity (right) and 22 μ m luminosity (left) versus 151 MHz radio luminosity. Upper limits are indicated as arrows.

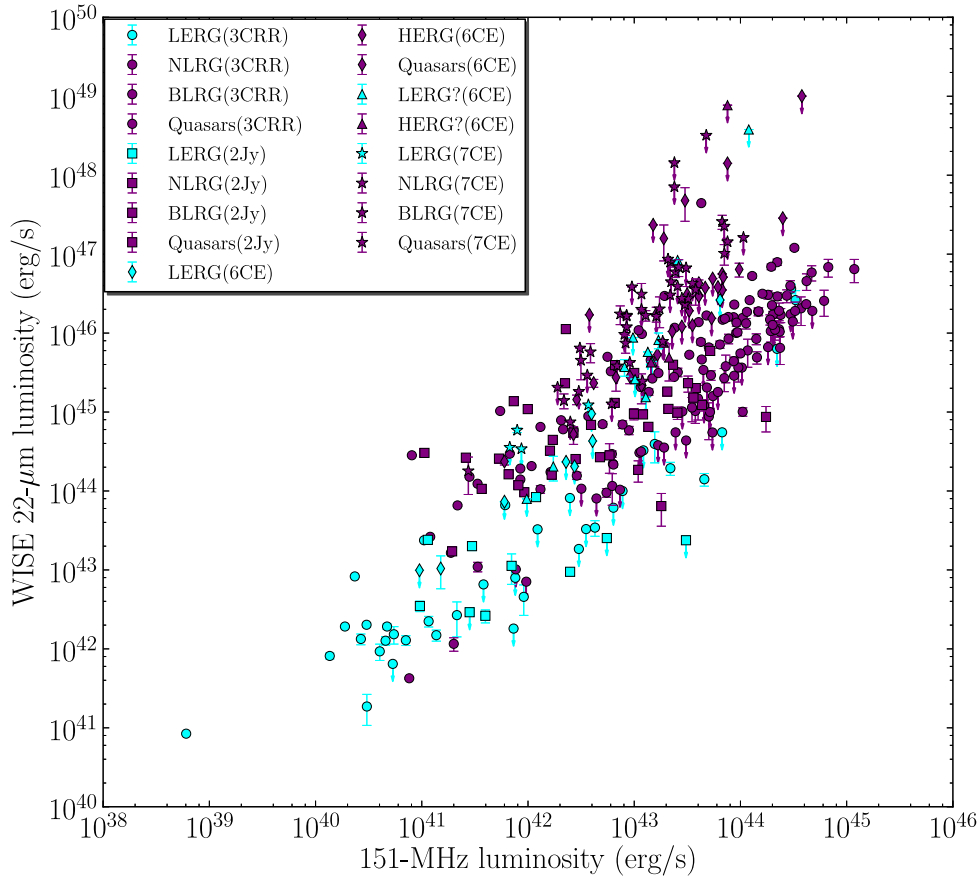


Figure 3.8: Plot of $22\ \mu\text{m}$ luminosity versus 151 MHz radio luminosity. Upper limits are indicated as arrows. In order to show the distribution of HERGs and LERGs clearly, HERGs are plotted as purple filled circles and LERGs are as cyan filled circles.

Abscissa	Ordinate	Subsample	Number	Correlation	τ/σ
L_{151}	$L_{22\mu m}$	All	335	Yes	7.97
		LERGs	69	No	1.89
		HERGs	266	Yes	6.08
L_5	$L_{22\mu m}$	All	219	Yes	9.38
		LERGs	47	Yes	4.67
		BLRGs	23	No	-0.12
		NLRGs	101	No	2.41
		Quasars	48	No	2.96

Table 3.3: Results of partial correlation analyses. All sources and subsamples that have relevant luminosities used for the analysis are given in column 3. The number of objects included in the analysis can be seen in column 4. τ/σ gives an indication of the strength of the partial correlation in the presence of redshift; a cutoff of τ/σ is adopted as $\tau/\sigma > 3$ for a significant correlation.

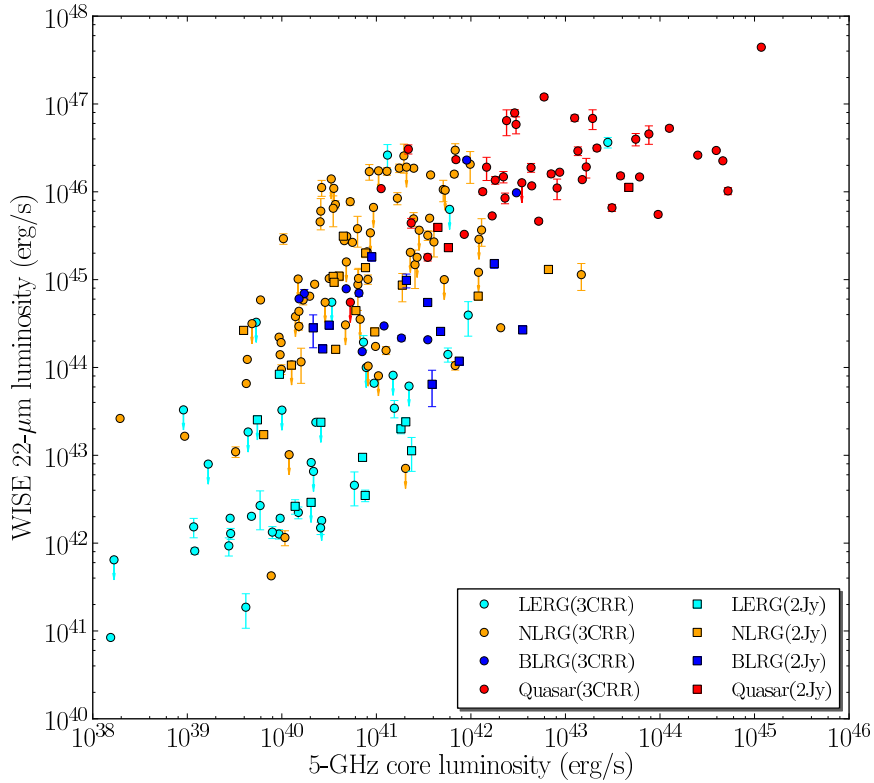


Figure 3.9: Plot of 22 μm luminosity versus 5 GHz core luminosity. The 6CE and 7CE samples do not have radio core observations so I only present the 3CRR and 2Jy samples.

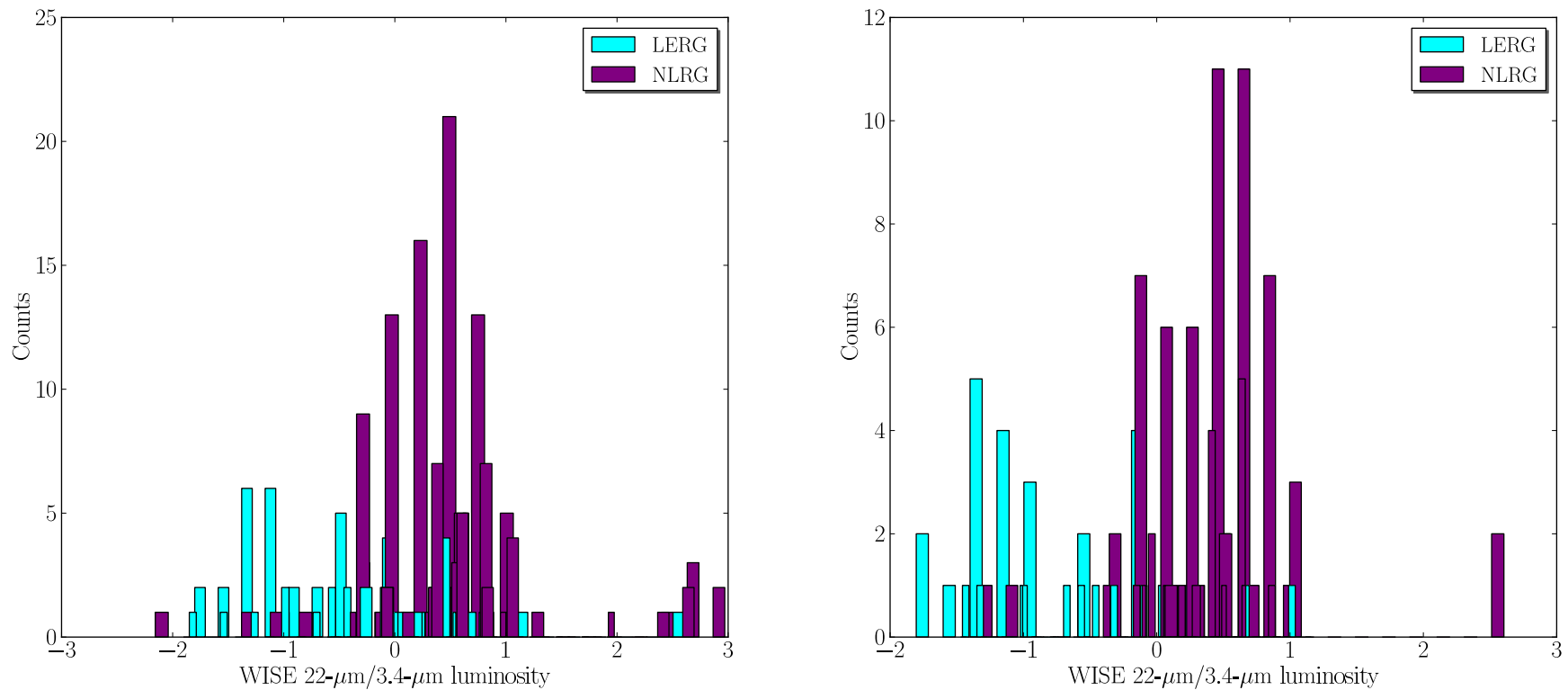


Figure 3.10: Histogram of the distribution of 22 μm luminosity over 3.4 μm luminosity (a proxy of the Eddington-scaled accretion rate). In the left plot all sources are used and in the right objects with upper limits are excluded.

3.5 Summary and Conclusions

I have used *WISE* to establish the near and mid-IR properties of four radio samples; 3CRR, 2Jy, 6CE and 7CE. The main results are as follows.

- I evaluated the objects in *WISE* colour-colour diagrams. Various *WISE* colour cuts and criteria have been suggested for selecting AGN (Assef et al. 2010; Jarrett et al. 2011; Mateos et al. 2012; Stern et al. 2012; Assef et al. 2013). Although these criteria are detecting some AGN, they are not successful for covering all types of AGN. It can be seen in the diagrams (Figure 3.3) that LERGs and many NLRGs cannot be selected using a simple *WISE* colour cut or by other criteria proposed in the literature.
- The near-IR luminosity–redshift relation reinforces the picture in which radio galaxies are hosted by giant ellipticals that formed their stars at high redshifts and evolved passively thereafter. At high redshifts ($z > 0.7$) 3CRR objects differ from 6CE and 7CE object having higher near-IR luminosities. This suggests that 3CRR galaxies are more massive systems with higher masses of stars at high redshifts compared to 6CE and 7CE radio galaxies.
- The investigations of quasar-radio galaxy unification indicate that quasars are systematically more luminous in the mid-IR than radio galaxies, and more so at $12 \mu\text{m}$ than $22 \mu\text{m}$. The results are consistent with the predictions of smooth torus models which show a strong effect of anisotropy (e.g. Schartmann et al. 2005).
- I have shown for the first time with a large complete sample that low- and high- excitation radio-loud AGN have completely different mid-IR luminosities. While LERGs have extremely weak mid-IR luminosities—in fact many of them are not detected and have only upper limits—HERGs are mostly luminous sources in the mid-IR. The results obviously favour previously established accretion models (e.g. Hine & Longair 1979; Laing et al. 1994; Evans et al. 2006; Ogle et al. 2006; Hardcastle et al. 2007b; Janssen et al. 2012; Best & Heckman 2012; Russell et al. 2013); LERGs do not hold any conventional AGN properties and accrete in a radiatively inefficient manner, while HERGs are powered by radiatively efficient accretion. This accretion-mode classification can now be *explicitly* identified in the mid-IR–radio plane.

The distribution of each population is quite distinct in the $22\ \mu\text{m}$ –151 MHz luminosity plot. An empirical cutoff stands out in the radio-IR plane (Figure 3.8), which leads to the conclusion that any object below $4\text{--}5 \times 10^{43}\ \text{erg s}^{-1}$ at $22\ \mu\text{m}$ is a LERG. Classification of radio sources, hitherto, have relied on expensive optical spectroscopy. Here, I propose that *WISE* data can be effectively used to identify radiatively inefficient and efficient radio-loud AGN.

- One model of the difference between LERGs and HERGs is that there is a limiting value of the Eddington-scaled accretion rate above which radiatively efficient accretion takes place. Using the $22\ \mu\text{m}$ and $3.4\ \mu\text{m}$ luminosities I calculated the ratio of $22\ \mu\text{m}/3.4\ \mu\text{m}$ as a proxy of the Eddington-scaled accretion rates for NLRGs and LERGs. Although there is some overlap, LERGs ($\sim 0.01\text{--}0.3$) and NLRGs ($\sim 0.3\text{--}10$) differ from each other in this ratio. Different accretion rates for LERGs and HERGs were also found by others (Best & Heckman 2012; Russell et al. 2013; Mingo et al. 2014). Since the classification of some objects in the 6CE and 7CE sample is not complete and secure, we may expect to have some overlap in the accretion-rate histograms. Other uncertainties such as the effect of different environments on the radio power of radio galaxies as well as the calculation of black hole mass can contribute to this overlap (see Mingo et al. (2014)).

Chapter 4

Herschel-ATLAS: The connection between star formation and AGN activity in radio-loud and radio-quiet active galaxies

“I have little patience with scientists who take a board of wood, look for the thinnest part, and drill a great number of holes where drilling is easy.”

Albert Einstein, Einstein’s Philosophy of Science

4.1 Abstract

I examine the relationship between star formation and AGN activity by constructing matched samples of local ($0 < z < 0.6$) radio-loud and radio-quiet AGN in the *Herschel-ATLAS* fields. Radio-loud AGN are classified as HERGs and LERGs using their emission lines and *WISE* 22 μm luminosity. AGN accretion and jet powers in these active galaxies are traced by [OIII] emission-line and radio luminosity, respectively. SFRs and SSFRs were derived using *Herschel* 250 μm luminosity and stellar mass measurements from the SDSS–MPA–JHU catalogue. In the past, star formation studies of AGN have mostly focused on high-redshift sources to observe the thermal dust emission that peaks in the far-infrared, which limited the samples to powerful

objects. However, with *Herschel* we can expand this to low redshifts. The stacking analyses show that SFRs and SSFRs of both radio-loud and radio-quiet AGN increase with increasing AGN power but that radio-loud AGN tend to have lower SFR. Additionally, radio-quiet AGN are found to have approximately an order of magnitude higher SSFRs than radio-loud AGN for a given level of AGN power. The difference between the star formation properties of radio-loud and -quiet AGN is also seen in samples matched in stellar mass.

4.2 Introduction

Since their discovery AGN have formed an important part of astrophysics research. Investigations of AGN are not only crucial in their own right, but also essential for galaxy formation and evolution studies. Accumulating observational data clearly show that the masses of black holes in massive galaxies are correlated with various properties of their hosts such as the galaxy luminosities (e.g. Kormendy & Richstone 1995; Marconi & Hunt 2003; Gültekin et al. 2009), the galaxy bulge masses (e.g. Magorrian et al. 1998; McLure & Dunlop 2002) and the velocity dispersions (e.g. Ferrarese & Merritt 2000; Gebhardt et al. 2000; Merritt & Ferrarese 2001). Furthermore, the anti-hierarchical evolution of AGN (e.g. Miyaji et al. 2000; Hasinger et al. 2005; Bongiorno et al. 2007; Rigby et al. 2011), i.e. the fact that the space density of low-luminosity AGN peaks around $z < 1$ and that of high-luminosity AGN peaks around $z \sim 2$, is very similar to the cosmic downsizing of star forming galaxies (e.g. Cowie et al. 1996; Menci et al. 2008; Fontanot et al. 2009) and spheroidal galaxies (e.g. Cimatti et al. 2006; Thomas et al. 2010). In addition to these, both the integrated cosmic star formation rate and the black hole accretion rate increase rapidly from $z \sim 0$ out to $z \sim 2$ (Dickinson et al. 2003; Babić et al. 2007; Hopkins et al. 2007; Wilkins et al. 2008; Rigby et al. 2011). All these relationships indicate that the formation and growth of the black holes and their host galaxies are fundamentally intertwined.

Although these relationships are observed, there is not yet a clear understanding of how black holes grow, the link between the growth of black holes and their host galaxy properties, and what leads to these connections. To explain the observed co-evolution of black holes and their hosts, interactions (AGN feedback) between the black hole at the centre of a galaxy and the gas and dust that it contains have been invoked in theoretical models (e.g. Granato et al. 2004; Springel et al. 2005; Croton et al. 2006; Hopkins et al. 2006; Sijacki et al. 2009; Cen & Chisari 2011). Major mergers have

been widely suggested as a triggering mechanism of AGN activity (e.g. Kauffmann & Haehnelt 2000; Hopkins et al. 2005). Secular processes (disk instabilities, minor mergers, recycled gas from dying stars, galaxy bars etc.) have also been discussed as a mechanism responsible for fuelling, in particular for low-luminosity AGN (e.g. Johansson et al. 2009; Genzel et al. 2008; Ciotti et al. 2010).

Models often represent the effects of feedback in two ways, denoted ‘quasar mode’ and ‘radio mode’ (e.g. Croton et al. 2006). In quasar mode the energy release occurs as winds with sub-relativistic outflows and wide opening angle driven by the radiative output of AGN. The generated radiation interacts with the gas and dust in the host galaxies and the resulting winds (either energy driven winds or momentum driven winds, see Cattaneo et al. (2009) for further information) can expel the gas from the galaxy. This can stop the accretion of matter onto a black hole and further quench the formation of stars (e.g. Page et al. 2012). However, studies of X-ray luminous AGN do not show any evidence for this (e.g. Harrison et al. 2012, but see Cano-Díaz et al. 2012, Barger et al. 2015 and Brusa et al. 2015).

In radio-mode feedback, the accretion of the matter does not lead to powerful radiative output; instead we see the production of highly energetic jets. The jets may play an important role in the fate of the host galaxy by heating up the cold gas and suppressing star formation (e.g. Best et al. 2005; Hardcastle et al. 2013). There is even an indication for this in radio-quiet quasars (e.g. Harrison et al. 2015). In the most dramatic scenario, the jets can expel the molecular gas from the host galaxy and stop star formation. Radio mode feedback has been widely used in simulations as a mechanism to prevent the overproduction of stars (by shutting down the star formation) in massive galaxies in order to produce observed “red and dead” early-type galaxies (e.g. Bower et al. 2006; Werner et al. 2014; Chen et al. 2013b). However, a positive radio mode feedback has also been suggested (Silk & Nusser 2010; Kalfountzou et al. 2012, 2014; Gaibler et al. 2012). In this scenario, the radio jets drive shocks in the interstellar medium which enhance the star formation (e.g. Eales & Rawlings 1990; Best et al. 1998a; Jarvis et al. 2001b; Inskip et al. 2005).

Different types of AGN might be able to provide feedback in multiple ways. It is known that LERGs do not have radiatively efficient accretion, which removes the possibility of quasar-mode feedback. They are believed to be fuelled by ADAFs (e.g. Narayan & Yi 1995b) which can create an environment where the energy release occurs kinetically by the radio jets. These jets are able to provide ‘radio-mode’ feedback. Radio-quiet active galaxies and radio-quiet quasars have typical AGN properties where

we see the radiative output but no strong radio jets, and so we can only expect to see ‘quasar mode’ feedback. On the other hand, radio-loud quasars and HERGs have radiative output produced by highly efficient accretion as well as kinetic energy release seen as strong radio jets. Therefore, both feedback mechanisms might be expected to be observed in these powerful objects.

The anticipated relationship between AGN luminosity (or black hole accretion rate) and SFR has been investigated many times previously with mixed results (for recent reviews on black holes and galaxy evolution see Alexander & Hickox 2012, Kormendy & Ho 2013 and Heckman & Best 2014). For instance, some studies have found a slight correlation between these quantities (e.g. Lutz et al. 2008; Serjeant & Hatziminaoglou 2009; Bonfield et al. 2011; Silverman et al. 2009; LaMassa et al. 2013), some others found a strong correlation (e.g. Hao et al. 2005; Satyapal et al. 2005; Netzer 2009; Shi et al. 2009; Chen et al. 2013a) whereas others (e.g. Harrison et al. 2012; Rosario et al. 2012; Rovilos et al. 2012; Mullaney et al. 2012; Bongiorno et al. 2012) found a flat relationship (or no evidence for a correlation). On the other hand, the results of Page et al. (2012) indicate a *suppression* of star formation due to AGN feedback (see Caputi 2014 for a recent review on the IR perspective of AGN). This wide variety of results is puzzling. It is important to note that although there are some overlaps between samples, fields and indicators used for SFR and AGN luminosity, in general both the sample selection and the star-formation indicator used varies from study to study. These may cause biases in the conclusions derived. Thus, performing complete and coherent surveys of AGN, minimising the systematic uncertainties, and proposing revised models and testing them are crucial for future AGN research. Additionally, it has been pointed out that the different variability time scale of AGN activity and star formation can lead to these different results (e.g. Hickox et al. 2014; Wild et al. 2010; Hopkins & Hernquist 2009). For this reason, instead of concentrating on individual sources and instantaneous AGN activity, averaging the AGN luminosity over the populations should provide a clearer view of the relation between SFR and AGN activity (e.g. Chen et al. 2013a).

Another interesting aspect is to search for differences in the relationship between the AGN activity and SFR for radio-loud and radio-quiet AGN. This has been investigated previously: Dicken et al. (2012) found that at low redshifts radio-quiet AGN hosts have stars forming at higher rates than radio-loud counterparts while Chen et al. (2013b) observed two times more actively star-forming galaxies among radio-quiet AGN than radio-loud AGN for galaxies with stellar masses $M_* > 10^{11.4} M_\odot$. These

studies have provided important information on investigations of AGN–SFR relation for different types of AGN. However, it is still important to investigate similarities or differences between the relationship of AGN outputs (kinetic or radiative) and SFR using radio-quiet and radio-loud AGN samples matched in AGN power and stellar mass, and the possible reasons for these.

In this work I investigate the role of AGN activity in regulating the host galaxy evolution as a function of the different types of AGN. In the pre-*Herschel* era, star-formation studies of radio-loud AGN concentrated on high-redshift sources in order to observe the thermal dust emission peaking in the far-infrared/sub-mm, which limited the samples to powerful objects (e.g. Archibald et al. 2001; Reuland et al. 2004). However, it is now possible with *Herschel* to expand this to low redshifts (e.g. Hardcastle et al. 2010; Jarvis et al. 2010; Hardcastle et al. 2013; Virdee et al. 2013). Therefore, I have been able to create matched samples of radio-loud and radio-quiet AGN with redshifts $0 < z < 0.6$ in terms of the relationship between their star formation properties and their AGN activity.

The layout of this chapter is as follows. A description of the sample and, the classification of the AGN are given in Section 2. The key results are given in Section 3, where the comparison of the stacking analysis between radio-loud and radio-quiet AGN as well as between HERGs and LERGs are presented. I also form a sample of sources matched in their stellar mass in order to investigate the star formation properties of these sources by excluding the effect of mass. Additionally the relation between SFR and black hole accretion rate (\dot{M}_{BH}) for radio-loud and radio-quiet AGN samples is examined. In Section 4 I interpret the results. Section 5 presents a summary of the results and conclusions.

4.3 Data

4.3.1 Sample and classification

To construct my sample I selected galaxies from the seventh data release of SDSS (Abazajian et al. 2009) catalogue with the value-added spectroscopic measurements produced by the group from the MPA-JHU¹. It has 31001 sources spanning a redshift range $0 < z < 0.7$. The sample does not include quasars and Type-I Seyferts because the AGN outshine the host galaxies for these objects which makes it difficult to study

¹<http://www.mpa-garching.mpg.de/SDSS/>

their host galaxy properties. The H-ATLAS-NGP (Eales et al. 2010a) and the three equatorial GAMA fields (Driver et al. 2011) data were used to obtain far-IR fluxes of the sample galaxies. Stellar mass estimates are available for most of the sources in the catalogue (Kauffmann et al. 2003b).

Best & Heckman (2012) (BH12 hereafter) constructed a radio-loud AGN sample by combining the seventh data release of the SDSS sample with NVSS (Condon et al. 1998) and FIRST survey (Becker et al. 1995) following the methods described by Best et al. (2005) and Donoso et al. (2009). I will briefly summarize their method, further details are given by Best et al. (2005) and Donoso et al. (2009). Firstly, each SDSS source was checked to see whether it has a NVSS counterpart: in the case of multiple-NVSS-component matches the integrated flux densities were summed to obtain the flux density of a radio source. If there was a single NVSS match, then FIRST counterparts of the source were checked. If a single FIRST component was matched, accepting or rejecting the match was decided based on FIRST properties of these sources. If there were multiple FIRST components the source was accepted or rejected based on its NVSS properties. Since this classification is sensible and re-producible I use the classification of BH12 for my work here.

I firstly cross-matched the initial sample of galaxies with the BH12 catalogue, and all objects that they classified as AGN form the ‘radio-loud’ subsample, which has 613 objects. The remaining ‘radio-quiet’ AGN sample are classified using the modified emission-line diagnostics given by Kewley et al. (2006). This classification is shown in Figure 4.1. Composite objects were separated from star-forming objects using a classification line given by Kauffmann et al. (2003c). This classification line utilizes the $[\text{NII}] \lambda 6584 / [\text{H}_\alpha]$ ratio so it is not shown in Fig. 4.1.

The classification done by using optical emission line ratios and this process gave me 8035 star-forming objects, 1190 objects classified as Seyferts, 2490 composite objects and 319 LINERs (Table 6.1). Emission lines were not detected for 17741 objects in the sample so they could not be classified in this way. This classification biases me towards massive, low redshift galaxies. The sample has a mean stellar mass, $\log_{10}(M/M_\odot) = 9.55$ and a mean redshift = 0.14. After the classification using optical emission lines the mean stellar mass is $\log_{10}(M/M_\odot) = 10.08$ and the mean redshift equals 0.09 (Figure 4.2 - bottom plot). The final sample has a redshift range $0 < z < 0.56$. I do not consider objects that are not classified using the BPT diagram (Fig. 4.1) further in this chapter, and I also discarded: star-forming objects, LINERs and the objects in the BH12 sample classified as star-forming sources from the AGN

Population type	Counts
Radio-loud AGN	613
Seyferts	1190
Composites	2490
Star-forming objects	8035
LINERs	319

Table 4.1: The number of sources in each population after the optical emission-line classification.

sample. The end result is that a combination of Seyferts and composite objects classified using optical emission lines formed the radio-quiet AGN sample, which has 3680 objects.

The treatment of composite objects is discussed in detail in Section 4.4.1. For the analysis I use stellar mass estimations of the sources to be able to calculate their SSFRs. There are only 206 objects in the sample that do not have these measurements. These sources were excluded from the parts of the analysis that involve SSFRs. These sources are systematically at higher redshifts so the sample used in the parts of analysis that involve SSFRs will be biased.

To be able to evaluate the properties of radio-loud AGN as a function of emission-line class, the radio galaxies in the sample were classified as HERGs and LERGs. I initially used classification information provided by BH12. There are 191 sources which are not classified either as HERG or LERG by BH12. For these sources I used the *WISE*-based (details with regard to *WISE* data are given in Section 2.3) classification given in Chapter 3. The final radio-loud AGN sample has 404 LERGs and 209 as HERGs.

There are various diagnostics using radio and optical measurements to classify sources as radio-loud or radio-quiet AGN. I did not use any of these diagnostics to classify the objects as radio-loud or radio-quiet AGN. This is because the objects are Seyferts 2s and radio galaxies and the estimation of optical luminosities for such objects, even when they are radiatively efficient, is difficult. However, I checked whether the radio-loud and radio-quiet AGN classifications coincide with traditional classifications. In order to do this assessment, I used radio and emission-line measurements available to us. I calculated the ratio of radio luminosity (at 1.4 GHz) to an estimate of optical luminosity (at 5100 Å). As the AGN are mostly Type II Seyferts, I do not know their intrinsic optical luminosities and to derive these I used the bolometric luminosities (L_{bol} , see Section 2.4) and the relation between L_{bol} and L_{5100} given by

Runnoe et al. (2012a). I have 1.4 GHz fluxes of the radio-loud sources from BH12. I cross-matched the catalogue of the radio-quiet AGN sample to the FIRST catalogue to obtain their 1.4 GHz fluxes. This provided 131/1190 Seyfert detections and 211/2490 detections of composites. For the sources that are not detected in FIRST I used the measured minimum flux in the catalogue as an upper limit. I assumed a spectral index 0.8 ($S_\nu \propto \nu^{-\alpha}$) which is a typical expected value for radio sources (e.g. Kellermann 1964; Hardcastle et al. 2010) and derived the 1.4 GHz radio luminosities using FIRST fluxes of the sources.

I exclude LERGs from the analysis because they do not have significant AGN-related optical continuum emission. The results of this analysis are plotted in Fig. 4.3. I see that there is a clear separation between the radio-loud and radio-quiet samples using this parameter, in the sense that the vast majority of objects that I have classified as radio-loud following BH12 have $r = \log_{10}(L_{\text{radio}}/L_{\text{optical}}) > 0.5$, while almost none of the radio-quiet objects exceed this value. It is important to note that traditionally a threshold $r > 1$ is used to select radio-loud objects (solid line on Fig. 4.3) adopting this threshold would classify some of my radio sources as radio-quiet. However, (i) this is an essentially arbitrary dividing line, and (ii), given the systematic uncertainties in computing r for this sample introduced by the use of bolometric corrections, I cannot really be certain that the discrepancy between the observed threshold in r and the traditional one is significant. Reclassifying the very few radio-loud sources with $r \ll 0.5$ as radio-quiet would not affect my analysis in any way. Given the broad consistency between the two radio-loudness estimates I choose to retain my original classification based on the BH12 analysis, which is easily reproducible by future workers. I also calculated two different radio loudness parameters which are commonly used: the ratio of 5-GHz flux density to the flux density at 2500 Å (e.g. Stocke et al. 1992) and the ratio of 5-GHz flux density to the flux density at 4400 Å (e.g. Kellermann et al. 1989). 5-GHz radio flux densities were extrapolated assuming a spectral index 0.8. In the same way, I used the relations given by Runnoe et al. (2012a) between L_{bol} and L_{5100} , and L_{bol} and L_{3000} to estimate fluxes at 5100 Å and at 3000 Å, respectively. Considering my sources are at low redshift these values will be approximately equal to the fluxes at 4400 Å and 2500 Å. By comparing these parameter estimations with the example shown in Fig. 4.3 I found that there is an agreement between different radio-loudness ratios in terms of radio-quiet AGN having ratios lower than the given parameter value. For all the reasons mentioned above I did not use any of these parameters to classify these sources. All of the estimations are provided in the online table. We can also see

from this figure that the redshift range is higher for radio-loud objects than radio-quiet sources. This is because there is not enough volume at low redshift coupled with the steep evolution of radio sources. Additionally, radio sources' host galaxies, which tend to be massive ellipticals, can be easily observed by SDSS to higher redshifts.

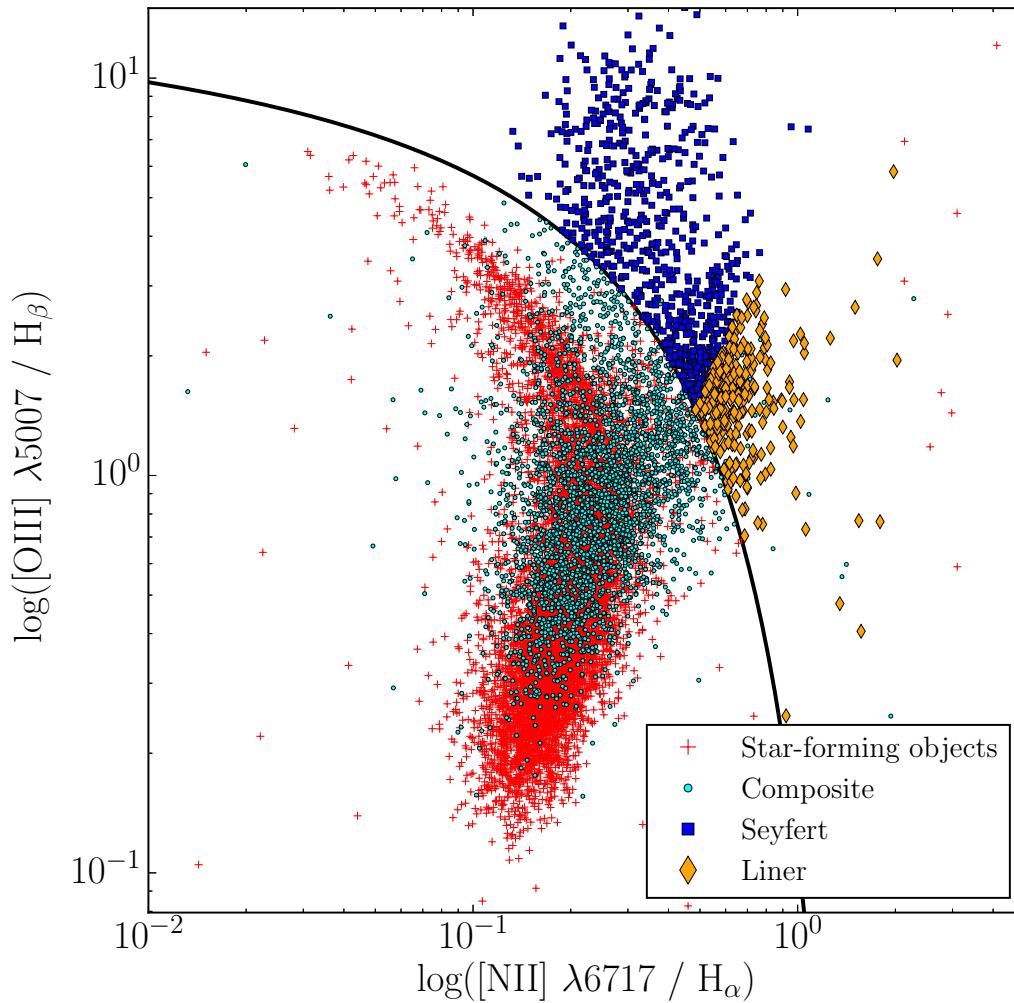


Figure 4.1: In order to present the clear separation between Seyferts and Liners I show here the [NII]/[H $_{\alpha}$]-[OIII]/[H $_{\beta}$] diagnostic diagram for galaxies in the sample, excluding sources from the radio-loud sample. A solid line represents the main AGN/SF division line summarized by Kewley et al. (2006).

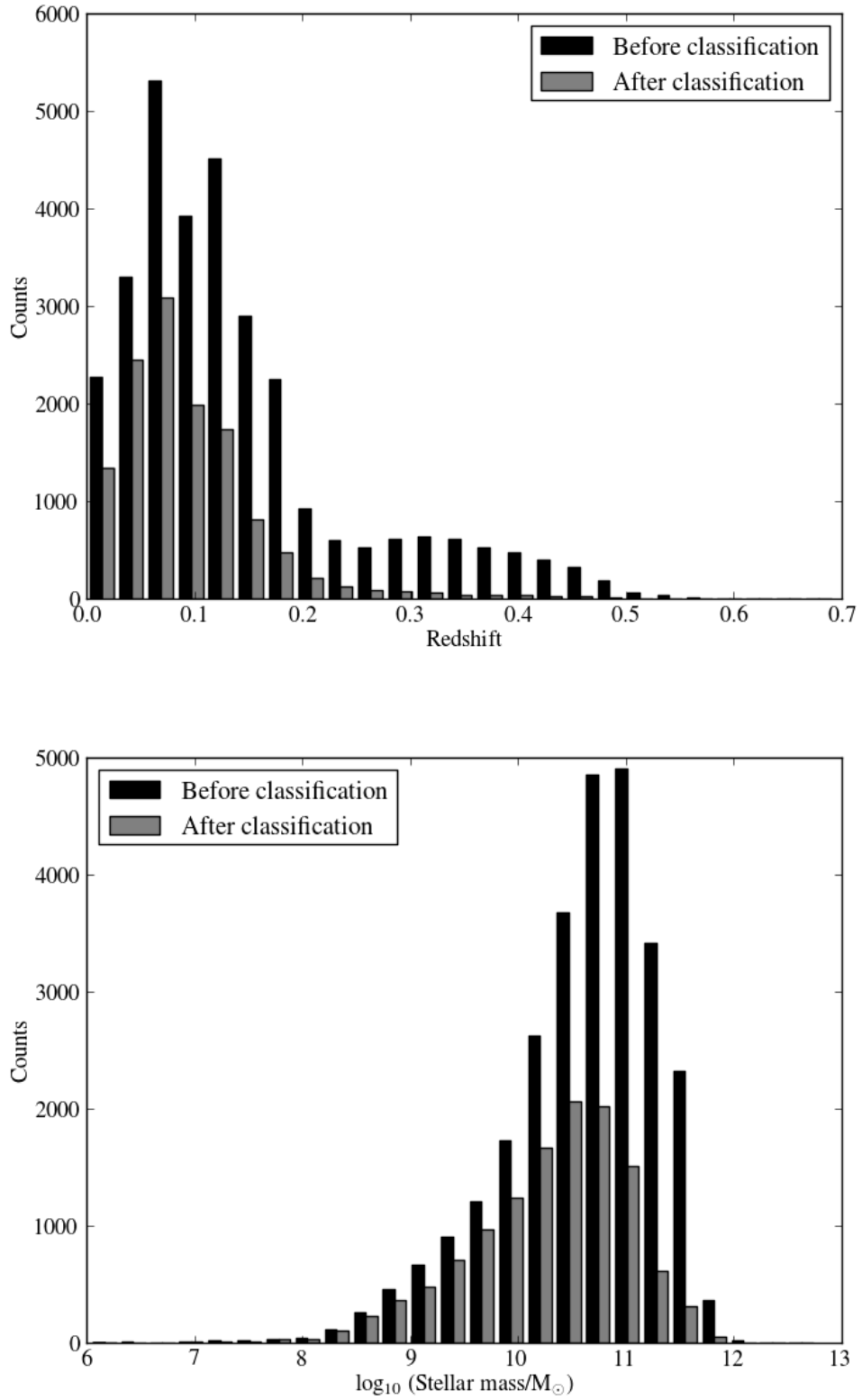


Figure 4.2: Redshift (top panel) and stellar mass (lower panel) distribution of the whole sample before implementing the emission-line classification (black) and the distribution of the same properties of the sample after the classification process (grey).

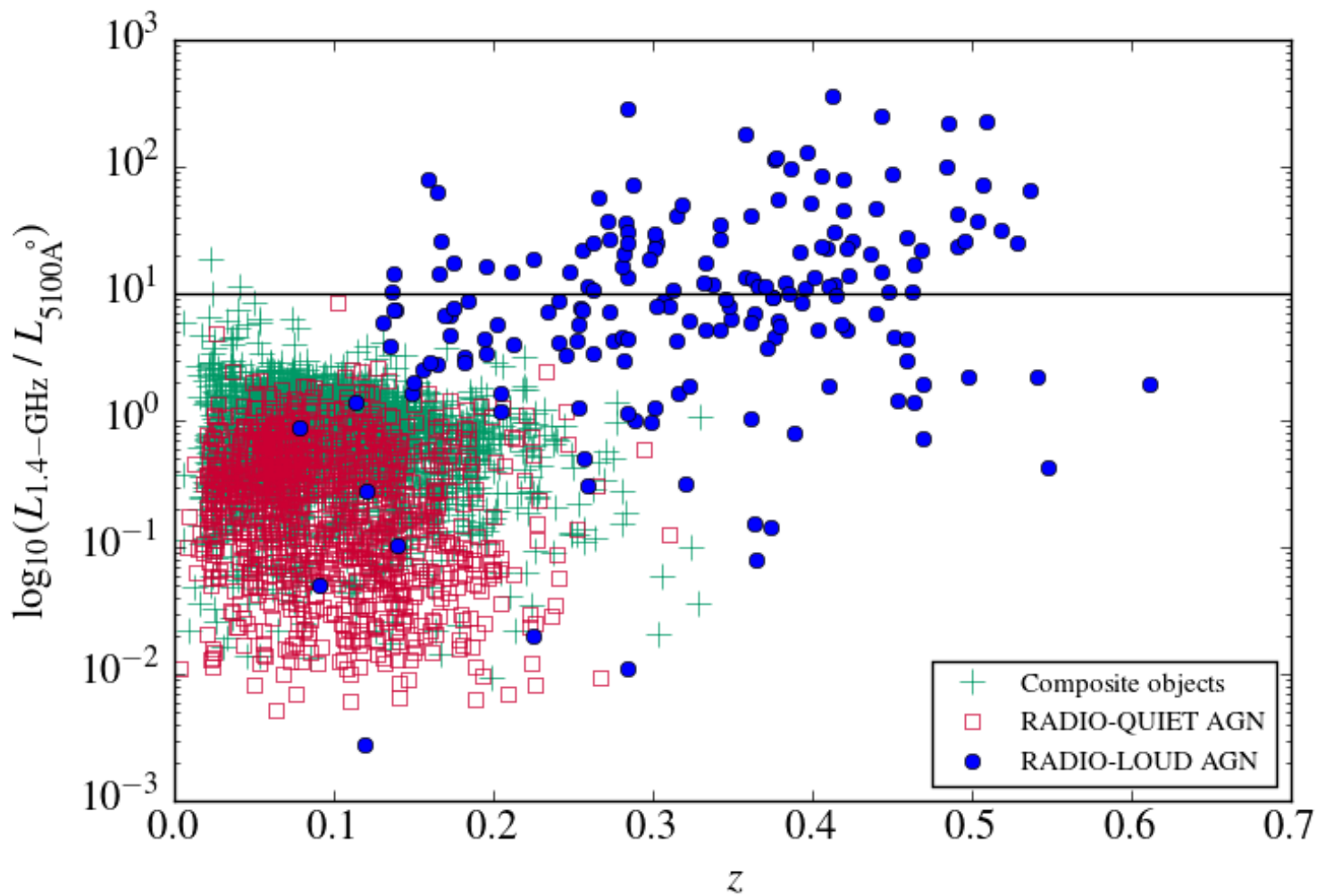


Figure 4.3: The distribution of the radio-loudness parameter for the sample of radio-quiet AGN and HERGs used in this work. LERGs are not shown as they are not radiatively efficient AGN. I used an estimate of optical luminosity at 5100 \AA and 1.4-GHz radio luminosity to calculate the parameter.

4.3.2 Far-infrared data, star formation and specific star formation rates

Herschel-ATLAS provides imaging data for ~ 600 square degrees using the Photo-detector Array Camera and Spectrometer (PACS; at $100 \mu\text{m}$, $160 \mu\text{m}$ Ibar et al. 2010; Poglitsch et al. 2010a) and the Spectral and Photometric Imaging Receiver (SPIRE; at $250 \mu\text{m}$, $350 \mu\text{m}$ and $500 \mu\text{m}$, Griffin et al. 2010a; Pascale et al. 2011, Valiante et. al. in prep.). To derive the maximum-likelihood estimate of the flux densities at the positions of objects in the SPIRE bands the flux density from the PSF-convolved H-ATLAS images were measured for each source together with the error on the fluxes. Further details about flux measurements can be found in Hardcastle et al. (2010, 2013).

Far-IR luminosity is widely used to measure star formation activity. As discussed by Hardcastle et al. (2013) neither the integrated far-IR luminosity nor the $250 \mu\text{m}$ luminosity is a completely reliable estimator of SFR because of the contribution by cold dust heated by old stellar populations (da Cunha et al. 2010; Smith et al. 2012a). However, we are secure using them as long as the far-IR emission is dominated by warm dust heated by star formation which, gives rise to dust temperatures ~ 25 K or more. I utilised $250 \mu\text{m}$ luminosity, as the star-formation indicator that is least affected by dust heated by the AGN (e.g. Hatziminaoglou et al. 2010; Hardcastle et al. 2010; Barthel et al. 2012). For the sources with PACS and SPIRE detections I used a modified black-body spectrum for the far-IR SED ($f_\nu \propto \frac{\nu^{3+\beta}}{e^{\frac{h\nu}{kT}} - 1}$); I fixed the emissivity index β as 1.5 and allowed temperatures to vary to obtain the best fitting temperatures, integrated luminosities (L_{IR}) and rest-frame luminosities at $250 \mu\text{m}$ (L_{250}) provided by the minimum χ^2 values. To calculate the K -corrections the same emissivity index ($\beta=1.5$) and the mean of the best-fitting temperatures for each class were used (See Table 4.2 for the temperatures). These corrections were included in the derivation of $250 \mu\text{m}$ luminosities.

Table 4.2 shows the best-fitting temperatures for each type of AGN in the sample, together with uncertainties derived by the bootstrap method. The results show that the mean temperatures of the populations in the sample are around 25 K (identical temperature estimates for star-forming galaxies were also reported by Smith et al. 2013). This indicates that the far-IR measurements of my sources are not strongly affected by cold dust heated by the old stellar populations. It has been suggested that SFRs derived from far-IR luminosity overestimate SFRs of the sources with SFR below $\sim 1 M_\odot \text{ yr}^{-1}$ due to the contribution by old stars (e.g. Clemens et al. 2013). However, most of the sources in the sample have SFRs above $1 M_\odot \text{ yr}^{-1}$ (Fig. 4.10) and any possible

Population type	Temperature (K)	σ (K)
Radio-loud AGN	19.6	1.06
Radio-quiet AGN	25.6	0.37
Composites	27.2	0.23
Star-forming objects	25.8	0.12

Table 4.2: The mean temperature values for different populations with errors on them derived by the bootstrap technique.

contribution by old stellar population should not be a problem for the SFR estimates.

Another source of contamination that we may observe at far-IR wavelengths is synchrotron emission from the jets of a radio-loud AGN. In order to check any possible synchrotron contamination in the *Herschel* 250 μm band I cross matched the radio-loud AGN objects to the GMRT catalogue by following the method described by Mauch et al. (2013). This provided 325 MHz GMRT fluxes for 165 out of 613 objects. The reason for this low success is that the GMRT survey only covers 36 per cent of the GAMA and NGP fields, and has incomplete sky coverage and variable sensitivity. Assuming that this sub-sample is representative of the whole sample, spectral indices of the matched objects, derived using the NVSS and GMRT fluxes, were used to gain extrapolated fluxes at 250 μm . Comparison of these with 250 μm far-IR fluxes showed that 100/165 objects have steep spectra and accordingly have much lower extrapolated flux than the measured far-IR flux at 250 μm . 65 out of 165 sources have extrapolated fluxes higher than their far-IR fluxes at 250 μm , but of these, almost all (59) are not detected at 250 μm *Herschel* band. This demonstrates that the synchrotron contamination in the far-IR is not a serious issue for the sample.

SFR measurements for galaxies in the SDSS DR7 catalogue, calculated using the H_α emission line, corrected for dust attenuation and fiber aperture effects, can be found in the MPA-JHU data base (Brinchmann et al. 2004). To determine the SFR/ L_{250} relation, I chose star-forming objects, classified using emission lines (Section 2.1), and which have both L_{250} and SFR estimates. I then used the median likelihood SFR estimates derived using the H_α emission line given in the catalogue to calibrate the relationship between SFR and L_{250} ². The errors in SFRs were estimated using the 16th and 84th percentiles. I then used a MCMC regression to obtain the relation between

²It would be desirable to use additional data to estimate the true SFRs of galaxies taking into account the unobscured fraction that is not observed at far-IR bands. However, by calibrating the SFR relation using SFR determined using the H_α emission line, I take into account the unobscured fraction in my estimates.

SFR and L_{250} , considering the errors on both SFRs and L_{250} , and incorporating an intrinsic dispersion in the manner described by Hardcastle et al. (2010). The derived Bayesian estimate of the slope and intercept of the correlation are

$$\log_{10}(L_{250}/W \text{ Hz}^{-1}) = 23.5(\pm 0.01) + 0.90(\pm 0.02)\log_{10}(\text{SFR}/M_{\odot} \text{ yr}^{-1}).$$

The slope shown as the red line is very close to unity and the derived relation is in agreement with the results of Hardcastle et al. (2013). The relationship between SFR and L_{250} is presented in Figure 4.4. The relation between SFR and the integrated 8-1000 μm far-IR luminosity was also verified and it is found to be in agreement with the results reported by Kennicutt (1998) and Murphy et al. (2011).

For a further evaluation of L_{250} as a star-formation indicator I compared the median-likelihood SFR estimates derived from MAGPHYS (da Cunha et al. 2008; Smith et al. 2012a), where cold dust and unobscured far-IR emission are taken into account, and the SFR estimates from L_{250} . This comparison showed that SFRs derived from these different methods are consistent with each other once the uncertainties are taken into account. In particular, I found that the slope of a regression line between the two SFR estimates, and the mean ratio of $\text{SFR}_{L_{250}}$ to $\text{SFR}_{\text{Magphys}}$, are both consistent with unity.

4.3.3 Near- and mid-infrared data

Mid-IR luminosity can be used as an AGN power indicator because emission due to accretion is obscured by dust and gas structure (if it is present) and re-radiated in the mid-IR. The *WISE* mission has observed the whole sky in four mid-IR bands (*W1* [3.4 μm], *W2* [4.6 μm], *W3* [12 μm], *W4* [22 μm]) with an angular resolution of 6.1, 6.4, 6.5 and 12 arcsec, respectively. The *WISE* all-sky catalogue was searched for all objects in the samples. This was done by searching the catalogue within 3 arcsec from the coordinates of the sample sources. 30416 sources of the sample before classification had *WISE* detections. The *WISE* measurements are given in Vega magnitudes so the magnitudes of the sources were converted into Jy using the standard *WISE* zero-points³.

In order to compute the luminosity at 22 μm , 12 μm –22 μm , spectral indices ($F_{\nu} \propto \nu^{-\alpha}$ assuming a power law slope for the SED) were calculated based on the *WISE* photometry for detected sources. K-corrections were not derived using SEDs because

³The relation used for the conversion can be found at <http://wise2.ipac.caltech.edu/docs/release/allsky/expsup/>

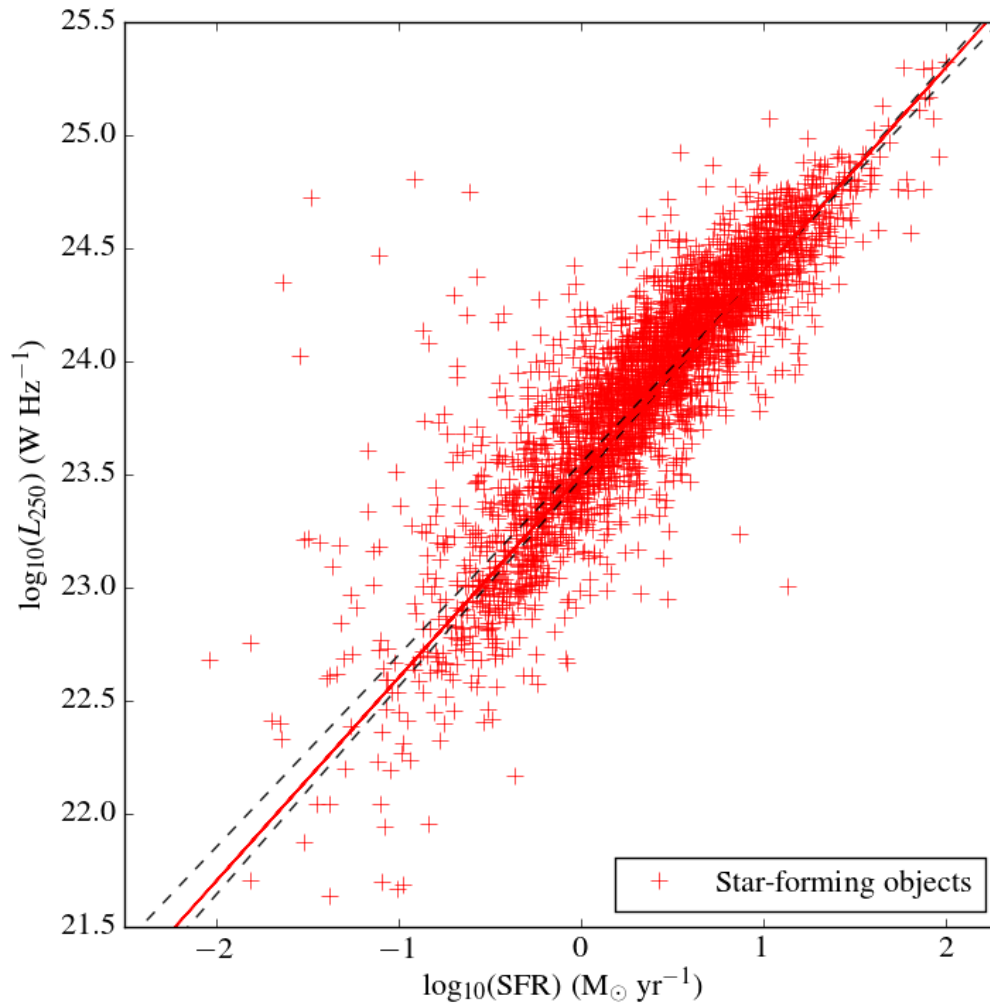


Figure 4.4: The distribution of the luminosity at 250 μm of the star-forming objects as a function of their SFRs. The best fit between the quantities is presented by a red line and $\pm\sigma$ errors of this fit are shown with grey dash lines.

different components (old stellar population, torus and star formation) emit in the mid-IR. In order to be consistent I derived the index to be used for K -corrections by taking the mean value of the indices of all sources. The mean index is 2.26 ($\sigma=1.08$).

4.3.4 AGN power indicators

The 22 μm and [OIII] $\lambda 5007$ fluxes and luminosities are available to us, and can both be used as AGN power indicators. In order to see from where the mid-IR emission originates I carried out MCMC regression analysis to obtain the relation between the L_{250} (W Hz^{-1}), as obtained from the temperature fitting, and the νL_ν luminosity at 22 μm (L_{22} erg s^{-1}). For this analysis I used the star-forming objects that were detected in both *Herschel* 250 μm and *WISE* 22 μm bands. This provided the following relation:

$$\log_{10}(L_{22}/\text{erg s}^{-1}) = -7.93 + 1.18 (\pm 0.04) \log_{10}(L_{250}/\text{erg s}^{-1}).$$

I then used this relation to derive the expected 22 μm luminosities due to star formation alone of all objects in the sample and the star-forming objects. In order to understand the effect of star formation on the 22 μm *WISE* band I subtracted these estimations from the actual 22 μm luminosity measurements. These residuals were then plotted as a function of mid-IR luminosity. In Figure 4.5 and 4.6 I show the results of this analysis. In Fig. 4.5 the relationship between $\log_{10}(L_{22})$ and $\log_{10}(L_{250})$ of the sources in the sample is seen, and we can see that there is a close relationship between $\log_{10}(L_{22})$ and $\log_{10}(L_{250})$. It is also apparent that radio-quiet and radio-loud sources have similar distributions to star-forming objects. Fig 4.6 present the residual 22 μm luminosities of star-forming objects (left) and sources of the radio-loud and radio-quiet AGN sample (right) as function of L_{22} (erg s^{-1}). The comparison of these clearly shows that the mid-IR emission is dominated by star formation even for the AGN. As expected, star-forming objects cluster around the residual luminosity of 0.

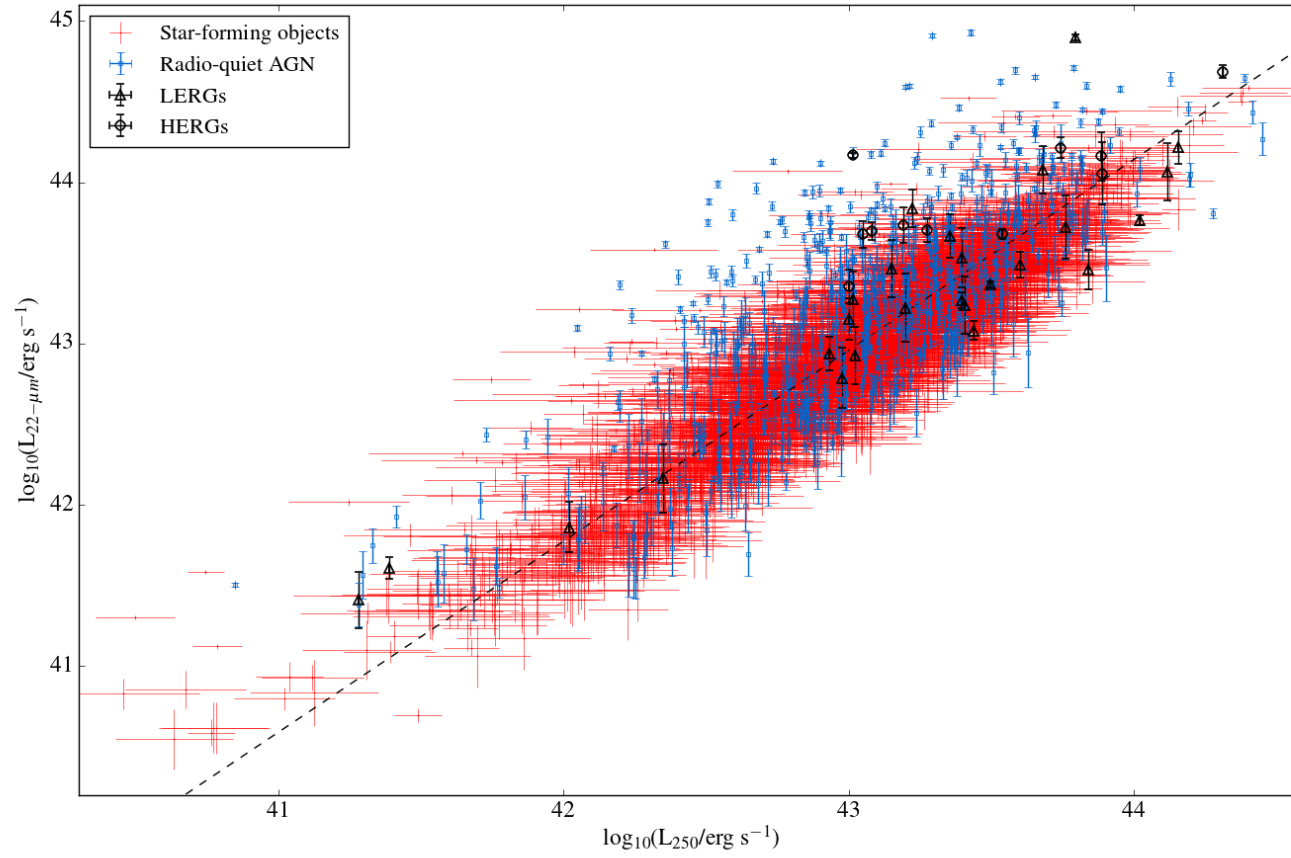


Figure 4.5: The relation between L_{22} and L_{250} for star-forming objects and the sample sources that are detected in *WISE*-22 μm band. The dashed line shows the best fit for star forming objects. Star-forming objects are plotted as red crosses, radio-quiet AGN as blue squares, HERGs as open black circles and LERGs as open black triangles.

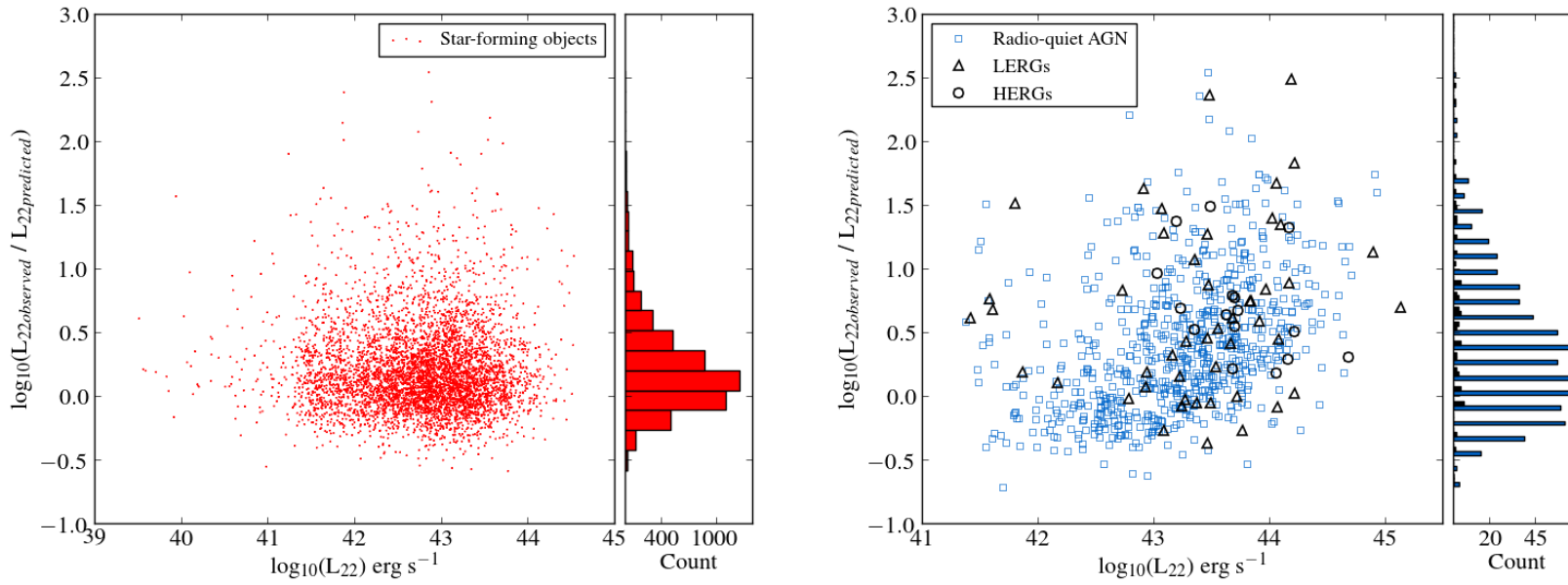


Figure 4.6: The distribution of the residual luminosities of the star-forming objects (left) and AGN in the sample detected at $22 \mu\text{m}$ (right) as a function of L_{22} together with a histogram of the counts are seen.

I implemented the same process using $L_{[\text{OIII}]}$ for a comparison, obtaining the relation for pure star-forming objects as follows:

$$\log_{10}(L_{[\text{OIII}]}/\text{erg s}^{-1}) = -10.93 + 1.16 (\pm 0.05) \log_{10}(L_{250}/\text{erg s}^{-1}).$$

In the same way this relation was used to derive $L_{[\text{OIII}]}$ for all objects in the AGN sample and for the star-forming objects. In order to understand the effect of star formation on the [OIII] luminosities I subtracted these estimates from the actual $L_{[\text{OIII}]}$ measurements. In Figure 4.7 and 4.8 the results of this analysis are shown. In Fig. 4.7 we see that there is a correlation between $\log_{10}(L_{[\text{OIII}]})$ and $\log_{10}(L_{250})$. However, radio-quiet and some radio-loud objects clearly have higher emission-line luminosities in comparison with star-forming sources. In the right panel of Fig. 4.8, a boost in $\log_{10}(L_{[\text{OIII}]})$ of the sources stands out when we compare with the distribution of star-forming objects seen in the left panel, although we see some trend of accumulation of sources around a residual of 0. To determine the cause of this the density maps for composite objects and radio-quiet AGN were produced. I also calculated the mean value of the residuals for both samples together with the error in these using the bootstrap method, which all are shown in Fig 4.9. It is clear in this figure that the composites peak around zero value of the residuals (the mean of residuals is 0.19 with $\sigma=0.01$) whereas the radio-quiet AGN are distributed above zero (the mean of residuals is 0.84 with $\sigma=0.02$).

These results shows that 22 μm luminosity cannot be used as an AGN power estimator for this sample, (a similar result was recently reported by Rosario et al. 2013) but that [OIII] emission is not dominated by star formation. Therefore, I used [OIII] luminosity in the calculation of the AGN powers. In order to compute radiative power I used the following relation: $P_{\text{AGN}} = 3500 \times L_{[\text{OIII}]}$ given by Heckman et al. (2004) which takes into account an average value for dust extinction. We can see in both left panels of Fig. 4.6 and 4.8 that there is a scatter to positive residual values between L_{250} and L_{22} , and $L_{[\text{OIII}]}$. At 22 μm star formation dominates the band. Conversely, [OIII] is predominantly due to AGN with only a small contribution from SF.

To derive the jet powers, I utilised the relation $Q(\text{W}) = 3 \times 10^{38} \times f L_{151}^{6/7}$, where L_{151} is the luminosity at 151 MHz, in units of $10^{28} \text{W Hz}^{-1} \text{sr}^{-1}$, given by Willott et al. (1999) and f is $10^{3/2}$ (see Hardcastle et al. 2007b). I derived the fluxes at 151

Population type		AGN Power
Radio-loud AGN	LERGs	Jet power
	HERGs	Jet power+Radiative power
Radio-quiet AGN		Radiative power

Table 4.3: Table shows AGN power definitions for different type of objects used in this work. As previously explained, Jet power was derived using extrapolated 151 MHz flux densities of both HERGs and LERGs. Radiative power was derived using [OIII] emission line luminosities for radio-quiet AGN sample and HERGs.

MHz using available fluxes at 1.4-GHz assuming the spectral index⁴ to be 0.8. The jet power provides the best estimate of the AGN power for LERGs. It is worth noting that in principle the environment should be taken into account carefully in the conversion between radio luminosity and jet power (e.g. Hardcastle & Krause 2014). However, I cannot do this with the data available to us. For HERGs I combined the calculated jet powers and radiative powers to obtain the AGN power as discussed by Mingo et al. (2014). AGN powers used in this work are summarised in Table 4.3.

Boroson & Green (1992), Shen & Ho (2014) and Sun & Shen (2015) have found that for a given AGN continuum luminosity radio-loud AGN have higher [OIII] magnitudes or fluxes than radio-quiet AGN as a result of having different Eddington accretion rates. Most of the radio-loud AGN contain LERGs which have different accretion mode than typical AGN. With regard to the SFR-AGN relation discussed in the following section HERGs only dominate the third and fourth AGN power bins. If I take into account the bias mentioned above I would expect HERGs to be included in AGN power bins lower than their current bins. This would not make much difference to the results since they would still have lower SFRs than their radio-quiet counterparts considering the trend of their SFRs as a function of AGN power.

⁴In order to be consistent I use the same spectral index for all galaxies in the sample. However, I also used the GMRT estimates where available as a sanity check and found that this gave the same results.

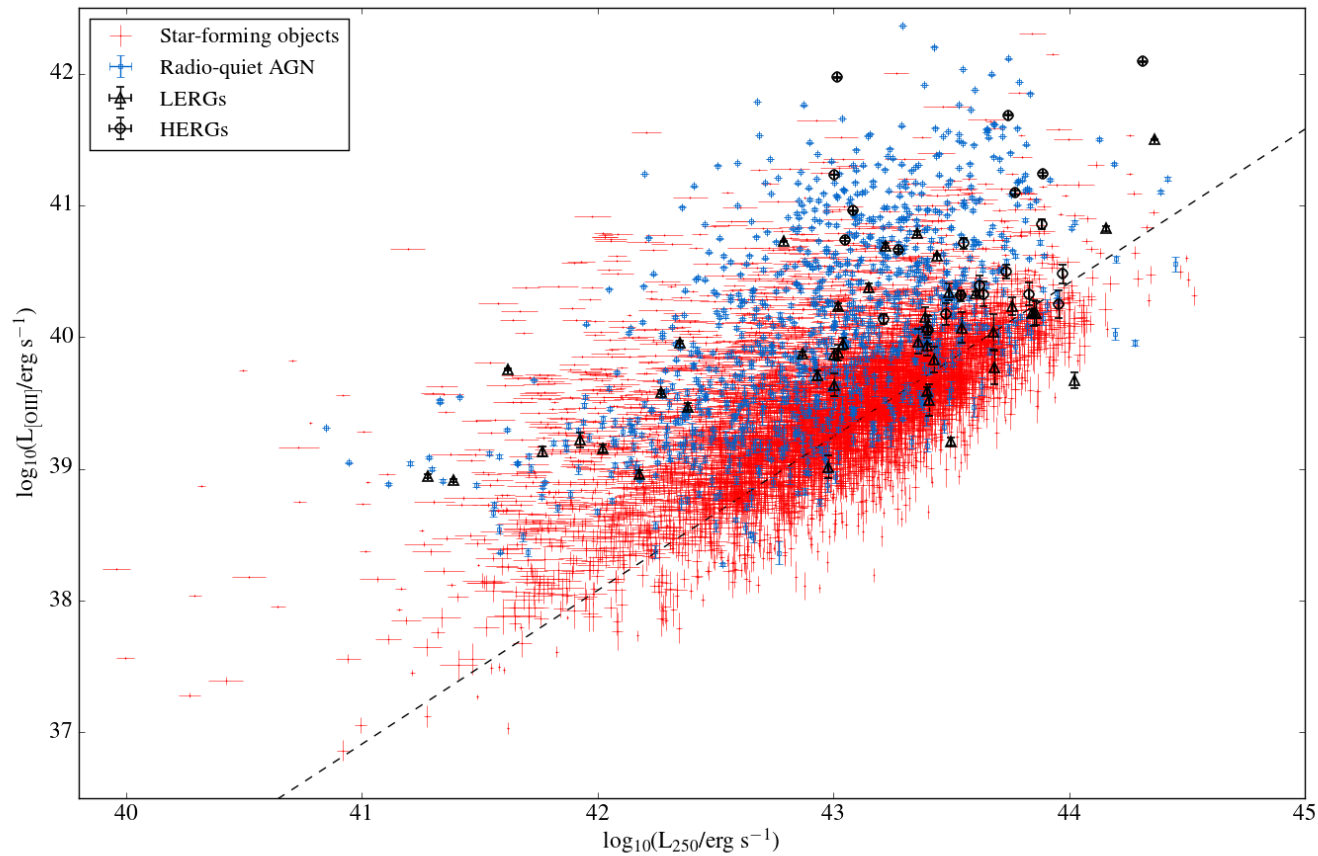


Figure 4.7: The graph shows the relation between $L_{[\text{OIII}]}$ and L_{250} for star-forming objects and the sample sources that are significantly (3σ) detected in their [OIII] emission-lines. The dashed line on the top panel shows the best fit for star forming objects. Star-forming objects are plotted as red crosses, radio-quiet AGN as blue squares, HERGs as open black circles and LERGs as open black triangles.

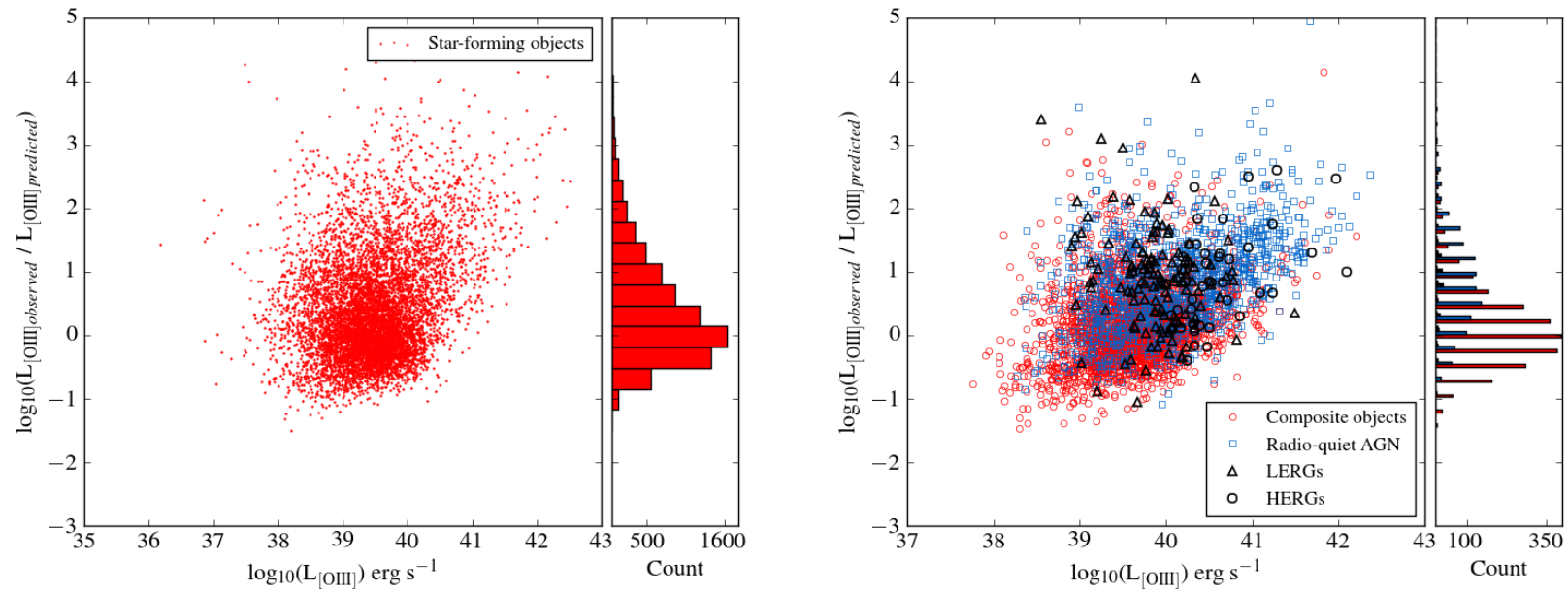


Figure 4.8: The distribution of the residual luminosities of the star-forming objects (left) and detected AGN in the sample (right) as a function of $L_{[\text{OIII}]}$ together with a histogram of the counts are seen.

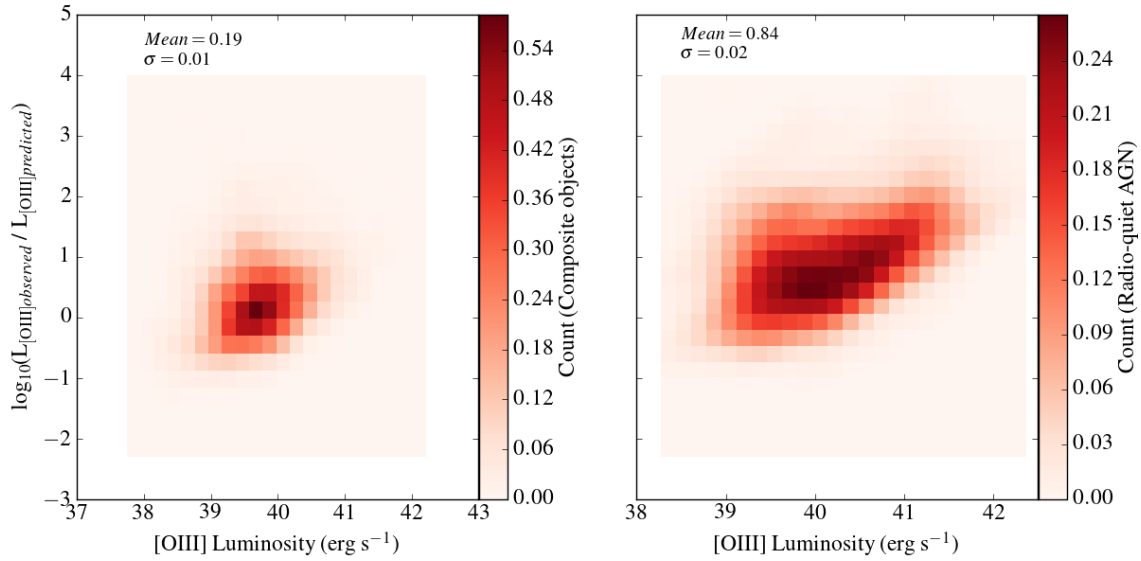


Figure 4.9: The comparison of density maps of the residuals ($\log_{10}(L_{[\text{OIII}]}^{\text{observed}} / L_{[\text{OIII}]}^{\text{measured}})$) both for the composites (left) and radio-quiet AGN (right) is shown. The mean values of these calculated for both samples are also shown together with the errors on them derived using the bootstrap technique.

4.4 Results

4.4.1 Stacking SFR: Radio-loud and radio-quiet comparison

In Figure 4.10 I show the distribution of SFRs of the star-forming objects, and radio-loud and radio-quiet AGN sample against their stellar masses. From the figure it can also be seen that radio-quiet and radio-loud AGN have lower SFRs compared to star-forming objects. Radio-loud galaxies not detected at 5σ in *Herschel* 250 μm band are indicated with arrows.

To compare the star formation properties of radio-loud and radio-quiet AGN as a function of AGN power I used the *Herschel* 250 μm band fluxes. However, the majority of the sources are not detected at the 5σ level in the *Herschel* 250 μm band. Therefore, I stacked SFRs, SSFRs and stellar masses of the sources in 5 AGN power bins.

I determined the mean values of the SFRs and SSFRs of the samples in all bins. While calculating SFRs I first found the mean value of L_{250} in each bin and then calculated the mean SFR in the corresponding bin by using the relationship derived

in Section 4.3.2. This allows me to not be biased against sources that are weak or not formally detected. For the derivation of SSFRs, I divided the sum of L_{250} by the sum of the stellar mass in individual bins. This gave me the mean SSFR in the corresponding bins. The errors on these quantities were calculated using the bootstrap technique which enables me to derive the errors empirically, making no assumptions about the distribution of the luminosity. The 68 percentile confidence intervals derived from the bootstrap samples were used as errors on SFRs. Errors on SSFRs were calculated by combining the uncertainties throughout the bootstrap analysis for SFRs and stellar masses in quadrature. All these estimates for both radio-loud and radio-quiet samples can be found in Table 4.4.

It can clearly be seen in Figure 4.11 that SFRs and SSFRs increase with increasing AGN power for both radio-loud and radio-quiet samples. I also show the mean stellar masses for the bins to see the effect of mass on the observed relation between SFR and AGN power. Most of the sources in the radio-loud AGN sample are LERGs hosted by galaxies that are presumably massive ellipticals as indicated in (Fig. 4.11, 4.14 and 4.18). We see that radio-loud AGN reside in more massive galaxies in comparison with their radio-quiet counterparts. The results show that in general radio-quiet AGN of a given AGN power are found to have higher SFR and SSFRs than radio-loud AGN. The difference between the SSFRs of radio-loud and radio-quiet AGN goes up to an order of magnitude.

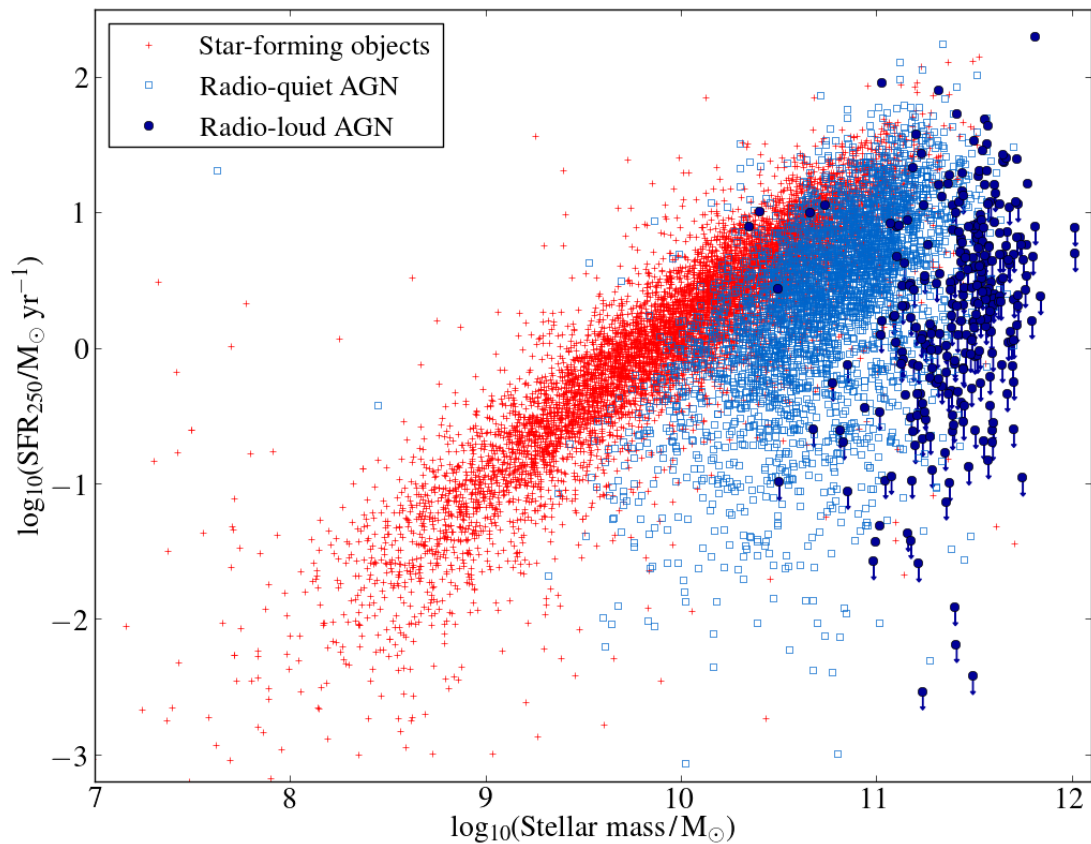


Figure 4.10: The distributions of SFRs of the sources in the sample detected in $250 \mu\text{m}$ *Herschel* band and star-forming galaxies plotted as a function of their stellar masses. Star-forming objects are plotted as red crosses, radio-quiet AGN as blue squares and radio-loud AGN as navy filled circles. Radio-loud galaxies not detected at 5σ the *Herschel* $250 \mu\text{m}$ band are indicated with arrows. I do not show these for radio-quiet objects in order to present the distribution of the sources clearly as the number of radio-quiet AGN is high.

Stacked measurements in confused images can be biased by the presence of correlated sources because the large PSF can include flux from nearby sources. Several methods have been proposed to account for this bias, including the flux measurements in GAMA apertures by Bourne et al. (2012). This method explicitly deblends confused sources and divides the blended flux between them using PSF information, so that average flux is conserved and not counted multiple times in the stack. I checked for the effects of clustering in the stacks by comparing to the results obtained from average flux measurements in the catalogue given by Bourne et al. (2012), for the 1758 objects overlapping between the two samples. Average fluxes for the matched sample are slightly higher using the deblended apertures method compared with the stacking method, which indicates that the method is not biased by the effects of clustering and the results are robust. The reason for the slightly higher fluxes using the catalogue from Bourne et al. is likely because they account for extended flux outside of the central beam. These results are consistent with the trends in the full stacked samples.

Effects of the intrinsic correlation between SFR and redshift, and the Malmquist bias

It has been shown that SSFRs of galaxies evolve with redshift (e.g. Oliver et al. 2010, and references therein). The effect of this intrinsic correlation found between SSFR and z should be taken into account. In order to check if the results are affected by this relation I tried deriving the relation between SSFRs and z using the star-forming objects but found an unrealistically strong correlation between SFR and z . The reason for this is that the sample used here is biased in the sense of having star-forming objects that are selected using optical emission lines. This causes me to only select objects with high star formation at high redshifts. I am not able to match the samples in redshift and stellar mass because of the small size of the radio-loud AGN sample. Instead I used the relation given by Oliver et al. (2010) where they showed that late-type galaxies have $\text{SSFR} \propto (1+z)^{3.36}$. I then took this relation into account and re-derived the relationships of SFRs and SSFRs as a function of AGN power (Fig. 4.12). Comparison of this with the initial results (Fig. 4.11) clearly shows that the results are not affected by the intrinsic correlation between z and SSFR because the trends I initially observed between SFR/SSFR and AGN power do not change. Although I assume the same SSFR evolution with redshift for all types of galaxies here, radio-loud AGN have been found in more evolved galaxies in comparison to radio-quiet AGN and star-forming objects in the local Universe. Accordingly a less strong evolution is expected for these

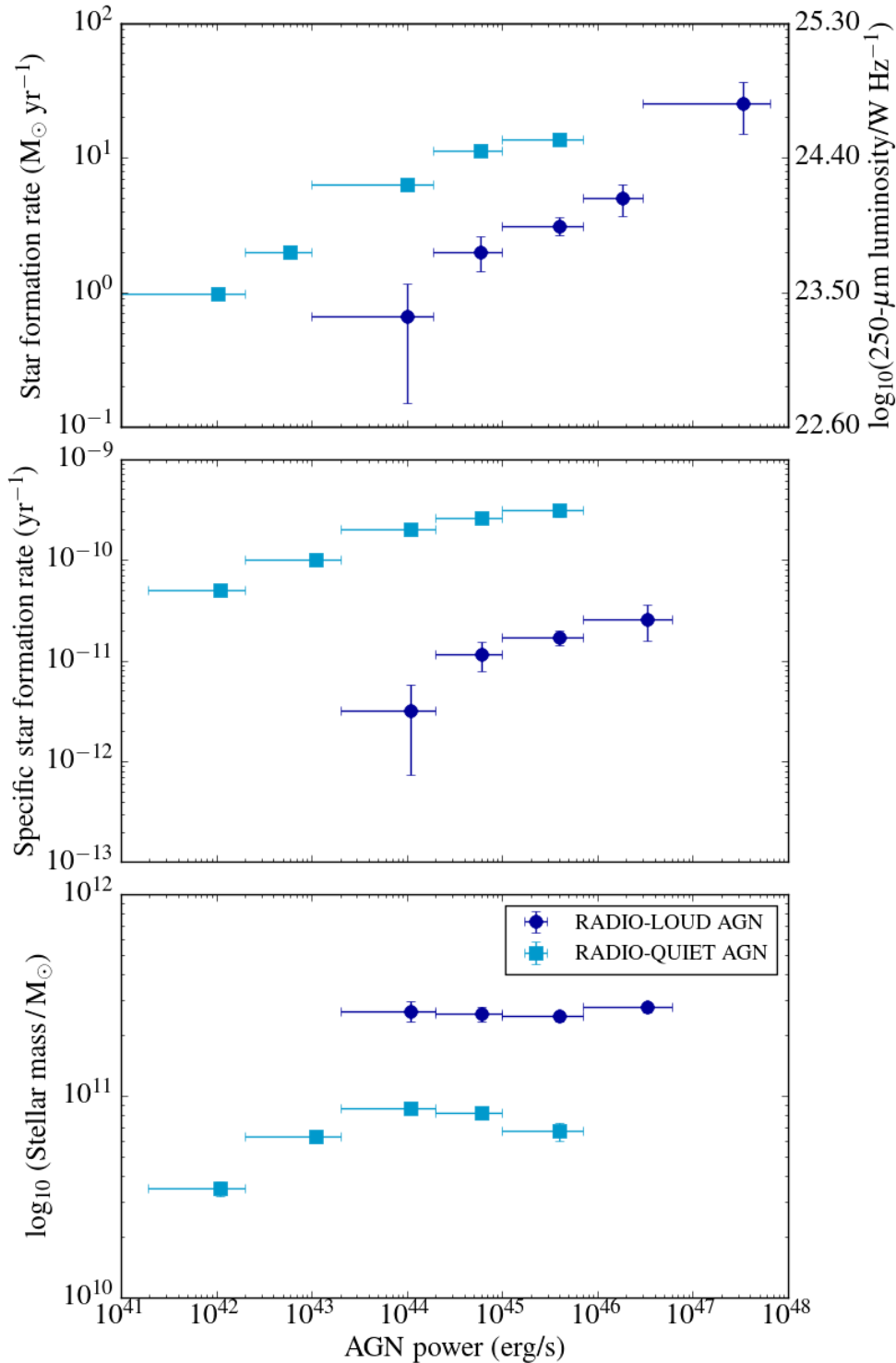


Figure 4.11: The results of stacking analysis of radio-loud and radio-quiet AGN. From bottom to top the graphs show: the comparison of SSFRs, stellar masses and SFRs of the samples stacked in their AGN powers. Since I included sources that do not have mass measurements in the stacking analysis of SFRs, this allowed me to have more sources and accordingly more bins for radio-loud AGN. The first two AGN power bins did not have enough radio-loud AGN but I still show the mean value of SFR corresponding to radio-quiet AGN.

sources. Therefore, by assuming a stronger correlation between SSFR and z for radio-loud AGN I may overestimate this effect on these particular galaxies.

I note that Malmquist bias does not affect the derived SFRs in the stacking analysis since I include all objects, including non-detections, in the stacking. The parent sample is of course flux-limited in [OIII] and/or radio luminosity, giving a correlation between AGN power and redshift, but this is included by taking the SSFR– z relation into account described above.

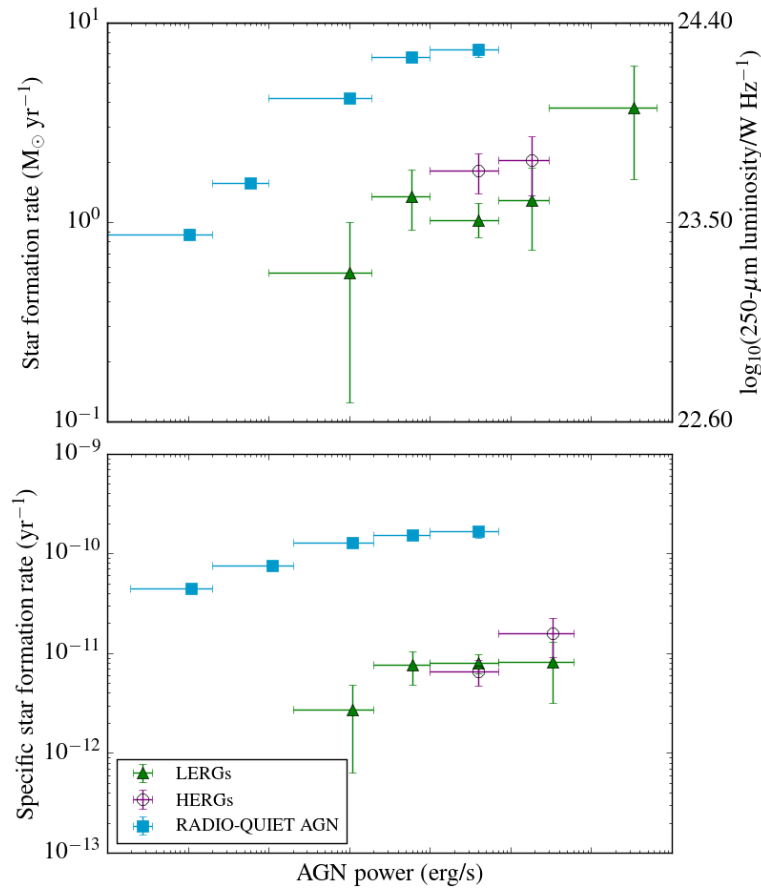


Figure 4.12: The results of stacking analysis of radio-loud and radio-quiet AGN where the intrinsic relation between z and SSFR given by Oliver et al. (2010) was taken into account.

As indicated above due to limited sample size I am not able to carry out the stacking analysis by binning in both redshift and AGN power. However, I implement a separate analysis in order to check the effect of universal SFR/SSFR evolution with redshift. For this I estimated AGN power/SFR ratios for HERGs, LERGs and radio-quiet AGN.

In Figure 4.13 I show the distribution of the AGN power/SFR ratio for all populations in the sample. Due to a large scatter, I binned the data in 3 redshift bins and calculated the median of the AGN power/SFR ratio for each bin for all populations. Errors on these values were derived by the bootstrapping. In the first 2 redshift bins radio-quiet AGN have lower AGN power/SFR ratio than HERGs and LERGs. This indicates that at all redshifts radio-quiet AGN have higher SFR compared to HERGs and LERGs. Somewhat surprisingly I find that HERGs and LERGs have similar AGN power/SFR ratios in most of the redshift bins. Therefore, I conclude that the difference between SFR of radio-loud and radio-quiet AGN is not due to the redshift effect.

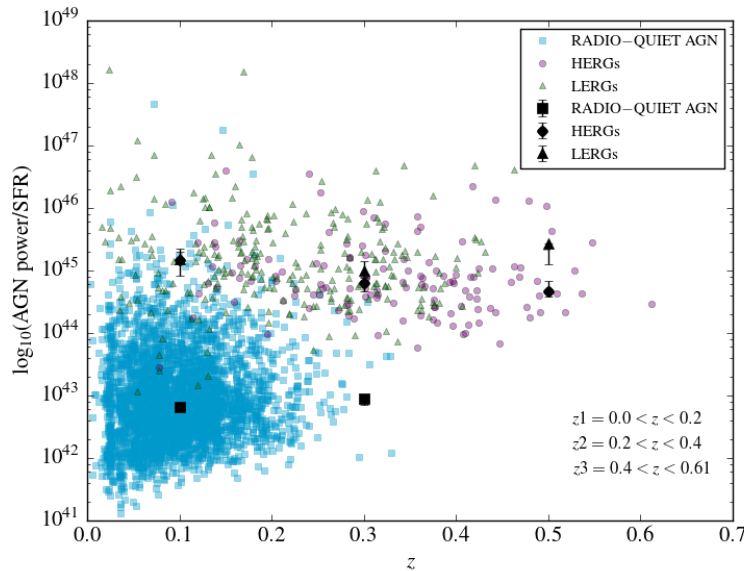


Figure 4.13: The distribution of AGN power/SFR versus redshift for radio-quiet AGN, HERGs and LERGs. Black points show the median estimations of the AGN power/SFR ratio for all population for 3 redshift bins. Errors on these estimations were derived from the bootstrapping.

Effect of the composite objects

Composites are sources that have emission-line characteristics intermediate between pure AGN and star-forming objects, have intermediate mass and SFR and lie on a typical BPT diagram (Baldwin et al. 1981) between pure star-forming objects and AGN (e.g. Salim et al. 2007; Trouille et al. 2011). I implemented the stacking process described above excluding the composite objects from the sample to see if the results

were affected by the inclusion of these objects. A striking difference would mean that while selecting the composites I mostly pick sources with high levels of star formation. However, this comparison showed that there is no difference between the SFRs and SSFRs of the samples with and without the composite sources (compare Figs. 4.11 and 4.14). Furthermore, Elbaz et al. (2011) demonstrated that the expected SSFR of star-forming objects is around $2.5 \times 10^{-10} \text{ yr}^{-1}$. In both Figures 4.11 and 4.14 the highest mean SSFRs are lower than this value. This also tells me that the composites are not dominated by star forming galaxies. Therefore, I kept the composites in the radio-quiet AGN sample for all analyses presented in this chapter. Corresponding measurements are given in Table 4.8.

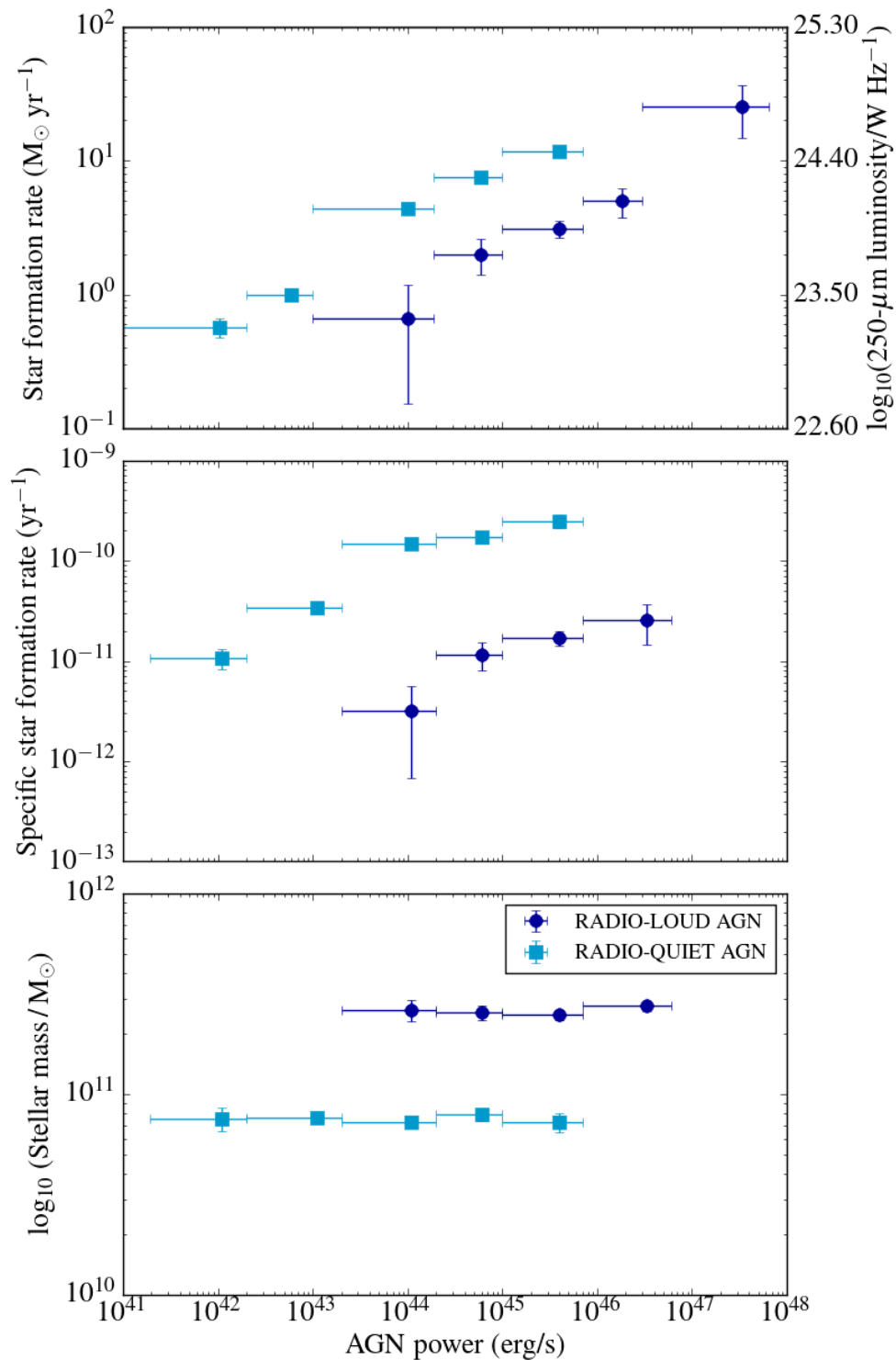


Figure 4.14: The result of stacking analysis of radio-loud and -quiet AGN where composite objects are not included. Similar to Figure 4.11 from bottom to top the graphs show: the comparison of SSFRs, stellar masses and SFRs of the samples stacked in their AGN powers.

Sample	AGN power bins erg s ⁻¹	Mean z	N	Mean SFR M _⊙ yr ⁻¹	AGN power bins erg s ⁻¹	Mean z	N	Mean SSFR (×10 ⁻¹¹ yr ⁻¹)	Mean stellar mass (×10 ⁺¹¹ M _⊙)
Radio-quiet AGN	1.0e+41–2.0e+42	0.03	170	0.98 ^(0.06) (0.06)	1.9e+41–2.0e+42	0.03	170	4.99 ^(0.50) (0.50)	0.35 ^(0.03) (0.03)
	2.0e+42–1.0e+43	0.06	1099	1.99 ^(0.05) (0.05)	2.0e+42–2.0e+43	0.08	1864	9.97 ^(0.28) (0.26)	0.63 ^(0.01) (0.02)
	1.0e+43–1.9e+44	0.11	2082	6.29 ^(0.10) (0.11)	2.0e+43–2.0e+44	0.13	1333	20.15 ^(0.62) (0.59)	0.87 ^(0.02) (0.04)
	1.9e+44–9.8e+44	0.14	278	11.37 ^(0.69) (0.70)	2.0e+44–1.0e+45	0.15	260	25.69 ^(2.09) (2.08)	0.82 ^(0.04) (0.07)
	9.8e+44–7.0e+45	0.18	50	13.66 ^(1.12) (1.15)	1.0e+45–7.0e+45	0.18	49	30.86 ^(3.99) (4.24)	0.67 ^(0.08) (0.29)
Radio-loud AGN	1.0e+43–1.9e+44	0.04	15	0.66 ^(0.51) (0.51)	2.0e+43–2.0e+44	0.05	16	0.32 ^(0.25) (0.25)	2.64 ^(0.29) (0.21)
	1.9e+44–9.8e+44	0.10	57	2.01 ^(0.62) (0.58)	2.0e+44–1.0e+45	0.11	60	1.16 ^(0.38) (0.27)	2.56 ^(0.21) (0.13)
	9.8e+44–7.0e+45	0.25	342	3.12 ^(0.47) (0.46)	1.0e+45–7.0e+45	0.22	266	1.70 ^(0.31) (1.09)	2.48 ^(0.14) (0.16)
	7.0e+45–3.0e+46	0.34	178	5.05 ^(1.27) (1.23)	7.0e+45–6.0e+46	0.26	93	2.59 ^(1.09) (1.05)	2.75 ^(0.16) (0.18)
	3.0e+46–6.5e+47	0.35	20	25.38 ^(9.64) (10.44)	–	–	–	–	–
HERGs	9.8e+44–7.0e+45	0.30	120	4.85 ^(1.02) (1.07)	1.0e+45–7.0e+45	0.23	68	1.43 ^(0.40) (0.42)	3.05 ^(0.41) (0.44)
	7.0e+45–3.0e+46	0.40	75	7.27 ^(2.45) (2.11)	7.0e+45–6.0e+46	0.27	22	3.88 ^(1.76) (1.65)	2.91 ^(0.36) (0.38)
LERGs	1.0e+43–1.9e+44	0.05	15	0.66 ^(0.51) (0.51)	2.0e+43–2.0e+44	0.05	16	0.32 ^(0.25) (0.25)	2.64 ^(0.31) (0.32)
	1.9e+44–9.8e+44	0.10	51	1.94 ^(0.66) (0.70)	2.0e+44–1.0e+45	0.10	53	1.10 ^(0.38) (0.36)	2.56 ^(0.22) (0.23)
	9.8e+44–7.0e+45	0.23	222	2.23 ^(0.50) (0.41)	1.0e+45–7.0e+45	0.21	198	1.67 ^(0.36) (0.32)	2.29 ^(0.11) (0.12)
	7.0e+45–3.0e+46	0.30	103	3.49 ^(1.59) (1.49)	7.0e+45–6.0e+46	0.25	71	1.91 ^(1.24) (1.29)	2.70 ^(0.18) (0.19)
	3.0e+46–6.5e+47	0.35	13	11.65 ^(7.23) (7.11)	–	–	–	–	–

Table 4.4: The results of the stacking analysis regarding the samples. In column 2 the chosen AGN power bins are shown. N indicates number of sources included in each bin. The mean measurements of SFRs in each bin with their errors calculated by the bootstrap technique are presented in column 5. New AGN power bins were defined for the mean measurements of SSFRs and stellar mass as the number of sources in the sample decreased by excluding sources that do not have stellar mass measurements. In column 6 the new AGN power bins are shown. The mean SSFRs and the mean stellar mass for each bin with their errors are shown in column 9 and 10, respectively.

Sample	AGN power bins erg s ⁻¹	Mean z	N	Mean SFR M _⊙ yr ⁻¹	AGN power bins erg s ⁻¹	Mean z	N	Mean SSFR (×10 ⁻¹¹ yr ⁻¹)	Mean stellar mass (×10 ⁺¹¹ M _⊙)
Radio-quiet AGN	1.0e+41–2.0e+42	0.02	23	0.57 ^(0.09) _(0.10)	1.9e+41–2.0e+42	0.02	23	1.07 ^(0.23) _(0.24)	0.76 ^(0.10) _(0.10)
	2.0e+42–1.0e+43	0.05	268	1.00 ^(0.06) _(0.07)	2.0e+42–2.0e+43	0.06	443	3.35 ^(0.20) _(0.21)	0.76 ^(0.03) _(0.03)
	1.0e+43–1.9e+44	0.10	657	4.35 ^(0.18) _(0.19)	2.0e+43–2.0e+44	0.11	490	14.72 ^(0.86) _(0.86)	0.73 ^(0.03) _(0.03)
	1.9e+44–9.8e+44	0.14	201	7.48 ^(0.56) _(0.56)	2.0e+44–1.0e+45	0.14	191	17.06 ^(1.75) _(1.74)	0.79 ^(0.05) _(0.05)
	9.8e+44–7.0e+45	0.17	40	11.80 ^(0.96) _(1.07)	1.0e+45–7.0e+45	0.17	40	24.65 ^(3.75) _(3.42)	0.72 ^(0.09) _(0.08)
Radio-loud AGN	1.0e+43–1.9e+44	0.05	15	0.66 ^(0.52) _(0.51)	2.0e+43–2.0e+44	0.05	16	0.32 ^(0.25) _(0.25)	2.64 ^(0.32) _(0.33)
	1.9e+44–9.8e+44	0.10	57	2.01 ^(0.57) _(0.61)	2.0e+44–1.0e+45	0.11	60	1.16 ^(0.35) _(0.36)	2.56 ^(0.21) _(0.21)
	9.8e+44–7.0e+45	0.25	342	3.12 ^(0.46) _(0.45)	1.0e+45–7.0e+45	0.22	266	1.70 ^(0.27) _(0.27)	2.48 ^(0.14) _(0.15)
	7.0e+45–3.0e+46	0.34	178	5.05 ^(1.19) _(1.29)	7.0e+45–6.0e+46	0.26	93	2.59 ^(1.07) _(1.12)	2.75 ^(0.16) _(0.18)
	3.0e+46–6.5e+47	0.36	20	25.38 ^(11.10) _(10.59)	–	–	–	–	–

Table 4.5: The results of the stacking analysis of the sample where the composite objects are not included. In column 2 chosen AGN power bins are presented. N indicates number of sources included in each bin. The mean measurements of SFRs in each bin with their errors calculated by the bootstrap technique are shown in column 5. New AGN power bins were defined for the mean measurements of SSFRs and stellar mass as the number of sources in the sample decreased by excluding sources that do not have stellar mass measurements. In column 6 the new AGN power bins are shown. The mean SSFRs and the mean stellar mass for each bin with their errors are presented in column 9 and 10, respectively.

Stacking SFR: Radio-loud and radio-quiet comparison using mass-matched samples

One of the possible effects that may cause the correlation between SFR and AGN power we see in the results is the mass of the host galaxy. In order to judge its influence and to eliminate it, I implemented the same analysis for sources matched in their stellar mass. I carried out mass matching using the method described by Virdee et al. (2013). In summary, I randomly discarded 1 per cent of the galaxies of the comparison sample (the radio-quiet AGN sample). I then ran a K–S test to compare the distributions of stellar masses for the main sample (the radio-loud AGN sample) and comparison sample (the radio-quiet AGN sample). Repeating this process N times, where N is the number of comparison sources, enables me to select the best reduced catalogue. Once I obtain the best matching catalogue, 1 per cent of the remaining sources in the comparison sample is discarded and the process is repeated. I repeat this process until the null hypothesis probability returned by the K–S test exceeds 10 percent. This mass-matching process was implemented for the sources in each AGN power bin separately. Although this method provides me the best matched catalogue, I lose the majority of the original comparison sample. The loss is around 96 per cent so that the final sample of radio-quiet AGN contains 98 objects. Figure 4.15 shows the distribution of stellar mass for each sample before and after the matching process.

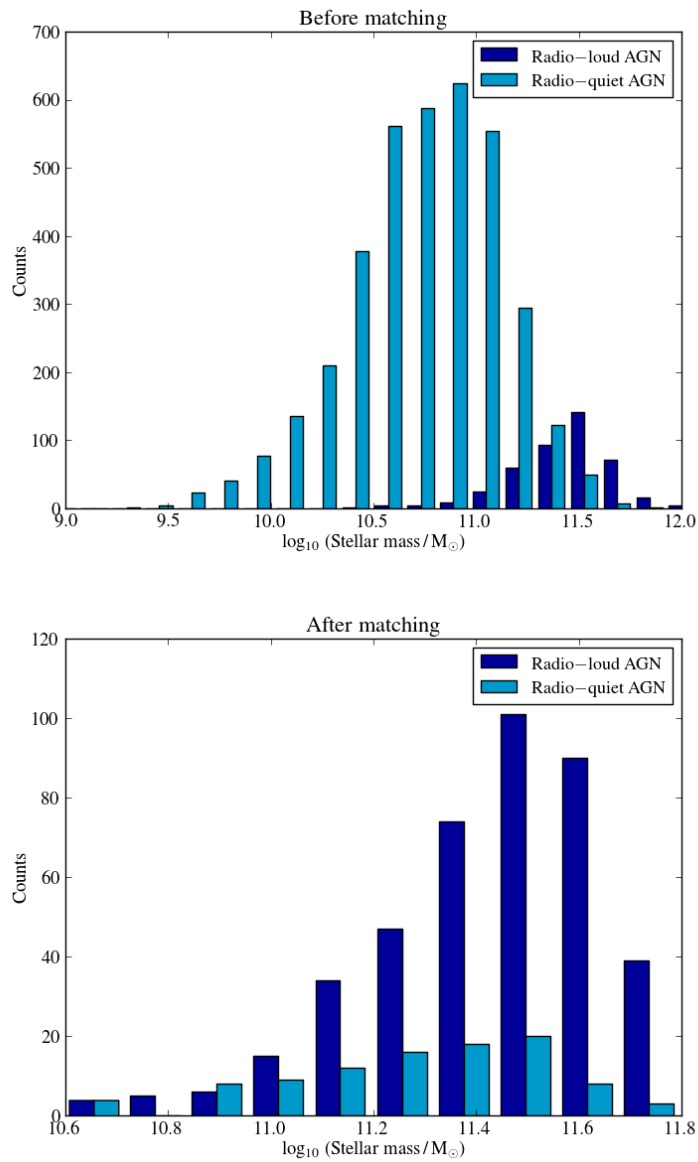


Figure 4.15: Stellar mass distribution of each AGN sample before (top plot) and after (bottom plot) the matching process.

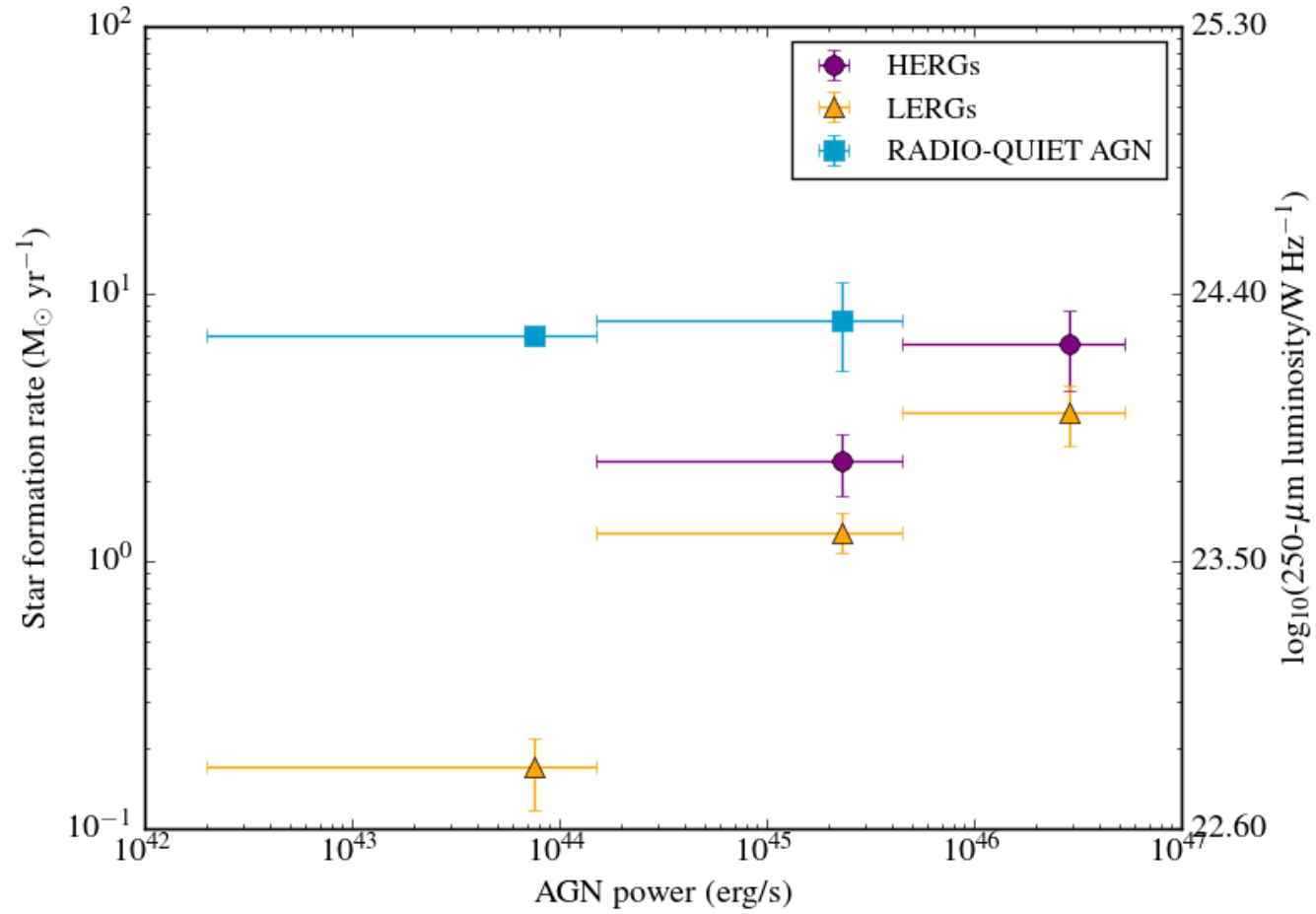


Figure 4.16: The result of the SFR stacking analysis of radio-loud and radio-quiet AGN using mass-matched samples. The radio-loud objects are separated into emission-line class.

The results of this analysis are presented in Figure 4.16. Although there seems to be a slight increase in SFR of radio-quiet AGN with AGN power the steepness of increase softened to a more gentle slope by leaving out the effect of galaxy mass.

I also show emission-line radio galaxies separately in this figure. LERGs, in all bins, have the lowest rate of star formation as expected, since LERGs have been found in large ellipticals with little star formation (e.g. Best et al. 2005). For a given AGN power HERGs' host galaxies have comparatively higher star formation rates than LERGs but less than host galaxies of radio-quiet AGN.

Sample	AGN power bins erg s ⁻¹	Mean z	N	Mean SFR M _⊙ yr ⁻¹	Mean stellar mass (×10 ⁺¹¹ M _⊙)
Radio-quiet AGN	2.0e+42–1.5e+44	89	0.12	6.98 ^(0.53) _(0.56)	2.08 ^(0.11) _(0.10)
	1.5e+44–4.5e+45	8	0.18	7.93 ^(3.10) _(3.01)	3.25 ^(0.51) _(0.49)
HERGs	1.5e+44–4.5e+45	59	0.21	2.38 ^(0.61) _(0.70)	3.08 ^(0.16) _(0.16)
	4.5e+45–5.3e+46	36	0.27	6.45 ^(1.70) _(2.14)	3.28 ^(0.19) _(0.17)
LERGs	2.0e+42–1.5e+44	7	0.04	0.17 ^(0.05) _(0.05)	1.12 ^(0.11) _(0.12)
	1.5e+44–4.5e+45	208	0.17	1.28 ^(0.22) _(0.21)	2.63 ^(0.08) _(0.08)
	4.5e+45–5.3e+46	105	0.25	3.60 ^(0.90) _(0.97)	3.58 ^(0.11) _(0.13)

Table 4.6: The stacking analysis results of radio-loud (HERGs and LERGs) and radio-quiet AGN samples matched in their stellar masses. Similar to Table 4.4 in column 2 chosen AGN power bins are shown. In column 3 the mean redshift measurements are given for each bin. N indicates number of sources included in each bin. The mean measurements of SFRs and stellar mass in each bin with their errors calculated by the bootstrap technique are presented in column 5 and 6, respectively. I also show here emission-line radio galaxies included in each bin and their corresponding measurements as a reference.

4.4.2 Correlation between black hole accretion rate and star formation rate

If SFR and AGN power are coupled then a correlation should be expected between black hole accretion rates (\dot{M}_{BH}) and star formation rates (\dot{M}_{SFR}) of these samples. In order to assess this, \dot{M}_{BH} were calculated using $P_{\text{AGN}} = \eta \dot{M}_{\text{BH}} c^2$ where P_{AGN} is the AGN power, whose derivation was discussed in Section 2.4 (see also Table 4.3), η is an efficiency factor, \dot{M}_{BH} is the black hole accretion rate and c is the speed of light. I assumed the value of efficiency to be 0.1 for all sources. However, it should be noted that since the efficiency depends on the nature of accretion disk and accretion flows, a range of efficiencies can be found for different types of AGN. Especially in CDAF (e.g. Narayan et al. 2000), ADAF (e.g. Narayan & Yi 1995b) and ADIOS (e.g. Blandford & Begelman 1999) accretion flow models only a small fraction of the matter contributes to the mass accretion rate at the black hole because of turbulence and strong mass loss. For this reason, much lower radiative efficiencies ($\eta \ll 0.1$) are expected but the efficiency of the jet-generation process is not known. On the contrary, thin-disk accretion onto a black hole may lead to high efficiency factors ($\eta > 0.1$, Abramowicz et al. 1988; Yu & Tremaine 2002). The use of a single efficiency factor is therefore only an approximation.

A proxy of the rate of black hole growth (\dot{M}_{BH}) as a function of star formation rate (a proxy of the rate of galaxy growth) is presented in Figure 4.17 where I see a strong relationship between the rate of matter accreted onto black hole and that of star formation for both types of active galaxy samples.

I show the standard relation between bulge and black hole mass (e.g. Marconi & Hunt 2003; Heckman et al. 2004) with black solid line for a comparison to the relations we see between the rate of black hole growth and galaxy growth for the samples. When I compare the results with the observed standard correlation suggests that low-power AGN have black holes growing slower than expected to maintain the $M_{\text{BH}} - M_{\text{Bulge}}$ relation (for example for a source with $\dot{M}_{\text{SFR}} = 9 \times 10^{-1} M_{\odot} \text{ yr}^{-1}$, the expected value of \dot{M}_{BH} is around $10^{-3} M_{\odot} \text{ yr}^{-1}$) and black holes in high-power AGN are growing faster (for an object with $\dot{M}_{\text{SFR}} = 2.5 \times 10^1 M_{\odot} \text{ yr}^{-1}$, the expected \dot{M}_{BH} is to be about $9 \times 10^{-1} M_{\odot} \text{ yr}^{-1}$). The implications of this result are discussed in Section 4.5.1.

I also checked whether any possible contribution from star formation to the [OIII] luminosity can affect the relation that I obtained between SFR and \dot{M}_{BH} . The red dashed line shows the expected relationship between accretion rate, derived by using the [OIII] luminosity, and \dot{M}_{SFR} for star-forming objects. The comparison of the red

line with the results of stacking analysis for AGN demonstrates that the contribution from star formation to the [OIII] luminosity can only have an effect on sources in the lowest AGN power bin.

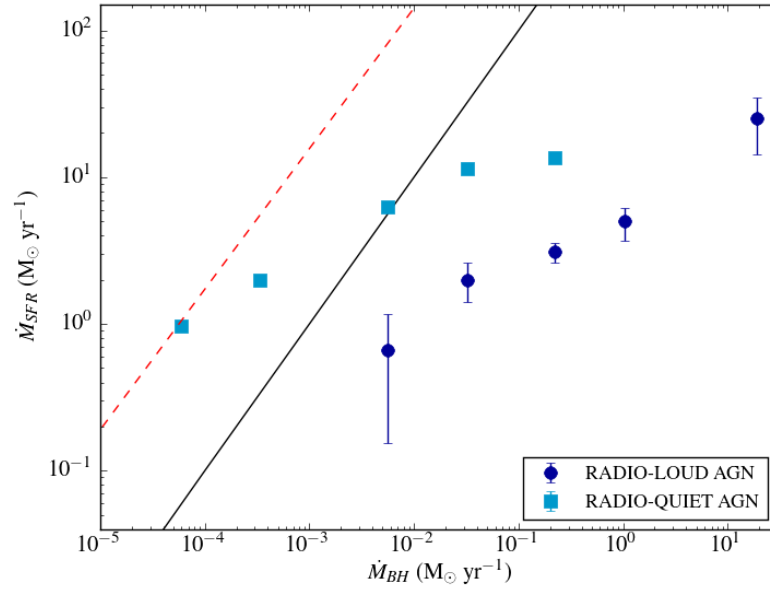


Figure 4.17: The relation between the rate of black hole growth and the rate of galaxy growth is presented for the AGN samples. Assuming \dot{M}_{SFR} is proportional to bulge mass and \dot{M}_{BH} is proportional to black hole mass, the black solid line represents the standard relation between the bulge and black hole mass. (e.g. Marconi & Hunt 2003; Heckman et al. 2004). Low-power AGN have black holes growing slower than expected value and black holes in high-power AGN are growing faster. The red dashed line represents the relationship between \dot{M}_{SFR} and \dot{M}_{BH} that would be observed if star-forming objects were incorrectly classified as AGN. It can be seen that such contamination of the AGN sample cannot account for the observed trend.

4.4.3 Stacking SFR: HERG and LERG comparison

The radio-loud AGN sample was investigated on its own to study the possible difference in the star formation properties of the sources as a function of emission-line type, discussed previously by Hardcastle et al. (2010, 2013). Since I want to compare the SFRs and SSFRs for HERGs and LERGs, I defined new AGN power bins to include the similar numbers of sources in each bin for both classes. I present the results in Figure 4.18. In the top graph we can see that the change in the SFRs is dependent on

Population type	\dot{M}_{BH} range	SFR/ \dot{M}_{BH}
Radio-quiet AGN	$10^{-5} - 2 \times 10^{-3}$	15000-1500
	$2 \times 10^{-3} - 2 \times 10^{-1}$	1500-100
Radio-loud AGN	$10^{-3} - 2 \times 10^{-1}$	150-15
	$2 \times 10^{-1} - 2 \times 10^1$	15-2.0

Table 4.7: SFR/ \dot{M}_{BH} ratios for radio-loud and radio-quiet AGN are given for different range of accretion rates.

the AGN power. SFRs increase, for both HERGs and LERGs, with increasing AGN power. The increase in SSFRs for LERGs is more gentle in comparison to the increase of their SFRs whereas we still see a clear increasing trend of SSFRs for HERGs. In two out of three SFR bins (and three out of four bins of SSFR), LERGs have lower SFRs/SSFRs than HERGs, but the error bars are large.

Since the size of the radio-loud AGN sample is small I only have four AGN bins for the stacking analysis of SFR, and this is reduced to three bins for the estimates of SSFRs when the galaxies with no stellar mass estimates were excluded. Therefore, a quantitative analysis was carried out to find the magnitude of any possible difference between the SFRs of LERGs and HERGs. I divided the SFRs of LERGs by the SFRs of HERGs for each AGN power bin to calculate the SFR ratio and the corresponding errors on these ratios. The mean ratio was then computed using these estimates. The mean ratio of $\text{SFR}_{\text{LERGs}}/\text{SFR}_{\text{HERGs}}$ is 0.60 ± 0.32 . This result indicates that within the errors there is at most a slight difference between the SFRs of LERGs and HERGs of matched AGN power.

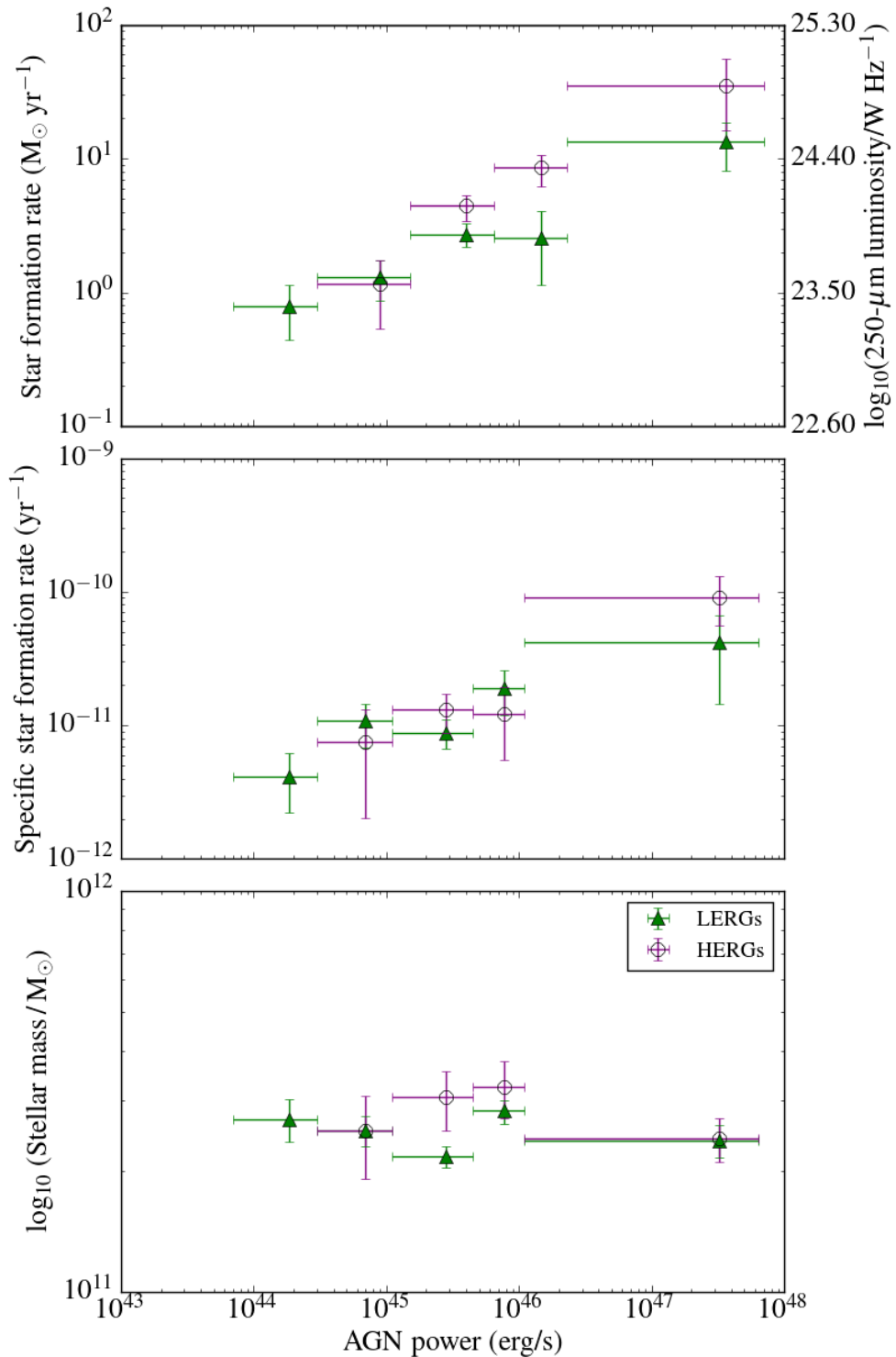


Figure 4.18: The result of stacking analysis of radio-loud AGN sample. Different AGN power bins were used in order to have the appropriate number of sources in each bin to be able to compare different emission classes. From bottom to top the graphs shows: the comparison of SSFRs, stellar masses and SFRs of the samples stacked in their AGN powers.

Sample	AGN power bins erg s ⁻¹	Mean z	N	Mean SFR M _⊙ yr ⁻¹	AGN power bins erg s ⁻¹	Mean z	N	Mean SSFR (×10 ⁻¹¹ yr ⁻¹)	Mean stellar mass (×10 ⁺¹¹ M _⊙)
LERGs	7.0e+43–3e+44	0.05	22	0.78 ^{0.35} _{0.35}	7.0e+43–3.0e+44	0.05	22	0.41 ^(0.21) _(0.19)	2.69 ^(0.32) _(0.32)
	3.0e+44–1.5e+45	0.13	77	1.29 ^{0.43} _{0.42}	3.0e+44–1.1e+45	0.12	54	1.09 ^(0.37) _(0.41)	2.52 ^(0.23) _(0.22)
	1.5e+45–6.5e+45	0.24	186	2.71 ^{0.55} _{0.52}	1.1e+45–4.5e+45	0.21	149	0.87 ^(0.24) _(0.19)	2.17 ^(0.13) _(0.13)
	6.5e+45–2.3e+46	0.30	101	2.57 ^{1.46} _{1.44}	4.5e+45–1.1e+46	0.25	76	1.89 ^(0.69) _(0.69)	2.83 ^(0.18) _(0.21)
	2.3e+46–7.0e+47	0.34	18	13.56 ^{5.08} _{5.43}	1.1e+46–6.4e+47	0.25	37	4.14 ^(2.54) _(2.71)	2.39 ^(0.23) _(0.23)
HERGs	3.0e+44–1.5e+45	0.16	23	1.17 ^{0.57} _{0.63}	3.0e+44–1.1e+45	0.14	10	0.75 ^(0.55) _(0.55)	2.52 ^(0.57) _(0.61)
	1.5e+45–6.5e+45	0.32	96	4.43 ^{0.94} _{1.03}	1.1e+45–4.5e+45	0.22	51	1.30 ^(0.41) _(0.42)	3.05 ^(0.51) _(0.53)
	6.5e+45–2.3e+46	0.39	78	8.62 ^{2.12} _{2.42}	4.5e+45–1.1e+46	0.27	26	1.23 ^(0.71) _(0.68)	3.24 ^(0.52) _(0.54)
	2.3e+46–7.0e+47	0.40	11	35.25 ^{21.24} _{19.06}	1.1e+46–6.4e+47	0.28	10	9.09 ^(3.85) _(3.55)	2.41 ^(0.31) _(0.31)

Table 4.8: Table shows the stacking analysis results for HERGs and LERGs. In column 2 the chosen AGN power bins are shown. N indicates number of sources included in each bin. The mean measurements of SFRs in each bin with their errors calculated by the bootstrap technique are presented in column 5. New AGN power bins were defined for the mean measurements of SSFRs and stellar mass as the number of sources in the sample decreased by excluding sources that do not have stellar mass measurements. In column 6 the new AGN power bins are shown. The mean SSFRs and the mean stellar mass for each bin with their errors are shown in column 9 and 10, respectively.

4.5 Discussion

I have investigated the possible link between black-hole activity and star formation by probing star formation properties of large matched samples as a function of AGN power. Results of this work indicate that AGN and star formation are coupled to some degree for radio-quiet and radio-loud AGN, and also for different emission-line types of radio-loud AGN. A contrast between the SFRs and SSFRs of different types of active galaxies stands out in the results. Host galaxies of radio-quiet AGN have more stars forming than their radio-loud counterparts. In the case of the different emission-line classes, HERGs have higher SFR/SSFR than LERGs.

The galaxy masses are different for these objects and the influence of this should be taken into account. Therefore, a stacking analysis has also been carried out for radio-loud and radio-quiet AGN samples that are matched in galaxy mass. Mass-matched samples still indicate similar results; there is a slight increase in SFR of radio-quiet AGN as the AGN power increases. This rate is higher in radio-quiet AGN than HERGs and LERGs, but an increase in SFR and SSFR is also seen for HERGs and LERGs. I found a wide range of \dot{M}_{BH} which are correlated with the SFRs of both samples. In the following section I interpret the results.

4.5.1 Interpretation of the correlation between SFR and AGN power

In the simplest interpretation the correlation found between the rate of star formation and black-hole activity could be taken to be evidence for the synchronised growth of black holes and their host galaxies (Fig. 4.11, 4.14, 4.16, 4.18). This would then suggest that the existing cool gas supply on the host galaxy scale can feed the black hole in the centre of the galaxy at the same time as it allows for many more stars to form in the host galaxies of both radio-loud and radio-quiet active galaxies. In order to have this relationship, the available gas on host galaxy scales should be transported to the central regions by some physical mechanisms e.g. major mergers and secular processes. Major mergers are thought to be responsible for carrying a large amount of gas to the nuclear region of a galaxy (e.g. Bournaud et al. 2005; Hopkins et al. 2010), thereby triggering powerful AGN and resulting in the co-evolution of black hole and its host galaxy in high accreting sources at high redshifts. Secular processes (large galaxy bars, disc instabilities, minor mergers etc.) are considered to be sufficient to move some of the available gas to the inner regions of galaxies to feed black holes

(e.g. Ellison et al. 2011), especially in low accretion systems at low redshifts. Morphological studies of AGN host galaxies indicate that the correlations observed between the properties of black holes and that of their host galaxy are tight for ellipticals and bulge galaxies but not for disk galaxies with pseudo bulges (e.g. Greene et al. 2008). The growth of ellipticals and bulge-dominated galaxies are commonly associated with mergers that can feed the most powerful quasars whereas low mass black holes have mostly been found in pseudobulges. The sources in the sample have low and moderate AGN powers at $z < 0.6$. I do not have complete and detailed morphological studies of all sources but the rough analysis (Section 4.2) shows that most of the radio-loud AGN have elliptical hosts whereas radio-quiet AGN hosts tend to have more spiral characteristics. As mentioned above secular processes are often suggested to be responsible for fuelling disk (disk galaxies and pseudobulges), moderate luminosity galaxies in the low-redshift universe (e.g. Kormendy & Kennicutt 2004; Fisher & Drory 2011). Considering all these implications for the galaxies in the sample, it is likely that internal processes are in many cases responsible for the formation of stars and driving the gas into the nuclear regions to feed black holes in their centre.

There is no clear answer to the question of when SFR correlates with AGN luminosity. However, the results of earlier studies indicate that a relation between AGN luminosity and SFR has been mainly observed for high-power sources ($L_{\text{AGN}} > 10^{43}$ erg s $^{-1}$). Low-power (or quiescent galaxies) objects do not show such a relationship between these quantities in earlier works. For instance, Diamond-Stanic & Rieke (2012) found no significant correlation between galaxy-wide SFR and \dot{M}_{BH} in local Seyferts (the mean distance is around 22 Mpc). Shao et al. (2010), Lutz et al. (2010) and Rosario et al. (2013) used hard X-ray selected local Swift-BAT galaxies ($z < 0.3$) and did not observe any correlation between L_{AGN} and L_{SF} . Here in this work I also analyse a sample of low redshift AGN ($z < 0.6$). However, the work is different from that of Rosario et al. (2013) in that I take all components of different AGN types into account and calculate the total AGN power (by considering both mechanical and radiative output of AGN when it is present). I then derive average SFRs for the objects that are matched in total AGN power. The analysis clearly shows that there is a relation between AGN power and SFR for mass matched samples of high power and low power AGN (Fig. 4.11, 4.16 and 4.17). This is a manifestation of a connection between AGN power and SFR that holds for low- and moderate-power sources at low redshifts as well. As mentioned above, Shao et al. (2010), Lutz et al. (2010) and Rosario et al. (2013) have come to different conclusions: What leads to this difference? First of all,

Shao et al. (2010) and Rosario et al. (2013) used 60 μm far-IR luminosity, and Lutz et al. (2010) used 870 μm submillimeter luminosity as a SFR indicator, while I derive the SFRs using the 250 μm luminosity, which should be minimally contaminated by AGN, old-stellar populations and torus. Another important difference is that the host galaxies of X-ray selected AGN may be different from the host galaxies of mid-IR or optical selected AGN (e.g. Hickox et al. 2009; Juneau et al. 2013). Furthermore, the hard X-ray luminosity comes directly from the accretion disk whereas the [OIII] luminosity is derived from the extended narrow-line region of AGN. For this reason, the hard X-ray is expected to show more variation on short time scales (years) compared to the [OIII] luminosity, introducing scatter into any relationship based on the power derived from X-rays.

Another point to consider is the duty cycle of AGN. Some authors (e.g. Hopkins et al. 2005) have attempted to explain the discrepancy between the observed \dot{M}_{BH} -SFR relation and the expected one in luminous objects using a simple duty cycle model in which it is assumed that the growth of black holes occurs at high accretion rates at a fixed Eddington ratio and time, and they are off (accreting at unobservably low rates) otherwise. However, Fig. 4.17 shows clearly that black holes can grow slowly at lower accretion rates. Low-power AGN have black holes growing slower than expected from the $M_{\text{BH}}-M_{\text{Bulge}}$ relationship and black holes in high-power AGN are growing faster. There is actually a continuous smooth growth of black holes instead of an on and off phases and, therefore, the results cannot be explained with a simple duty cycle scenario. It is worth noting that with the available data I cannot examine whether the available gas reservoir for star formation is in the galaxy bulge or arms. Therefore, it would be interesting to implement the same analysis using SFRs of de-composed bulge and galaxy disk.

Galaxy merger simulations have also predictions for the relation between SFR and AGN activity. In these models (e.g. Di Matteo et al. 2005) it has been suggested that the $\text{SFR}/\dot{M}_{\text{BH}}$ ratio ranges between 200–600 at the peak of star formation and this value is expected to be around 1000 for low accretion rate objects ($\dot{M}_{\text{BH}}=10^{-2} M_{\odot} \text{yr}^{-1}$). The results agree to some level with the predictions of this model. However, I have low and moderate luminosity galaxies with spiral (mostly in the radio-quiet AGN sample) and elliptical morphologies at low redshifts so many of the ellipticals in the sample may have ongoing mergers. Ballantyne (2008) used starburst disk models proposed by Thompson et al. (2005) to study local AGN with hard X-ray luminosities of $10^{43}-10^{44} \text{ erg s}^{-1}$ and they found that $\text{SFR}/\dot{M}_{\text{BH}}$ should be around ~ 250 (for $\dot{M}_{\text{BH}} \sim$

$0.3 M_{\odot} \text{ yr}^{-1}$) for a disk with $R_{out}=100$ pc. This can only be observed for the whole galaxy of the radio-quiet AGN sample for black hole growth rates of $\dot{M}_{BH} = 2 \times 10^{-3} - 2 \times 10^{-1} M_{\odot} \text{ yr}^{-1}$. Recently, Thacker et al. (2014) examined the correlation between \dot{M}_{BH} and SFR of all galaxies for various AGN feedback models using the time evolution of a merger simulation and they found that although most feedback models produce the observed M- σ relation, there are distinct differences between the results of various models. Some of these models result in predictions that are in qualitative agreement with the results reported here (see Wurster & Thacker (2013) for details of these models.)

4.5.2 Probable reasons for the difference between SFR/SSFR of radio-loud and radio-quiet AGN

As mentioned in the previous section, radio-quiet and radio-loud AGN present a moderately strong relationship between their SFRs and AGN powers. If the observed trends are examined in detail it can be seen that for radio-quiet AGN at the high power end there is a tendency of constant SFR with increasing AGN power. This may be due to AGN feedback that starts having a significant effect on star formation when the gas supply reaches a certain level. In radio-loud AGN, black holes grow continuously. Kauffmann & Heckman (2009) also reached similar conclusions. They analysed nearby galaxies selected from SDSS and found that the growth of black holes in local galaxies is present in two ways: if there is enough gas in the bulge the black hole can regulate itself; when the galaxy runs out of gas, the growth of black hole is regulated by the rate of mass loss due to evolved stars.

Another question that arises from this work is: What could be the possible reason for the difference between the SFRs and SSFRs of radio-loud AGN and their radio-quiet cousins? The obvious difference between these AGN is the radio-emitting strong jets that we see in radio-loud AGN but not in their radio-quiet counterparts. If I especially focus on the results I have from the mass-matched samples where I eliminate the effect of mass, the striking difference in their SFRs may be suggesting that these strong jets are responsible for this difference, in the sense that there is the difference between the SFRs of radio-loud and radio-quiet AGN (lower/suppressed star formation in radio-loud AGN ⁵).

⁵The relation between radiative power and SFR could also be examined as a further test. This can only be done using HERGs and radio-quiet AGN since only these galaxies have radiative outputs. However, the number of HERGs is not large enough in the sample to carry out a statistically significant

Another reason for this difference may be due to the difference between the morphology of galaxies in the mass sample. To check if I am comparing galaxies with similar morphologies, I searched the database of the Galaxy Zoo Project 2 (GZ2; Willett et al. 2013). This was done by scanning the GZ2 catalogue sources with redshift⁶ $z < 0.25$. Although I did not have classifications for all of the sources, this process gave an idea of their morphologies. I found that most radio-loud AGN are ellipticals but radio-quiet AGN have mixed morphologies (some of them are spirals and some are ellipticals). However, it should be pointed out that I cannot consider bulge and disk separately for radio-quiet AGN with the available data.

4.5.3 The differences between SFR/SSFR in HERGs and LERGs

I also had the advantage of exploring the star formation properties of large samples of emission-line classified radio galaxies using SFRs estimated by 250 μm *Herschel* luminosity matched in their AGN powers (Fig. 4.18). It is apparent that there is a relationship between the star formation and black hole accretion rates.

With regard to the comparison of SFRs and SSFRs for these galaxies, there is only very tentative evidence for a difference, in the contrast to the results of other studies (e.g. Hardcastle et al. 2013; Herbert et al. 2010; Baldi & Capetti 2008). Previously Hardcastle et al. (2013) examined star formation properties of HERGs and LERGs by binning in radio luminosity and found a clear difference between these galaxies. It is important to note that in the present work I have matched the samples in total AGN power rather than luminosity, to compare SFRs of emission-line radio galaxies. Separating by radio luminosity (a proxy of the kinetic output) gives rise to a clear difference in the SFRs of HERGs and LERGs whereas this is less apparent when I take into account both kinetic and radiative outputs of HERGs. I cannot rule out a model in which the AGN power–SFR relation is the same for both radio-loud galaxy types, with the only difference being the way in which the accretion power manifests itself, though the HERG sample size in the current work is small.

We also see a rise in SSFRs of both samples with AGN power. When stellar mass is taken into account the rising trend of SSFRs of LERGs is not as sharp as we see for their SFRs. This may be expected, as we know that LERGs are hosted by massive red

analysis. It can be seen in Figure 4.16 that I have only two AGN power bins with both radio-quiet AGN and HERGs.

⁶This redshift cut provides reliable classifications of galaxies, considering the SDSS image resolution.

ellipticals where most of the galaxy is dominated by an old stellar population, whereas HERGs tend to have lower mass and to be less evolved than LERGs. Other differences between these emission-line galaxies are the environment in which they are found (e.g. Hardcastle 2004; Tasse et al. 2008) and the galaxy colours (e.g. Smolčić 2009). If the HERG/LEERG difference is understood as an accretion rate switch (Best & Heckman 2012; Mingo et al. 2014) then I would expect LERGs to have lower accretion rates and/or more massive black holes, implying smaller amounts of cold gas and/or more massive (hence more evolved) host galaxies.

4.6 Summary and Conclusions

In this work, I have explored star formation properties, derived using $250 \mu\text{m}$ *Herschel* luminosity, of radio-quiet and radio-loud AGN samples and investigated whether they depend on black hole activity. I have also compared these features of radio-quiet and radio-loud AGN samples matched in their stellar mass and redshifts. The main results I have obtained are as follows.

- Examination of radio-loud and radio-quiet AGN samples matched only in their AGN powers shows that for both AGN samples the rate of star formation is increasing with increasing AGN activity. The same conclusion can be drawn for their relative galaxy growth rates (Fig. 4.11).
- A comparison of the star formation properties regarding these samples indicates that the host galaxies of radio-quiet AGN are forming more stars for a given black hole activity than their radio-loud cousins. This difference in the level of star formation per unit stellar mass goes up to an order of magnitude (Fig. 4.11).
- I also classified the radio-loud AGN sample in terms of emission-line type in order to compare their star formation properties. Both LERGs and HERGs present the same trend of increasing SFR with rising black-hole growth. In terms of their SSFRs both types of galaxies present a similar trend; their SSFRs are also increasing towards to higher AGN powers. They present almost a constant relative galaxy growth rate. There is only a marginal tendency for HERGs to have higher SFRs and SSFRs than LERGs when matched by AGN power (Fig. 4.18).
- To account for the likely influence of stellar mass I composed radio-loud and radio-quiet AGN samples matched in their galaxy masses. The same stacking

analysis has been implemented for these samples. The findings suggest that the black-hole growth and the star formation rate are coupled. The amount of stars forming for a given time increases with increasing AGN power for both AGN samples (Fig. 4.16).

- When I take into account the effect of intrinsic correlation between redshift and SFR in the stacking analysis I have shown that the strong correlation between SFR and AGN power for radio-loud and radio-quiet AGN sample does not vanish. Furthermore, I have evaluated the effect of SFR evolution with redshift. This analysis showed that the difference between SFRs of radio-loud and radio-quiet AGN is not due to this effect.
- I have also assessed the relation between SFR and \dot{M}_{BH} and found that both radio-quiet and radio-loud AGN have a range of ratios of $\text{SFR}/\dot{M}_{\text{BH}}$. A comparison of the results with the observed correlation suggests that low-power AGN have black holes growing slower than expected from the $M_{\text{BH}}-M_{\text{Bulge}}$ relationship and black holes in high-power AGN are growing faster. The results cannot be explained with a simple model of duty cycle of AGN (Fig. 4.17).
- Reasons behind the apparent difference in SFR of radio-quiet AGN and HERGs and LERGs have been explored. This difference is still seen when comparing the samples of radio-loud and radio-quiet AGN matched in their stellar mass (Fig. 4.16). There may be two possible reasons for this. Either the strong jets we observe in radio-loud AGN suppress star formation in these galaxies or the difference between the galaxy morphology of the AGN samples leads to this observed disparity, or some combination of the two. Nevertheless, a direct role for feedback from the radio jets is not ruled out.

Chapter 5

The deep LOFAR survey of the H-ATLAS NGP field

“Sometimes glass glitters more than diamonds because it has more to prove.”

Terry Pratchett, The Truth

5.1 Introduction

The *Herschel*-ATLAS NGP field was observed with LOFAR (van Haarlem et al. 2013) between 2013 April 26 and 2014 May 15 as a part of the LOFAR SKSP (Röttgering et al. 2006). The aim of the SKSP is to survey in the Northern sky with r.m.s. noise around $100 \mu\text{Jy beam}^{-1}$ at 150 MHz reaching a depth 7 times greater than FIRST’s for the same angular resolution (assuming a source with spectral index $\alpha=0.7$).

Since the first serendipitous discovery of radio emission (Jansky 1933), radio astronomy has developed rapidly. In recent years, with technological developments, it has been possible to build computers that can perform complex tasks such as the correlation of signals from hundreds to thousands of antennas. This has accelerated the growth of radio synthesis telescopes in terms of both number and diversity. Some examples of newly constructed or upgraded instruments, include the Expanded Very Large Array (EVLA, Perley et al. 2004), the Karoo Array Telescope and the Australian Square Kilometer Array Pathfinder (Johnston et al. 2007) and in future the Square Kilometer Array (Schilizzi 2005). Examples of radio telescopes that can observe at lower

radio frequencies are GMRT¹, the Long Wavelength Array (Taylor 2007), the Murchison Wide-field Array (Lonsdale et al. 2009; Tingay et al. 2013) and the Low Frequency Array (van Haarlem et al. 2013). Deep radio surveys at low radio frequencies (~ 150 MHz) are rare. The Tata Institute of Fundamental Research (TIFR) GMRT (TGSS²) and the VLA Low-Frequency Sky Survey (VLSS, Cohen et al. 2007) surveys are two such surveys, but they provide relatively low angular resolutions of 20 arcsec and 80 arcsec, respectively. Table 5.1 shows a number of low-frequency radio surveys and a comparison of their nominal parameters.

The LOFAR High Band Array (HBA) is capable of observing the sky at these low radio frequencies with a resolution of much lower than 20 arcsec and this will give us a chance to address various interesting questions related to AGN, star-forming galaxies, diffuse emission, relics etc. In particular, an innovative direction-dependent (or ‘facet’) calibration scheme (van Weeren et al. 2016) applied to LOFAR observations makes it possible for the LOFAR HBA observations to reach the resolution (~ 5 arcsec) and sensitivity (~ 0.1 mJy beam⁻¹) that were initially targeted by the Tier-1 survey (Röttgering et al. 2011). Some recent work using LOFAR data has already shown the capabilities of the LOFAR and the facet calibration technique (e.g. van Weeren et al. 2016; Williams et al. 2016).

This chapter will briefly explain the basics of radio interferometry, LOFAR and the LOFAR observations that were carried out as a part of the SKSP. I will also describe the data reduction, including facet calibration, and imaging techniques that were used. Finally, I will describe the steps leading to the final data products such as the survey catalogue.

It is important to note that this has been a project in which a number of people were involved in the LOFAR/NGP analysis. The list of tasks and people who were involved are given in Table 5.2.

5.2 LOFAR

LOFAR is a radio interferometric array operating in the frequency range from 10–240 MHz (30–1.2 m), designed and constructed by the Netherlands Institute for Radio Astronomy (ASTRON). LOFAR is the world’s biggest connected radio telescope and it has officially been collecting data for science since 2012 (van Haarlem et al. 2013).

¹http://gmrt.ncra.tifr.res.in/gmrt_hpage/Users/Help/help.html

²<http://tgss.ncra.tifr.res.in>

Survey	Frequency	Sensitivity	Resolution	Area	Refs.
MSSS-LBA	30-78 MHz	$\lesssim 50 \text{ mJy beam}^{-1}$	$\lesssim 150''$	$20\,000 \text{ deg}^2 (\delta > 0^\circ)$	Heald et al. (2015)
8C	38 MHz	$200\text{-}300 \text{ mJy beam}^{-1}$	$4.5' \times 4.5'$	$3\,000 \text{ deg}^2 (\delta > +60^\circ)$	Rees (1990)
VLSS	74 MHz	$100 \text{ mJy beam}^{-1}$	$80''$	$30\,000 \text{ deg}^2 (\delta > -30^\circ)$	Cohen et al. (2007)
MSSS-HBA	120-170 MHz	$\lesssim 10\text{-}15 \text{ mJy beam}^{-1}$	$\lesssim 120''$	$20\,000 \text{ deg}^2 (\delta > 0^\circ)$	Heald et al. (2015)
7C	151 MHz	20 mJy beam^{-1}	$70'' \times 70''$	$5\,000 \text{ deg}^2$ (irregular coverage)	Hales et al. (2007)
TGSS	150 MHz	$7\text{-}9 \text{ mJy beam}^{-1}$	$20''$	$32\,000 \text{ deg}^2 (\delta > -30^\circ)$	Intema et al. (2016)
WENNS	325 MHz	$3.6 \text{ mJy beam}^{-1}$	$54'' \times 54''$	$10\,000 \text{ deg}^2 (\delta > +30^\circ)$	Rengelink et al. (1997)
NVSS	1400 MHz	$0.45 \text{ mJy beam}^{-1}$	$54''$	$35\,000 \text{ deg}^2 (\delta > -40^\circ)$	Condon et al. (1998)

Table 5.1: Comparison of nominal parameters of low-frequency radio surveys, reproduced from Heald et al. (2015).

People who are involved in the project	Tasks
Prof. Martin J. Hardcastle	Reduction, calibration and imaging of the NW, NE and Central fields. Evaluation of the image quality, production of the raw catalogue, comparison of the survey catalogue with other surveys for quality checks. Primary (Central field) and secondary visual inspections. Source counts and AGN science. Details of these are given by Hardcastle et al. (2016).
Gülay Gürkan Uygun	Reduction, calibration and imaging of the SW field. Developing a software for primary visual inspection, primary visual inspection (SW, NE and NW fields) and secondary visual inspection. Producing the final catalogue. Science related to the far-IR/radio correlation and the low-frequency radio luminosity/SFR relation (Chapter 6).
Shaun Read	Primary (NE field) visual inspection.
Dr. Daniel J. Smith	Secondary visual inspection.
Dr. Wendy L. Williams	Secondary visual inspection.

Table 5.2: People who were involved in the LOFAR/NGP project and the tasks they each carried out are shown.

LOFAR is formed from an array of dipole antenna stations that are deployed in the Netherlands and Europe. There are 40 stations in the Netherlands, consisting of 24 core stations out to 3.5 km and 16 remote stations out to 120 km, and 8 international stations in Europe (Fig. 5.1). LOFAR consists of two arrays: the low-band array (LBA; Fig. 5.2—the top left panel) and the HBA (Fig 5.2—the top right panel). The LBA antennas operate from ~ 10 up to 90 MHz whereas the HBA antennas are designed to operate in the 110–250 MHz range. The bottom right and left panels in Fig. 5.2 show the median averaged spectrum for the LBA and HBA antennas.

The signals from all dipoles in a given station are combined digitally into a phased array (i.e. the information from all antennas in each station is combined and summed in order to reduce the instantaneous field-of-view [FOV] of each station by making a spatial selection on the sky³) and a beam-forming technique⁴ is utilised. This allows the system to work rapidly as well as simultaneous is allowing for observations of multiple and independent areas of the sky (van Haarlem et al. 2013). A high-speed fibre network infrastructure is used in order to stream data from all stations and send them to a central processing (CEP) facility in the Netherlands. The University of Groningen has a computing centre where data from all stations are aligned and combined. Fibre networks and supercomputers are necessary to handle the LOFAR data because the raw data rate generated by the entire array is very large due to the effectively all-sky coverage of the component dipoles (van Haarlem et al. 2013). Initially the combined data are further processed which also allows for other processing operations such as correlation for standard interferometric imaging, tied-array beam-forming for high time resolution observations, etc. In 2013, the correlator has been upgraded to COrrrelator and Beam-forming Application platform for the LOFAR Telescope (COBALT⁵) to be able to utilise a central processing unit (CPU)—graphic processing units (GPU) based system as the central correlator and beam-forming platform for LOFAR.

³http://doc.utwente.nl/75100/1/LOFAR_IIEEE_Phased_Array_Paper_Xplore.pdf

⁴This method briefly shapes the beam by calculating the right delay for each antenna, weight them and summing the signals.

⁵<https://www.astron.nl/r-d-laboratory/ska/completed-projects/cobalt/cobalt>



Figure 5.1: The top panel shows the location of LOFAR stations throughout Europe and the bottom panel is a view of the superterp station. Credit: ASTRON

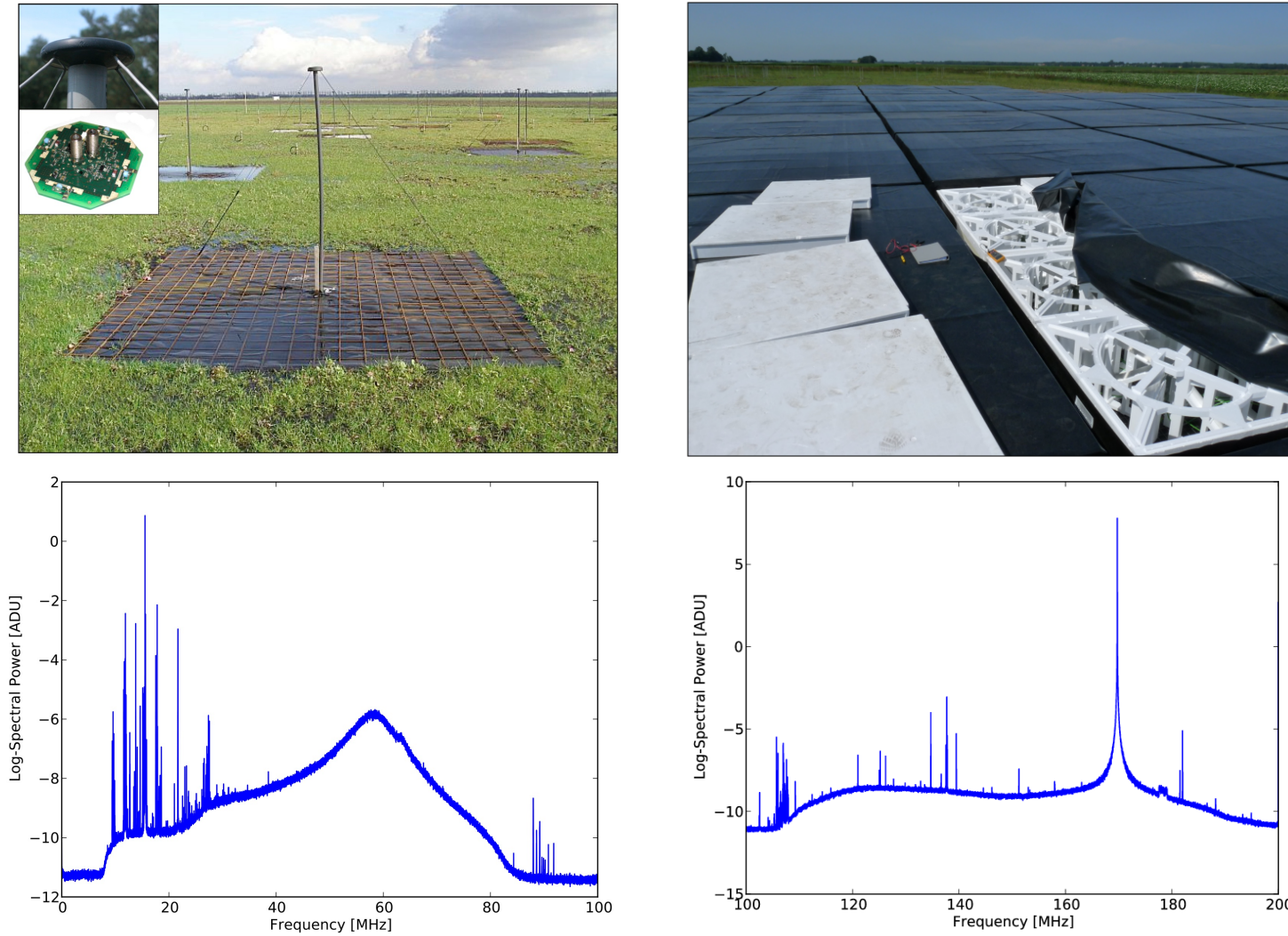


Figure 5.2: The median averaged spectrum for the LBA (left panel) and HBA (right panel) antennas. Credit: ASTRON

After correlation, the processed raw data are then written to a storage cluster for a variety of processing operations such as reducing the data using suitable pipelines in order to obtain relevant science data products. In the standard case, standard processing flagging of the data to eliminate radio frequency interference, averaging and calibration pipelines are run. The final output data are then sent to the LOFAR long-term archive (LTA) for cataloguing and distribution to the community (van Haarlem et al. 2013).

As the data used in this thesis were collected by the HBA antennas I will focus on the HBA observations in the rest of the section. I refer the reader to van Haarlem et al. (2013) for detailed information about LOFAR.

5.3 LOFAR Observations

Although the basis of LOFAR observations is similar to the principles given in Section 1.2 there are a few challenges that we can experience when we observe with LOFAR. Before I describe the observations I will briefly mention these difficulties. Radio frequency interference (RFI) affects the frequency range covered by both the LBA and HBA (RFI is also a problem for radio observations at cm wavelengths) so removal of this interference is necessary in order to obtain high fidelity images. Another problem can be caused by strong radio sources in the sky (the so called A-team sources: Cassiopeia A, Cygnus A, Virgo A, etc...). Since these sources are so bright, if they are in the observed field (or even if they are along way off-axis) they will significantly affect the observations so removing this effect is essential to calibrate the observations properly. As mentioned above, the electrons in the ionosphere interfere with the radio waves passing through the atmosphere causing a frequency dependent phase shift. The strength of this effect varies based on the total electron content (TEC) along the line between the receiving station and the source. TEC varies as a function of time and physical position in the ionosphere. Since the FOV of LOFAR is large the effect of both should be taken into account while calibrating the data.

As a part of the SKSP the H-ATLAS NGP field was observed in four separate pointings (or fields) with the HBA. Throughout the observations the HBA DUAL INNER mode was used. This mode means that the station beams of the core and remote stations match each other and gives the widest possible FOV. The first observation, which was made early on in LOFAR operations, was of slightly longer duration (~ 10 h) than the others (~ 8 h). Each observation was observed in 8 bit mode. Each frequency band was divided into sub-bands (in total each observation had 366 sub-bands) that are

Field name	RA	DEC	Start date/time	Duration (h)
Central	13h24m00s	+27d30m00s	2013-04-26 17:42:15	9.7
NW	13h00m00s	+31d52m00s	2014-04-22 18:30:30	8.0
SW	13h04m00s	+25d40m00s	2014-04-25 18:17:00	8.0
NE	13h34m00s	+32d18m00s	2014-07-15 13:28:38	8.0

Table 5.3: LOFAR observations of the NGP field.

195.3125 kHz wide giving a total bandwidth of 72 MHz between 110 and 182 MHz. All four correlation products were recorded, by default. In each case, the target field was observed and followed by short, 10-minute observations of calibrator sources (3C 196 at the start of the run and 3C 295 at the end). The data were later averaged by the observatory to 4 channels per sub-band and a 5-second integration time. Since none of the A-team sources were in or near any of the target fields no removal of contribution of bright off-axis sources was carried out by the observatory. For all of the further data reduction and imaging the University of Hertfordshire high-performance computing facility was used. Table 5.3 summarises the LOFAR observations of the NGP field. In Fig. 5.3 example of the uv -data of the SW field is seen.

5.4 LOFAR Data Reduction, Calibration and Imaging

The data reduction and calibration were carried out in two stages: first a direction-independent calibration, followed by a direction-dependent calibration scheme in order to obtain deep, high-fidelity, high-resolution radio images. For all calibration steps the BLACKBOARD SELFCAL (BBS) software system (Pandey et al. 2009) was used the other data processing was carried out using the LOFAR Default Pre-Processing Pipeline (DPPP).

5.4.1 Direction-independent Calibration

The following steps were taken for the data processing:

- ◆ Initially each sub-band of the target and calibrator observation was flagged using RFICONSOLE (Offringa et al. 2010, 2012) to remove the RFI.
- ◆ 3C 196 was used as a primary calibrator for all four observations. The gain solutions for the calibrator were obtained for each frequency channel. The solutions for the common rotation angle per station per channel were also derived

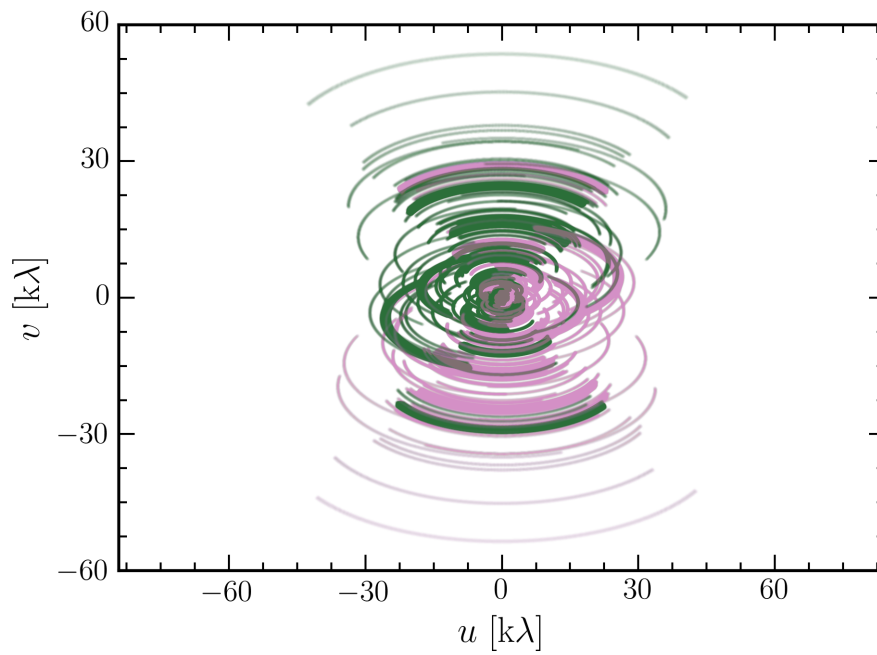


Figure 5.3: uv -coverage for the H-ATLAS/NGP SW field at 120–129 MHz. The maximum baseline is 120 km (or 60 $k\lambda$). Only one out of every ten uv -points in time and one out of every 40 points in frequency are plotted. The two colours show the symmetric uv -points obtained from the conjugate visibilities.

simultaneously. These solutions were obtained using a high-resolution model of 3C 196 (supplied by V.N. Pandey). The derived solutions on the calibrator were then used to determine the direction independent and time invariant instrumental calibrations including amplitude calibration, correction for clock delays between the core and remote stations. Since each individual sub-band was calibrated separately, this step was done in parallel for all other sub-bands. Then the solutions on the calibrator for individual sub-bands were combined using the LoSoTo package⁶.

- ◆ Bad stations or sub-bands were flagged from the calibrator data by checking for large r.m.s values or gain outliers. If any station(s) had corrupted data these data were flagged and the calibration was re-performed.
- ◆ The effects of clock delays between the core and remote stations (which introduces frequency dependent offsets in the phases), caused by the unsynchronised clocks of the remote stations with respect to the core station clock should be removed from the data. In order to do this, the clock values from an observation of a bright calibrator source were derived and the determined solutions were then used to correct the target field observations via BBS. In this step, the clock-TEC separation technique (van Weeren et al. 2016), fitting the phase solutions of the calibrator along the frequency axis for the clock and TEC terms, was used to separate the clock errors from the ionospheric effects. Figures 5.4 and 5.5 show the phase offsets between stations, the fitted clock and TEC differences based on the calibrator (3C 196) for the SW field observations.
- ◆ Following the clock-TEC separation, the determined clock and phase offset values were transferred along with the gain amplitudes to the target field data for each sub-band. The derived TEC values were not transferred because the ionosphere varies as a function of direction and it is expected to be different for the target field.
- ◆ The target field sub-bands, corrected for the clock, were concatenated into bands of ten sub-bands each. Each band has a bandwidth about 2 MHz and 20 channels. Concatenating sub-bands provides high enough S/N on the target field to be able to carry out the phase calibration for individual concatenated bands.

⁶<https://github.com/revoltek/losoto>



Figure 5.4: The phase offsets between XX and YY phases for the stations for the SW field observations.

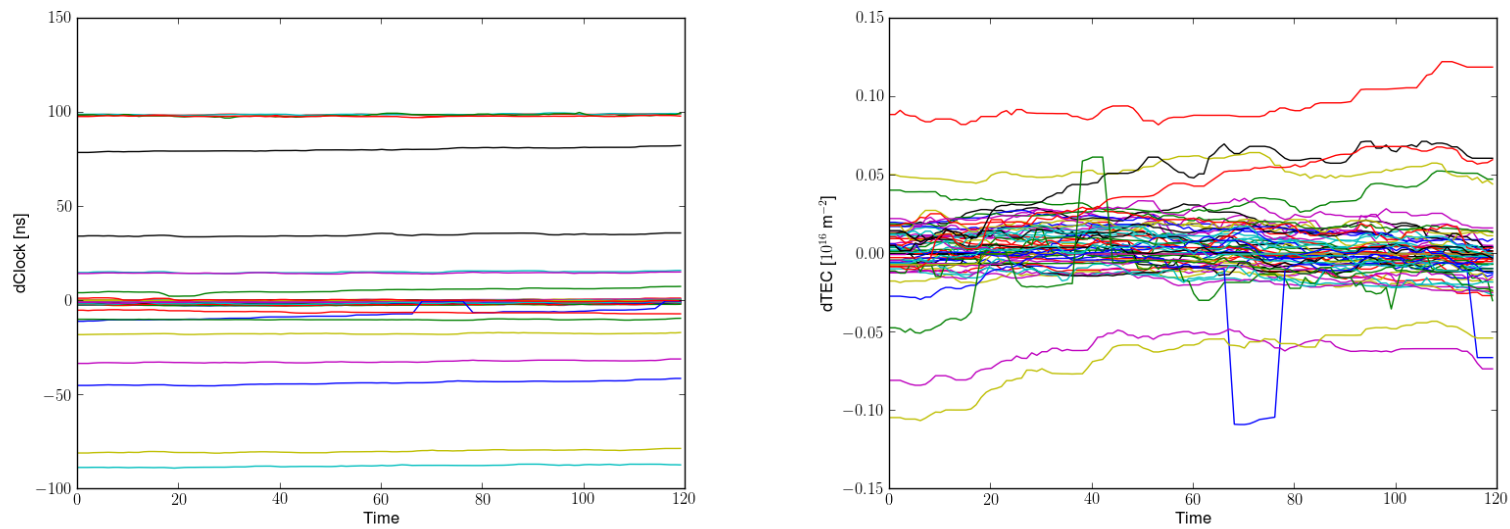


Figure 5.5: The fitted clock (left panel) and TEC differences (right panel) as a function of time (in seconds) based on the calibrator (3C 196) for the SW field observations.

- ◆ Initially phase calibration was performed for the data at frequencies of 150-152 MHz (band 20—the most stable frequency range for the HBA, e.g. Fig. 5.2) using the LOFAR ‘Global Sky Model (GSM)’ which was generated by low-resolution observations from other telescopes.
- ◆ This band was then imaged using AWIMAGER (Tasse et al. 2013), which can perform a beam correction across the field-of-view, at ~ 10 arcsec resolution. A catalogue of Gaussian sources was compiled from the image with the Python Blob Detection and Source Measurement software (PYBDSM). PYBDSM is a tool designed to extract sources by processing radio interferometric images and provide some properties of these sources such as the total and peak flux densities, the position angle of the major axis of the source etc. PYBDSM calculates background r.m.s. and mean images, finds islands of emission, fits Gaussians to the islands, and groups the Gaussians into sources. Furthermore, the task called “process_image” encompasses a number of modules that allow for decomposing an image into shapelets, calculating source spectral indices, deriving source polarization properties, and correcting for PSF variations across the image. For comprehensive information I refer the reader to the PYBDSM documentation⁷. Cross-matching this catalogue with the FIRST catalogue provided a list of sources detected both at 1.4 GHz and 150 MHz. This cross-matched catalogue was later used for phase-only self calibration.
- ◆ Before the phase-only calibration, RFICONSOLE was performed again on each band in order to remove lower-level RFI.
- ◆ The data were then averaged by a factor of two in time and frequency in order to improve the computational speed in the direction-dependent calibration. Each band is around 30 GB.
- ◆ Using BBS an initial phase-only calibration was performed for each band in parallel using the cross-matched catalogue.
- ◆ After the phase-only calibration, the data were corrected for the effect of the array beam using BBS and each band was imaged using WSCLEAN (Offringa et al. 2014) as the station beam correction was not applied at this stage.

⁷<http://www.astron.nl/citt/PyBDSM/index.html>

- ◆ In the final step before the direction-dependent calibration, the detected sources were subtracted from the band images using a two step approach as described by van Weeren et al. (2016). Briefly the process is the following: The clean components were subtracted and then the subtracted data were re-imaged at a lower resolution in order to detect faint sources in the sidelobes of the beam as well as low-surface brightness emission in the map. The clean components in the low-resolution images were subtracted with the direction independent self-calibration solutions in the same way as the high-resolution image components and a list of clean components for the high- and low-resolution images was obtained.

The final data products are 24 sets of 2 MHz residual data sets between 126 MHz and 173 MHz and 24 sets of clean components of the sources that were subtracted. All these data sets were used as input in the direction dependent calibration which is described below.

5.4.2 Direction-dependent Calibration (‘Facet’ Calibration)

The facet calibration was done in a slightly different manner from that described by van Weeren et al. (2016).

Images for each separate frequency ranges (spectral window) were produced in order to derive in-band spectral indices for detected sources and the facet calibration was run in parallel for the spectral windows (six spectral windows of which each has four bands, giving ~ 8 MHz bandwidth in total, Table. 5.4) which helped to speed up the process. In addition to this, the bands with frequencies lower than 126 MHz (the sensitivity at this range is worse than the higher HBA bands) and higher than 173 MHz (after flagging these were still badly affected by RFI) were discarded. The final data contain ~ 48 MHz in total. Table 5.4 shows the spectral windows, frequencies and the LOFAR sub-band/band numbers.

The following were taken for the facet calibration:

- ❖ Firstly, the high resolution maps were divided into facets (van Weeren et al. 2016). In order to perform this, square regions (with a size less than 50×50 arcmin) containing bright calibrator sources were selected depending on the number of sources available. Each region was chosen to contain sources with a total flux density normally greater than 0.4 Jy (apparent) at 150 MHz. Around 20-30 calibrator regions were chosen for each pointing, then the boundaries of these facets were formed using Voronoi tessellation (e.g. Okabe 2000).

Spectral window	Frequency range (MHz)	Band numbers	Sub-band numbers
1	126-134	8-11	80-119
2	134-142	12-15	120-159
3	142-150	16-19	160-169
4	150-158	20-23	200-239
5	158-166	24-27	240-279
6	166-173	28-31	280-319

Table 5.4: Spectral windows, frequencies and LOFAR band/sub-band numbers used.

✿ Then a self calibration process was performed for each calibrator region. Initially the facet calibration process was run for the data ranging between 150 and 158 MHz for each pointing. This allowed us to check that the chosen calibrators gave sufficiently good solutions and the residuals decreased after subtraction. In the case of such problems, either the size of the calibration region was increased in order to include more sources, or the phase/amplitude solution interval was increased. Once these issues were addressed the same calibration processes were implemented in parallel for the other spectral windows. Fig. 5.6 shows an example of a mosaicked LOFAR map of one of the pointings together with the calibrator groups and the facets.

It typically took 4-5 hours on a 16-core node to complete the self-calibration, imaging and subtraction step for one facet in one spectral window. The duration of these processes per pointing varied depending on the number of facets and the number of problems encountered. Thus, the overall process, for the six spectral windows, took between one and two weeks per pointing.

Once the facet calibration and imaging were completed the spectral window images were combined to form a mosaic image. In order to measure real sky fluxes a beam correction was applied to these images: AWIMAGER was used to make an image of the primary beam for each band. The images of each spectral window were divided by these. In the course of this procedure, MONTAGE was utilised in order to re-grid the band images to the scale of the facet calibration images. This process provided maps with the true flux densities of the sources. Fig. 5.7 shows map of the SW pointing and in Fig. 5.8 I show a zoomed version of the rectangular region seen in Fig. 5.7.

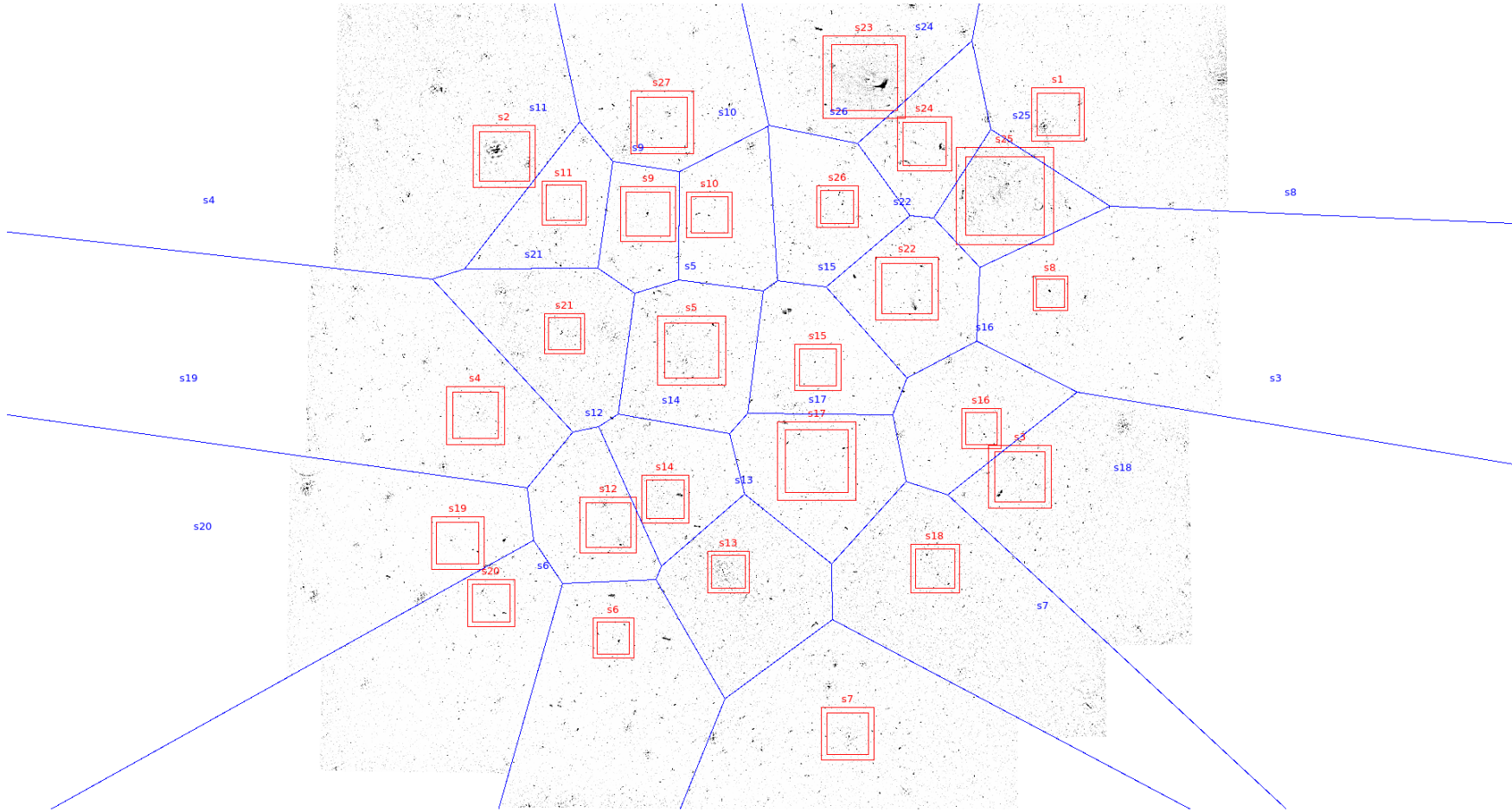


Figure 5.6: *LOFAR* map of the south-west corner of the H-ATLAS NGP field. Red squares show the calibrator regions selected based on bright sources and blue regions show the facets that were generated by Voronoi tessellation.

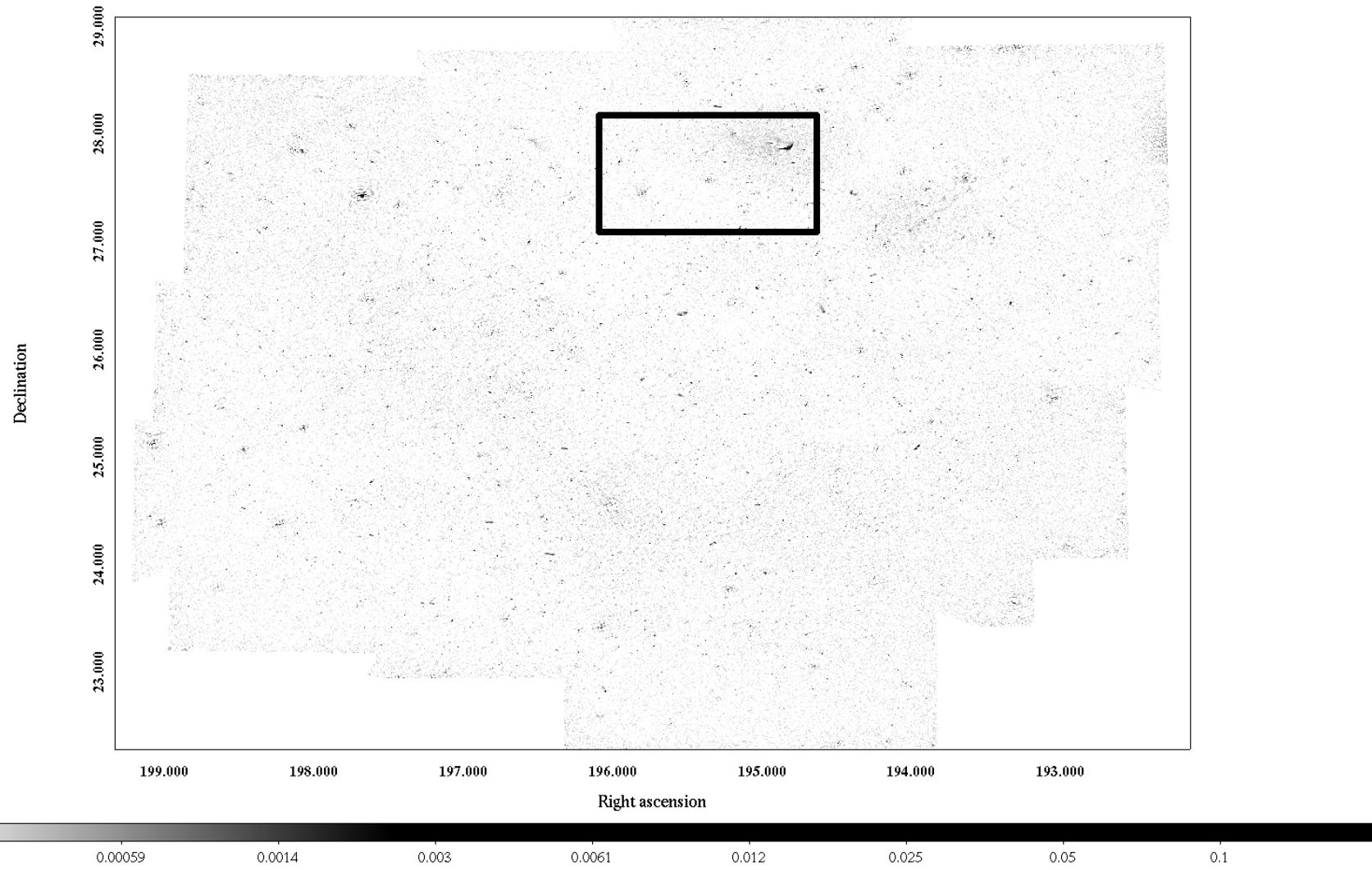


Figure 5.7: LOFAR map of the SW field of the NGP field.

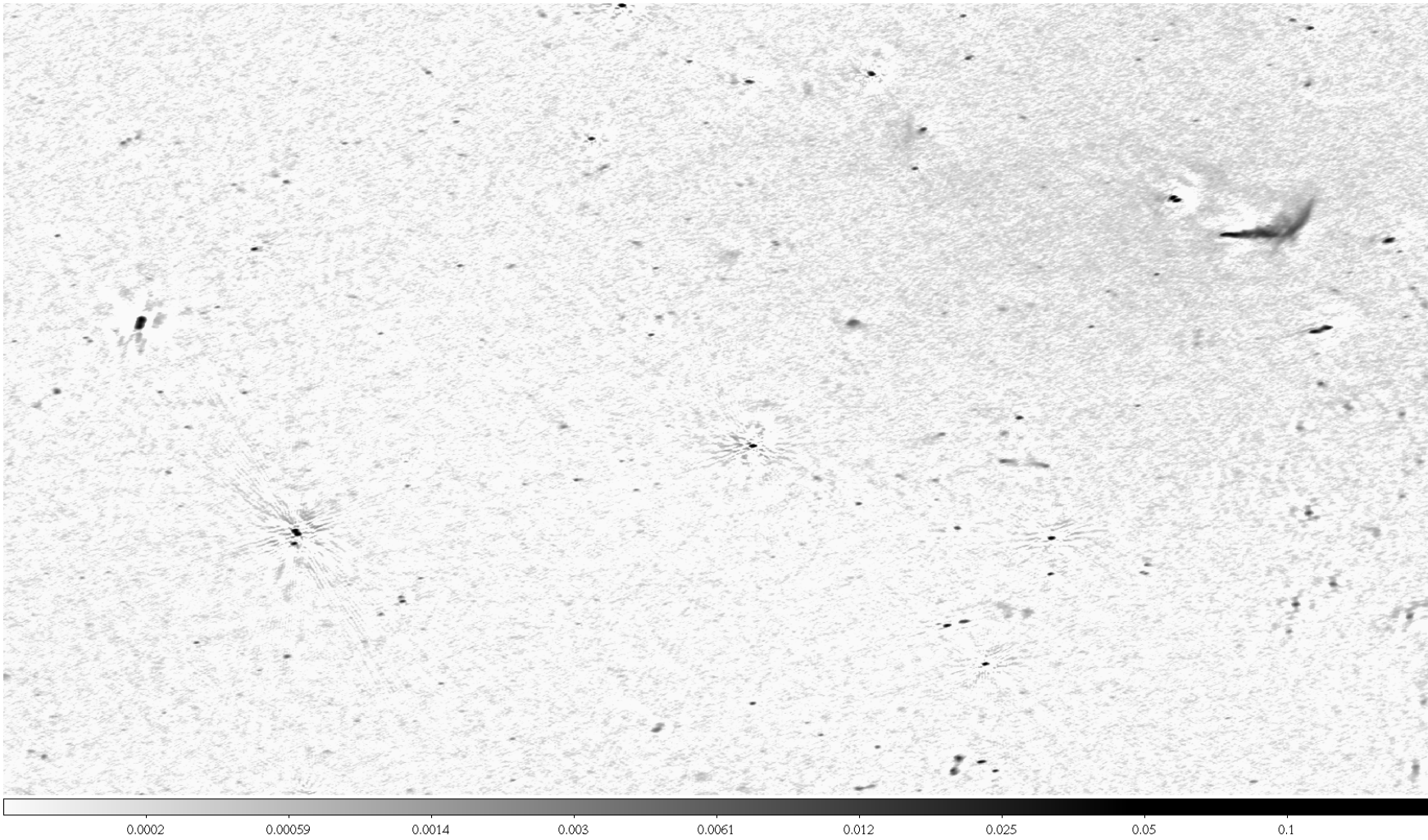


Figure 5.8: Zoomed version of the rectangular region showed in Fig. 5.7. On the upper right corner a part of the Coma cluster is seen.

5.5 Evaluation of the image quality

As mentioned above, the aim of the facet calibration is to produce low-frequency radio images that can reach to a depth of ~ 0.1 mJy beam $^{-1}$ (i.e. the Tier-1 survey depth, Röttgering et al. 2006) at around 5 arcsec resolution (van Weeren et al. 2016). Although a few facets failed, the facet calibration on average provided good quality of maps. As can be seen in Table 5.5, the central r.m.s. values are very close to the targeted r.m.s. value.

There are still artefacts (i.e. dynamic range limitation around bright sources) in these maps. This is because the amplitude self-calibration was not performed for every bright source. However, the quality of the catalogue is not expected to be strongly affected by this. As can be clearly seen in Fig. 5.9 a few facets failed the facet calibration at the edge of the maps of the NE and Central fields and these were discarded. For a source with a spectral index of $\alpha=0.7$, the expected r.m.s. values for FIRST and NVSS would be 0.8 and 2.4 mJy beam $^{-1}$ respectively. The LOFAR survey is therefore deeper than the NVSS survey and much deeper than the FIRST survey in the central 50 percent of the field. The GMRT survey of the equatorial H-ATLAS fields (Mauch et al. 2013) has a best r.m.s. value of 1 mJy beam $^{-1}$ at 325 MHz, corresponding to 1.8 mJy beam $^{-1}$ at 150 MHz. Thus, the LOFAR survey has also provided better data for this field than the GMRT did for the equatorial fields. Fig. 5.10 shows the cumulative histogram of the area below a given r.m.s. value, calculated from the r.m.s. maps.

Field	Area covered (sq. deg.)	central r.m.s. (μ Jy)	Median r.m.s. (μ Jy)	Image resolution (arcsec)	Catalogued sources
Central	44.5	223	782	9.62×7.02	2,473
NW	34.7	104	296	10.01×5.54	5,335
SW	36.1	111	319	9.87×5.49	5,747
NE	40.6	100	382	11.02×4.68	4,172

Table 5.5: Details of the LOFAR pointings. From left to right columns are: Name of the field, covered area, central r.m.s. noise of the pointing, median r.m.s. noise of the pointing, image resolution and the number of sources detected in each field map.

The Central field has the worst data in terms of noise although the data reduction was performed in the same way as the other fields. The observations of this field were the only ones carried out in Cycle 0. Additionally, a few bright sources (such as 3C 286, 3C 287 and 3C 284) are a couple of degrees away from the pointing centre of this field. The reason for the relatively poorer image obtained for this field is probably a combination of these.

5.6 The LOFAR catalogue of the H-ATLAS NGP field

5.6.1 The raw catalogue

After completing the facet calibration and imaging for all spectral windows of the four pointings, the beam corrected images of individual spectral windows were convolved to the same resolution using MIRIAD and concatenated to compose a single data cube. Then PYBDSM was used in its spectral window mode to extract flux densities of radio sources detected in each ‘channel’ of the cube. Since the concatenated broadband image without beam correction is expected to have roughly uniform noise across the field, this was used as a detection image. Flux densities are measured from matched apertures in each spectral window by using the spectral window mode of PYBDSM.

LOFAR flux calibration is problematic: since the calibrator and source are not at the same elevation the gain normalisation transferred from the calibrator to the source is not valid. Because of the flux calibration issue the measured flux densities using the frequency-averaged images as well as the individual channel flux densities are expected to be slightly offset (i.e. frequency-dependent flux scale problem). In order to correct for the flux scale problem other low-frequency surveys were utilised. Details of this procedure are given by Hardcastle et al 2016.

The raw LOFAR catalogue was filtered to select bright sources (>0.1 Jy) and these were positionally cross-matched with the VLSS, B2, WENSS and WSRT-Coma catalogues using STILTS. Throughout this process it was required that all of the LOFAR sources should be detected in VLSS and at least one of the three higher-frequency catalogues for further consideration. This gave around 60 matched sources per pointing. Then the LOFAR flux correction factors for each frequency were fitted and the derived factors from this process are given in Table 5.6. These correction factors were applied to the images and a new combined image at an effective frequency of 150 MHz, was generated.

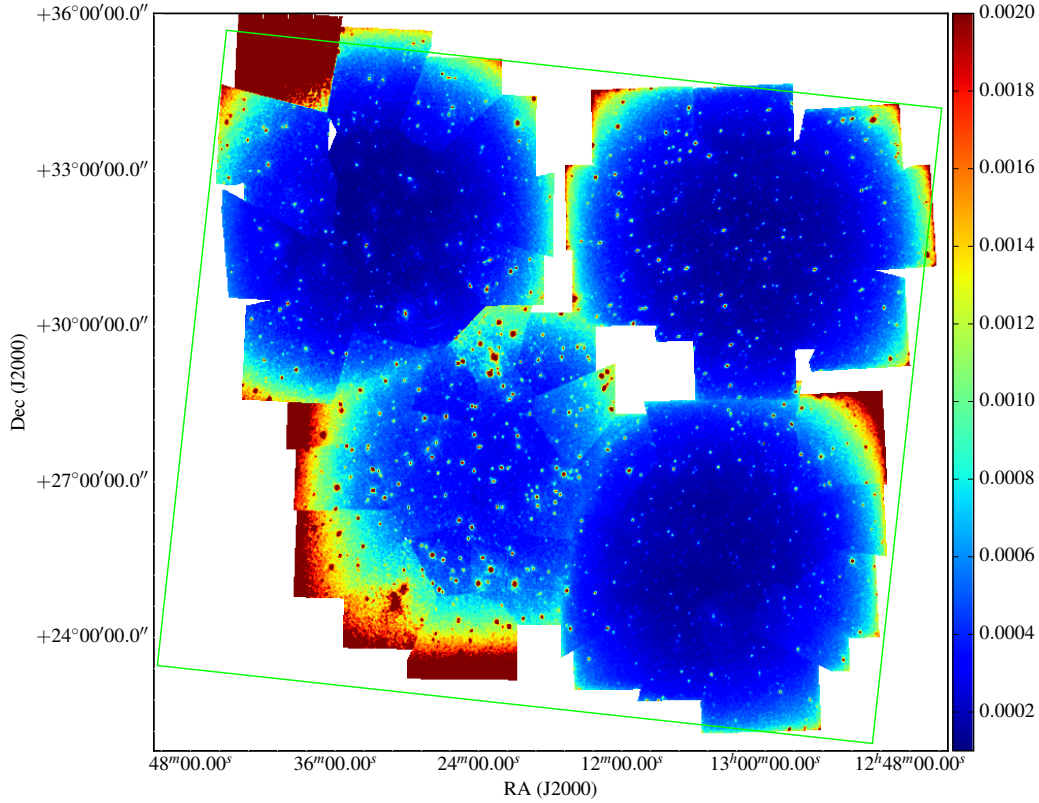


Figure 5.9: Map showing the sky coverage and r.m.s. values of the four facets, constructed as described in the text. Colour levels run from $100 \mu\text{Jy}$ to 2 mJy beam^{-1} . The green square shows the approximate boundary of the Herschel survey. The LOFAR survey is deeper than FIRST, the previous most sensitive radio survey of this area, in the blue regions of the image. The many ‘point-like sources’ in the image are the result of dynamic range limitations around bright objects, rather than the objects themselves: the pixel size in this image is 20 arcsec, significantly larger than the image resolution (Hardcastle et al. 2016).

Field	Spectral window number						Mean elevation	
	1	2	3	4	5	6	3C 196	Field
Central	1.02	1.08	1.17	1.29	1.42	1.52	85.3	51.6
NW	0.97	1.03	1.07	1.14	1.21	1.30	82.2	58.6
SW	0.93	1.00	1.09	1.17	1.29	1.34	82.4	53.4
NE	0.72	0.75	0.79	0.84	0.89	0.92	78.2	58.9

Table 5.6: Correction factors applied per field and spectral window, main calibrator and the target elevators.

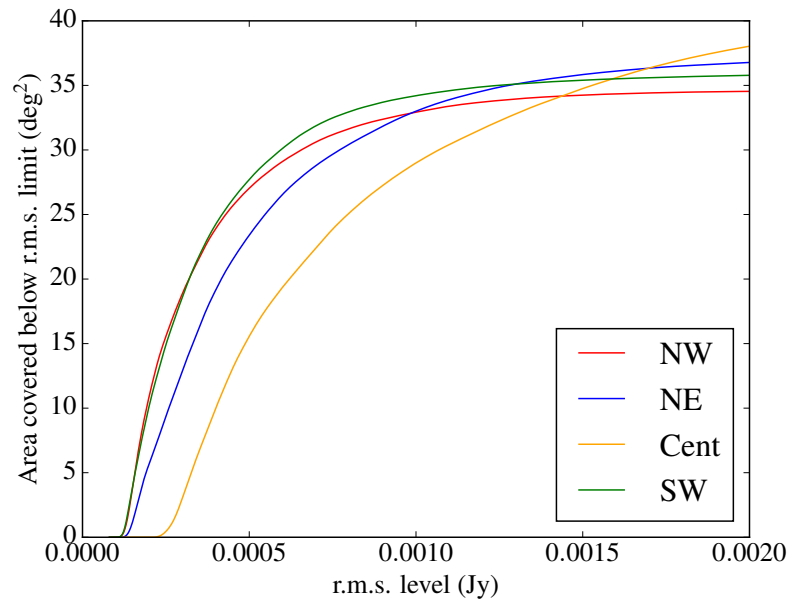


Figure 5.10: Cumulative histogram of the area below a given r.m.s. value, calculated from the r.m.s. maps.

5.6.2 The final catalogue

The corrected images of the four LOFAR pointings were used to generate a catalogue of detected sources. To extract sources in these maps PYBDSM was used in its spectral index mode once again. The ‘trous’ wavelet decomposition module was also used while cataloguing to recover extended emission and associate several sources as a single detection in the map by decomposing the residual image that results from the normal fitting of Gaussians into wavelet images of various scales. The cataloguing threshold was chosen to be 5σ . The final survey products are the catalogues of detected sources for each field at 150 MHz (contains flux densities at 150 MHz) and the catalogues of detected sources for each field in individual spectral windows (contains flux densities of sources detected at individual spectral windows, up to 6 windows). PYBDSM was also used to produce maps of the r.m.s. of the images. Figure 5.9 shows the sky coverage and r.m.s. values of the four pointings. The final catalogue has 17,132 sources covering 42.7 square degrees.

5.7 Source associations and optical identifications

Before any cross-matching and source classification, a number of quality checks were carried out such as flux scale tests by cross-matching the LOFAR/NGP catalogue with various catalogues, positional accuracy tests by cross-matching the LOFAR/NGP catalogue with the FIRST catalogue and evaluation of the in-band spectral indices. Details of all these examinations are given by Hardcastle et al. (2016).

5.7.1 Initial cross-matching

Initially in order to select single, compact LOFAR sources (i.e. non-AGN objects) I positionally cross-matched the MPA-JHU catalogue with the final LOFAR catalogue within a search radius of 8 arcsec. These objects are mostly observed as point sources by LOFAR unless the optical counterpart is a very close disk galaxy so their optical positions are expected to exactly match with the LOFAR positions. The number of sources selected by this process is 1048.

5.7.2 Source associations

In order to use the remaining sources in the catalogue for scientific purposes some additional processes were implemented.

As described in the general introduction of this thesis radio sources present extended emission for example jets and lobes. We also expect to see the plumes associated with FR I type radio objects. Some examples of these extended sources are shown in Fig. 5.11. If these structures are resolved by the telescope's beam then these components have to be treated properly. Therefore, firstly sources with multiple components were identified and treated. In order to obtain the true flux density of such sources, components associated with that source should be identified. The detection image (the LOFAR image in this case) only is not sufficient to carry out this task so some auxiliary data are necessary.

In the process of associating the components of these sources the radio core information becomes important. Radio cores are the unresolved pre-scale jets of radio sources, associated with the nucleus of radio galaxies and radio quasars (see Chapter 1 for detailed information). Since the core has a flat (or flatter than the radio lobes) radio spectrum high frequency radio observations may give us information about the radio cores of the radio sources detected by LOFAR. While associating multi components of

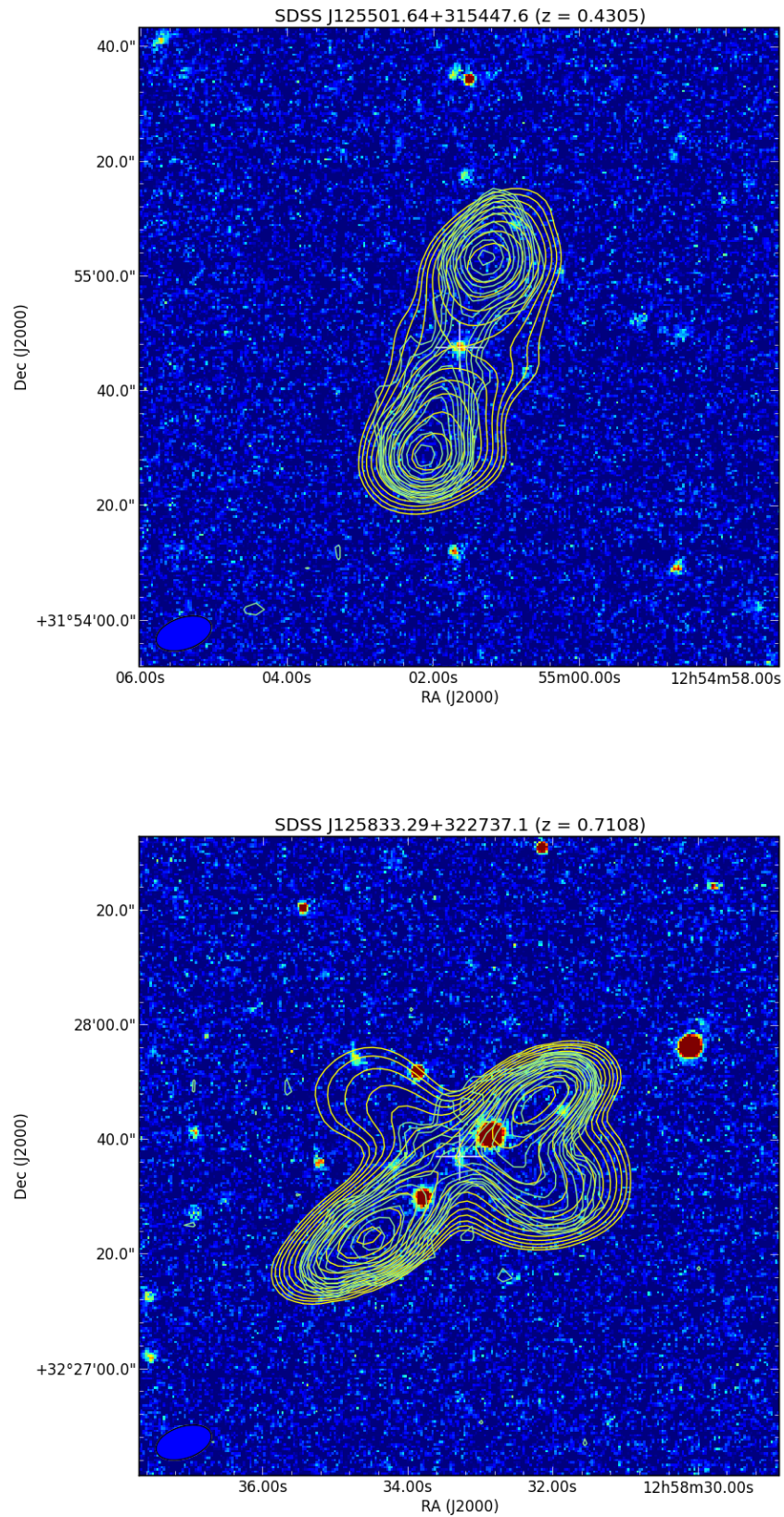


Figure 5.11: Examples SDSS *r*-band images of extended sources radio contours overlaid (the yellow contours indicate the LOFAR and the green contours are from FIRST). The white cross indicates the optical counterpart of the radio source.

radio sources the FIRST images of these sources were utilised. Detailed information about this survey is given in Chapter 2.

NVSS images were also used in the process of associating components of sources as NVSS is sensitive to extended emission like LOFAR, but has much lower resolution. Thus, these images were used to confirm the reality of faint extended LOFAR sources, which are expected to be visible in the NVSS maps. Detailed information about this survey is given in Chapter 2.

5.7.3 Optical identification of sources

In order to use the LOFAR catalogue for further science the identification of optical counterparts of the detected LOFAR sources was carried out. Naturally optical data are necessary to implement this task and I used the r -band frame corrected images from SDSS DR7 (Abazajian et al. 2009). Together with the optical identifications optical (u, g, r, i, z) band magnitudes of these sources, their spectroscopic redshifts (where available) and photometric redshifts were obtained.

Source association and optical identification require a visual inspection of these sources using the additional data mentioned above. In order to achieve these goals I developed software to display the LOFAR, SDSS, FIRST and NVSS fits images of each source using the astronomical imaging and data visualisation application SAOImage DS9, loading DS9 regions and interactively storing information for a given source.

The detailed steps of this process are as follows:

- ◆ For a given right ascension (RA) and declination (DEC) of each source detected by LOFAR, the programme displays the LOFAR field image and shifts it in order to place the source in the centre. It then loads a region file which was generated using the LOFAR field catalogue and displays unique names for each source. The unique names are used to store all information about sources in the new catalogue.
- ◆ The software finds the right SDSS r -band image of the source, gets a cut-out and displays it. Then it loads a region file that is generated by the program using the SDSS catalogue overlapping with the H-ATLAS NGP field. The SDSS catalogue includes all sources from the SDSS DR7 that were classified as galaxies, stars or unknown by the SDSS pipeline. I also combined this catalogue with the HMQ catalogue (Flesch 2015) to be able to identify possible quasars associated with the detected LOFAR sources.

- ◆ It then finds the corresponding FIRST image of the LOFAR source to be classified, displays it and shifts the image in order to place the FIRST counterpart in the centre.
- ◆ The software finds the corresponding NVSS image of the LOFAR source to be classified and it perform the same process as for the FIRST image, using the NVSS image.
- ◆ In order, the software asks a number of questions to the person carrying out the visual inspection (the classifier) to enter information about the source and its optical identification. The software first asks whether the source is a single source, multi-component source or an artefact.
 1. If a source is single or an artefact it asks if the classifier wants to leave any comment regarding this classification. This question was particularly useful for the sources whose optical counterparts were not certain. It then asks the question related to its optical identification. It initially asks the classifier to enter the number of possible optical counterparts. Afterwards, it asks for the source names (i.e. assigned unique names while the region file was generated) of possible optical counterparts. A unique SDSS identity (ID) number of a given optical counterpart is stored by entering the assigned region name.
 2. If a source is a multi-component radio source then the program asks the number of components that source has and their unique names to be entered. Then the above steps are taken to complete the classification of the source (i.e. leaving a comment, entering the number of optical identifications and their unique names).
- ◆ All entries are saved as a new catalogue generated by this process. Figs. 5.12, 5.13, 5.14, 5.15 and 5.16 show example screen-shots of the classification process.

The generated catalogue was processed in order to obtain the flux densities at 150 MHz and some other LOFAR measurements. In the course of this process the flux densities of the multi-component sources were summed and the average positions of these were calculated and stored. The final catalogue has information about the source classification (single, multi-component and artefact), the

Classification	Count	Single SDSS ID	Multiple SDSS ID
Single	13943	6275	7668
Multi-component	1349	713	636
Artefact	179	—	—

Table 5.7: The number of sources classified in the LOFAR/NGP catalogue as a single source, multiple-component or artefacts together with the number of optical identifications.

unique DR7 SDSS IDs if the source has an optical counterpart (or more than one optical counterpart) and the corresponding LOFAR measurements. Sources that have more than one optical counterpart were not used in the rest of the analysis as further observations are required in order to disambiguate these sources.

Over the course of classification the following selection criteria were followed:

- ✧ Whenever there was a possible optical counterpart, that source and its optical counterpart(s) was stored. If it was not certain whether the optical source was a counterpart of the source classified then the classifier left a comment explaining this.
- ✧ No decision was made based on only the NVSS images. The flat-spectrum core emission (if it was observed) in the FIRST map positionally matched with the position of the optical counterpart assisted the classification procedure.
- ✧ If a source was not real then it was classified as an artefact.

As a result of the association and optical identification 15471 sources were identified in the catalogue. Some source statistics are given in Table 5.7.

Assessment of the classification

Evaluation of the identifications was performed using overlapping regions between the fields. Sources in these regions were identified and this gave 298 sources in total. Then, their identifications were cross-checked and this showed that 82 per cent of them had the same optical identifications (excluding sources with no optical identifications). In terms of the classification of sources (i.e. as a single source, multi-component or an artefact), 89 per cent of them had the same classification.

Classification and the optical identification of one of the fields was also performed by another person to be able to evaluate the process of identification and classification.

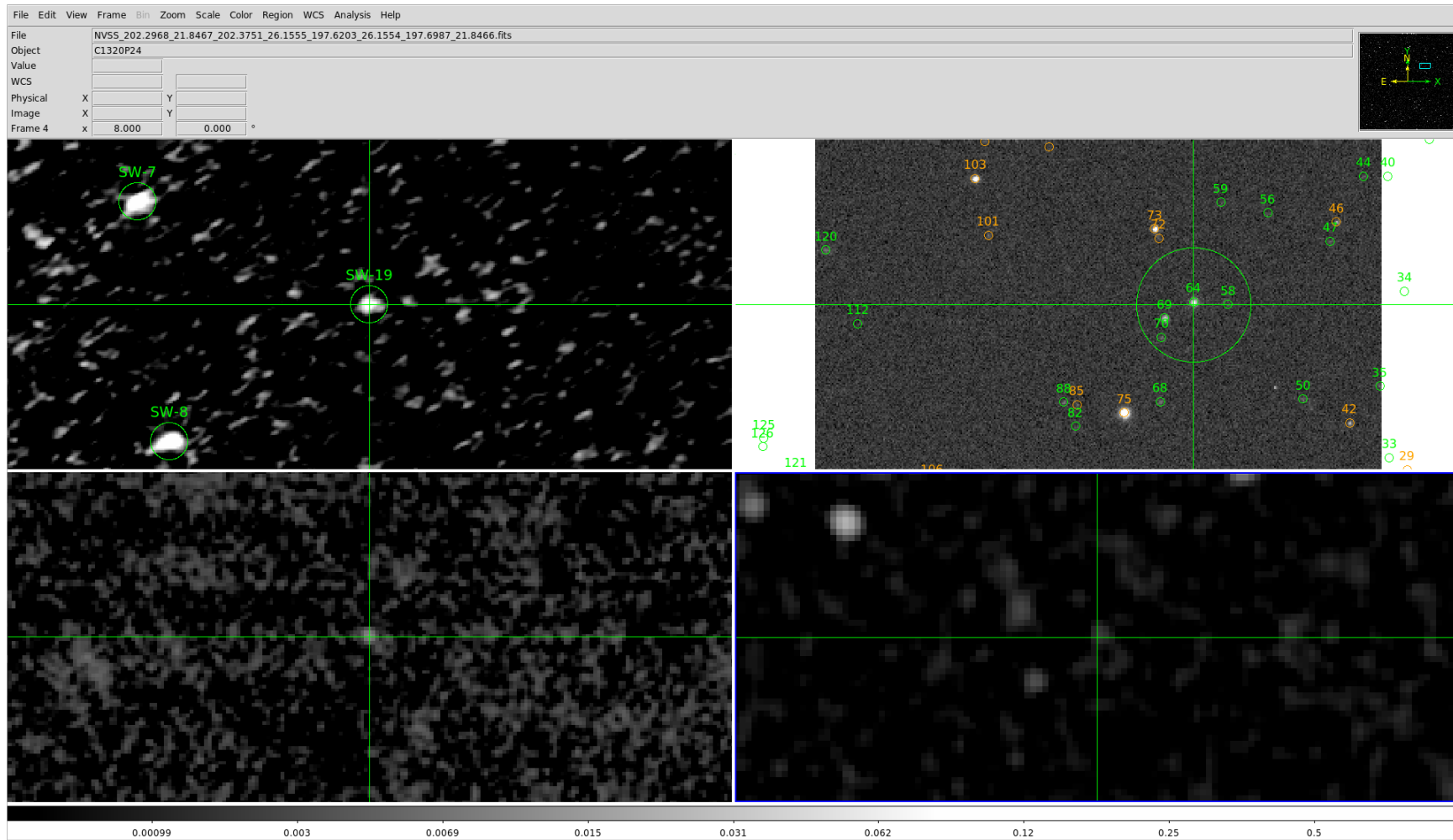


Figure 5.12: Example of a classification process: a single source case. Top-left: LOFAR map, a single component source is in the centre with a unique name (e.g. SW-19). Top-right: SDSS r -band image showing optical sources in the region (with assigned unique names). Bottom-left: FIRST map showing the source region. Bottom-right: NVSS map showing the source region.

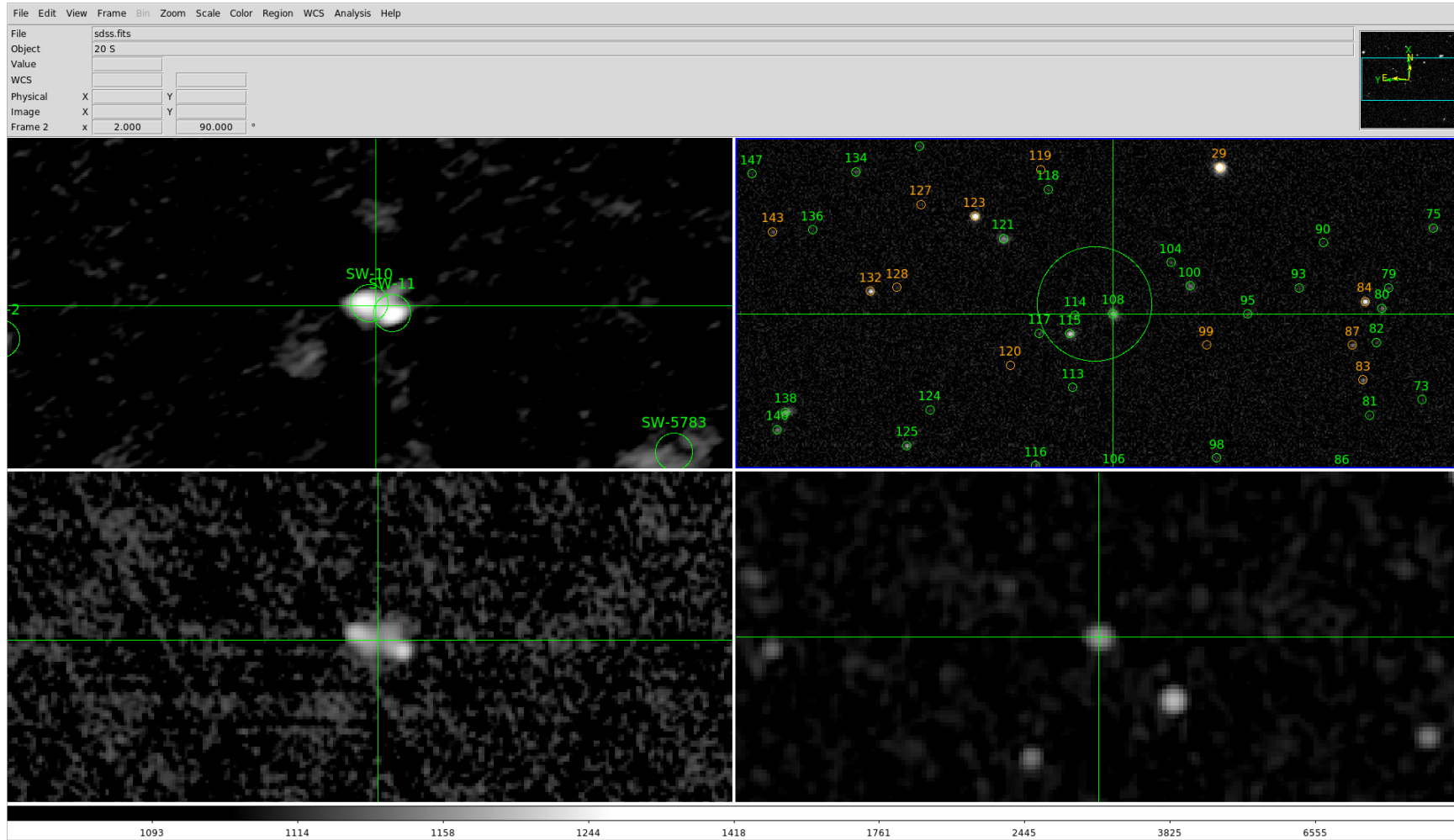


Figure 5.13: Example of a classification process: a multiple-component source case. The maps are the same with Fig. 5.12.

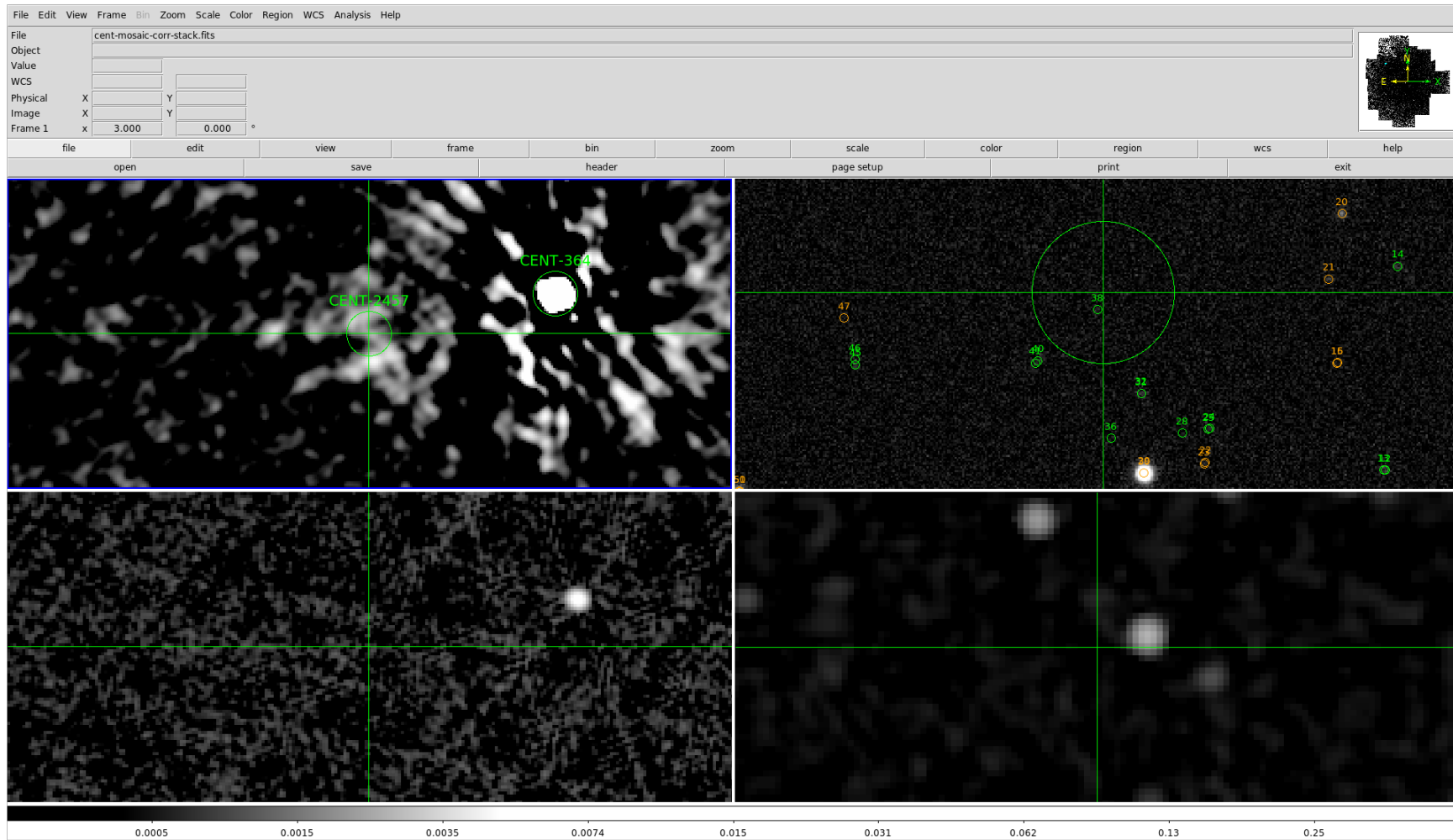


Figure 5.14: Example of a classification process: a case of an artefact. The maps are the same with Fig. 5.12.

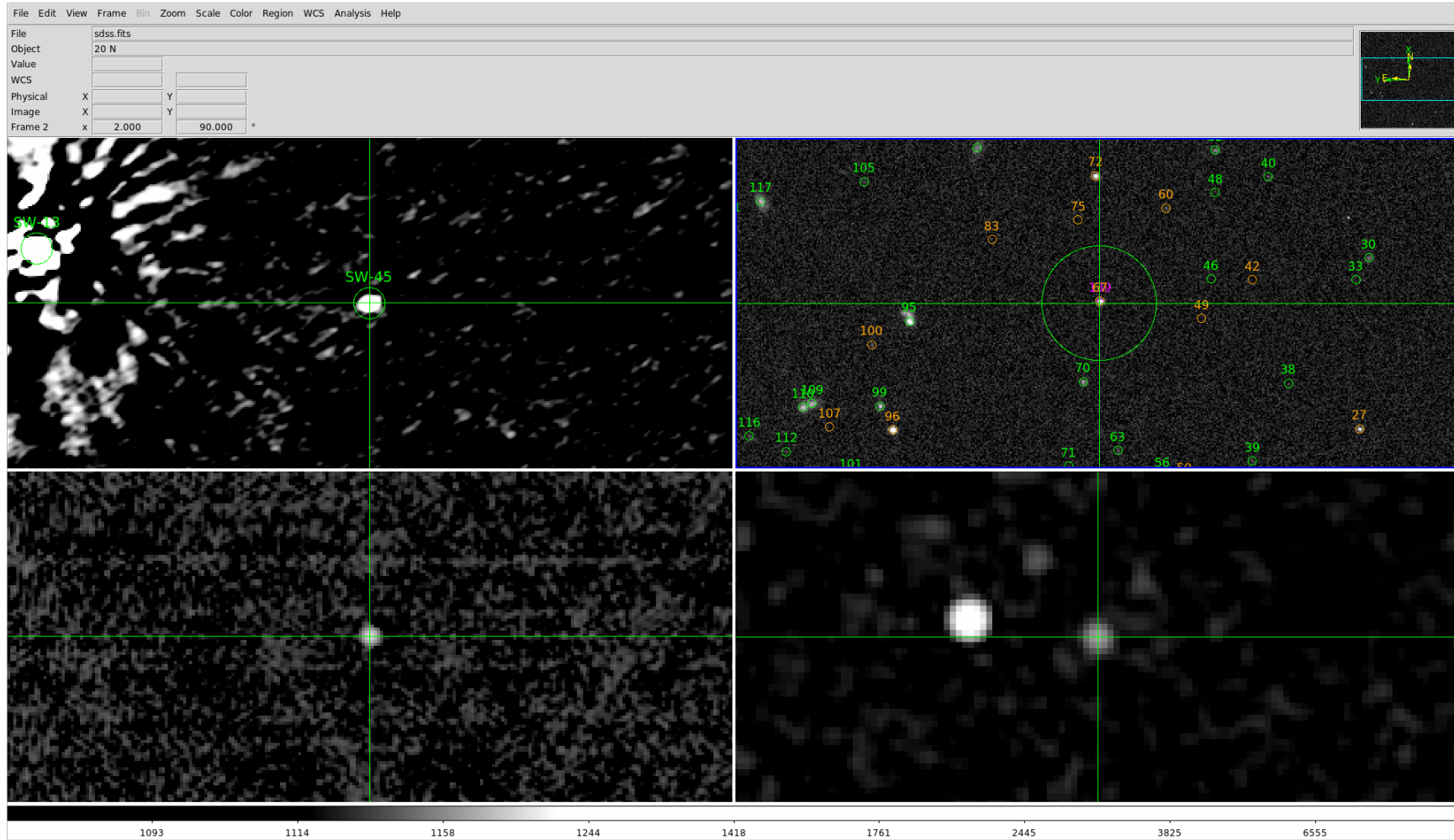


Figure 5.15: Example of a classification process: a case of a quasar counterpart. The maps are the same with Fig. 5.12.

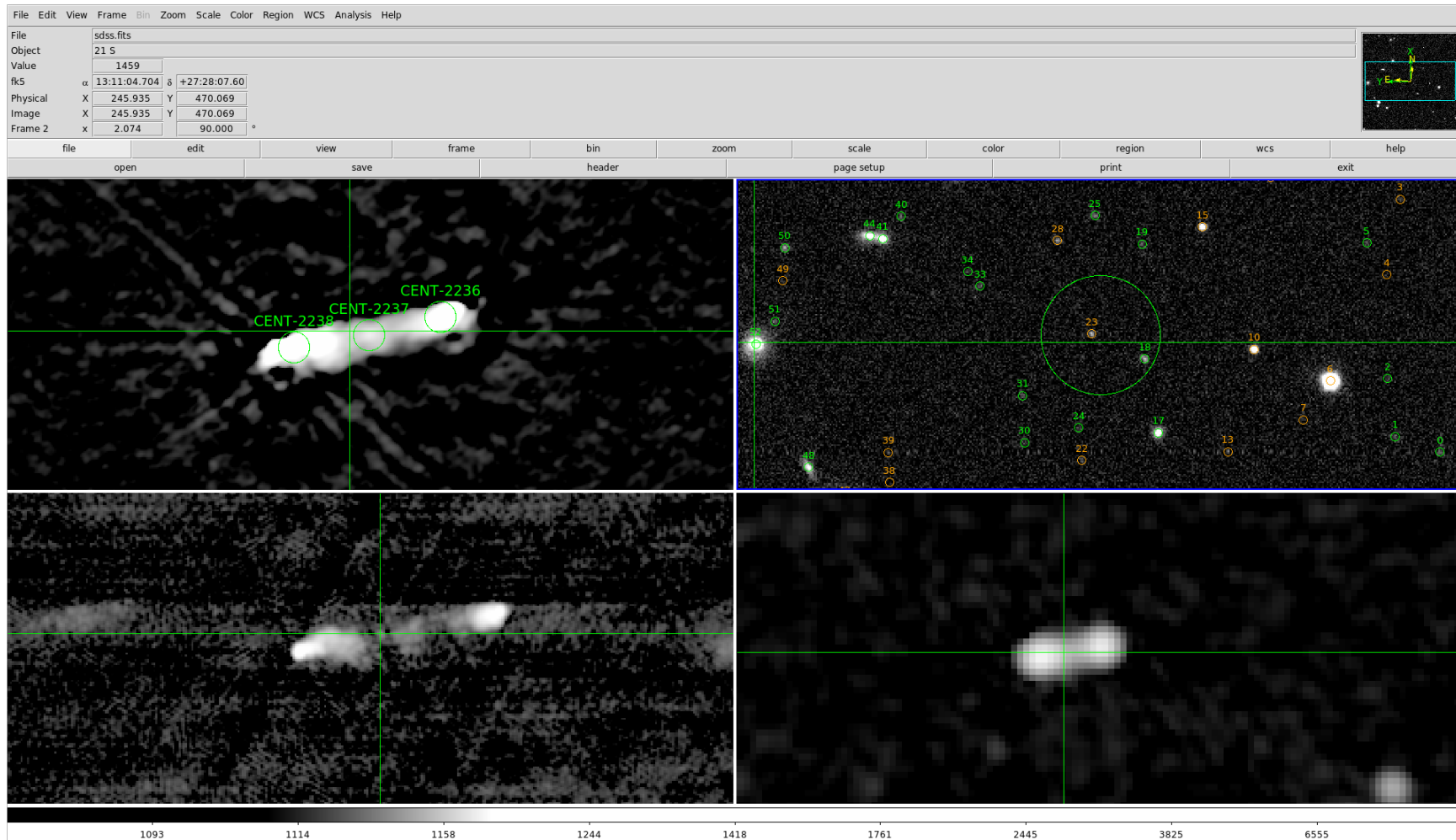


Figure 5.16: Example of a classification process: 3C284, resolved by the LOFAR and FIRST, is in the centre of the LOFAR, FIRST and NVSS maps. The maps are the same with Fig. 5.12.

Assessment of the same procedure of this field showed that 98 per cent of the sources with optical identifications had the same optical ID and 95 per cent of the sources had the same classification.

These results show that most of the time classifications and optical identifications agree with each other and this process provided reliable results. It is important to note that there may well be misidentifications, where a plausible foreground object is identified as the host instead of a true unseen background source, because of using shallow optical images for the process of optical identification. This is expected, in particular if the LOFAR source is large and no FIRST counterpart is seen. We cannot assess the level of such misidentifications in our catalogue. However, since most sources are not large in angular size we expect it to be low. Sensitive high-frequency imaging over the field, and/or deeper optical observations, would be needed to make further progress.

5.7.4 Spectroscopic/photometric redshifts and optical magnitudes

In order to obtain spectroscopic/photometric redshifts and optical magnitudes, the twelfth data release (DR12; Alam et al. 2015) of the SDSS catalogue was used. In SDSS DR8 and the subsequent data releases the designed unique SDSS IDs changed. Since the DR7 unique SDSS IDs were stored in the catalogue produced by the classification process I initially obtained the SDSS DR12 unique IDs of the sources which have DR7 IDs. From this 195 sources with DR7 IDs did not have matches in the DR12 catalogue. The reason for this is that the DR12 and later releases was processed with a different version of the pipeline, so if a source is around large, nearby galaxies or bright stars that source may not be present in the DR8 catalogue⁸. I made a random selection of these sources (~ 300) and consulted the SDSS images. This also showed that almost exclusively all sources were found to be either around a large, nearby galaxy or a bright star. Some of these unmatched sources were recovered by visual inspection (48 of them, Section 5.8.5)

Table 5.8 shows the number statistics of sources with spectroscopic (z_{spec}) and photometric redshifts (z_{phot}). The top panel in Fig. 5.17 shows a comparison between the spectroscopic and photometric redshifts and the bottom panel shows the r -band magnitude distribution of the sources as a function of their redshifts (both spectroscopic and photometric redshifts are shown).

⁸<http://www.sdss.org/dr12/imaging/caveats/timeout>

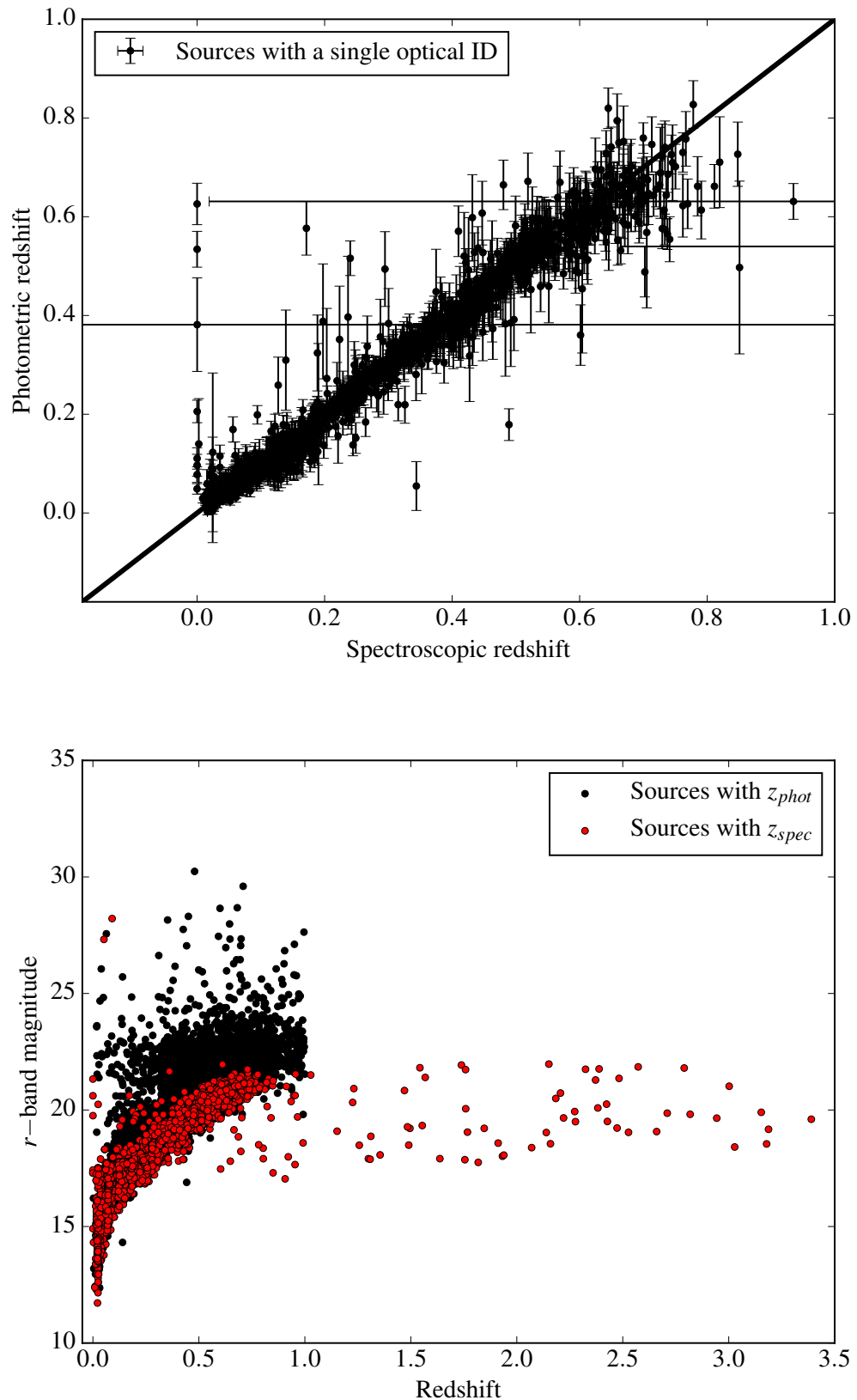


Figure 5.17: The top panel shows the comparison between the photometric and spectroscopic redshifts of sources in the final catalogue. The bottom one presents the r – band magnitude distribution of sources as a function of their redshifts.

Type	Count (z_{spec})	Count (z_{phot})
Galaxies	1856	5549
Quasars	51	84

Table 5.8: The count of sources with spectroscopic (z_{spec}) and photometric (z_{phot}) redshifts.

Radio Quasars

Among the classified sources 135 had quasar counterparts. The HMQ catalogue does not contain unique SDSS ID information, but rather the SDSS names (or some other survey names such as 3C, PKS etc.) are given. The majority of quasars in the HMQ catalogue are sourced from the SDSS. In the HMQ catalogue there are sources originally classified as stars or non-AGN by their discovery papers that were classified as quasars, and 114 new spectroscopically confirmed quasars. I refer the reader to Flesch (2015) for details about the construction of the HMQ catalogue. In order to obtain the unique SDSS IDs of the 135 quasars I carried out positional cross-matching within 2 arcsec. For the cross-match I used the SDSS positions stored in the catalogue throughout the classification and the SDSS positions given in the SDSS catalogue. Almost exclusively all quasars had matches within 0.2 arcsec. Fig. 5.18 shows the r -band magnitude distribution of radio quasars in the catalogue as a function of their redshifts.

5.7.5 Secondary review of the optical identification

As noted above over the course of the association and optical identification any possible optical identification was stored and the classifier left comments indicating that this may require another check. Since these sources were kept in the catalogue to be used, a secondary review of the classification process was necessary to eliminate any possible wrong optical identification, in particular the extended sources which were used to derive the luminosity function of low redshift AGN. In order to do this, sources with sizes larger than 20 arcsec were selected and the optical images overlaid with the radio contours from the FIRST and LOFAR images were visually inspected. This process gave 32 sources out of 292 with wrong optical identifications. Sources with wrong optical identifications were re-processed to obtain their true optical counterparts or removed from the catalogue altogether.

This catalogue was used to investigate the relation between the low-frequency radio luminosity and far-IR luminosity of AGN, presented in the next chapter. It will also

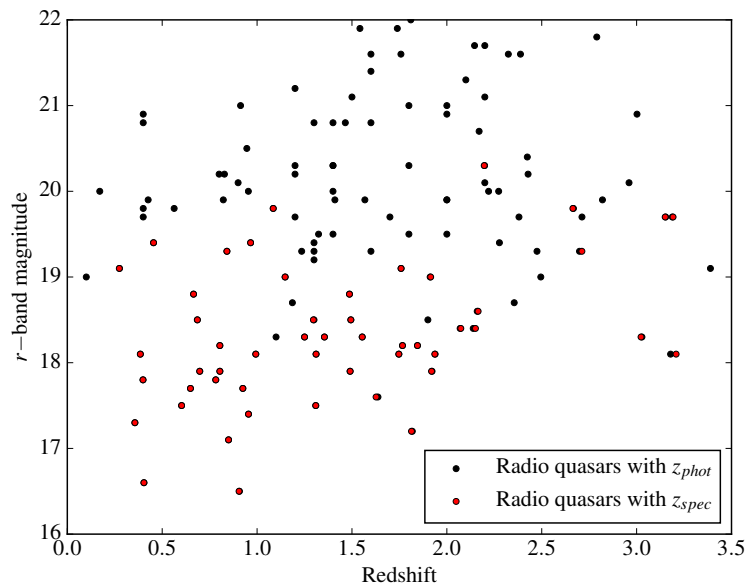


Figure 5.18: The r – $band$ magnitude distribution of radio quasars as a function of their redshifts.

be used to study AGN in detail and to derive the luminosity functions of low redshift AGN and star-forming galaxies: results of this work are presented by Hardcastle et. al (2016).

5.8 Summary and conclusions

The *Herschel*-ATLAS NGP field was observed with the LOFAR as a part of the LOFAR surveys KSP. The data reduction and calibration were performed in two steps: (i) a typical data calibration (independent of the directional effects) was carried out, (ii) a new technique called ‘facet’ calibration, which takes into account the direction effects, was implemented for this field. The final LOFAR images of the H-ATLAS NGP field have an effective frequency of 150 MHz and although the resolution of each pointing is different, it is around 10×5 arcsec. One of the conclusions that can be drawn from this chapter is that LOFAR provides excellent data that can be used for science. Additionally, the facet calibration method improves low-frequency radio images taken by LOFAR, pushing the sensitivity down to $100 \mu\text{Jy beam}^{-1}$ with a resolution of ~ 5 arcsec. This makes it possible to address various interesting questions related to AGN and normal galaxies. The main difficulties of the LOFAR data reduction and the facet

calibration are the computing systems and the time required by this procedure.

The most prominent challenge in the process of gathering a sample of AGN detected in these radio images is that identifying multi-component AGN and the optical counterparts requires visual inspection. This process was carried out in this work and a detailed inspection of the LOFAR/NGP images provided a large sample of AGN (3900 objects with redshifts) and star-forming galaxies (1667 with redshifts) with secure optical identifications, many of which have spectroscopic redshifts provided by SDSS DR12. For the first time, using a large sample of AGN and normal galaxies observed at low radio frequencies the following interesting topics have been investigated:

- The radio power–size relation of active radio galaxies (Hardcastle et al. 2016)
- The low-frequency radio luminosity–SFR relation (Chapter 6)
- The low-frequency radio luminosity–far-IR relation (Chapter 6)

Chapter 6

The low-frequency radio luminosity–SFR relation

“A calm sea does not make a skilled sailor.”

Anonymous

6.1 Abstract

Radio emission is a key indicator of star-formation activity in galaxies, but the relationship between star formation and radio luminosity has to date been studied almost exclusively at 1.4 GHz and above. At lower radio frequencies thermal radio emission becomes increasingly negligible in comparison to high frequencies. Therefore, one might expect to observe deviations from the relations derived earlier. As part of the LOFAR SKSP, the Herschel-ATLAS NGP field was surveyed with LOFAR at an effective frequency of 150 MHz. A sample of galaxies is selected from the MPA-JHU value-added catalogue of SDSS galaxies in this area: the combination of *Herschel*, optical data and available infrared data provides excellent constraints on star-formation rates (SFRs), allowing a detailed study of the low-frequency radio/star-formation relation in the nearby universe. I show that the slope of L_{150}/SFR is less than unity and not universal for all star-forming galaxies (SFGs) in the local Universe ($0 < z < 0.3$). The slope of L_{150}/SFR relation is also found to be steeper than the $L_{1.4}/SFR$ relation, probably due to the contribution from thermal radio emission at 1.4 GHz. If the L_{150}/SFR relation is explained naively by electron calorimetry, I conclude that

low luminosity sources are not ideal calorimeters and differ from the main locus of SFGs at low redshifts. Different gradients which were obtained from the analysis of far-IR/radio correlation using samples selected at different frequencies reveal the selection effects on relations derived in this study.

6.2 Introduction

The star formation rate of a galaxy is a fundamental parameter of its evolutionary state and various SFR indicators of galaxies have been used in the literature over the years. For recent reviews, see Kennicutt & Evans (2012) and Calzetti (2013). Two important SFR calibrations can be derived using the IR and radio continuum emission from galaxies. In the first of these, optical and ultraviolet emission from young stars (age ranges 0–100 Myr with masses up to several solar masses) is partially absorbed by larger dust grains (relative to grains whose emission peaks at shorter IR wavelengths) in the interstellar medium (ISM) of galaxies and re-emitted in the FIR. Therefore, the thermal FIR emission provides a probe of the energy released by star formation. On the other hand, radio emission from non-active galaxies is a combination of free-free emission from ionised gas due to massive stars and synchrotron emission which arises from charged particles accelerated by supernova explosions, the end products of massive stars. Therefore, radio emission (from non-active galaxies) can be used as an indirect probe of the recent number of massive stars and therefore of SFR.

Since both processes trace star formation, one would naturally expect to see a correlation between these quantities. In the early 1970s van der Kruit (1971, 1973) showed that a correlation exists between the FIR emission and radio emission from spiral galaxies. Since then the far-IR/radio correlation (FIRC, hereafter) has been a topic of several studies aiming to understand the physical reasons behind the FIRC and its cosmological evolution (e.g. Harwit & Pacini 1975; Rickard & Harvey 1984; de Jong et al. 1985; Helou et al. 1985; Hummel et al. 1988; Condon 1992; Appleton et al. 2004; Jarvis et al. 2010; Ivison et al. 2010a,b; Bourne et al. 2011; Smith et al. 2014; Magnelli et al. 2015). These studies have suggested that the FIRC holds for galaxies ranging from dwarfs (e.g. Wu et al. 2008) to ultra-luminous infrared galaxies (ULIRGs; $L_{IR} \geq 10^{12.5} L_{\odot}$; e.g. Yun et al. 2001) and is linear across this luminosity range. On the other hand, Bell (2003), Boyle et al. (2007) and Beswick et al. (2008) argued that at low luminosities the FIRC may deviate from the well-known tight correlation. Although there are various factors which affect the results obtained in these

studies, one explanation for the contradictory results might be selecting samples from flux-limited surveys carried out at different wavelengths. I will return to this point below.

The naive explanation of the linearity of this relation assumes that galaxies are electron *calorimeters* (all of the energy from the cosmic-ray electrons [CRe] is radiated away as radio synchrotron emission before these electrons escape the galaxies) and *UV calorimeters* [galaxies are optically thick in the UV light from young stars so that the intercepted UV emission is re-radiated in the far-IR: Voelk (1989)]. This latter assumption is probably not completely true, because the observed UV luminosities and the observed far-IR luminosities from SFGs are similar to each other (e.g. Bell 2003; Martin et al. 2005). Furthermore, the electron calorimetry model might not hold either for our own galaxy or lower mass galaxies, as the typical synchrotron cooling time is expected to be longer than the inferred diffusion escape time of electron in these galaxies (e.g. Lisenfeld et al. 1996); non-thermal radio emission has been observed in the haloes of spiral galaxies (e.g. Heesen et al. 2009) which shows that the diffusion escape time of electrons is comparable to the typical energy loss time scale. Non-calorimeter theories have also been proposed (Helou & Bicay 1993; Niklas & Beck 1997; Lacki et al. 2010). For example, Lacki et al. (2010) and Lacki & Thompson (2010) presented a non-calorimeter model taking into account different parameters (e.g. energy losses, the strength of magnetic field and gas density etc.) as a function of the gas surface density and argued that the correlation breaks down for low surface brightness dwarfs due to the escape of CRe. Such models imply that stellar mass (or galaxy size) has an effect in a non-calorimeter model. This is because the time scale for CRe to diffuse and escape the galaxy before they radiate all their energy in radio depends on the size of a galaxy.

To date the radio luminosity/SFR relation and the FIRC have been studied almost exclusively at GHz bands, because sensitive radio surveys have mostly been carried out at these radio frequencies (e.g. Becker et al. 1995; Condon et al. 1998). Due to lack of available data, most of the time the radio luminosity of SFGs has been considered as a function of SFR only. However, there is a well-known tight relation (the ‘main sequence’ of star formation) which has been observed between SFR and stellar mass of SFG with a ~ 0.3 dex scatter (e.g. Noeske et al. 2007). This relation holds for SFGs in the local Universe (e.g. Brinchmann et al. 2004; Elbaz et al. 2007) all the way to $z \sim 4$ (e.g. Noeske et al. 2007; Karim et al. 2011). Therefore, taking the stellar masses of galaxies into account is important to give a true picture of the radio luminosity/SFR

relation.

With new radio interferometer arrays such as LOFAR we are able to move toward lower radio frequencies, at which thermal radio emission becomes increasingly negligible. In addition, with the increasing number of surveys at other wavebands and the data provided it is possible to use multi-wavelength data sets to derive galaxy properties (such as SFR, galaxy mass etc.) using SED modelling. The goal of this chapter is to investigate the relationship between low-frequency radio luminosity, using LOFAR observations at 150 MHz, and physical properties of galaxies such as SFR and stellar mass. Results obtained in this work will be crucial for the interpretation of future surveys with various radio interferometer arrays, such as LOFAR and the SKA.

The layout of this chapter is as follows. A description of the sample, classification and data are given in Section 6.3. The key results are given in Section 6.4, where I present the results of the regression analysis using MCMC and stacking analysis. In Section 6.5 I interpret the findings and I summarise this work and give my conclusions in Section 6.6.

6.3 DATA

6.3.1 Sample and emission line classification

To construct the sample I selected galaxies from SDSS DR7 (Abazajian et al. 2009) catalogue with the value-added spectroscopic measurements produced by the group from the MPA-JHU¹ in the *Herschel*-ATLAS NGP field (Eales et al. 2010a). This provided 16,943 sources spanning a redshift range $0 < z < 0.7$. The sample does not include quasars because the AGN outshine the host galaxies for these objects which makes it difficult to study their host galaxy properties. H-ATLAS/NGP images were used to obtain far-IR fluxes of the sample galaxies, as described in Section 2.3.

BH12 constructed a radio-loud AGN sample by combining the MPA-JHU sample with the NVSS (Condon et al. 1998) and the FIRST survey (Becker et al. 1995) following the methods described by Best et al. (2005) and Donoso et al. (2009). I firstly cross-matched the initial sample of galaxies with the BH12 catalogue, and all objects that they classified as AGN form a radio AGN subsample, which has 312 objects. The remaining galaxies are classified as SFGs, Composite objects, Seyferts, LINERs using the modified emission-line diagnostics given by Kewley et al. (2006). Composite

¹<http://www.mpa-garching.mpg.de/SDSS/>

Population type	Classified	<i>Herschel</i> -3σ	<i>LOFAR</i> -3σ	Detected at both bands
Radio AGN (HERG&LERG)	309	95	305	94
Seyferts	285	181	195	140
Composites	1029	842	705	620
SFGs	3632	2958	2332	2026
LINERs	97	44	48	30
HERG/LERG?	140	72	138	71
Unclassified by BPT	7921	2117	3964	1272

Table 6.1: The number of sources in each population after the optical emission-line classification.

objects were separated from star-forming objects using the classification line given by Kauffmann et al. (2003c). One of the detection criterion is to select objects having optical emission lines detected at 3σ to be able to classify galaxies accurately. This requirement constrains the sample of SFGs to $\sim z \leq 0.2$ and biases due to this selection are explained in Section 6.5 where I interpret the results. As we move to higher redshifts ($z \geq 0.2$) we cannot detect strong optical emission lines from normal star-forming objects. Only a few high redshift SFGs ($z < 0.35$) that have optical emission lines detected at 3σ and these galaxies are probably starbursts at higher redshifts. There are a number of galaxies not detected in their optical emission-lines at 3σ which are therefore unclassified by BPT (Baldwin et al. 1981). Counts and detection statistics of the whole sample are given in Table 6.1. I refer the reader to Chapter 4 for details of the sample and classification.

6.3.2 Radio data

Flux densities at 150 MHz

Radio flux densities at 150 MHz for all the SDSS galaxies in the sample were directly measured from the final LOFAR maps, whose production and LOFAR data reduction were described by Hardcastle et al. (2016). I estimated the flux densities to be the value in the image at the source position within an aperture of 14 arcsec in radius, which was chosen considering the resolution of the LOFAR maps (~ 10 arcsec \times 5 arcsec). The errors on these flux densities were estimated using the LOFAR r.m.s. maps, taking the noise value in the image at the pixel coordinate of a given source scaled by the square root of the number of beams in the aperture. To convert the 150 MHz flux densities

to 150-MHz luminosities (L_{150} in W Hz^{-1}) I adopt a spectral index $\alpha = 0.7$, where $S \propto \nu^{-\alpha}$ [the value that was observed by Hardcastle et. al (2016)]. Since the radio maps do not fully cover the H-ATLAS/NGP field only 13,360 sources have a measured LOFAR flux density of which ~ 50 per cent were detected at 3σ .

Fig. 6.1 shows the 150 MHz luminosity distribution of the detected galaxies as a function of redshift. Recently, Hardcastle et al. (2016) showed that the radio luminosity function (at 150 MHz) of SFGs selected in radio shows an evolution with redshift ($0.0 < z < 0.3$). As can be seen from Fig. 6.1, I include all SFGs in the sample with a similar redshift range ($0.0 < z < 0.35$), because this allows me to investigate any variation in the relations studied here for the star-forming populations with different luminosities at relatively low-redshifts. Therefore, I take in to account possible degeneracies between redshift and luminosity when I interpret the results in Section 6.5.

Flux densities at 1.4 GHz

I obtained the FIRST images and the r.m.s. map of the H-ATLAS/NGP field and, as for the LOFAR flux density measurements, I measured the flux densities at the source position within an aperture of 10 arcsec in radius. Errors on these flux densities were estimated in the same way as the estimation of LOFAR flux errors, using the 1.4 GHz r.m.s. maps. The 1.4 GHz luminosities of the sources in the sample were estimated using these flux densities and a spectral index $\alpha = 0.7$. These luminosities were used to derive the relation between $L_{1.4}$ (in W Hz^{-1}) and L_{250} and $L_{1.4}$ and SFR.

6.3.3 Far-IR data

Herschel-ATLAS provides imaging data for ~ 600 square degrees of the northern, equatorial and southern sky using PACS (at $100 \mu\text{m}$ and $160 \mu\text{m}$: Ibar et al. 2010; Poglitsch et al. 2010a) and SPIRE (at $250 \mu\text{m}$, $350 \mu\text{m}$ and $500 \mu\text{m}$ Griffin et al. 2010a; Pascale et al. 2011, Valiante et. al. in prep.). To derive a maximum-likelihood estimate of the flux densities at the positions of objects in the SPIRE bands in the field the flux density from the PSF-convolved H-ATLAS images were measured for each source together with the error on the fluxes. Further details of the flux measurement method are given by Hardcastle et al. (2010, 2013).

In order to estimate $250 \mu\text{m}$ luminosities (L_{250} in W Hz^{-1}) of sources I used a modified black-body spectrum for the far-IR SED; I fixed the emissivity index β to 1.8

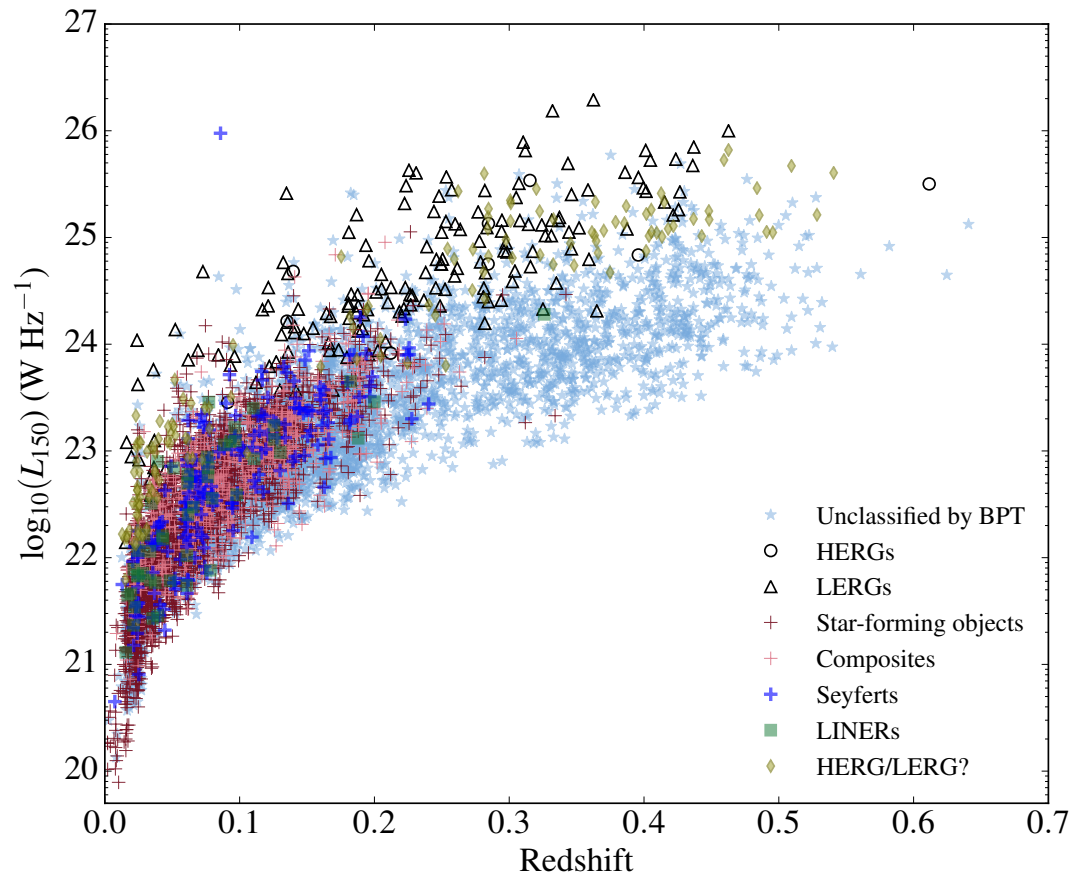


Figure 6.1: The distribution of the luminosity at 150 MHz of all galaxies in the sample as a function of their redshifts. Colours and different symbols indicate different emission-line classes: SFG (red crosses), Composites (pink crosses), Seyferts (blue crosses), LINERs (blue squares). Radio AGN classified by their emission-lines: HERGs (open black circles) and LERGs (open black triangles). There are sources in the BH12 sample that were not classified either as a HERG or LERG, these are shown as green filled diamonds. Blue filled stars represent sources that were not classified using emission-line diagnostics.

[the best-fitting value derived by Hardcastle et al. (2013) and Smith et al. (2013) and allowed temperatures to vary to obtain the best fitting temperatures, integrated luminosities (L_{IR}) and rest-frame luminosities at $250 \mu\text{m}$ (L_{250}) provided by the minimum χ^2 values. To calculate the K -corrections the same emissivity index and the mean of the best-fitting temperatures for each class were used. These corrections were included in the derivation of $250 \mu\text{m}$ luminosities.

6.3.4 Star formation rates

SFRs from MAGPHYS

Due to the large range of multi-wavelength data that are available over the *Herschel*-ATLAS NGP field, it is desirable to consistently model the properties of the sources that we observe using all of the photometric data simultaneously. In order to do this the MAGPHYS code (da Cunha et al. 2008) was used. For full details of the code and processes involved I refer the reader to the source paper by da Cunha et al. (2008), I will only briefly mention the steps that were taken to estimate the SFRs.

The basic idea behind MAGPHYS is that the energy absorbed by dust at UV-optical wavelengths is reradiated in the far-infrared. Therefore, using the the entire SED (from UV to millimetre wavelengths) should provide sufficient information about galaxies with respect to their starlight and dust emission. For this purpose, I use the precise spectroscopic redshifts along with MAGPHYS to consistently model 14 bands of photometric data available over the *Herschel*-ATLAS NGP field. These include the SDSS *ugriz* bands (York et al. 2000), data from the *WISE* survey (Wright et al. 2010b) in bands centred on 3.4, 4.6, 12 and $22 \mu\text{m}$, and data from the *Herschel*-ATLAS survey (Eales et al. 2010b) from the PACS (Poglitsch et al. 2010b, centred on 100 and $160 \mu\text{m}$) and SPIRE (Griffin et al. 2010b, centred on 250, 350 and $500 \mu\text{m}$) instruments measured as discussed in Chapter 4, in Section 4.3.2.

To ensure that the measured fluxes in different bands are as consistent as possible, appropriate photometry for each band was utilised: for optical bands the suggested method given in the SDSS documentation² was followed, at mid-infrared wavelengths, a photometry from UNWISE (Lang 2014) was adopted and corresponding photometric details for the *Herschel* data are given in Chapter 4.

²The relevant SDSS documentation can be found at <http://www.sdss.org/dr12/algorithms/magnitudes/>

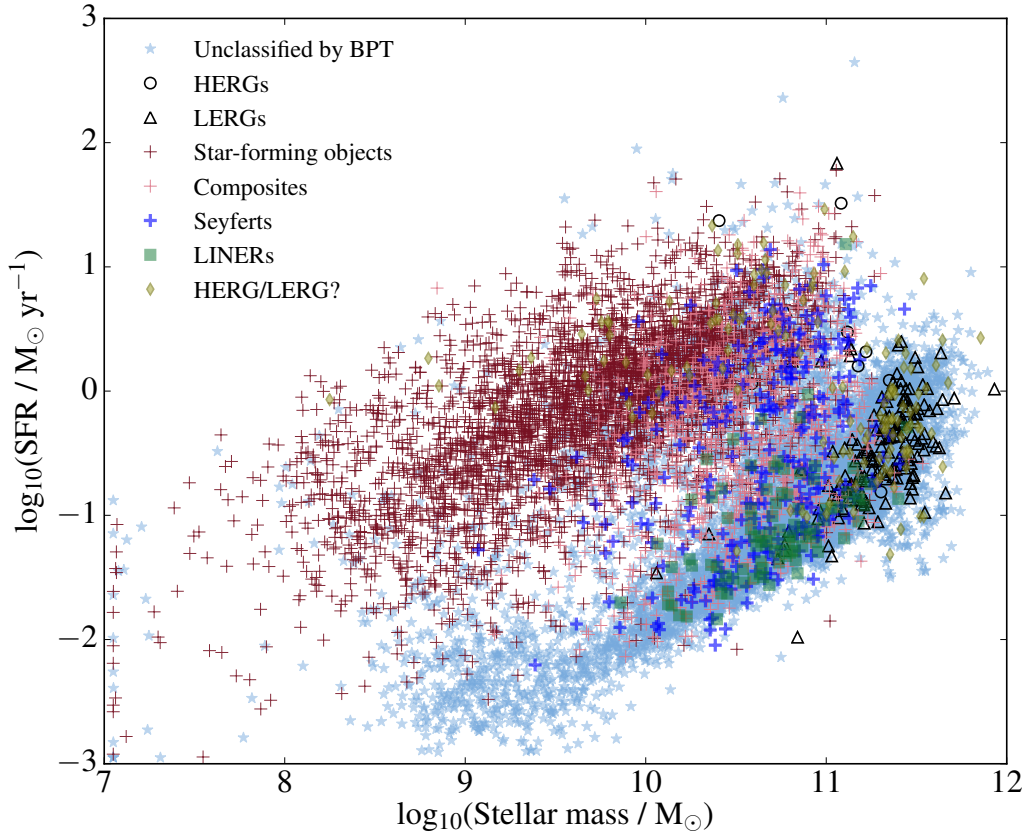


Figure 6.2: Plot of SFR derived by MAGPHYS as a function of MAGPHYS stellar mass of all galaxies in the sample. Symbols and colours as for Fig. 6.1.

Then these multi-wavelength data sets were used to determine physical properties of galaxies in the sample, estimating the χ^2 goodness-of-fit parameter for every valid combination, allowing the best-fit model and parameters to be identified. To account for residual uncertainties in the aperture definitions and zeropoint calibrations, 10 percent in quadrature to the SDSS, *WISE* and *PACS* photometry, and 7 percent in quadrature to the *SPIRE* photometry was added, following Smith et al. (2012b). In the rest of the chapter I used Bayesian estimates of SFRs and stellar masses for all galaxies in the sample. In Fig. 6.2 I present Bayesian estimates of SFRs for all galaxies in the sample derived by MAGPHYS against their stellar masses which were also estimated using MAGPHYS.

SFRs from $H\alpha$ emission lines

SFR measurements for galaxies, calculated using the $H\alpha$ emission line, corrected for dust attenuation and fibre aperture effects, are available in the MPA-JHU data base (Brinchmann et al. 2004).

In Chapter 4 I used the same sample to study star formation properties of AGN samples using SFRs derived via the $H\alpha$ emission line due to lack of availability of the MAGPHYS code with the full photometric data sets described above. For a sanity check I compare SFRs of galaxies in the sample derived by the two different methods. In Fig. 6.3 I show MAGPHYS–SFRs as a function of $H\alpha$ –SFRs of star-forming objects (left panel) and for all objects in the sample (right panel). From the left panel of Fig. 6.3 we see that for a given $H\alpha$ -SFR MAGPHYS estimates an SFR ~ 0.2 dex larger than the $H\alpha$ method for SFGs classified by BPT. This is also true for most of different classes of galaxies as seen in the right panel of the same figure.

There are various differences in the derivations of these SFRs which might cause a ~ 0.2 dex difference between SFRs of galaxies in the sample; I will only briefly mention them in this part of the thesis because a detailed comparison analysis is out of the scope of this chapter.

First of all, the correction of dust attenuation was calculated differently in the two different SFR estimation methods. For the $H\alpha$ -SFRs dust attenuation was estimated from $H\alpha/H\beta$ assuming a fixed unattenuated Case B ratio (Brinchmann et al. 2004). As stated by Brinchmann et al. (2004), using a single conversion factor is not fully correct but is a reasonable approximation. On the other hand, MAGPHYS uses a more complicated procedure to estimate dust attenuation (see da Cunha et al. 2008, for details). Furthermore, the extragalactic dust law is not fully known. Although for both $H\alpha$ -SFRs and MAGPHYS–SFRs the same dust law (Charlot & Fall 2000) was used, the extragalactic dust law might vary as a function of galaxy properties. Recently, Wang et al. (2016) compared different SFRs estimated by different methods and found around ~ 0.2 dex difference between $H\alpha$ -SFRs and those derived from the far-IR and UV data, and they also observed variations as a function of galaxy parameters. Another recent work by Davies et al. (2016) compared various SFR estimators including $H\alpha$ and found differences between different methods. Taking into account all different and complicated processes involved in the derivation of SFRs a systematic offset of 0.2 dex between $H\alpha$ -SFR and MAGPHYS–SFR is not unexpected. As a conclusion, it is not known which one is a true SFR estimator so I adopt the MAGPHYS results for the rest of the chapter. This is because I think MAGPHYS probably provide more

accurate estimates of SFRs as this method applies a physically meaningful obscuration correction via SED modelling.

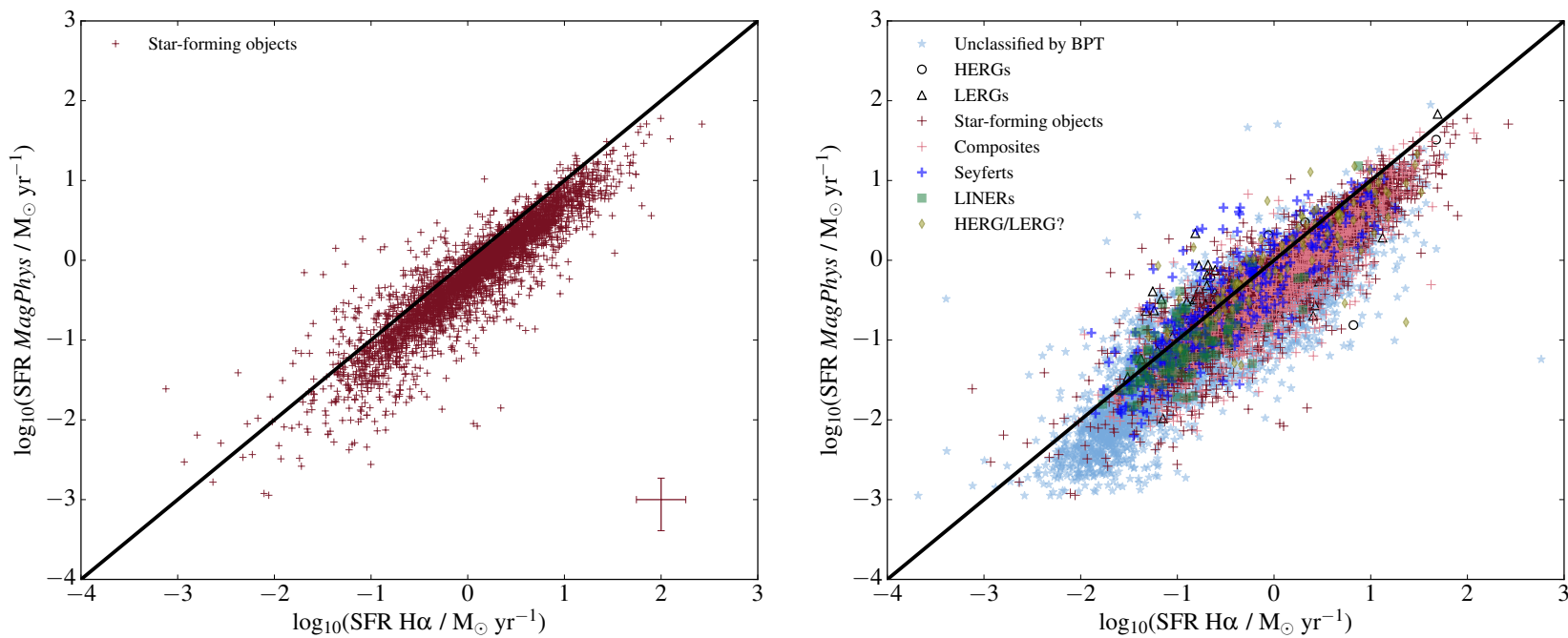


Figure 6.3: Left panel: MAGPHYS–SFRs as a function of H α -SFRs of star-forming objects. Average errors on MAGPHYS–SFRs and H α -SFRs are seen as red crosses. Right panel: MAGPHYS–SFRs as a function of H α -SFRs of all galaxies in the sample. Black solid lines show one-to-one relation.

6.4 Analysis and results

6.4.1 The low-frequency radio luminosity–SFR relation

The main motivation of this work is to evaluate whether radio luminosity at low radio frequencies can be used as a SFR indicator, and to investigate how the results can be compared with the relations obtained using radio luminosity at high radio frequencies in the literature.

I initially investigated the L_{150} /SFR relation carrying out a stacking analysis as used previously in Chapter 4. L_{150} of SFGs classified by the BPT, independent of being detected at 3σ at 150 MHz, were stacked in 8 SFR bins. I then determined the mean values of the L_{150} samples in all bins which are shown as black large crosses in Fig. 6.4. The stacking analysis allows us not to be biased against sources that are weak or not formally detected. None of the fitting analysis was implemented using stacks but I show them in the plots for visualisation of the data including non-detections.

In order to quantitatively examine whether sources in the bins were significantly detected, I measured 150 MHz flux densities from 100,000 randomly chosen positions in the field and a Kolmogorov–Smirnov (KS) test was used to see whether the sources from the sample were consistent with being drawn from a population defined by the random positions. All these estimates with SFR bins, number of sources included in each bin and the results of the KS test are given in Table 6.3. It can be seen from these values that SFG in each bin are significantly detected, except the first bin (sources with negative flux densities dominate this bin so this affects the result of the KS test). Low values of the KS test (p -value below 1 per cent) indicate that target sample in each bin and sources selected randomly were not derived from the same distribution.

In order to quantify the relationship between SFR and the low-frequency radio luminosity I used SFRs of objects classified on the BPT as SFGs and their LOFAR 150 MHz luminosities (including non-detections). The relationship was obtained using MCMC (implemented in the *emcee* PYTHON package) considering the errors on both SFR and L_{150} , and incorporating an intrinsic dispersion in the manner described by Hardcastle et al. (2010). The derived Bayesian estimates of the slope and intercept of the correlation are:

$$L_{150} = \psi^{0.95(\pm 0.004)} \times 10^{22.33(\pm 0.02)}. \quad (6.1)$$

where ψ is the SFR in $M_{\odot} \text{ yr}^{-1}$. To be able to make a consistent comparison with the

high-frequency radio luminosity–SFR relation I used 1.4 GHz luminosities of SFG ($L_{1.4}$ is used to indicate this in the rest of the chapter), derived using FIRST fluxes as described in Section 2.2.3, and $\alpha = 0.7$. This gave the following relation:

$$L_{1.4} = \psi^{0.85(\pm 0.01)} \times 10^{22.35(\pm 0.03)} \quad (6.2)$$

Fig. 6.4 shows the distribution of 150 MHz luminosity of SFGs detected at 150 MHz against their SFRs and the best fits that were obtained from the regression analysis. In the bottom panel of the same figure I show calculated ratios of L_{150}/ψ . In the left panel of Fig. 6.5 I show the L_{150} luminosity of sample sources colour-coded by redshift as a function of L_{150} predicted by the relation (Eq. 6.1) derived by the regression analysis.

As mentioned in Section 6.2, galaxy mass has an important role, in particular for non-calorimeter models, in the relation of L_{radio} and ψ because the galaxy size has an impact in the competition of radiative loss and diffusion of CRE. Therefore, in order to understand how L_{150} changes with stellar mass and SFR I fitted the data taking into account both stellar mass and SFR of SFGs, using the following parametrisation:

$$L_{150} = L_o \psi^\alpha \left(\frac{M_*}{10^{10} M_\odot} \right)^\gamma \quad (6.3)$$

This gave me $\alpha = 0.53 \pm 0.007$, $\gamma = 0.42 \pm 0.008$ and normalisation (L_o) = $10^{22.41(\pm 0.02)}$. The distribution of actual L_{150} of sample sources as against their L_{150} predicted by this new relation is seen in the right panel of Fig. 6.5. Once the effect of mass is taken into account the scatter decreases, as seen in the right panel in comparison with the scatter in the left panel. In the low luminosity (or low SFR) end we can see that there are sources that lie below the green line (which shows one-to-one relation). This may suggest that SFGs with low SFRs have a different relation between L_{150} and SFR than the average locus of SFGs which lie on the line. Additionally, disagreement between the actual and predicted L_{150} at the high luminosity end indicates that sources with high SFRs (or high luminosities) might be parameterised by a different power-law with respect to SFGs at the low-end of the diagram as previously proposed by Chi & Wolfendale (1990); Bell (2003). In the bottom panel of Fig. 6.4 calculated ratios of $= L_{150}/\psi$ for each bin are shown. Estimates of these ratios additionally indicate that ratios in the last three bin have close values ($\psi > 1 M_\odot \text{ yr}^{-1}$) whereas there is a slight decrease towards low-SFRs (the first four bins, $\psi < 1 M_\odot \text{ yr}^{-1}$). In order to evaluate this I selected sources with SFR higher than $1 M_\odot \text{ yr}^{-1}$ and lower than $1 M_\odot \text{ yr}^{-1}$ and

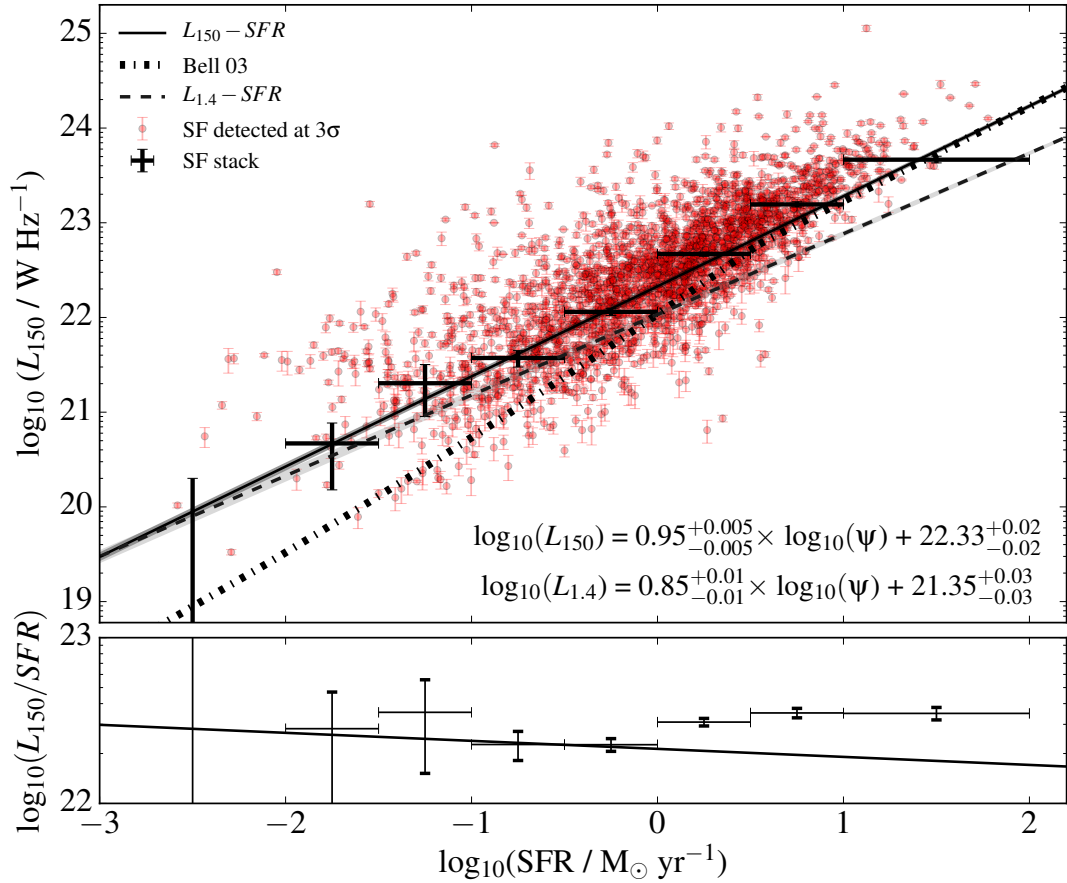


Figure 6.4: The distribution of LOFAR 150 MHz luminosities of SFG detected at 150 MHz as a function of their SFRs. The solid black line is the best fit obtained using all SFG and the dashed black line shows the best fit to all data points of SFG obtained using $L_{1.4}$ and scaled to 150 MHz. Shaded black and grey regions around the best fits show 1σ errors of these fits, determined by bootstrapping. The prediction of Bell (2003) scaled to 150 MHz assuming $\alpha = 0.7$ is shown with dotted-dashed line. Results of the stacking analysis are also shown for L_{150} with large black crosses. The L_{150}/SFR ratios and the best fit divided by the SFR (black line) are seen in the bottom panel.

obtained Bayesian estimates of SFR index α , stellar mass index γ and normalisation L_o for both sub-samples. These are for (i) $\psi < 1 \text{ M}_\odot \text{ yr}^{-1}$ $\alpha = 0.52 \pm 0.02$, $\gamma = 0.45 \pm 0.01$, $L_o = 10^{22.31(\pm 0.02)}$ and (ii) for $\psi > 1 \text{ M}_\odot \text{ yr}^{-1}$ $\alpha = 1.23 \pm 0.03$, $\gamma = 0.25 \pm 0.02$, $L_o = 10^{22.27(\pm 0.02)}$. Results of the regression analyses are presented in Fig. 6.6.

As stated above, the data indicate that low-luminosity and high-luminosity SFGs might be parameterised by a different power-law, which is consistent with earlier findings (e.g. Bell 2003). This led me to parameterise the data using the following relation in order to see whether a broken power-law can better explain the L_{150} /SFR relation for SFGs with different luminosities:

$$L_{150} = L_o \psi^\alpha \left[1 + \left(\frac{\psi}{\psi_c} \right)^\beta \right] \left(\frac{M_*}{10^{10} \text{ M}_\odot} \right)^\gamma \quad (6.4)$$

where ψ is SFR ($\text{M}_\odot \text{ yr}^{-1}$), ψ_c ($\text{M}_\odot \text{ yr}^{-1}$) is the critical SFR at which I would expect a transition of the slope and M_* represents stellar mass. Results of this regression analysis are seen in Fig. 6.7 where I plot actual L_{150} luminosities of SFG as a function of L_{150} predicted by the relation given in Eq. 6.4. Although we observe a tight correlation in this figure, in comparison to the right panel of Fig. 6.5 a broken power-law parameterisation does not improve the disagreement between the actual L_{150} and L_{150} predicted by the relation which we see for low and high-luminosity galaxies. Estimated fit parameters for different parameterisation are given in Table 6.2.

Parameterisation	Normalisation (L_{\odot}) 10^N	α	β	γ	ψ_c $M_{\odot} \text{ yr}^{-1}$
$L_{150} = L_o \psi^{\alpha} M_*^{\gamma}$ for all data	22.41 ± 0.02	0.53 ± 0.007	0.42 ± 0.008		
$L_{150} = L_o \psi^{\alpha} M_*^{\gamma}$ for $SFR > 1$	22.27 ± 0.02	1.23 ± 0.03	0.25 ± 0.02		
$L_{150} = L_o \psi^{\alpha} M_*^{\gamma}$ for $SFR < 1$	22.31 ± 0.02	0.52 ± 0.01	0.45 ± 0.01		
$L_{150} = L_o \psi^{\alpha} \left[1 + \left(\frac{\psi}{\psi_c} \right)^{\beta} \right] M_*^{\gamma}$ for all data	21.93 ± 0.05	0.17 ± 0.02	0.77 ± 0.03	0.36 ± 0.01	0.57 ± 0.1

Table 6.2: Parameterisations that were used from the regression analyses and the best fit parameters obtained are shown.

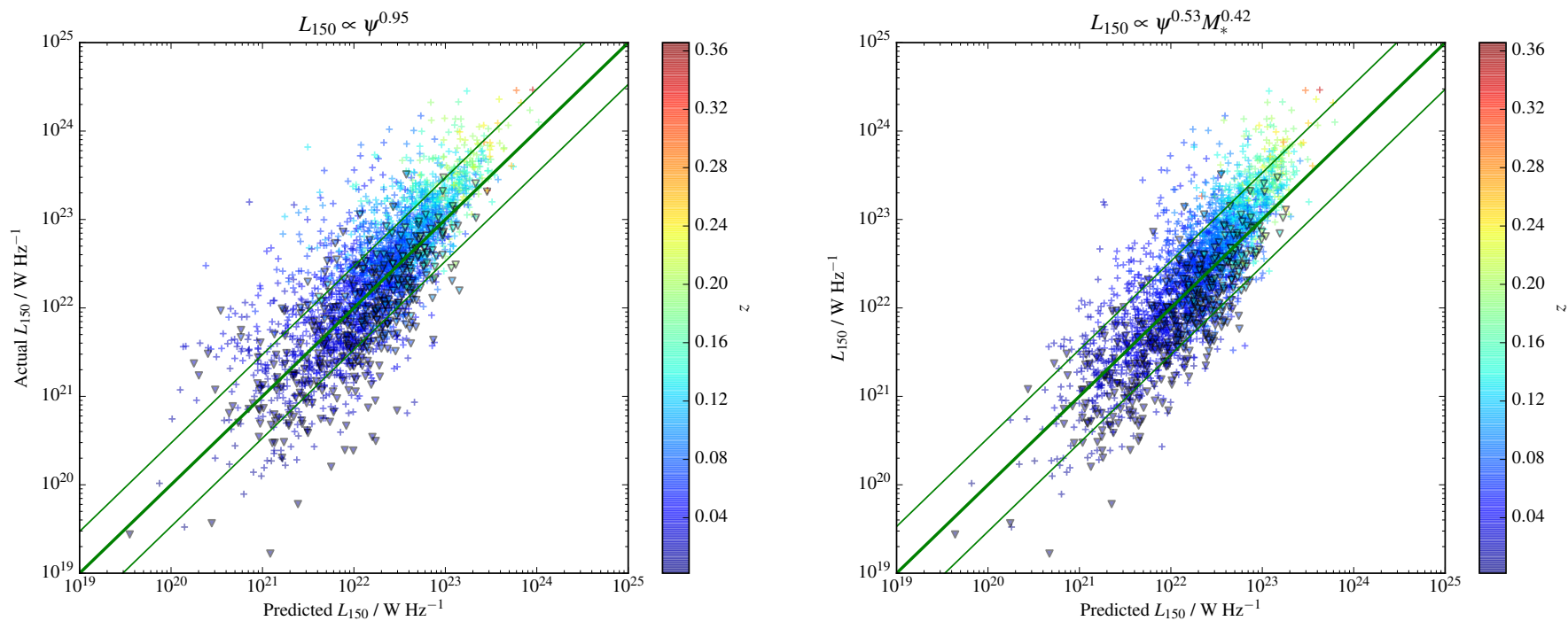


Figure 6.5: Left panel: L_{150} distribution of SFG as a function of predicted- L_{150} by Eq. 6.1 we obtained from the regression analysis. Right panel: L_{150} distribution of SFG as a function of predicted- L_{150} by Eq. 6.3, in which both the effects of stellar mass and SFR are taken into account. In all panels limits are indicated by triangles and points are colour-coded by source redshift. The thick green line shows one-to-one relation between luminosities and the thin green lines indicate the fitted intrinsic scatter.

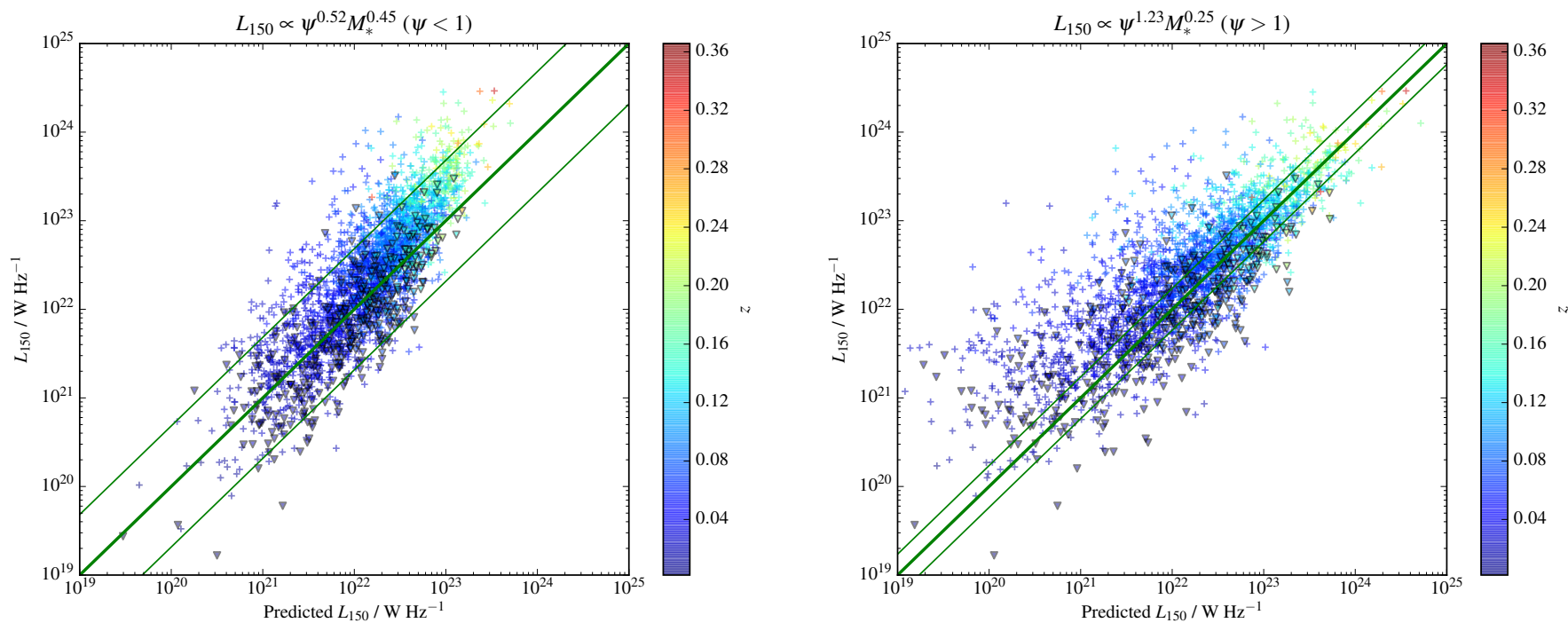


Figure 6.6: Left panel: L_{150} distribution of SFG with $\psi < 1 \text{ M}_{\odot} \text{ yr}^{-1}$ as a function of L_{150} predicted by Eq. 6.3. Right panel: L_{150} distribution of SFG with $\psi > 1 \text{ M}_{\odot} \text{ yr}^{-1}$ as a function of L_{150} predicted by Eq. 6.3. In all panels limits are indicated by triangles and points are colour-coded by source redshift. The thick green line shows one-to-one relation between luminosities and the thin green lines indicate the fitted intrinsic scatter.

Sample	SFR Bins M_{\odot}/yr	Mean z	N	$L_{150-MHz}$ $\times 10^{22}$ (W/Hz)	L_{150}/SFR $\times 10^{22}$	KS probability
SFGs	-2.0--1.5	0.05	95	$0.047^{+0.03}_{-0.03}$	$2.824^{+1.87}_{-1.87}$	0.17
	-1.5--1.0	0.06	289	$0.202^{+0.11}_{-0.12}$	$3.545^{+2.05}_{-2.05}$	$\ll 1\%$
	-1.0--0.5	0.06	598	$0.374^{+0.06}_{-0.06}$	$2.267^{+0.39}_{-0.39}$	$\ll 1\%$
	-0.5-0.0	0.07	1013	$1.146^{+0.10}_{-0.10}$	$2.261^{+0.20}_{-0.20}$	$\ll 1\%$
	0.0--0.5	0.08	1068	$4.685^{+0.24}_{-0.25}$	$3.095^{+0.17}_{-0.17}$	$\ll 1\%$
	0.5--1.0	0.09	444	$15.621^{+0.99}_{-0.97}$	$3.514^{+0.23}_{-0.23}$	$\ll 1\%$
	1.0--2.0	0.12	85	$46.364^{+3.94}_{-4.13}$	$3.492^{+0.32}_{-0.32}$	$\ll 1\%$

Table 6.3: Results of the stacking analysis that was implemented using L_{150} of SFG in each SFR bin. Column 1: Type of galaxies in the sample. Column 2: Range of bins (L_{250}) defined for the stacking analysis. Column 3: Counts in each bin. Column 4 gives the calculated weighted average of L_{150} . Column 5: Ratio of the mean of L_{150} to the mean of SFR in each SFR bin. Column 6: Results of KS test which was carried out to evaluate whether sources in the bins were significantly detected.

In Fig. 6.8 we additionally show the distribution of L_{150} of all classified galaxies in the sample as a function of their SFRs. The correlation discussed above between L_{150} and SFR for SFGs is apparent. Although there is a scatter we can see that composite objects also follow this correlation. Seyferts mostly occupy a region between SFG and AGN. Emission-line radio AGN occupy the top left part of the diagram, as expected because radio emission from AGN will be much higher than normal galaxies. A tail of objects following the radio AGN down to bottom left corner are sources that could not be classified by emission-line diagnostics (i.e. not detected at 3σ level in their emission-lines H_{β} , $O_{III} \lambda 5007$, H_{α} , $[N II] \lambda 6584$ and $[S II] \lambda 6717$). These sources clearly have higher radio luminosities than normal galaxies but mostly are less radio luminous than radio AGN. In this region sources that are classified as LINERs and Seyferts are also seen, which mostly occupy the bottom part of this tail.

In Fig. 6.9 we present the actual L_{150} luminosities of all galaxies in the sample as a function of L_{150} predicted by the relation given in Eq 6.4. Once again it is clear that parameterisation the data with a broken power-law show that SFGs in the sample and unclassified galaxies together with AGN have a different relation between L_{150} and SFR.

6.4.2 The far-IR–radio correlation

With the data I can investigate the radio–far-IR correlation as well using low-frequency radio data following the earlier investigation of this by Hardcastle et al. (2016). Fig.

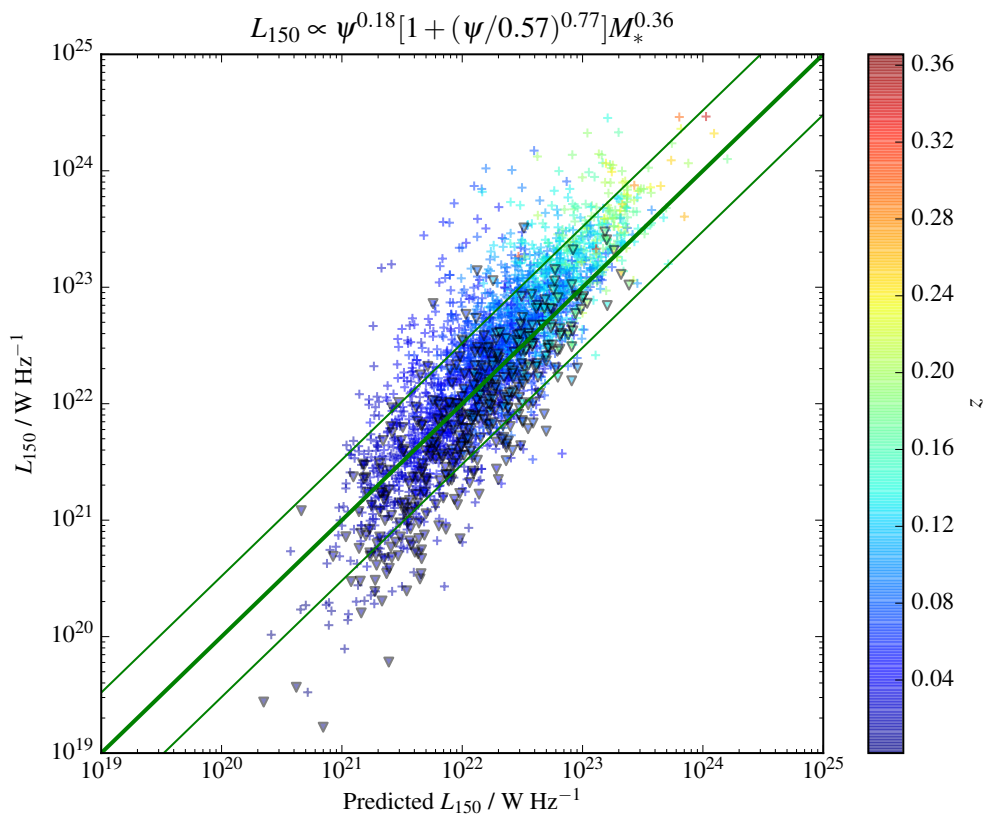


Figure 6.7: L_{150} distribution of SFG as a function of L_{150} predicted by the relation in Eq. 6.4. Limits are indicated by triangles and points are colour-coded by source redshift. The thick green line shows one-to-one relation between luminosities and the thin green lines indicate the expected intrinsic scatter.

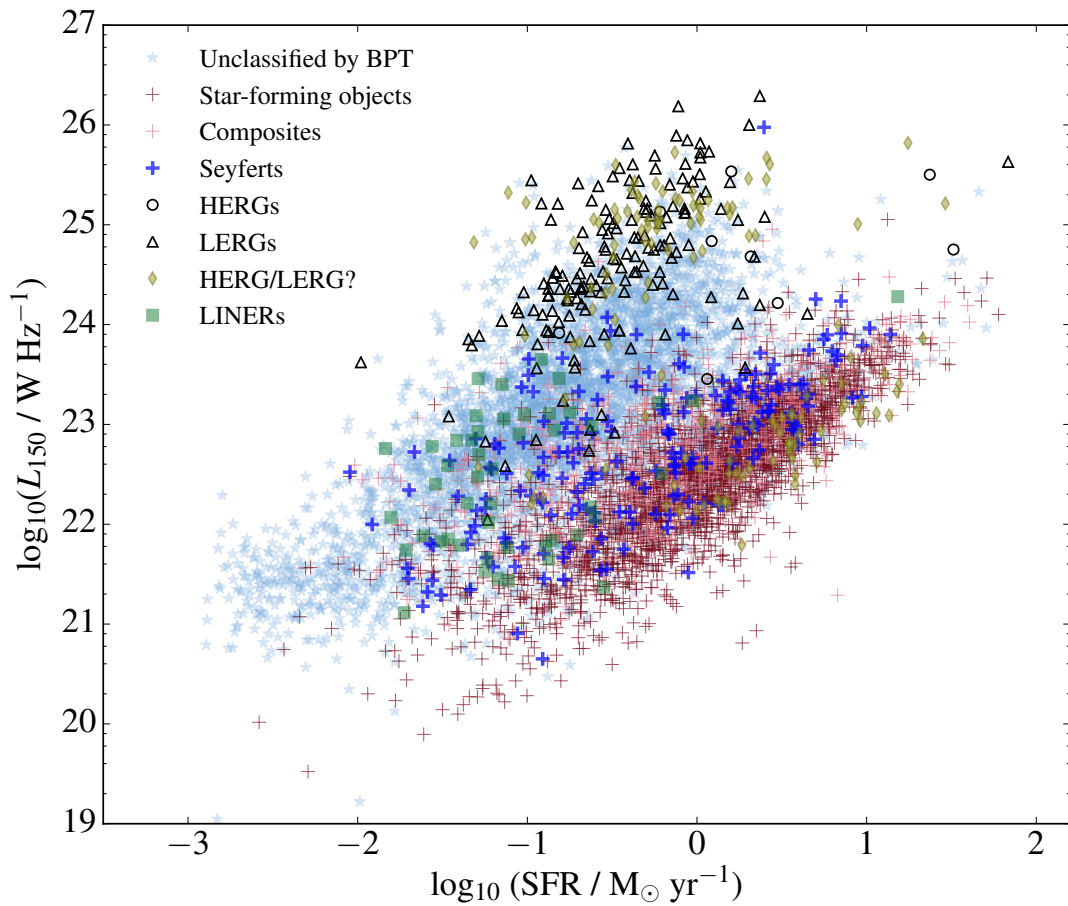


Figure 6.8: The distribution of LOFAR 150 MHz luminosities of different classes of objects which are detected (3σ) at 150 MHz in the sample as a function of their SFRs. Symbols and colours as for Fig. 6.1.

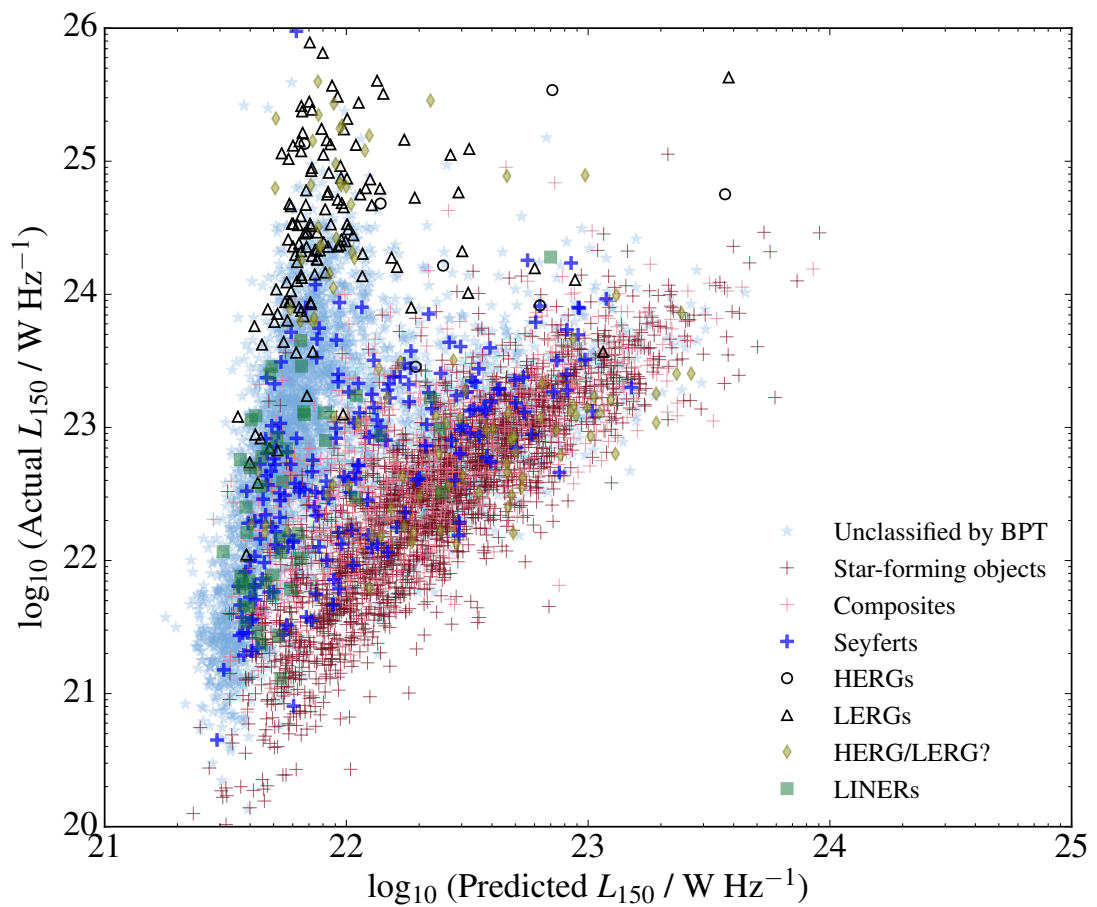


Figure 6.9: The distribution of LOFAR 150 MHz luminosities of different class of objects in the sample as a function of 150 MHz luminosities predicted by the relation given in Eq. 6.4. Symbols and colours as for Fig. 6.1.

6.10 shows the distribution of L_{150} of SFGs detected in the far-IR against their L_{250} . A tight correlation between L_{150} and L_{250} is clearly seen for SFGs detected at 3σ . As discussed above in Section 6.4.1, I initially carried out a stacking analysis to see the FIRC including non-detections. These were calculated by dividing L_{250} of SFGs detected at $250 \mu\text{m}$ into a number of bins in which the average was taken to be a stack point (Fig. 6.10).

In order to obtain the FIRC correlation I used MCMC in the same way as explained in the previous section. While implementing this procedure I used SFGs detected at $250 \mu\text{m}$ and fitted to their L_{150} independent of whether they were detected or not. This allows me to take into account non-detections in the LOFAR band and derive relations in an unbiased manner. The same fitting procedure was carried out using $L_{1.4}$ to obtain the $L_{1.4} - L_{250}$ relation. This allowed me to make a consistent comparison of the relations derived using radio luminosities at different radio frequencies for the same sample. As outlined in the introduction, to date both the FIRC and the radio luminosity–SFR relation have been derived almost exclusively using high frequency radio luminosities.

The derived Bayesian estimate of the slope and intercept of the correlations are:

$$L_{150} = L_{250}^{1.00(\pm 0.01)} \times 10^{-1.28(\pm 0.24)} \quad (6.5)$$

$$L_{1.4} = L_{250}^{0.95(\pm 0.01)} \times 10^{-1.24(\pm 0.28)} \quad (6.6)$$

$L_{1.4}$ gives a slightly shallower slope than L_{150} . A shallower slope was also observed in the $L_{1.4}/\text{SFR}$ relation derived in the previous section. In the bottom panel of Fig. 6.10 the corresponding values of $q = \log_{10}(L_{250}/L_{150})$ for the same sources are shown. In Fig. 6.11 we show the L_{150} distribution of different class of galaxies as a function of L_{250} .

Effects of sample selection on the FIRC have been observed (e.g. Bell 2003; Jarvis et al. 2010); samples selected at different bands present different correlations. The available data also allow me to probe this feature of the correlation. In order to evaluate this the same relation was derived using sources detected at 150-MHz as function of L_{250} . Fig. 6.13 shows the results of this analysis together with stacking results of L_{250} for SFGs (see Table 6.5 for the results of stacking and KS test). Fitting was implemented in the same way using MCMC and the best-fit relations derived from this

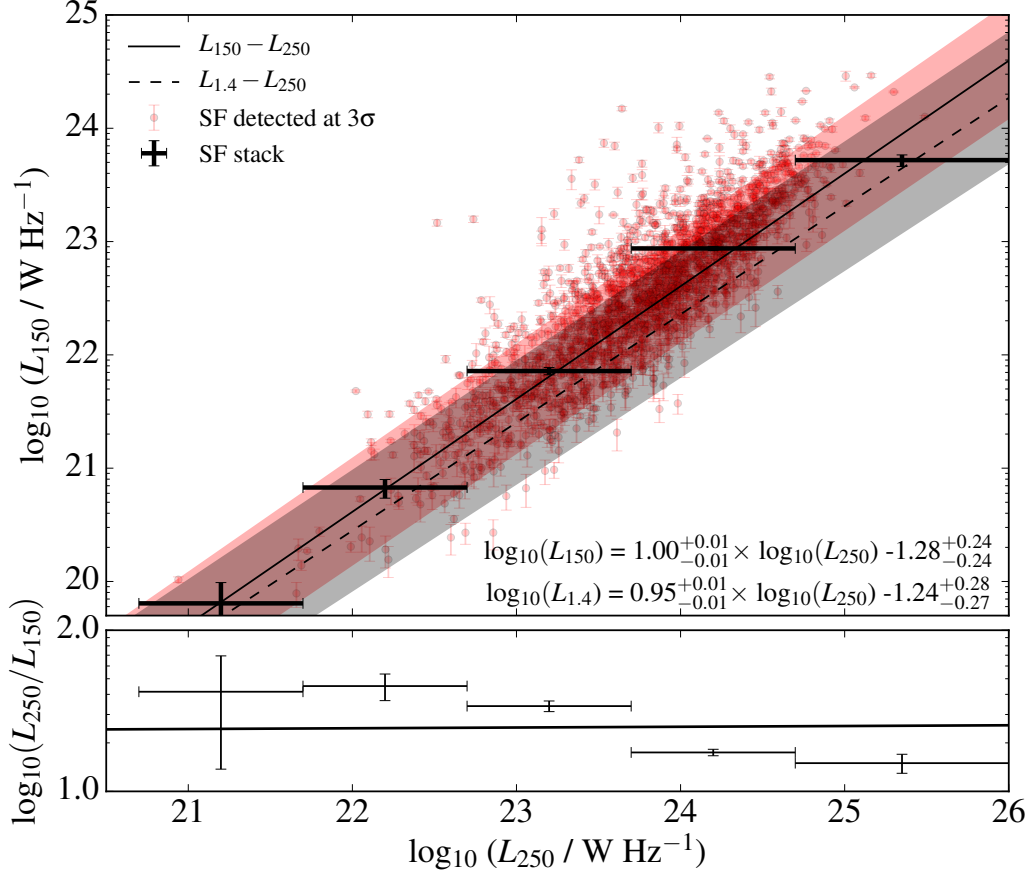


Figure 6.10: The distribution of LOFAR 150 MHz luminosities of SFGs as a function of their *Herschel* 250 μm luminosities. The solid black line is the best fit obtained using all SFGs detected at L_{250} . Shaded red and black region around the best fit shows $\pm\sigma$ errors. Results of the stacking analysis are also shown for L_{150} (large black crosses).

Sample	$\log_{10}(L_{250})$ bins	Mean z	N	L_{150} $\times 10^{21} (\text{W/Hz})$	L_{250}/L_{150}	KS probability
SFGs	20.7-21.7	0.05	10	$0.06^{+0.05}_{-0.03}$	$41.22^{+28.36}_{-28.36}$	0.81
	21.7-22.7	0.05	174	$0.69^{+0.14}_{-0.12}$	$43.79^{+8.40}_{-8.40}$	$\ll 1\%$
	22.7-23.7	0.06	1210	$7.28^{+0.53}_{-0.58}$	$33.32^{+2.58}_{-2.58}$	$\ll 1\%$
	23.7-24.7	0.09	1504	$89.73^{+3.59}_{-3.61}$	$16.72^{+0.73}_{-0.73}$	$\ll 1\%$
	24.7-26.0	0.11	57	$561.74^{+63.09}_{-79.29}$	$13.73^{+1.95}_{-1.95}$	$\ll 1\%$

Table 6.4: Results of the stacking analysis that was implemented using L_{150} of SFGs in each L_{250} bin. Columns as for Table 6.3.

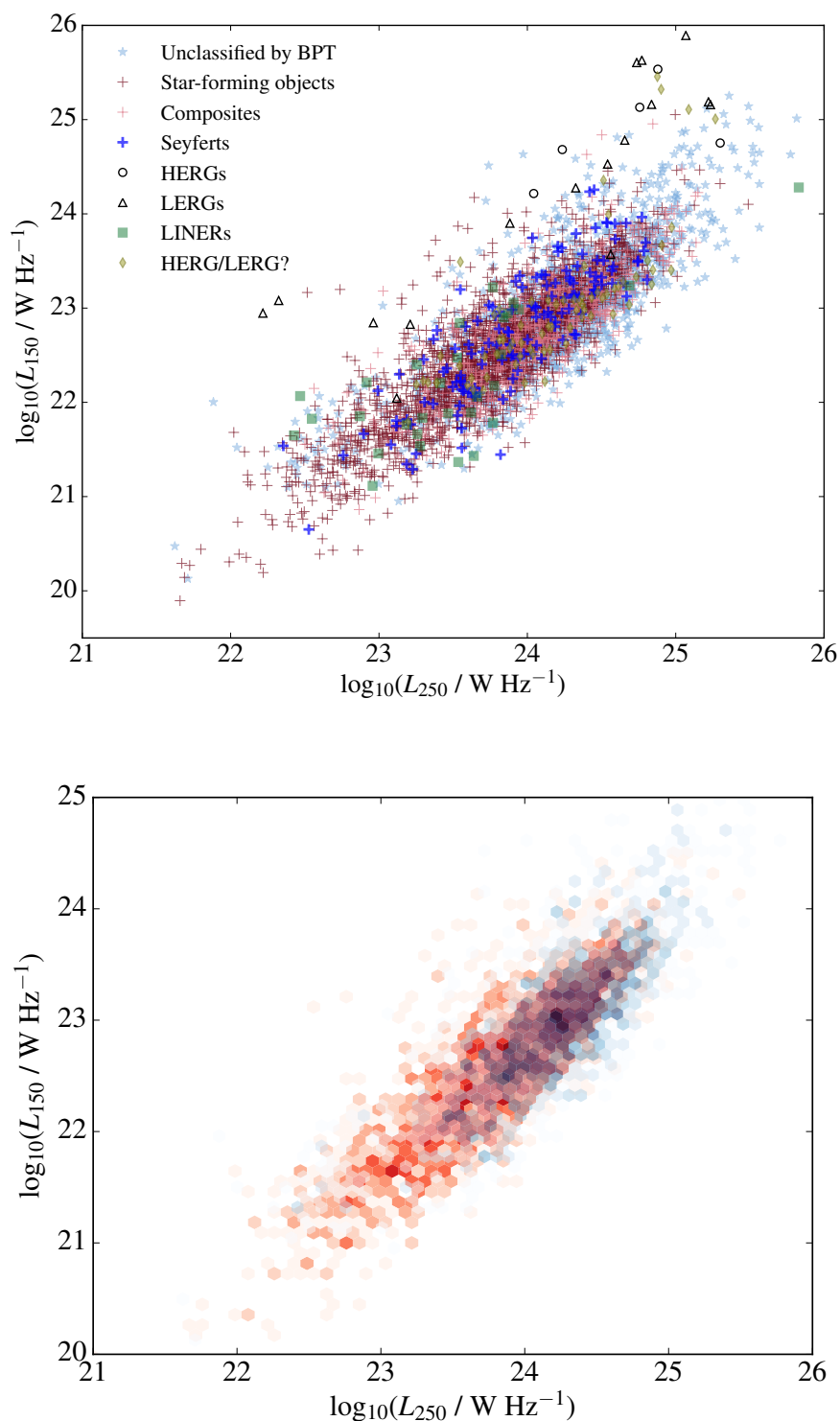


Figure 6.11: Top panel: The distribution of LOFAR 150 MHz luminosities of different class of objects in the sample detected at 3σ as a function of their *Herschel* $250\mu\text{m}$ luminosities. Symbols and colours as for Fig. 6.1. Bottom panel: Density plot of galaxies that are unclassified by BPT (shown as blue) and SFGs classified by BPT (shown as red), detected at 3σ in both bands.

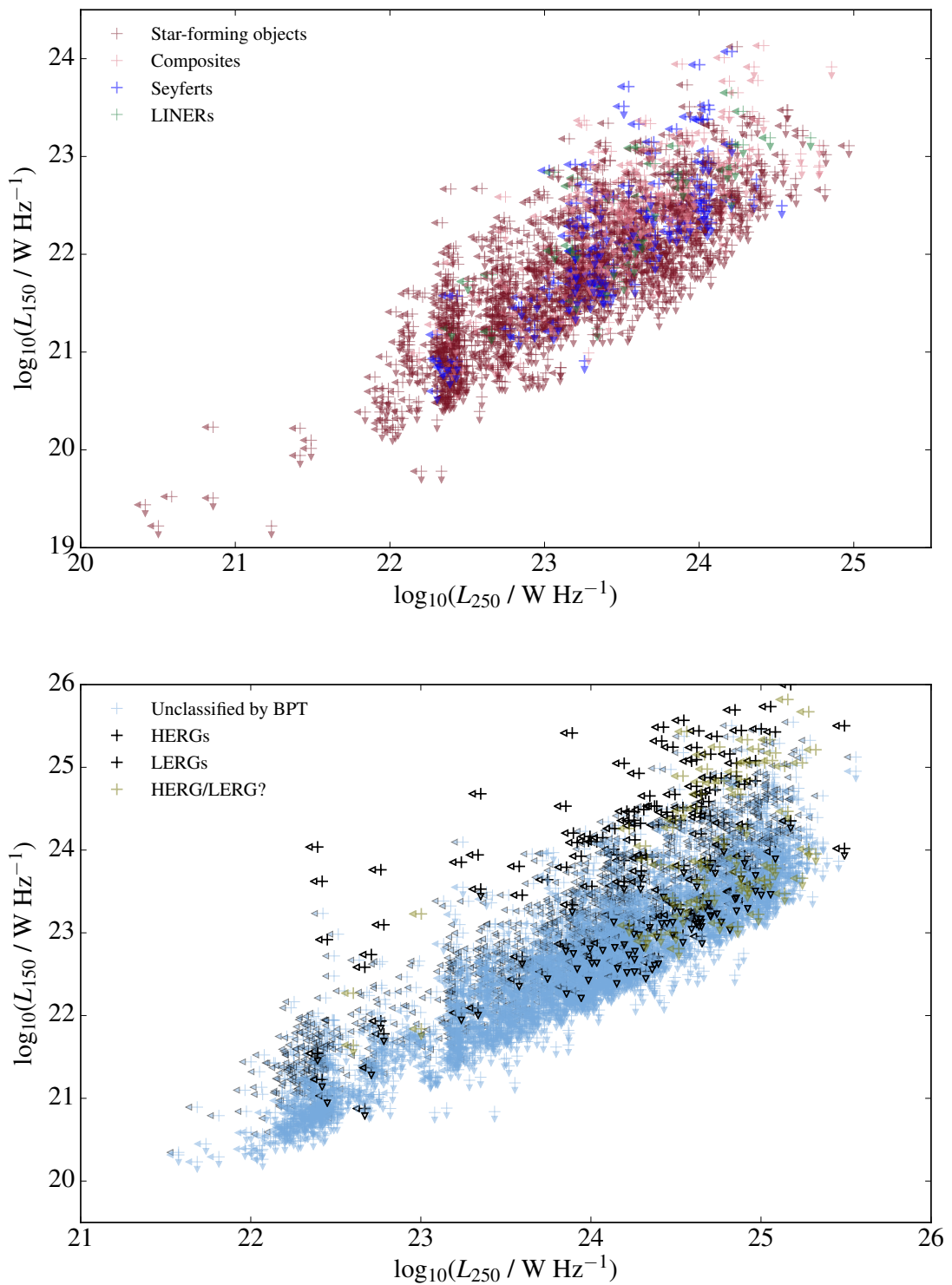


Figure 6.12: Top panel: Limits of SFGs, Composites, Seyferts and LINERs. Symbols and colours as for Fig. 6.1. Bottom panel: Limits of objects that are unclassified objects by BPT and radio AGN (HERGs, LERGs and HERG/LERG?). Symbols and colours as for Fig. 6.1. In both panels down-pointing arrows are limits at 150 MHz and left-pointing arrows are limits at 250 μm *Herschel* band.

Sample	$\log_{10}(L_{150})$ bins	Mean z	N	$L_{250-\mu m}$ $\times 10^{22}$ (W/Hz)	L_{250}/L_{150}
SFGs	18.0–20.5	0.04	6	$0.35^{+0.13}_{-0.14}$	$29.60^{+11.80}_{-11.80}$
	20.5–21.3	0.05	79	$4.07^{+0.43}_{-0.43}$	$32.42^{+3.72}_{-3.72}$
	21.3–21.9	0.05	259	$12.17^{+0.75}_{-0.65}$	$28.58^{+1.68}_{-1.68}$
	21.9–22.3	0.06	365	$32.71^{+1.31}_{-1.17}$	$25.53^{+0.95}_{-0.95}$
	22.3–22.9	0.08	607	$75.67^{+2.00}_{-1.87}$	$19.57^{+0.77}_{-0.77}$
	22.9–23.3	0.08	422	$171.49^{+5.53}_{-5.46}$	$14.35^{+0.44}_{-0.44}$
	23.3–23.9	0.11	231	$369.06^{+13.57}_{-14.93}$	$11.58^{+0.52}_{-0.52}$
	23.9–24.9	0.12	43	$642.00^{+99.78}_{-106.43}$	$4.52^{+0.88}_{-0.88}$

Table 6.5: Results of the stacking analysis that was implemented using L_{150} of SFGs in each L_{250} bin. Columns as for Table 6.3.

are as follows:

$$L_{150} = L_{250}^{0.74(\pm 0.01)} \times 10^{+7.16(_{-0.16}^{+0.16})} \quad (6.7)$$

$$L_{1.4} = L_{250}^{0.71(\pm 0.01)} \times 10^{+8.31(_{-0.24}^{+0.23})} \quad (6.8)$$

6.5 Interpretation

6.5.1 The L_{150} /SFR relation

The slope obtained from the regression analysis of L_{150} against SFR using SFGs is less than unity. In the bottom panel of Fig. 6.4 I show the ratio of averaged mean of L_{150} to SFR in each bin (see Table 6.3 for values of these ratios) as well as the regression line (the solid black line in the top panel) divided by SFR. The results of L_{150} /SFR ratios in the bottom panel show that the relation between SFR and non-thermal emission from SFGs as a function of SFR is almost the same for sources with high radio luminosities (or $\psi > 1 M_{\odot} \text{ yr}^{-1}$) whereas low-luminosity sources present slightly lower ratios. Garn et al. (2009) reported different results from the results found in this work; they found no variation for $L_{610\text{-MHz}}/\psi$ as a function of SFR. It is worth noting that Garn et al. (2009) used a sample of radio-selected SFGs which covers a wider redshift range ($0 < z < 2$). In this work, the sample consists of local SFGs. More importantly, these SFGs were selected using optical emission lines. All these differences might cause disagreement between the results and the results of Garn et al. (2009). Additionally, a wide redshift range can mask any real variation in the link between any L_{Radio} /SFR

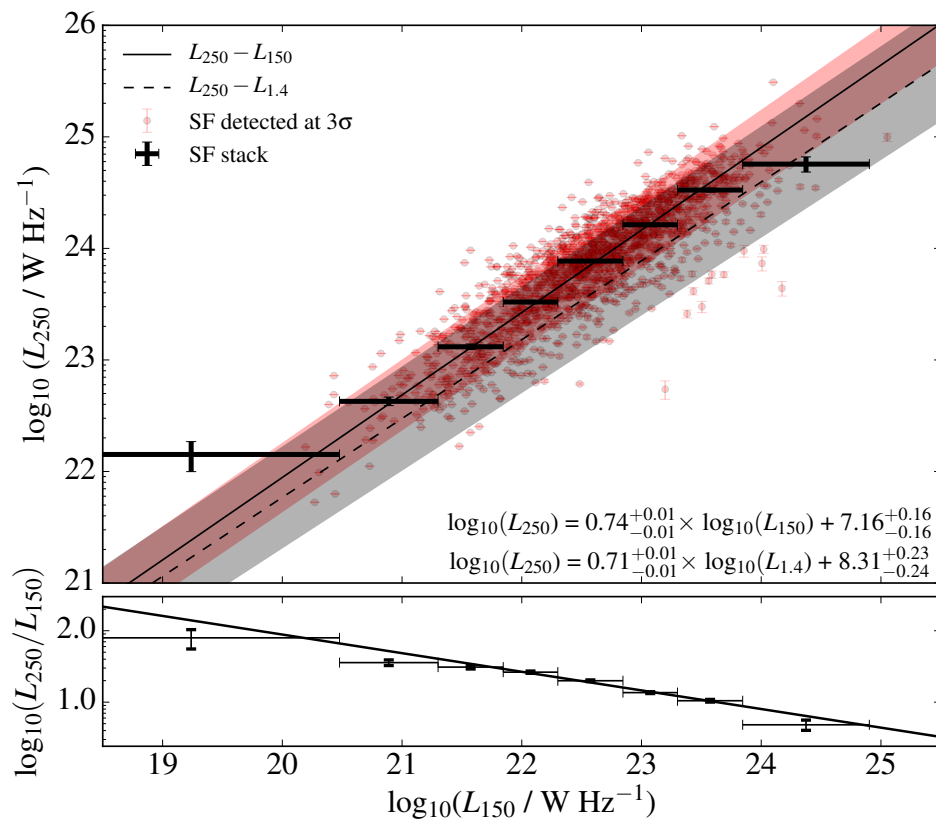


Figure 6.13: The distribution of *Herschel*-250 μm luminosities of SFGs as a function of their LOFAR 150-MHz luminosities. The solid black line is the best fit obtained using all SFGs detected at L_{150} and the dashed black line shows the best fit to all data points of SFG obtained using $L_{1.4}$ and scaled to 150 MHz. Shaded red and grey regions around the best fits show $\pm\sigma$ errors of these fits. Results of the stacking analysis are also shown for L_{250} as large black crosses.

and SFR, whereas here I am focusing on a very narrow range in redshift using a large sample.

Non-universality of the L_{150} –SFR relation is particularly clearly seen in the panels of Fig. 6.5. In the left panel, a large scatter is apparent at the low-luminosity end of the distribution which was seen by others (e.g. Chi & Wolfendale 1990; Helou & Bica 1993; Bell 2003). We also see, for a given L_{150} predicted by the relation derived by the regression analysis, the actual L_{150} is higher than the expected values for sources with $\sim L_{150} > 5 \times 10^{22} \text{ W Hz}^{-1}$. In the right panel of Fig. 6.5, in which the data were parameterised including a dependence on both stellar mass and SFR, the correlation is tighter and the disagreement between the predicted– and actual– L_{150} for sources with $\sim L_{150} > 5 \times 10^{22} \text{ W Hz}^{-1}$ is also prominent. First of all, the results of these two fitting procedures indicate that low-luminosity SFGs with large scatter are the main driving population of the fit. Furthermore, Fig. 6.6 demonstrates the effect of the SFG population at the low-end of the diagrams in the fitting analysis: the large scatter disappears in the left panel because we are fitting the data of SFGs with $\psi < 1 \text{ M}_{\odot} \text{ yr}^{-1}$ whereas in the right panel the scatter is large as galaxies with $\psi > 1 \text{ M}_{\odot} \text{ yr}^{-1}$ were used for the fitting. Although some studies (e.g. Yun et al. 2001) observed a scatter for high luminosity sources, we do not see a scatter as high as we observe for low luminosity sources. However, the majority of high luminosity sources are detections here and since the sample was created in the way explained in Section 6.3.1, the sample is biased towards selecting high SFR galaxies in this luminosity regime.

The sample consists of SFGs selected in a consistent way (using optical emission lines) and cover a very narrow redshift so why do SFGs with different luminosities differ from each other in terms of the $L_{150} - SFR$ relation? Clearly there is some level of deficiency in the observed L_{150} in comparison to the predicted L_{150} for low-luminosity sources. As discussed in Section 6.1, this can be explained in a non-calorimeter model. This is because electron calorimetry assumes that all $\text{CR}e$ are retained by magnetic fields and all energy contained within the $\text{CR}e$ is radiated as synchrotron radiation so independent of the strength of magnetic field (i.e. the total emitted energy will be the same whether the $\text{CR}e$ energies are radiated away over a short time in a strong magnetic field, or over a long time in a relatively weak magnetic field). Moreover, the time scale for $\text{CR}e$ to radiate all energy is expected to be shorter than the time scale that is needed for them to escape the galaxy according to the electron calorimetry model. However, some studies (e.g. Klein 1991; Price & Duric 1992; Lisenfeld et al. 1996; Bell 2003, Kitchener et al. submitted) have suggested that the electron *calorimetry*

might fail for low-mass (or low-luminosity) galaxies and cause radio luminosity deficiency due to the escape of CRe from the galaxy as a result of small galaxy sizes. Lacki et al. (2010) presented a non-calorimeter model taking into account different parameters (e.g. energy losses, magnetic field and gas density etc.) as a function of the gas surface density and argued that the correlation breaks down for low surface brightness dwarfs.

In a non-calorimeter model, the size (or mass) of a galaxy matters, as CRe might escape the galaxy before they radiate all their energy if the time scale required for them to diffuse is shorter than the radiative loss time scale, which is indirectly defined by the galaxy size. For this reason, we included a dependence on galaxy mass in Section 6.4.1. As seen in the right plot of Fig. 6.5 I take into account stellar masses of SFGs in the fits to sample but we still see a discrepancy between the observed and predicted L_{150} for low-luminosity sources. I conclude that either the diffusion losses are important and this is important in particular for low-luminosity galaxies or properties of magnetic fields in these galaxies are different than their bright counterparts.

There are SFGs, some of which are upper limits, that deviate from the green line in Fig. 6.7 at the high luminosity end. Here I use a sample of SFGs that are classified by their optical-emission-lines. Because of using a flux limited sample, as well as the detection threshold that I apply, the sample is biased towards selecting high SFR galaxies at the high end of the sample. As I mentioned in Section 6.3.1 these objects are probably starbursts at high redshift with strong optical emission lines. Furthermore, as pointed out above, Hardcastle et al. (2016) observed an evolution in the radio luminosity function of SFGs so we might start seeing the effect of this evolution for these sources as well.

As can be seen in Fig. 6.7 a broken power-law with a smooth transition provides a much tighter relationship between the predicted and the actual L_{150} and most SFGs lie on the green line. The transition point of SFR (ψ_c) was constrained to be $\sim 0.6 M_\odot \text{ yr}^{-1}$ (broadly corresponding to $L_{150} \sim 10^{22} \text{ W Hz}^{-1}$) by the fitting procedure, which is lower than the value of $3.5 M_\odot \text{ yr}^{-1}$ estimated by Bell (2003). Although in Fig. 6.7 the relation is much tighter, we can still see that most of the low-luminosity sources are not explained by the best fit. This once again reinforces the idea that low-luminosity SFGs basically are not perfect calorimeters. Likewise, there are high luminosity sources that deviate towards higher radio luminosities, which is due to being only able to detect galaxies with high SFR as a result of the classification of sources and using the BPT and a flux limited sample.

There is a correlation expected between mass (or luminosity) and size (or surface brightness) of galaxies with different morphologies that is around R_e (half-light radius) $\propto M_*^{0.1-0.4}$ (Lange et al. 2015). As discussed above, galaxy size is crucial for a non-calorimeter model. Parameterising the data by taking into account both SFR and stellar mass show that stellar mass index of SFGs are in the range $0.2 < \gamma < 0.45$, which is in agreement with the observed mass-size relation. On the other hand, the L_{150}/ψ relation is changing quickly with SFR; in particular, comparison of the right panel in Fig. 6.5 and Fig. 6.7 show that the index of SFR is changing from 0.53 to 0.77. Additionally, the SFR index changes from 0.52 to 1.23 between the sample with $\psi < 1 M_\odot \text{ yr}^{-1}$ and $\psi > 1 M_\odot \text{ yr}^{-1}$. If the low luminosity sources are not perfect calorimeters we expect to see relatively strong dependence on mass as the galaxy size determines whether CRE produced by SFR will have a chance to radiate all their energy in radio before they escape the galaxy. This is actually what we see in the left panel of Fig. 6.6 where we carry out fitting for low SFR SFGs; the mass index is 0.45. However, if I compare this to the right panel of the same figure where the fitting was performed for high luminosity sources (or high SFR), which are expected to be ideal calorimeters, although there is a slight decrease in the mass index we still see a weak dependence on stellar mass.

With the current models it is not straightforward to explain the result I obtain here: Why does radio luminosity of SFGs studies here change quickly with changing SFR? Why does stellar mass still matter for high SFR sources which are expected to be ideal electron calorimeters? There is a break in the L_{150}/ψ relation but where does this exactly occur? Is this break determined by stellar mass of a galaxy or its SFR? This is because there are complicated processes involved in the L_{150}/ψ relation and with the available data we cannot carry out a detailed analysis taking into account all these complications to answer above questions. The only clearly emerging picture in this work is the different nature of low luminosity (or SFR) and high luminosity SFGs in the nearby Universe. Assuming the calorimetry is the reason for the L_{150}/ψ correlation, as expected star-forming galaxies with high SFR are most likely ideal electron calorimeters whereas the picture is changing towards low luminosity SFGs.

Frequency dependence of the relation

The slope of the $L_{1.4}/\psi$ relation derived using $L_{1.4}$ is lower than the slope obtained using L_{150} . This has been previously observed in the studies of the FIRC (e.g. Price & Duric 1992; Niklas 1997) and it was argued that thermal radio emission dominates mainly at higher radio frequencies whereas non-thermal radio emission dominates at

lower radio frequencies, giving steeper correlation with SFR. This is because thermal radio emission has a spectrum $\propto \nu^{-0.1}$ whereas this is steeper for non-thermal radio emission ($\propto \nu^{-0.7}$). Radio luminosity from SFGs at 150 MHz should have a negligible level of contamination from thermal radio emission. However, at 1.4 GHz we might expect to observe some contribution from thermal emission (Condon 1992). Therefore, the different slopes might be attributed to differing contributions from thermal emission at 150 MHz and 1.4 GHz.

Nature of unclassified objects by BPT diagrams

The most prominent picture in Fig. 6.8 is that sources with AGN signatures clearly stand out. More importantly, sources that are not strongly (at 3σ) detected in their optical emission-lines do not follow the same relation between L_{150} and SFR with SFGs. I think that a high fraction of these sources are low-luminosity AGN which do not have strong optical emission-lines so cannot be classified by the BPT diagrams. Probably some fraction are SFGs at high redshifts, which are simply missed by the BPT classification because of the detection threshold used while classifying galaxies, but those that have L_{150} above the SFR prediction are most likely AGN. These are a very important contaminating population in any attempt to estimate SFR from radio data alone.

6.5.2 The far-IR/radio correlation of SFGs

In Fig. 6.10 there are two outstanding features: (i) the slope of the $L_{150} - L_{250}$ relation is unity, while the slope is less than unity for $L_{1.4}$, (ii) $q (=L_{250}/L_{150})$ is constant with increasing L_{250} . A scaled version of the slope at 1.4 GHz approximately equals to $q = L_{1.4\text{GHz}}/L_{250\mu\text{m}} = 1.8$, which is slightly lower than earlier reports ($2 < q < 2.5$; e.g. Jarvis et al. 2010; Smith et al. 2014). As observed for the L_{150}/SFR relation, the impact of thermal emission from SFGs observed at 1.4 GHz also presents itself in the relation between far-IR and radio luminosity: we obtain flatter slope when we use $L_{1.4}$ ($\alpha = 0.95$) whereas $\alpha = 1.0$ for L_{150} .

On the other hand, in Fig. 6.13 where a radio detection is required we see that the slope is a lot flatter and the q value decreases towards high L_{250} ($L_{250} \propto L_{150}^{0.74}$). This is somewhat flatter than the slope reported by Cox et al. (1988) where they found $L_{FIR} \propto L_{151}^{0.87}$. A negative trend of q with increasing L_{250} has been observed by others as well (e.g. Price & Duric 1992; Yun et al. 2001; Jarvis et al. 2010). One reason

that might be causing this is a contamination from AGN as we move toward to higher luminosities. In particular, it is expected that radio AGN and SFGs populations overlap around $L_{150} \sim 5 \times 10^{23} \text{ W Hz}^{-1}$ (see the left panel in Fig. 17 of Hardcastle et al. (2016) in which they show the derived radio luminosity functions of both SFGs and radio AGN). In that case, galaxies included in the last four bins in Fig. 6.13 might be AGN classified as SFG by the BPT diagnostics, affecting the ratio q . This is because they will have relatively higher radio luminosities which will affect in a negative way the measured ratio of q . The slopes that were obtained for L_{150} and $L_{1.4}$ are similar but $L_{1.4}$ still gives slightly flatter slope.

As pointed out by Sargent et al. (2010) and some others, relations that are derived using samples from different selection bands in flux-limited surveys will be biased. Comparison of the slopes obtained using samples selected at different wavelengths show the impact of selection effects on the FIRC derived in this paper. In Fig. 6.13 we see that the slope is much less than unity where we use SFGs detected in radio whereas SFGs detected in far-IR, as in Fig. 6.10 gives a slope of unity.

Although I do not exclude non-detections in any analyses carried out here, we are still biased by constraining the data to galaxies detected in one band and including non-detections in the other. In order to bring the true FIRC to light deep high-sensitive surveys are necessary. We will then be able to generate a sample of galaxies fully detected in one or both bands, which will provide an unbiased relation between the far-IR and radio luminosity for star-forming galaxies.

The far-IR/radio correlation of all galaxies

In the top panel of Fig. 6.11 I show the relationship between L_{250} and L_{150} for all galaxies in the sample detected at both bands at 3σ . Since over-plotted data in common luminosity regions will hide the real distribution of galaxies, in the bottom panel I present a density plot of SFGs and galaxies that are unclassified by BPT, detected at both bands. From the top panel we can see that different classes of galaxies detected in both bands tend to follow the same relation with SFGs detected in the same bands. There are a few AGN with higher radio luminosities, which is expected as there is additional radio emission from AGN along with the radio emission due to star formation. In the bottom panel, it is clearly seen that although there is some overlap between SFGs and unclassified objects that are both detected in radio and far-IR, unclassified objects occupy the high end of the diagram. Some of these have slightly higher radio luminosities than SFGs for a given far-IR luminosity. These results indicate that

some of the detected unclassified objects are probably SFGs missed by BPT diagrams due to high redshifts whereas some of these are low-luminosity AGN. This is more apparent if we compare both panels in Fig. 6.12 in which we show limits in radio and far-IR bands for different classes of galaxies. Unclassified galaxies have in general higher radio luminosities than other galaxies in the sample and radio-AGN occupy the upper corner of the bottom panel as they have much higher radio luminosities. All these agree with the picture we see in Fig. 6.8, most of the unclassified sources are most likely low-luminosity AGN, but some fraction of them are SFGs at higher redshifts ($z < 0.35$). Seyferts, Composites and LINERs broadly follow the same relation as SFGs but there are also some Seyferts with high radio luminosities, occupying a region close to radio-loud AGN.

6.6 Conclusions and future work

A survey of the H-ATLAS/NGP field was carried out at low radio frequencies at an effective frequency of 150 MHz using LOFAR in order to explore the low-frequency radio luminosity/SFR relation of SFGs in the local Universe ($0 < z < 0.3$). SFRs of these objects were derived using SED fitting with MAGPHYS. *Herschel*-250 μm flux densities were also measured using *Herschel* maps, which allowed us to investigate the FIRC for the same objects.

The conclusions from this work are as follows:

- I carried out a number of regression analyses in order to quantify the relation between L_{150} and SFR for SFGs classified using BPT diagrams. In these, I used different parameterisations and included stellar mass in order to see its effect. I find that low-luminosity SFGs have a different relation between L_{150} and SFR than the main SFG locus, similar to earlier findings of others (e.g. Bell 2003).
- Galaxy mass is expected to be crucial in non-calorimeter models of the L_{radio}/ψ relation and there is a well-known relationship between stellar mass and SFR, the “main sequence”, thus taking into account stellar masses of SFGs in the analysis is important. The availability of stellar mass measurements of SFGs in the sample allowed me to investigate this and the results show that including the stellar mass in the parameterisation provided a tighter relationship (comparison of the left and right panel in Fig. 6.5). On the other hand, the different nature of low-luminosity sources is still striking.

- I then parameterised the relationship using a broken power-law relation (Eq. 6.4), in the hope of deriving the genuine relation between L_{150} , SFR and stellar mass for SFGs in the local Universe. Although this provides a tight correlation over most of the data we still see deviations from it for low-luminosity (or SFR) star-forming galaxies. All these findings clearly reinforce the idea that electron calorimetry does not hold for low-luminosity SFGs. A natural explanation for this would be the importance of the diffusion time scale of $\text{CR}e$ in these galaxies. Since low-luminosity galaxies have relatively smaller masses (accordingly smaller sizes) $\text{CR}e$ might escape the galaxies before they radiate all of their energies, which in turn causes dimming in the observed radio luminosity. The data suggest that the breaking point is around $\sim \psi_c = 0.6 M_\odot \text{ yr}^{-1}$, which is much lower than $3.5 M_\odot \text{ yr}^{-1}$ found by (e.g Bell 2003).
- Comparison of the slopes obtained from the regression analyses (both the FIRC and the radio luminosity/SFR relation) show that $L_{1.4}$ provides a flatter slope than we obtain for L_{150} . This has been observed before and it was argued that thermal radio emission dominates mainly at higher radio frequencies whereas non-thermal radio emission dominates at lower radio frequencies, giving steeper correlation with SFR. Therefore, these different slopes might be attributed to differing contributions from thermal emission at 150 MHz and 1.4 GHz.
- Although I include non-detections in all of the analyses using flux-limited samples selected at different frequencies (at 250 μm and 150 MHz) in order to quantify the FIRC, they provided different slopes (relations 6.5 and 6.7, Figs. 6.10 and 6.13). This demonstrates the impact of selection effects on the FIRC derived in this study. Here we are still biased by constraining the data to galaxies detected in one band and including non-detections in the other. In order to bring the true FIRC to light deep high-sensitivity surveys are necessary. We will then be able to generate a sample of galaxies fully detected in one or both bands, which will provide an unbiased relation between the far-IR and radio luminosity for star-forming galaxies.

Another step that can be taken is to investigate whether a break in the L_{150}/ψ relation occurs depending on the stellar mass instead of SFR. Furthermore, we have not yet investigated if these relations hold for high redshift galaxies actively forming stars. All these will be explored in future work.

The results of this study will be crucial for future star formation studies of normal

galaxies. This is because far-IR instruments are relatively expensive and there is no far-IR instrument currently surveying the sky whereas *LOFAR* is currently surveying the northern sky and in the near future the SKA will provide radio measurements of galaxies in the southern sky. All these deep surveys will provide a large sample of star-forming galaxies with a range of radio luminosities (or SFRs) and by means of this relation, SFRs of galaxies can be effectively derived.

Chapter 7

Conclusions and future prospects

*“With presidential primaries in full steam, with the country wrapped up in concern about the economy, immigration and terrorism, one might wonder why we should care about the news of a minuscule jiggle produced by an event in a far corner of the Universe. The answer is simple. While the political displays we have been treated to over the past weeks may reflect some of the worst about what it means to be human, this jiggle, discovered in an exotic physics experiment, reflects the best. Scientists overcame almost insurmountable odds to open a vast new window on the cosmos. **And if history is any guide, every time we have built new eyes to observe the universe, our understanding of ourselves and our place in it has been forever altered.**”*

Lawrence M. Krauss, Finding Beauty in the Darkness

This thesis aims to further our understanding of the accretion modes of radio-loud AGN, differences between the host galaxies of different AGN samples and the reasons behind this, and the low-frequency radio luminosity–SFR relation. For this, I conducted a number of investigations in order to address the points given in Section 1.6. I briefly remind the reader of these points below:

1. To date, investigations of either small samples of radio-loud AGN or single objects in the near- and mid-IR came to contradictory conclusions. Can we understand the reasons for this by defining complete large mid-IR samples of radio-loud AGN? In addition to this, do the different emission line classes of radio galaxies have characteristic mid-IR natures? How can we diagnose accretion modes in radio-loud AGN? How reliable are the infrared colour-colour diagrams to select AGN?
2. What are the star formation properties of different types of AGN in the local Universe ($0 < z < 0.6$) as a function of their AGN activity? Do we see any differences in the star-formation properties of HERGs and LERGs in the local Universe? Whether any correlation exists or not, what can we learn about the growth of massive black holes in the contemporary Universe?
3. What can we learn from low-frequency radio surveys with regard to AGN and normal galaxies? The low radio frequency window is one of the few spectral windows that still remain to be explored. In particular, surveys of large fields are necessary in order to obtain large samples and so comprehend the nature of low energy electrons which will further our understanding of the nature of normal galaxies and AGN. With *LOFAR* we are now able to produce high fidelity images that can be used for scientific purposes such those mentioned above.
4. What can we learn from low-frequency radio observations with regard to the radio–FIR relation that we observe in local star-forming galaxies? What is the relation between the low-frequency radio luminosity and star formation rate in these galaxies?

I will detail my conclusions derived from these investigations and describe the future prospects in four parts:

7.1 Probing radio-loud AGN at high-redshifts with *WISE*

In Chapter 3, for the first time, I provided a complete mid-IR study of the complete and relatively large sample of radio-loud AGN. In order to do this, I combined four samples namely 3CRR, 2Jy, 6CE and 7CE which provided a sample of radio-loud AGN at $0.003 < z < 3.395$ and I used the data taken by *WISE*. This work can be divided into five sections:

- **Selection of AGN using infrared colours:** I evaluated commonly used colour-colour diagrams for selecting AGN using my own sample as well as coherent mid-IR data taken by *WISE*. This evaluation showed that although these colour-colour diagrams or colour cuts help us to select some type of AGN, they are not successful for selecting all types of AGN. In particular, with the used method defined by Mateos et al. (2012) and in both panels of Fig. 3.3 we can clearly see that all LERGs and almost half of NLRGs are omitted if these colour cuts are used. For this reason, we have to use infrared criteria to select AGN with caution.
- **Near-IR characteristics of the radio-loud AGN sample:** I also evaluated the near-IR luminosity– z relation of the sample used in this work. The results reinforce the picture in which radio galaxies are hosted by giant ellipticals that formed their stars at high redshifts and evolved passively thereafter. At high redshifts ($z > 0.7$) 3CRR objects differ from 6CE and 7CE object having higher near-IR luminosities. This suggests that 3CRR galaxies are more massive systems with higher masses of stars at high redshifts compared to 6CE and 7CE radio galaxies.
- **Unification models:** I investigated the quasar-radio galaxy unification using the *WISE* 22 μm luminosity (AGN power indicator) and found that quasars are systematically more luminous in the mid-IR than radio galaxies, and more so at 12 μm than 22 μm . These results are consistent with the predictions of smooth torus models which show a strong effect of anisotropy. It should be noted that a number of studies showed that AGN torus is clumpy (e.g. Nenkova et al. 2008b). Note that, I did not use SED modelling of the sources in my sample as this was out of the scope of the work. Therefore, an interesting work would be to further this analysis to put better constraints on torus models.
- **Diagnosing accretion modes of radio-loud AGN:** I have shown for the first time with a large complete sample that low- and high- excitation radio-loud AGN have completely different mid-IR luminosities. While LERGs have extremely weak mid-IR luminosities—in fact many of them are not detected and have only upper limits—HERGs are mostly luminous sources in the mid-IR. These results obviously favour previously established accretion models (e.g. Hine & Longair 1979; Laing et al. 1994; Evans et al. 2006; Ogle et al. 2006; Hardcastle et al. 2007b; Janssen et al. 2012; Best & Heckman 2012; Russell et al. 2013); LERGs

do not hold any conventional AGN properties and accrete in a radiatively inefficient manner, while HERGs are powered by radiatively efficient accretion. This accretion-mode classification can now be *explicitly* identified in the mid-IR–radio plane for strong radio-loud AGN, like the sample used in this work. However, this may not work for sources with lower luminosity that are mostly found in the local Universe.

7.2 Probing the AGN activity–host galaxy relation in the low-redshift Universe with *Herschel*

In Chapter 4, I investigated the relation between AGN activity and host galaxy properties using radio-loud and radio-quiet AGN samples in the local Universe ($0 < z < 0.6$). In order to derive SFRs of sources I used *Herschel* 250 μm luminosity and the relationship between SFR and L_{250} was calibrated using SFRs derived from the $\text{H}\alpha$ emission line. The conclusions can be given in six parts:

- **The AGN power–SFR relation:** I examined the relation between AGN power and SFR for both radio-quiet and radio-loud AGN carrying out a stacking analysis. I binned the sources in the sample in their AGN power and stacked SFRs for each bin. Examination of radio-loud and radio-quiet AGN samples matched only in their AGN powers shows that for both AGN samples the rate of star formation increases with increasing AGN activity. The same conclusion can be drawn for their relative galaxy growth rates (Fig. 4.11).
- **SFR comparison between radio-loud and radio-quiet AGN:** A comparison of the star formation properties regarding these samples indicates that the host galaxies of radio-quiet AGN are forming more stars for a given black hole activity than their radio-loud cousins. This difference in the level of star formation per unit stellar mass goes up to an order of magnitude (Fig. 4.11).
- **SFR comparison in mass-matched samples:** To account for the likely influence of stellar mass I composed radio-loud and radio-quiet AGN samples matched in their galaxy masses. The same stacking analysis was implemented for these samples. The findings suggest that the black-hole growth and the star formation rate are coupled. The amount of stars forming for a given time increases with increasing AGN power for both AGN samples (Fig. 4.16).

The reason behind the apparent difference in SFR of radio-quiet and LERGs and HERGs were explored. We conclude that there are two possible classes of explanation for the observations. Either the strong jets we observe in radio-loud AGN suppress star formation in these galaxies or the difference between the galaxy morphology of the AGN samples leads to this observed disparity, or some combination of the two. Nevertheless, a direct role for feedback from the radio jets is not ruled out.

- **SFR comparison between HERGs and LERGs:** I also classified the radio-loud AGN sample in terms of emission-line type in order to compare their star formation properties. Both LERGs and HERGs present the same trend of increasing SFR with rising black-hole growth. In terms of their SSFRs both types of galaxies present a similar trend; their SSFRs are also increasing towards to higher AGN powers. They present almost a constant relative galaxy growth rate. There is only a marginal tendency for HERGs to have higher SFRs and SSFRs than LERGs when matched by AGN power (Fig. 4.18).
- **Black hole accretion rate—SFR relation:** I also assessed the relation between SFR and \dot{M}_{BH} and found that both radio-quiet and radio-loud AGN have a range of ratios of $\text{SFR}/\dot{M}_{\text{BH}}$. A comparison of the results with the observed correlation suggests that low-power AGN have black holes growing slower than expected from the $M_{\text{BH}}-M_{\text{Bulge}}$ relationship and black holes in high-power AGN are growing faster. The results obtained here cannot be explained with a simple model of the duty cycle of AGN (Fig. 4.17).

7.2.1 Future Prospects

With the available data I found out that mid-IR infrared luminosity provided by the *WISE* telescope cannot be used to predict AGN power for low-luminosity sources found in the local Universe due to star-formation contamination. For that reason, I used [OIII] emission-line luminosity as AGN power indicator. However, we know that [OIII] emission-line luminosity is also contaminated by star-formation (at lower level than the *WISE* 22 μm luminosity). For instance, Mingo et al. (2014) discussed that mid-IR luminosity is probably the best AGN power indicator. Using a more accurate AGN power indicator or using an SED fitting and implementing the same analysis would be useful to evaluate this aspect of the work. In this respect, as mentioned in the Introduction, we still do not understand the real relation between the radio power of

radio galaxies and the radio luminosity as various parameters are involved, thus using true estimate of jet power would improve the analysis. In this work, I used optically selected sample which has its own selection biases. Utilising the current sample in conjunction with samples selected at different wavelengths would be an interesting comparison to this particular work.

7.3 *LOFAR* survey of the H-ATLAS-NGP field and constructing a sample of AGN

The H-ATLAS/NGP field was surveyed by LOFAR as a part of SKSP. The effective frequency is 150 MHz. The survey field covers 42.7 square degrees and the LOFAR maps have around 10×8 arcsec resolution with the best $100 \mu\text{Jy}$ r.m.s. noise. The calibration and imaging were carried out using the method described by van Weeren et al. (2016). I carried out a process of source association and optical identification for sources detected at 5σ by *LOFAR* by visual inspection. This procedure provided 15292 sources. There are 6357 sources with secure single optical counterparts. The simple cross-matching gave 1048 of single, compact sources (non-AGN).

One of the conclusions that can be drawn from this work is that LOFAR provides excellent data that can be used for science. Additionally, the facet calibration method improves low-frequency radio images taken by LOFAR, pushing the sensitivity down to $100 \mu\text{Jy beam}^{-1}$ with a resolution of ~ 5 arcsec. The most prominent challenge in the process of gathering a sample of AGN detected in these radio images is that identifying multi-component AGN and the optical counterparts requires visual inspection.

7.3.1 Future Prospects

Low-frequency radio observations of AGN, in particular, are important because extended structures (such as plumes, lobes and hotspots) of radio AGN, which are produced by the interactions of powerful jets with their environment, can be better observed at low radio frequencies due to their steep-spectrum nature. The boundaries of extended structures of FR II sources are better constrained than low-luminosity sources. Therefore, low-frequency observations of FR I objects will be important to comprehend the interactions of low power jets with the external medium. Observations with high spatial resolution of selected interesting sources derived from existing identified samples such as 3CRR would present excellent opportunities to investigate

the physics of the interactions with their environments.

Another crucial aspect of the low-frequency radio observations is that they allow us to understand synchrotron-radiating electrons better. Observations of radio sources at GHz bands show a power-law synchrotron spectrum. However, at lower frequencies synchrotron self-absorption and a possible low-energy cutoff in the electron spectrum becomes important (Hardcastle et al. 2001). Therefore, studying the broadband nature of selected sources from these surveys together with follow-up radio observations will help us to reveal whether there is a spectral turnover at low frequencies and how (if) this is changing with source environment/properties. LOFAR and MWA are currently the only instruments that can assist us to investigate the low-frequency radio spectrum of galaxies and put some constraints on the low-energy electron spectrum.

7.4 Probing the validity of low-frequency radio data for SFR of local star-forming galaxies with *LOFAR*

- **The L_{150} /SFR relation of SFGs:** I carried out a number of regression analyses in order to quantify the relation between L_{150} and SFR for SFGs classified using BPT diagrams. In these, I used different models and included stellar mass in order to see its effect. The findings indicate that low-luminosity SFGs have a different relation between L_{150} and SFR from the main SFG locus, similar to earlier findings of others (e.g. Bell 2003). The availability of stellar mass measurements of SFGs in the sample allowed me to investigate the dependence of radio luminosity on stellar mass, and the results show that including the stellar mass in the modelling provided a tighter relationship (comparison of the left and right panel in Fig. 6.5). On the other hand, the different nature of low-luminosity sources is still striking. Modelling the data using a broken power-law relation (Eq. 6.4) provided a tight correlation over most of the data we still see deviations from it for low-luminosity (or SFR) star-forming galaxies. The clearly emerging conclusion from these analyses is the different nature of low luminosity (or SFR) and high luminosity SFGs in the nearby Universe. As expected, star-forming galaxies with high SFR are most likely ideal electron calorimeters whereas the picture is changing towards low luminosity SFGs. Additionally, comparison of the slopes which were obtained using the $L_{1.4}/\psi$ and the L_{150}/ψ relations showed that $L_{1.4}$ gives a flatter slope. This might be due to differing contributions from thermal emission at 150 MHz and 1.4 GHz.

- **Nature of unclassified objects in BPT diagrams:** Sources with AGN signatures clearly stand out in Fig. 6.8. I conclude that a high fraction of unclassified sources are low-luminosity AGN which do not have strong optical emission-lines and so cannot be classified by the BPT diagrams. Probably some fraction are SFGs at high redshifts, which are simply missed by the BPT classification because of the detection threshold used while classifying galaxies, but those that have L_{150} above the SFR prediction are most likely AGN. These are a very important contaminating population in any attempt to estimate SFR from radio data alone.
- **The far-IR/radio correlation of SFGs:** The slope of the $L_{150} - L_{250}$ relation is found to be unity whereas the slope is less than unity for $L_{1.4}$. The ratio q ($=L_{250}/L_{150}$) is constant with increasing L_{250} (Fig. 6.10). In Fig. 6.13, where a radio detection is required we see that the the slope is a lot flatter and the q value decreases towards high L_{250} . The reason for this might be a contamination from AGN as we move toward to higher luminosities as it is expected that radio AGN and SFG populations overlap around $L_{150} \sim 5 \times 10^{23} \text{ W Hz}^{-1}$ (e.g. Hardcastle et al. 2016). Another striking result from this analysis is the impact of samples that are selected from different observing bands in flux-limited surveys. Comparison of the slopes obtained using samples selected at different wavelengths show these effects on the FIRC derived in this analysis. In Fig. 6.13 we see that the slope is much less than unity where we use SFGs detected in radio whereas SFGs detected in far-IR, as in Fig. 6.10 gives a slope of unity. I conclude that deep sensitive surveys are necessary in order to uncover the true FIRC.

Both far-IR luminosity and radio luminosity are indicators of star formation in inactive galaxies. Far-IR instruments are relatively expensive and there is no far-IR instrument currently surveying the sky. With *LOFAR* we can obtain deeper and more sensitive maps of the sky than are available in current wide-area radio surveys such as FIRST. Therefore, the low-frequency radio luminosity/SFR relation derived will allow us to study galaxies with low luminosities. This will also be crucial for future star formation studies. *LOFAR* is currently surveying the northern sky and in the near future the SKA will provide radio measurements of galaxies in the southern sky. By means of this relation, SFRs of galaxies can be effectively derived.

7.4.1 Future Prospects

As mentioned in the previous section, the results of the low-frequency radio luminosity/SFR relation show that the relation is not very different from the relations derived using GHz luminosities. Further investigations of this relation and any effect of synchrotron self-absorption on the derived relation can be implemented using broadband spectra of the star forming galaxies in the sample. Sources with low luminosities (accordingly with low stellar masses) should be a particular interest as any break or a difference in the relation may be seen at low luminosities (Bell 2003). Combination of low-frequency radio surveys such as MSSS and the GaLactic and Extragalactic All-sky Murchison Widefield Array (MWA) survey (GLEAM) will provide a great opportunity to obtain wide area, shallow constraints on local galaxies where the radio luminosity/SFR relation can be estimated. In particular, the low-mass end of this relation will be crucial to understand the far-IR/radio relation better.

The next crucial step on my journey towards building up a full understanding of the low frequency radio/SFR relation is to investigate its evolution as a function of redshift. The current sample consists of only low-redshift galaxies. *LOFAR* also surveyed the GAMA fields over which we have *Herschel* measurements and much more extensive spectroscopic redshifts. This new data will provide a sample of galaxies over a wide range of redshifts with lower luminosities than FIRST can detect. Eventually, all these excellent data sets will enable us to explore the redshift evolution of this relation. This will be crucial for future star formation studies as the SKA will be capable of giving us reliable, dust free estimates of SFRs of galaxies at high redshifts, as long as the relation can be calibrated at lower redshifts.

Appendix A

Extended LOFAR radio sources

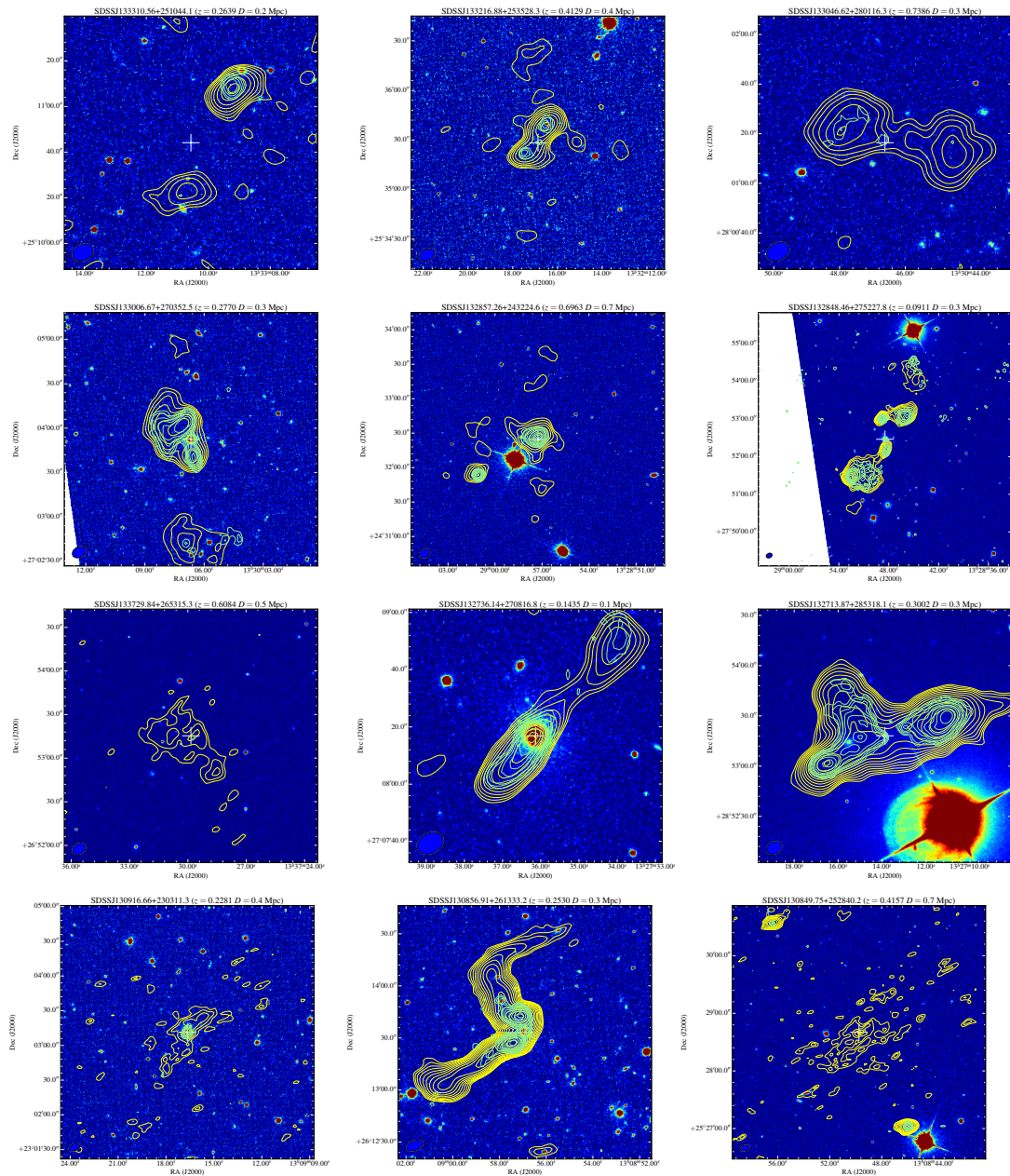


Figure A.1: Postage stamps of the optically identified objects at or close to 1 Mpc in physical size in the sample colours show SDSS *r*-band images: contours are LOFAR (yellow) and FIRST (green) contours starting at the local 3σ value and increasing by steps of a factor 2. An ellipse in the bottom left-hand corner shows the LOFAR beam.

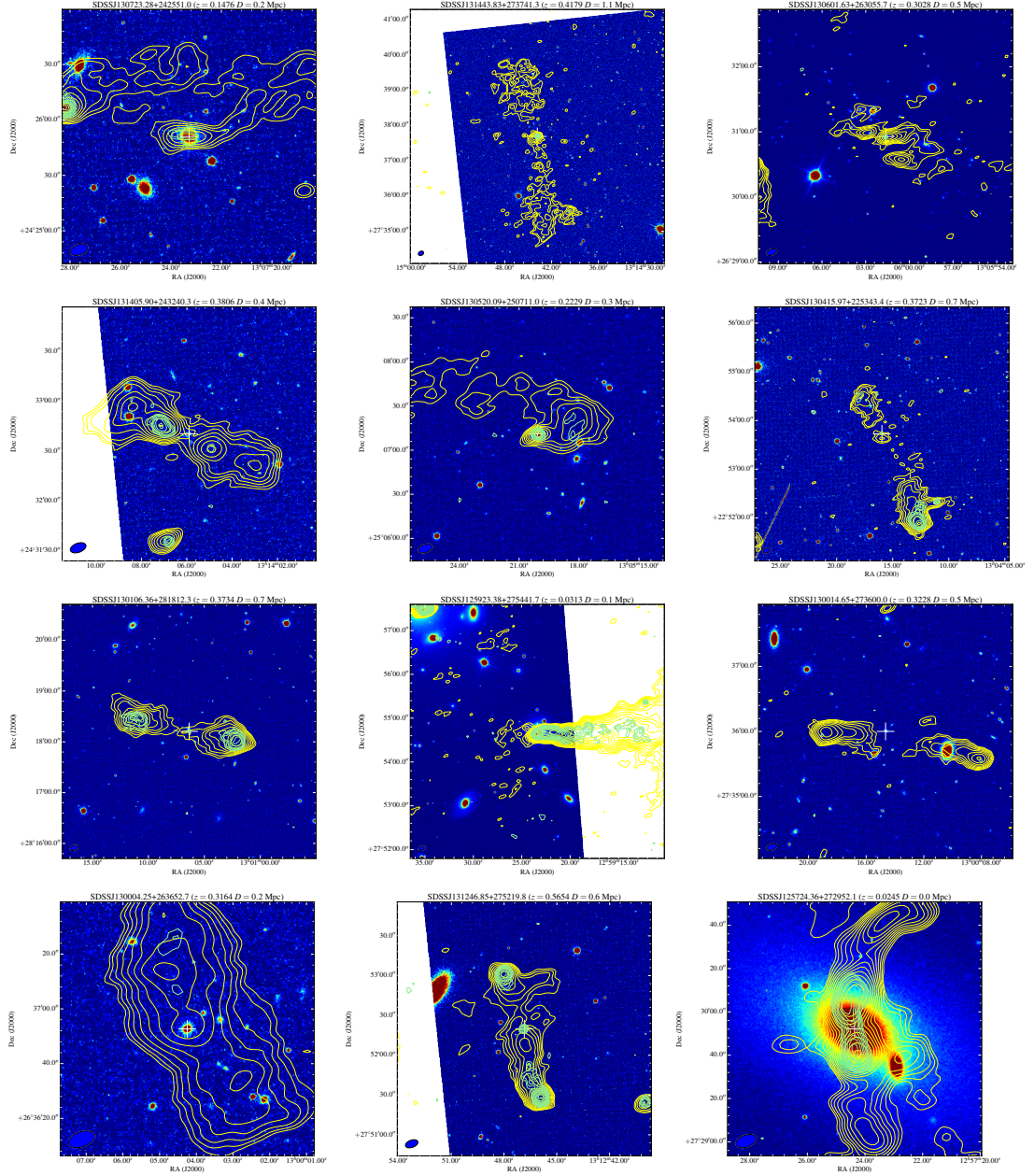


Figure A.2: Continued.

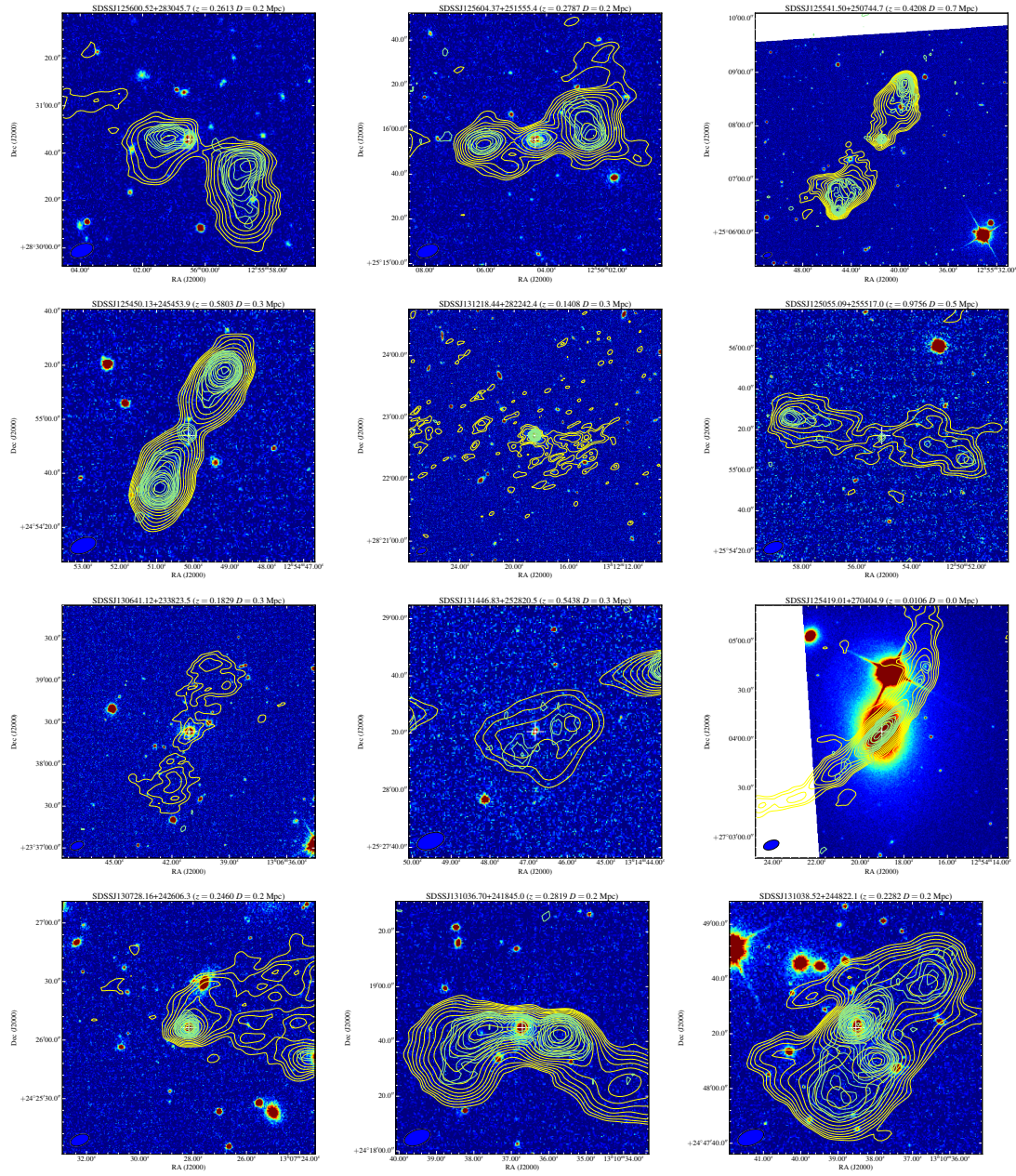


Figure A.3: Continued.

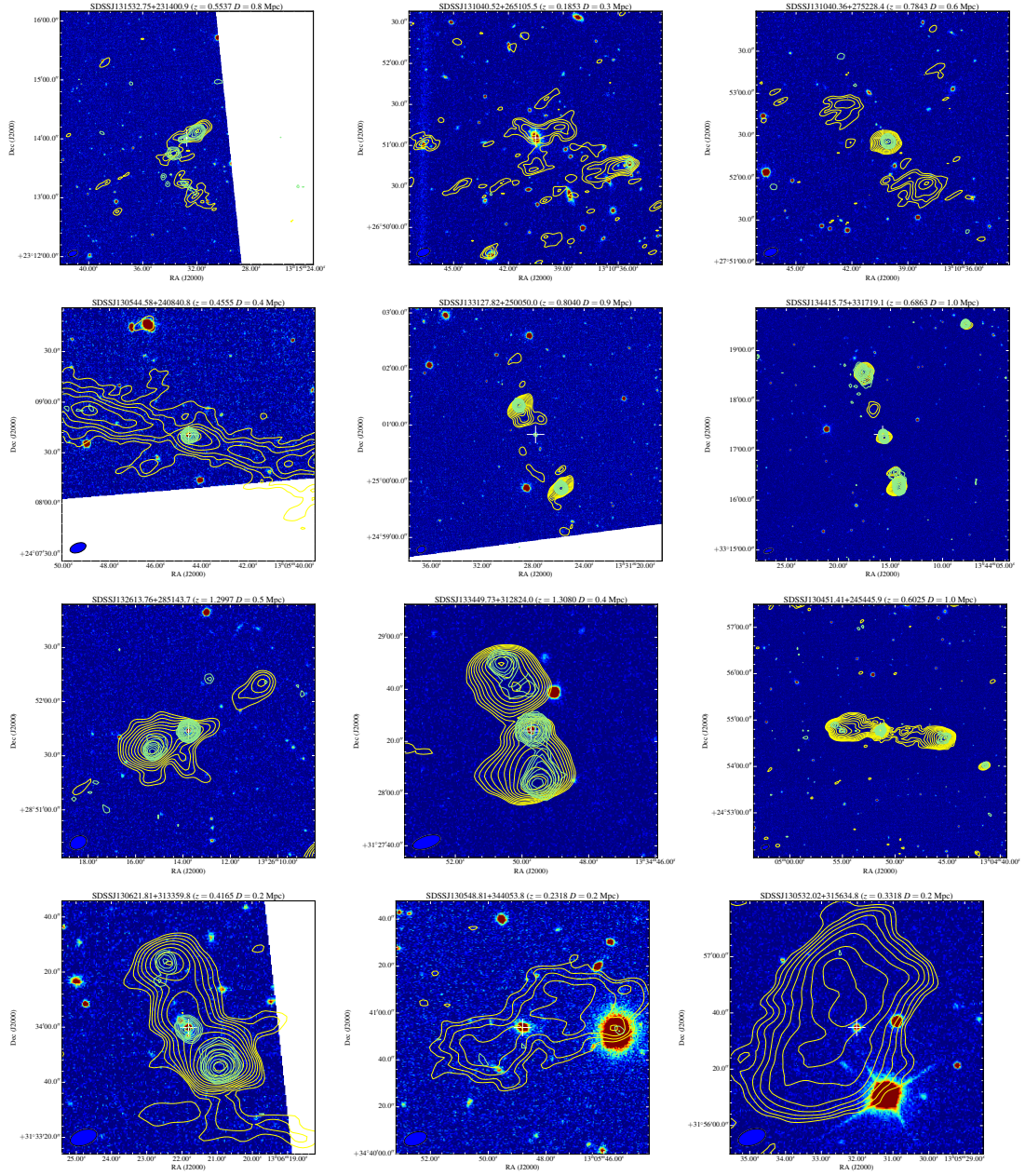


Figure A.4: Continued.

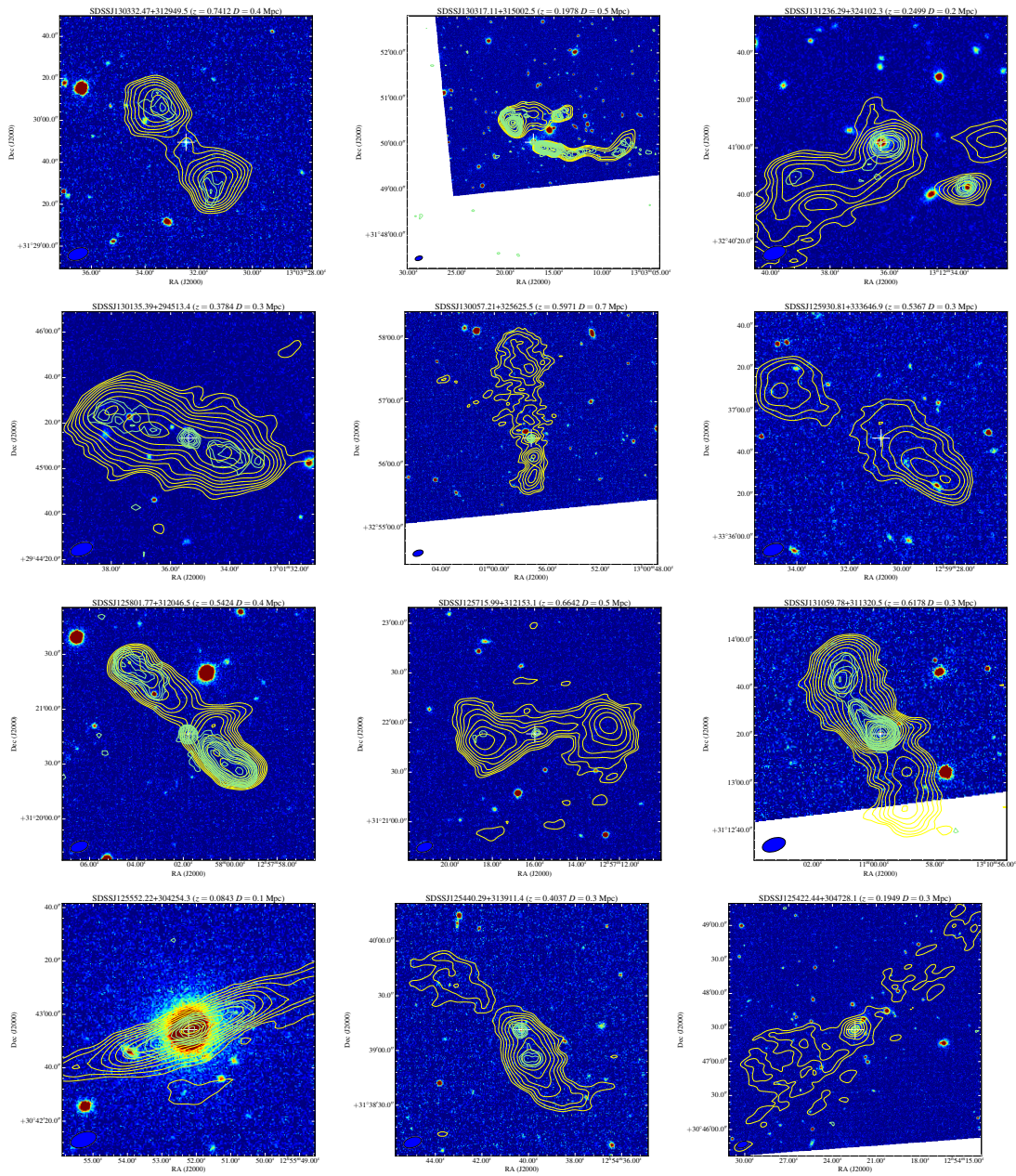


Figure A.5: Continued.

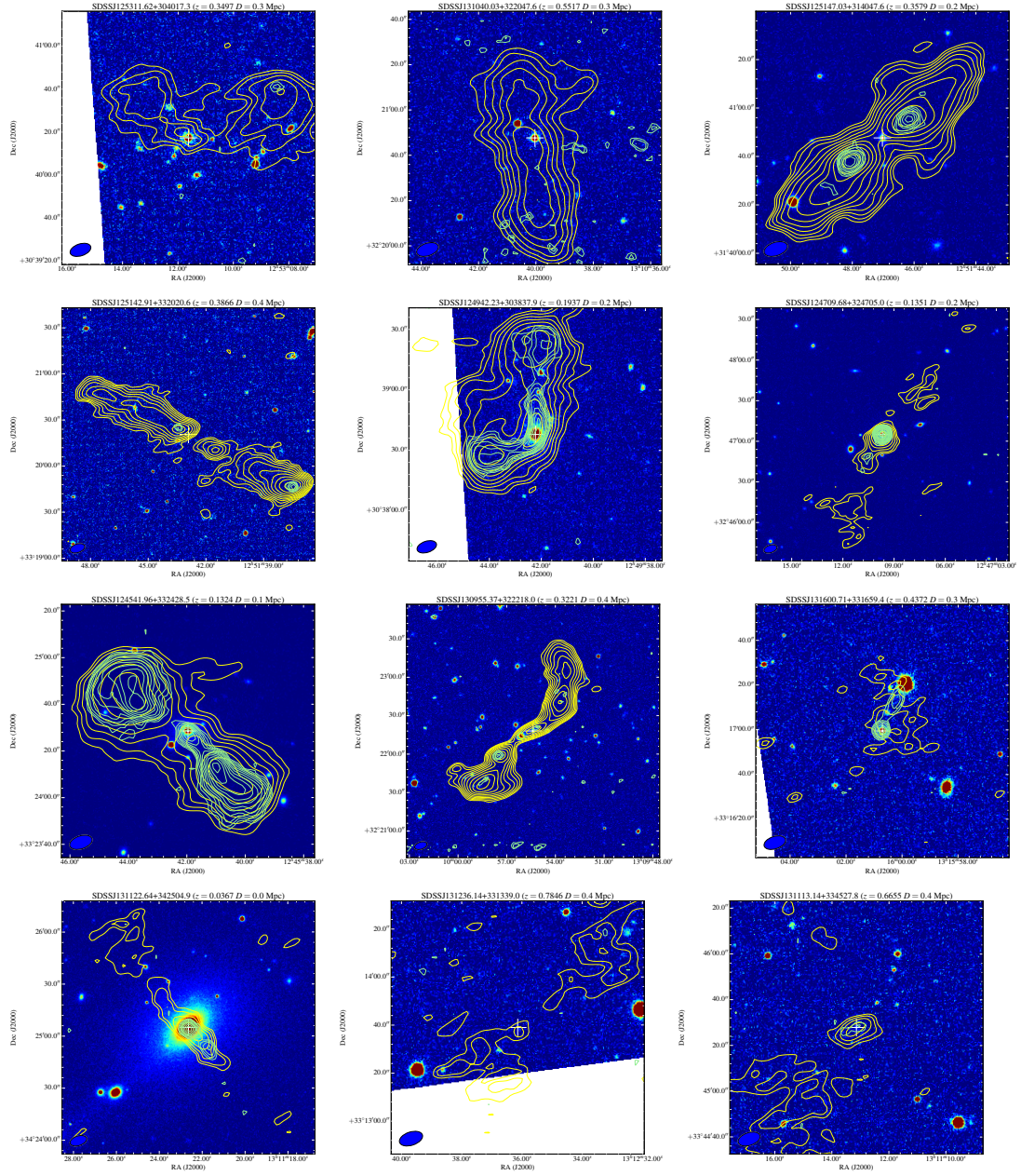


Figure A.6: Continued.

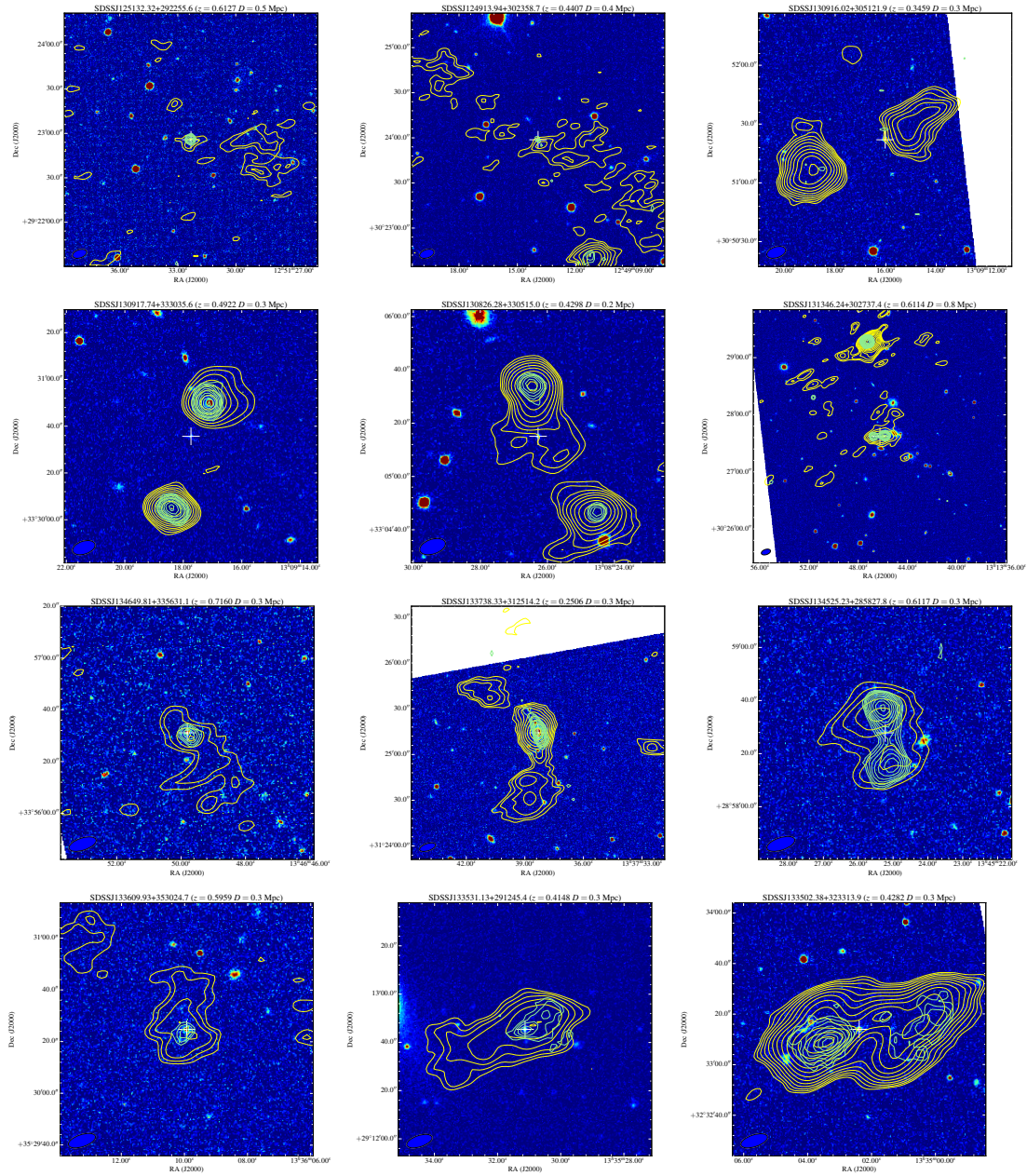


Figure A.7: Continued.

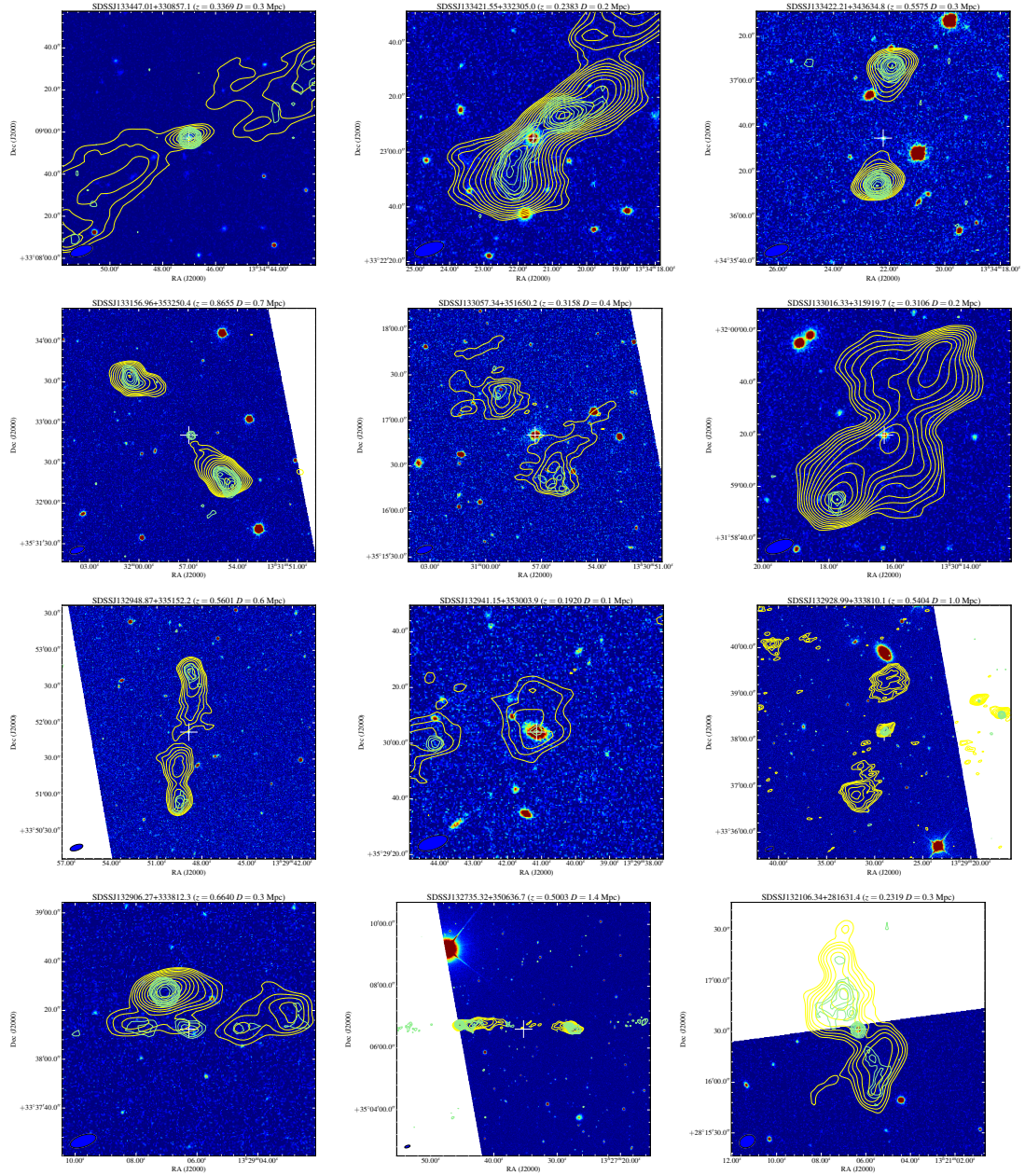


Figure A.8: Continued.

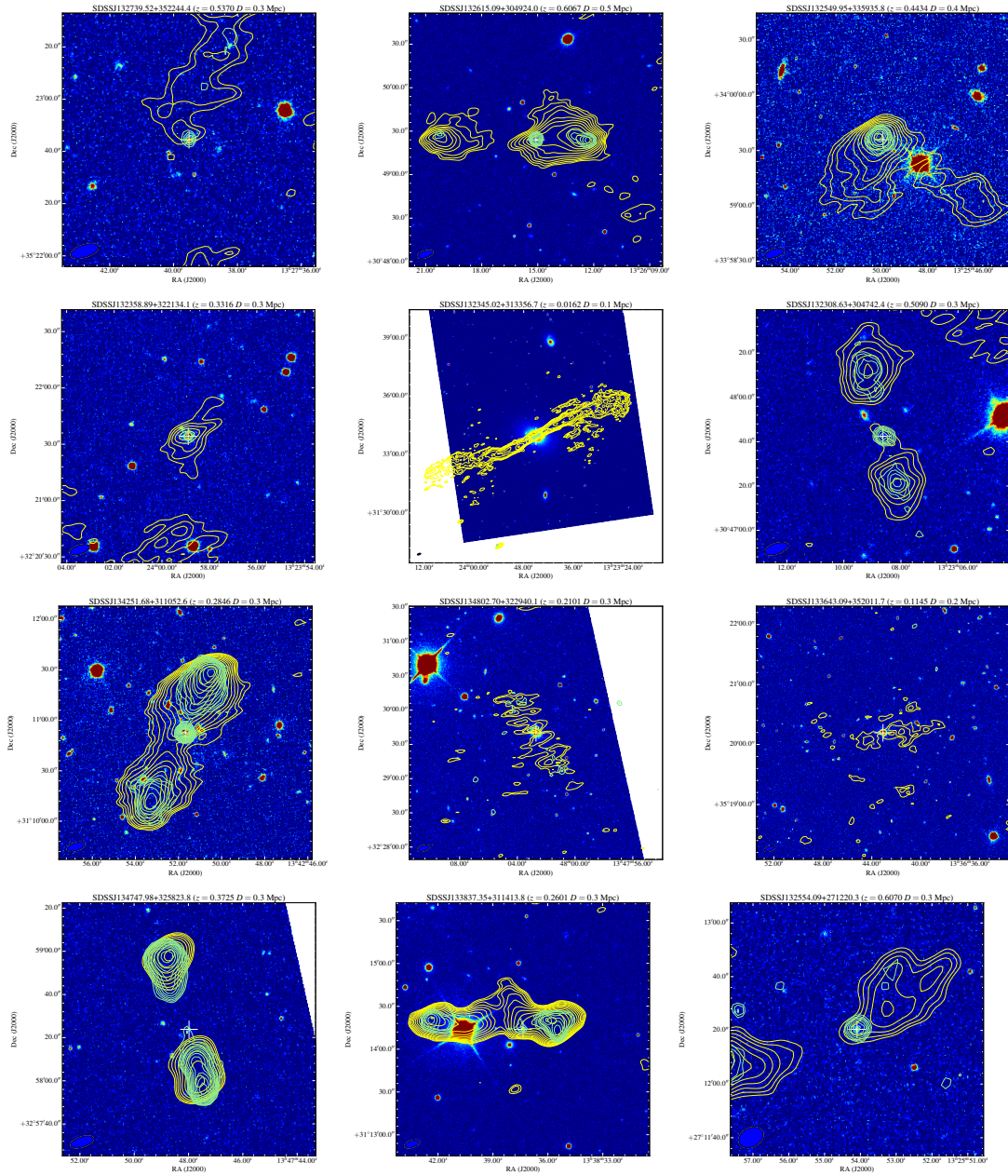


Figure A.9: Continued.

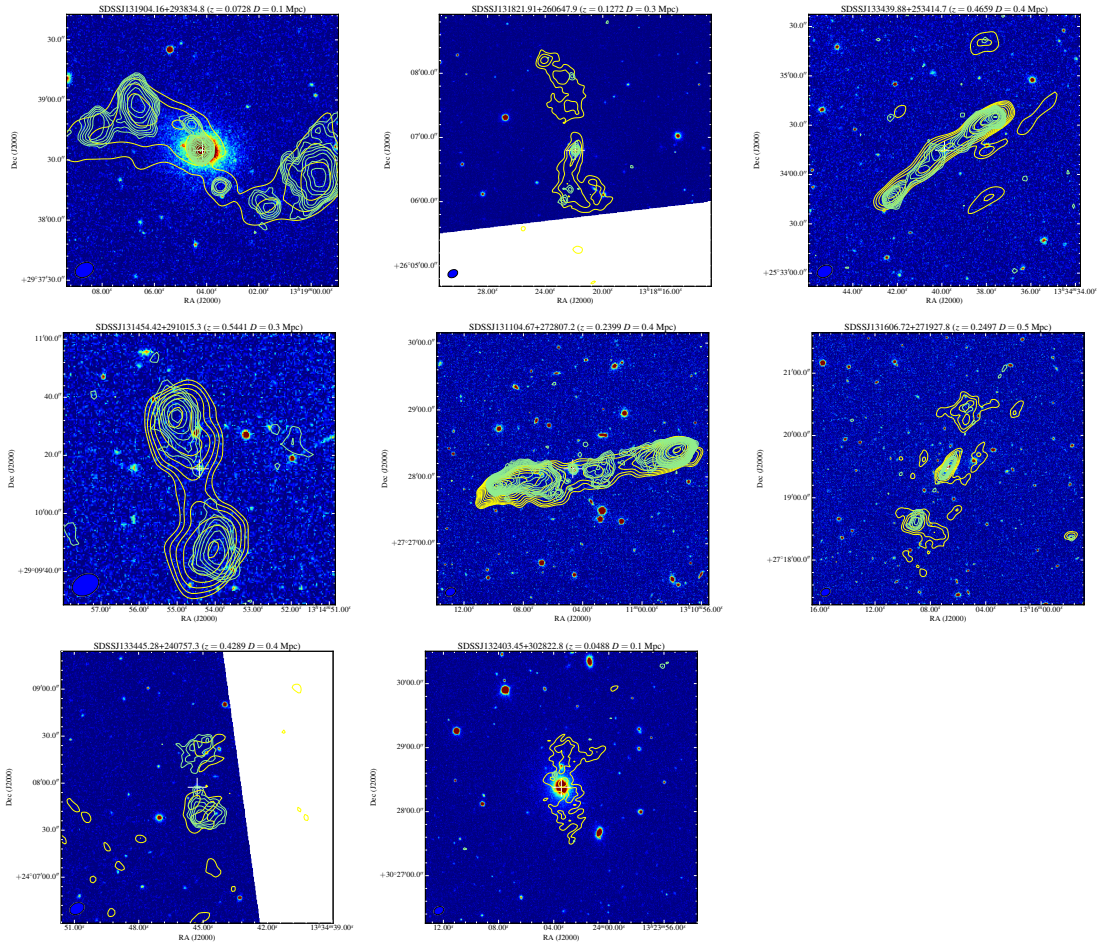


Figure A.10: Continued.

Bibliography

- Abazajian K.N., et al., 2009, *ApJS*, 182, 543
- Abramowicz M.A., Czerny B., Lasota J.P., Szuszkiewicz E., 1988, *ApJ*, 332, 646
- Akritas M.G., Siebert J., 1996, *MNRAS*, 278, 919
- Alam S., et al., 2015, *ApJS*, 219, 12
- Alexander D.M., Hickox R.C., 2012, *NewAR*, 56, 93
- Allen S.W., Dunn R.J.H., Fabian A.C., Taylor G.B., Reynolds C.S., 2006, *MNRAS*, 372, 21
- Allington-Smith J.R., Perryman M.A.C., Longair M.S., Gunn J.E., Westphal J.A., 1982, *MNRAS*, 201, 331
- Antonucci R., 1993, *ARA&A*, 31, 473
- Antonucci R., 2012, *Astronomical and Astrophysical Transactions*, 27, 557
- Antonucci R.R.J., 1984, *ApJ*, 278, 499
- Antonucci R.R.J., Miller J.S., 1985, *ApJ*, 297, 621
- Appleton P.N., et al., 2004, *ApJS*, 154, 147
- Archibald E.N., Dunlop J.S., Hughes D.H., Rawlings S., Eales S.A., Ivison R.J., 2001, *MNRAS*, 323, 417
- Assef R.J., et al., 2010, *ApJ*, 713, 970
- Assef R.J., et al., 2013, *ApJ*, 772, 26
- Babić A., Miller L., Jarvis M.J., Turner T.J., Alexander D.M., Croom S.M., 2007, *A&A*, 474, 755

- Baldi R.D., Capetti A., 2008, *A&A*, 489, 989
- Baldwin J.A., Phillips M.M., Terlevich R., 1981, *PASP*, 93, 5
- Baldwin J.E., Boysen R.C., Hales S.E.G., Jennings J.E., Waggett P.C., Warner P.J., Wilson D.M.A., 1985, *MNRAS*, 217, 717
- Ballantyne D.R., 2008, *ApJ*, 685, 787
- Barger A.J., Cowie L.L., Owen F.N., Chen C.C., Hasinger G., Hsu L.Y., Li Y., 2015, *ApJ*, 801, 87
- Barnes J.E., Hernquist L., 1992, *ARA&A*, 30, 705
- Barnes J.E., Hernquist L., 1996, *ApJ*, 471, 115
- Barthel P., Haas M., Leipski C., Wilkes B., 2012, *ApJL*, 757, L26
- Barthel P.D., 1989, *ApJ*, 336, 606
- Becker R.H., White R.L., Helfand D.J., 1995, *ApJ*, 450, 559
- Begelman M.C., 2012, *MNRAS*, 420, 2912
- Bell E.F., 2003, *ApJ*, 586, 794
- Bennett A.S., 1962, *MNRAS*, 125, 75
- Bennett A.S., Smith F.G., 1961, *MNRAS*, 122, 71
- Best P.N., Heckman T.M., 2012, *MNRAS*, 421, 1569
- Best P.N., Carilli C.L., Garrington S.T., Longair M.S., Rottgering H.J.A., 1998a, *MNRAS*, 299, 357
- Best P.N., Longair M.S., Roettgering H.J.A., 1998b, *MNRAS*, 295, 549
- Best P.N., Kauffmann G., Heckman T.M., Brinchmann J., Charlot S., Ivezić Ž., White S.D.M., 2005, *MNRAS*, 362, 25
- Best P.N., Kaiser C.R., Heckman T.M., Kauffmann G., 2006, *MNRAS*, 368, L67
- Best P.N., Ker L.M., Simpson C., Rigby E.E., Sabater J., 2014, *MNRAS*, 445, 955

- Beswick R.J., Muxlow T.W.B., Thrall H., Richards A.M.S., Garrington S.T., 2008, *MNRAS*, 385, 1143
- Bhatnagar S., 2001, Radio Study of Galactic Supernova Remnants and the Interstellar Medium. PhD in physics, National Centre for Radio Astrophysics Tata Institute of Fundamental Research – University of Pune, Pune - 411 007 India
- Blandford R.D., Begelman M.C., 1999, *MNRAS*, 303, L1
- Blandford R.D., Königl A., 1979, *ApJ*, 232, 34
- Blandford R.D., Rees M.J., 1974, *MNRAS*, 169, 395
- Bolton J.G., Stanley G.J., Slee O.B., 1949, *Nature*, 164, 101
- Bondi H., 1952, *MNRAS*, 112, 195
- Bonfield D.G., et al., 2011, *MNRAS*, 416, 13
- Bongiorno A., et al., 2007, *A&A*, 472, 443
- Bongiorno A., et al., 2012, *MNRAS*, 427, 3103
- Boroson T.A., Green R.F., 1992, *ApJS*, 80, 109
- Bournaud F., Jog C.J., Combes F., 2005, *A&A*, 437, 69
- Bourne N., Dunne L., Ivison R.J., Maddox S.J., Dickinson M., Frayer D.T., 2011, *MNRAS*, 410, 1155
- Bourne N., et al., 2012, *MNRAS*, 421, 3027
- Bower R.G., Benson A.J., Malbon R., Helly J.C., Frenk C.S., Baugh C.M., Cole S., Lacey C.G., 2006, *MNRAS*, 370, 645
- Boyle B.J., Cornwell T.J., Middelberg E., Norris R.P., Appleton P.N., Smail I., 2007, *MNRAS*, 376, 1182
- Bridle A.H., Perley R.A., 1984, *ARA&A*, 22, 319
- Bridle A.H., Hough D.H., Lonsdale C.J., Burns J.O., Laing R.A., 1994, *AJ*, 108, 766
- Brinchmann J., Charlot S., White S.D.M., Tremonti C., Kauffmann G., Heckman T., Brinkmann J., 2004, *MNRAS*, 351, 1151

- Bromm V., Coppi P.S., Larson R.B., 2002, *ApJ*, 564, 23
- Brusa M., et al., 2015, *MNRAS*, 446, 2394
- Burbidge G.R., Burbidge E.M., Sandage A.R., 1963, *Reviews of Modern Physics*, 35, 947
- Calzetti D., 2013, *Star Formation Rate Indicators*, p. 419
- Cano-Díaz M., Maiolino R., Marconi A., Netzer H., Shemmer O., Cresci G., 2012, *A&A*, 537, L8
- Caputi K.I., 2014, *International Journal of Modern Physics D*, 23, 30015
- Cattaneo A., et al., 2009, *Nature*, 460, 213
- Celotti A., Ghisellini G., Chiaberge M., 2001, *MNRAS*, 321, L1
- Cen R., Chisari N.E., 2011, *ApJ*, 731, 11
- Charlot S., Fall S.M., 2000, *ApJ*, 539, 718
- Chen C.T.J., et al., 2013a, *ApJ*, 773, 3
- Chen Y.M., et al., 2013b, *MNRAS*, 429, 2643
- Chi X., Wolfendale A.W., 1990, *MNRAS*, 245, 101
- Chiaberge M., Capetti A., Celotti A., 2002, *A&A*, 394, 791
- Cimatti A., Daddi E., Renzini A., 2006, *A&A*, 453, L29
- Ciotti L., Ostriker J.P., Proga D., 2010, *ApJ*, 717, 708
- Cleary K., Lawrence C.R., Marshall J.A., Hao L., Meier D., 2007, *ApJ*, 660, 117
- Clemens M.S., et al., 2013, *MNRAS*, 433, 695
- Cohen A.S., Lane W.M., Cotton W.D., Kassim N.E., Lazio T.J.W., Perley R.A., Condon J.J., Erickson W.C., 2007, *AJ*, 134, 1245
- Condon J.J., 1992, *ARA&A*, 30, 575
- Condon J.J., Cotton W.D., Greisen E.W., Yin Q.F., Perley R.A., Taylor G.B., Broderick J.J., 1998, *AJ*, 115, 1693

- Cowie L.L., Songaila A., Hu E.M., Cohen J.G., 1996, *AJ*, 112, 839
- Cox M.J., Eales S.A.E., Alexander P., Fitt A.J., 1988, *MNRAS*, 235, 1227
- Croston J.H., Hardcastle M.J., Harris D.E., Belsole E., Birkinshaw M., Worrall D.M., 2005, *ApJ*, 626, 733
- Croston J.H., Kraft R.P., Hardcastle M.J., 2007, *ApJ*, 660, 191
- Croston J.H., et al., 2009, *MNRAS*, 395, 1999
- Croton D.J., et al., 2006, *MNRAS*, 365, 11
- da Cunha E., Charlot S., Elbaz D., 2008, *MNRAS*, 388, 1595
- da Cunha E., Charmandaris V., Díaz-Santos T., Armus L., Marshall J.A., Elbaz D., 2010, *A&A*, 523, A78
- David L.P., Nulsen P.E.J., McNamara B.R., Forman W., Jones C., Ponman T., Robertson B., Wise M., 2001, *ApJ*, 557, 546
- Davies L.J.M., et al., 2016, *MNRAS*
- de Graauw T., et al., 2010, *A&A*, 518, L6
- de Jong T., Klein U., Wielebinski R., Wunderlich E., 1985, *A&A*, 147, L6
- de Vaucouleurs G., de Vaucouleurs A., 1968, *AJ*, 73, 858
- Di Matteo T., Springel V., Hernquist L., 2005, *Nature*, 433, 604
- Diamond-Stanic A.M., Rieke G.H., 2012, *ApJ*, 746, 168
- Dicken D., Tadhunter C., Morganti R., Buchanan C., Oosterloo T., Axon D., 2008, *ApJ*, 678, 712
- Dicken D., Tadhunter C., Axon D., Morganti R., Inskip K.J., Holt J., González Delgado R., Groves B., 2009, *ApJ*, 694, 268
- Dicken D., et al., 2012, *ApJ*, 745, 172
- Dickinson M., Papovich C., Ferguson H.C., Budavári T., 2003, *ApJ*, 587, 25

- Doi A., Asada K., Fujisawa K., Nagai H., Hagiwara Y., Wajima K., Inoue M., 2013, *ApJ*, 765, 69
- Donoso E., Best P.N., Kauffmann G., 2009, *MNRAS*, 392, 617
- Donzelli C.J., Chiaberge M., Macchetto F.D., Madrid J.P., Capetti A., Marchesini D., 2007, *ApJ*, 667, 780
- Driver S.P., et al., 2011, *MNRAS*, 413, 971
- Dunn R.J.H., Fabian A.C., Celotti A., 2006, *MNRAS*, 372, 1741
- Dunne L., et al., 2011, *MNRAS*, 417, 1510
- Eales S., Rawlings S., Law-Green D., Cotter G., Lacy M., 1997, *MNRAS*, 291, 593
- Eales S., et al., 2010a, *PASP*, 122, 499
- Eales S., et al., 2010b, *PASP*, 122, 499
- Eales S.A., 1985a, *MNRAS*, 217, 167
- Eales S.A., 1985b, *MNRAS*, 217, 149
- Eales S.A., Rawlings S., 1990, *MNRAS*, 243, 1P
- Eales S.A., Rawlings S., 1993, *ApJ*, 411, 67
- Eddington A.S., 1925, *MNRAS*, 85, 408
- Edge D.O., Shakeshaft J.R., McAdam W.B., Baldwin J.E., Archer S., 1959, *MmRAS*, 68, 37
- Ehman J.R., Dixon R.S., Kraus J.D., 1970, *AJ*, 75, 351
- Ekers J.A., 1969, *Australian Journal of Physics Astrophysical Supplement*, 7, 3
- Elbaz D., et al., 2007, *A&A*, 468, 33
- Elbaz D., et al., 2011, *A&A*, 533, A119
- Ellison S.L., Patton D.R., Mendel J.T., Scudder J.M., 2011, *MNRAS*, 418, 2043
- Ellison S.L., Mendel J.T., Patton D.R., Scudder J.M., 2013, *MNRAS*, 435, 3627

- Ellison S.L., Patton D.R., Hickox R.C., 2015, *MNRAS*, 451, L35
- Eracleous M., Halpern J.P., 2001, *ApJ*, 554, 240
- Evans D.A., Worrall D.M., Hardcastle M.J., Kraft R.P., Birkinshaw M., 2006, *ApJ*, 642, 96
- Fabian A.C., 1999, *MNRAS*, 308, L39
- Fabian A.C., 2012, *ARA&A*, 50, 455
- Fabian A.C., Sanders J.S., Taylor G.B., Allen S.W., Crawford C.S., Johnstone R.M., Iwasawa K., 2006, *MNRAS*, 366, 417
- Fanaroff B.L., Riley J.M., 1974, *MNRAS*, 167, 31P
- Fath E.A., 1909, *Lick Observatory Bulletin*, 5, 71
- Feigelson E.D., Nelson P.I., 1985, *ApJ*, 293, 192
- Fernandes C.A.C., et al., 2011, *MNRAS*, 411, 1909
- Fernandes C.A.C., et al., 2015, *MNRAS*, 447, 1184
- Ferrarese L., Merritt D., 2000, *ApJL*, 539, L9
- Filippenko A.V., 1992, In Filippenko A.V., ed., *Relationships Between Active Galactic Nuclei and Starburst Galaxies*, vol. 31 of *Astronomical Society of the Pacific Conference Series*, p. 253
- Fischer T.C., Crenshaw D.M., Kraemer S.B., Schmitt H.R., Trippe M.L., 2010, *AJ*, 140, 577
- Fisher D.B., Drory N., 2011, *ApJL*, 733, L47
- Flesch E.W., 2015, *PASA*, 32, e010
- Fontanot F., De Lucia G., Monaco P., Somerville R.S., Santini P., 2009, *MNRAS*, 397, 1776
- Frank J., King A., Raine D.J., 2002, *Accretion Power in Astrophysics: Third Edition*
- Fumagalli M., et al., 2014, *ApJ*, 796, 35

- Gaibler V., Khochfar S., Krause M., Silk J., 2012, MNRAS, 425, 438
- García-Burillo S., Combes F., Schinnerer E., Boone F., Hunt L.K., 2005, A&A, 441, 1011
- Garn T., Green D.A., Riley J.M., Alexander P., 2009, MNRAS, 397, 1101
- Gebhardt K., et al., 2000, ApJL, 539, L13
- Genzel R., et al., 2008, ApJ, 687, 59
- Godfrey L.E.H., Shabala S.S., 2016, MNRAS, 456, 1172
- Gower J.F.R., Scott P.F., Wills D., 1967, MmRAS, 71, 49
- Granato G.L., De Zotti G., Silva L., Bressan A., Danese L., 2004, ApJ, 600, 580
- Greene J.E., Ho L.C., Barth A.J., 2008, ApJ, 688, 159
- Griffin M.J., et al., 2010a, A&A, 518, L3
- Griffin M.J., et al., 2010b, A&A, 518, L3
- Grimes J.A., Rawlings S., Willott C.J., 2003, NewAR, 47, 205
- Gültekin K., et al., 2009, ApJ, 698, 198
- Gunn J.E., et al., 2006, AJ, 131, 2332
- Haardt F., 1993, ApJ, 413, 680
- Haardt F., Maraschi L., 1991, ApJL, 380, L51
- Haas M., Siebenmorgen R., Schulz B., Krügel E., Chini R., 2005, A&A, 442, L39
- Haas M., Willner S.P., Heymann F., Ashby M.L.N., Fazio G.G., Wilkes B.J., Chini R., Siebenmorgen R., 2008, ApJ, 688, 122
- Haas M., et al., 2004, A&A, 424, 531
- Haehnelt M.G., Rees M.J., 1993, MNRAS, 263, 168
- Hales S.E.G., Riley J.M., Waldram E.M., Warner P.J., Baldwin J.E., 2007, MNRAS, 382, 1639

- Hao C.N., Xia X.Y., Mao S., Wu H., Deng Z.G., 2005, *ApJ*, 625, 78
- Hardcastle M., 2015, In Contopoulos I., Gabuzda D., Kylafis N., eds., *The Formation and Disruption of Black Hole Jets*, vol. 414 of *Astrophysics and Space Science Library*, p. 83
- Hardcastle M.J., 1999, *A&A*, 349, 381
- Hardcastle M.J., 2004, *A&A*, 414, 927
- Hardcastle M.J., Krause M.G.H., 2013, *MNRAS*, 430, 174
- Hardcastle M.J., Krause M.G.H., 2014, *MNRAS*, 443, 1482
- Hardcastle M.J., Sakelliou I., 2004, *MNRAS*, 349, 560
- Hardcastle M.J., Worrall D.M., 1999, *MNRAS*, 309, 969
- Hardcastle M.J., Alexander P., Pooley G.G., Riley J.M., 1997, *MNRAS*, 288, L1
- Hardcastle M.J., Alexander P., Pooley G.G., Riley J.M., 1999, *MNRAS*, 304, 135
- Hardcastle M.J., Birkinshaw M., Worrall D.M., 2001, *MNRAS*, 323, L17
- Hardcastle M.J., Evans D.A., Croston J.H., 2006, *MNRAS*, 370, 1893
- Hardcastle M.J., Croston J.H., Kraft R.P., 2007a, *ApJ*, 669, 893
- Hardcastle M.J., Evans D.A., Croston J.H., 2007b, *MNRAS*, 376, 1849
- Hardcastle M.J., Evans D.A., Croston J.H., 2009, *MNRAS*, 396, 1929
- Hardcastle M.J., et al., 2010, *MNRAS*, 409, 122
- Hardcastle M.J., et al., 2013, *MNRAS*, 429, 2407
- Harrison C.M., Thomson A.P., Alexander D.M., Bauer F.E., Edge A.C., Hogan M.T., Mullaney J.R., Swinbank A.M., 2015, *ApJ*, 800, 45
- Harrison C.M., et al., 2012, *ApJL*, 760, L15
- Harwit M., Pacini F., 1975, *ApJL*, 200, L127
- Hasinger G., Miyaji T., Schmidt M., 2005, *A&A*, 441, 417

- Hatziminaoglou E., et al., 2010, *A&A*, 518, L33
- Heald G.H., et al., 2015, *A&A*, 582, A123
- Heckman T.M., 1980, *A&A*, 87, 152
- Heckman T.M., 1987, In Khachikian E.E., Fricke K.J., Melnick J., eds., *Observational Evidence of Activity in Galaxies*, vol. 121 of IAU Symposium, p. 421
- Heckman T.M., Best P.N., 2014, *ARA&A*, 52, 589
- Heckman T.M., Smith E.P., Baum S.A., van Breugel W.J.M., Miley G.K., Illingworth G.D., Bothun G.D., Balick B., 1986, *ApJ*, 311, 526
- Heckman T.M., Chambers K.C., Postman M., 1992, *ApJ*, 391, 39
- Heckman T.M., O’Dea C.P., Baum S.A., Laurikainen E., 1994, *ApJ*, 428, 65
- Heckman T.M., Kauffmann G., Brinchmann J., Charlot S., Tremonti C., White S.D.M., 2004, *ApJ*, 613, 109
- Heesen V., Beck R., Krause M., Dettmar R.J., 2009, *Astronomische Nachrichten*, 330, 1028
- Helou G., Bicay M.D., 1993, *ApJ*, 415, 93
- Helou G., Soifer B.T., Rowan-Robinson M., 1985, *ApJL*, 298, L7
- Herbert P.D., Jarvis M.J., Willott C.J., McLure R.J., Mitchell E., Rawlings S., Hill G.J., Dunlop J.S., 2010, *MNRAS*, 406, 1841
- Hey J.S., Parsons S.J., Phillips J.W., 1946, *Nature*, 158, 234
- Hickox R.C., Mullaney J.R., Alexander D.M., Chen C.T.J., Civano F.M., Goulding A.D., Hainline K.N., 2014, *ApJ*, 782, 9
- Hickox R.C., et al., 2009, *ApJ*, 696, 891
- Hicks E.K.S., Davies R.I., Maciejewski W., Emsellem E., Malkan M.A., Dumas G., Müller-Sánchez F., Rivers A., 2013, *ApJ*, 768, 107
- Hine R.G., Longair M.S., 1979, *MNRAS*, 188, 111
- Hönig S.F., Beckert T., Ohnaka K., Weigelt G., 2006, *A&A*, 452, 459

- Hönig S.F., Leipski C., Antonucci R., Haas M., 2011, *ApJ*, 736, 26
- Hopkins P.F., Hernquist L., 2009, *ApJ*, 698, 1550
- Hopkins P.F., Hernquist L., Cox T.J., Di Matteo T., Martini P., Robertson B., Springel V., 2005, *ApJ*, 630, 705
- Hopkins P.F., Hernquist L., Cox T.J., Di Matteo T., Robertson B., Springel V., 2006, *ApJS*, 163, 1
- Hopkins P.F., Richards G.T., Hernquist L., 2007, *ApJ*, 654, 731
- Hopkins P.F., Hernquist L., Cox T.J., Kereš D., 2008, *ApJS*, 175, 356
- Hopkins P.F., et al., 2010, *ApJ*, 715, 202
- Hughes P.A., 1991, *Beams and jets in astrophysics*
- Hummel E., Davies R.D., Pedlar A., Wolstencroft R.D., van der Hulst J.M., 1988, *A&A*, 199, 91
- Ibar E., et al., 2010, *MNRAS*, 409, 38
- Igumenshchev I.V., 2002, *ApJL*, 577, L31
- Ineson J., Croston J.H., Hardcastle M.J., Kraft R.P., Evans D.A., Jarvis M., 2015, *MNRAS*, 453, 2682
- Inskip K.J., Best P.N., Longair M.S., MacKay D.J.C., 2002, *MNRAS*, 329, 277
- Inskip K.J., Best P.N., Longair M.S., Röttgering H.J.A., 2005, *MNRAS*, 359, 1393
- Inskip K.J., Tadhunter C.N., Morganti R., Holt J., Ramos Almeida C., Dicken D., 2010, *MNRAS*, 407, 1739
- Intema H.T., Jagannathan P., Mooley K.P., Frail D.A., 2016, *ArXiv:1603.04368*
- Isobe T., Feigelson E.D., Nelson P.I., 1986, *ApJ*, 306, 490
- Iverson R.J., et al., 2010a, *A&A*, 518, L31
- Iverson R.J., et al., 2010b, *MNRAS*, 402, 245
- Jackson N., Rawlings S., 1997, *MNRAS*, 286, 241

- Jaffe W., et al., 2004, *Nature*, 429, 47
- Jansky K.G., 1933, *Nature*, 132, 66
- Janssen R.M.J., Röttgering H.J.A., Best P.N., Brinchmann J., 2012, *A&A*, 541, A62
- Jarrett T.H., et al., 2011, *ApJ*, 735, 112
- Jarvis M.J., Rawlings S., Eales S., Blundell K.M., Bunker A.J., Croft S., McLure R.J., Willott C.J., 2001a, *MNRAS*, 326, 1585
- Jarvis M.J., et al., 2001b, *MNRAS*, 326, 1563
- Jarvis M.J., et al., 2010, *MNRAS*, 409, 92
- Jenkins C.J., McEllin M., 1977, *MNRAS*, 180, 219
- Johansson P.H., Burkert A., Naab T., 2009, *ApJL*, 707, L184
- Johnston S., et al., 2007, *PASA*, 24, 174
- Juneau S., et al., 2013, *ApJ*, 764, 176
- Kalfountzou E., Jarvis M.J., Bonfield D.G., Hardcastle M.J., 2012, *MNRAS*, 427, 2401
- Kalfountzou E., et al., 2014, *MNRAS*, 442, 1181
- Karim A., et al., 2011, *ApJ*, 730, 61
- Kauffmann G., Haehnelt M., 2000, *MNRAS*, 311, 576
- Kauffmann G., Heckman T.M., 2009, *MNRAS*, 397, 135
- Kauffmann G., White S.D.M., Heckman T.M., Ménard B., Brinchmann J., Charlot S., Tremonti C., Brinkmann J., 2004, *MNRAS*, 353, 713
- Kauffmann G., et al., 2003a, *MNRAS*, 341, 33
- Kauffmann G., et al., 2003b, *MNRAS*, 341, 33
- Kauffmann G., et al., 2003c, *MNRAS*, 346, 1055
- Kauffmann G., et al., 2007, *ApJS*, 173, 357

- Kellermann K.I., 1964, *ApJ*, 140, 969
- Kellermann K.I., Sramek R., Schmidt M., Shaffer D.B., Green R., 1989, *AJ*, 98, 1195
- Kennicutt R.C., 1998, *ARA&A*, 36, 189
- Kennicutt R.C., Evans N.J., 2012, *ARA&A*, 50, 531
- Kewley L.J., Groves B., Kauffmann G., Heckman T., 2006, *MNRAS*, 372, 961
- King A.R., Zubovas K., Power C., 2011, *MNRAS*, 415, L6
- Kishimoto M., Hönig S.F., Antonucci R., Barvainis R., Kotani T., Tristram K.R.W., Weigelt G., Levin K., 2011, *A&A*, 527, A121
- Klein U., 1991, *Proceedings of the Astronomical Society of Australia*, 9, 253
- Kocevski D.D., et al., 2012, *ApJ*, 744, 148
- Kormendy J., Ho L.C., 2013, *ARA&A*, 51, 511
- Kormendy J., Kennicutt Jr. R.C., 2004, *ARA&A*, 42, 603
- Kormendy J., Richstone D., 1995, *ARA&A*, 33, 581
- Kraft R.P., Birkinshaw M., Hardcastle M.J., Evans D.A., Croston J.H., Worrall D.M., Murray S.S., 2007, *ApJ*, 659, 1008
- Lacki B.C., Thompson T.A., 2010, *ApJ*, 717, 196
- Lacki B.C., Thompson T.A., Quataert E., 2010, *ApJ*, 717, 1
- Lacy M., et al., 2004, *ApJS*, 154, 166
- Laing R., 1989, In Meisenheimer K., Roeser H.J., eds., *Hot Spots in Extragalactic Radio Sources*, vol. 327 of *Lecture Notes in Physics*, Berlin Springer Verlag, pp. 27–43
- Laing R.A., Riley J.M., Longair M.S., 1983, *MNRAS*, 204, 151
- Laing R.A., Jenkins C.R., Wall J.V., Unger S.W., 1994, In Bicknell G.V., Dopita M.A., Quinn P.J., eds., *The Physics of Active Galaxies*, vol. 54 of *Astronomical Society of the Pacific Conference Series*, p. 201

- LaMassa S.M., Heckman T.M., Ptak A., Urry C.M., 2013, *ApJL*, 765, L33
- Lang D., 2014, *AJ*, 147, 108
- Lange R., et al., 2015, *MNRAS*, 447, 2603
- Lawrence A., 1991, *MNRAS*, 252, 586
- Leahy J.P., Black A.R.S., Dennett-Thorpe J., Hardcastle M.J., Komissarov S., Perley R.A., Riley J.M., Scheuer P.A.G., 1997, *MNRAS*, 291, 20
- Li C., Kauffmann G., Heckman T.M., White S.D.M., Jing Y.P., 2008, *MNRAS*, 385, 1915
- Lilly S.J., 1989, *ApJ*, 340, 77
- Lilly S.J., Longair M.S., 1982, In Heeschen D.S., Wade C.M., eds., *Extragalactic Radio Sources*, vol. 97 of *IAU Symposium*, pp. 413–421
- Lisenfeld U., Voelk H.J., Xu C., 1996, *A&A*, 306, 677
- Longair M.S., 2011, *High Energy Astrophysics*
- Longair M.S., Ryle M., Scheuer P.A.G., 1973, *MNRAS*, 164, 243
- Lonsdale C.J., et al., 2009, *IEEE Proceedings*, 97, 1497
- Lutz D., et al., 2008, *ApJ*, 684, 853
- Lutz D., et al., 2010, *ApJ*, 712, 1287
- Madejski G., Życki P., Done C., Valinia A., Blanco P., Rothschild R., Turek B., 2000, *ApJL*, 535, L87
- Magnelli B., et al., 2015, *A&A*, 573, A45
- Magorrian J., et al., 1998, *AJ*, 115, 2285
- Mainieri V., et al., 2011, *A&A*, 535, A80
- Marconi A., Hunt L.K., 2003, *ApJL*, 589, L21
- Martin D.C., et al., 2005, *ApJL*, 619, L59
- Martínez-Sansigre A., Rawlings S., 2011, *MNRAS*, 414, 1937

- Mateos S., et al., 2012, MNRAS, 426, 3271
- Matt G., Fabian A.C., Reynolds C.S., 1997, MNRAS, 289, 175
- Matthews T.A., Sandage A.R., 1963, ApJ, 138, 30
- Mauch T., Klöckner H.R., Rawlings S., Jarvis M., Hardcastle M.J., Obreschkow D., Saikia D.J., Thompson M.A., 2013, MNRAS, 435, 650
- McConnell N.J., Ma C.P., 2013, ApJ, 764, 184
- McKinney J.C., Blandford R.D., 2009, MNRAS, 394, L126
- McLure R.J., Dunlop J.S., 2000, MNRAS, 317, 249
- McLure R.J., Dunlop J.S., 2001, MNRAS, 327, 199
- McLure R.J., Dunlop J.S., 2002, MNRAS, 331, 795
- McLure R.J., Willott C.J., Jarvis M.J., Rawlings S., Hill G.J., Mitchell E., Dunlop J.S., Wold M., 2004, MNRAS, 351, 347
- McNamara B.R., Rohanizadegan M., Nulsen P.E.J., 2011, ApJ, 727, 39
- McNamara B.R., et al., 2000, ApJL, 534, L135
- Meisenheimer K., Roser H.J., Hiltner P.R., Yates M.G., Longair M.S., Chini R., Perley R.A., 1989, A&A, 219, 63
- Meisenheimer K., Haas M., Müller S.A.H., Chini R., Klaas U., Lemke D., 2001, A&A, 372, 719
- Menci N., Fiore F., Puccetti S., Cavaliere A., 2008, ApJ, 686, 219
- Merloni A., Heinz S., 2007, MNRAS, 381, 589
- Merritt D., Ferrarese L., 2001, ApJ, 547, 140
- Middleton M., 2015, ArXiv:1507.06153
- Miller C.J., Nichol R.C., Gómez P.L., Hopkins A.M., Bernardi M., 2003, ApJ, 597, 142
- Miller J.S., Antonucci R.R.J., 1983, ApJL, 271, L7

- Mills B.Y., Slee O.B., 1957, *Australian Journal of Physics*, 10
- Mingo B., Hardcastle M.J., Croston J.H., Evans D.A., Hota A., Kharb P., Kraft R.P., 2011, *ApJ*, 731, 21
- Mingo B., Hardcastle M.J., Croston J.H., Dicken D., Evans D.A., Morganti R., Tadhunter C., 2014, *MNRAS*
- Miyaji T., Hasinger G., Schmidt M., 2000, *A&A*, 353, 25
- Mullaney J.R., et al., 2012, *MNRAS*, 419, 95
- Mullin L.M., Hardcastle M.J., 2009, *MNRAS*, 398, 1989
- Mullin L.M., Hardcastle M.J., Riley J.M., 2006, *MNRAS*, 372, 113
- Murphy E.J., et al., 2011, *ApJ*, 737, 67
- Murray N., Quataert E., Thompson T.A., 2005, *ApJ*, 618, 569
- Narayan R., Raymond J., 1999, *ApJL*, 515, L69
- Narayan R., Yi I., 1994, *ApJL*, 428, L13
- Narayan R., Yi I., 1995a, *ApJ*, 444, 231
- Narayan R., Yi I., 1995b, *ApJ*, 452, 710
- Narayan R., Yi I., Mahadevan R., 1995, *Nature*, 374, 623
- Narayan R., Igumenshchev I.V., Abramowicz M.A., 2000, *ApJ*, 539, 798
- Narayan R., Quataert E., Igumenshchev I.V., Abramowicz M.A., 2002, *ApJ*, 577, 295
- Nenkova M., Ivezić Ž., Elitzur M., 2002, *ApJL*, 570, L9
- Nenkova M., Sirocky M.M., Ivezić Ž., Elitzur M., 2008a, *ApJ*, 685, 147
- Nenkova M., Sirocky M.M., Nikutta R., Ivezić Ž., Elitzur M., 2008b, *ApJ*, 685, 160
- Netzer H., 2009, *MNRAS*, 399, 1907
- Niklas S., 1997, *A&A*, 322, 29
- Niklas S., Beck R., 1997, *A&A*, 320, 54

- Noeske K.G., et al., 2007, *ApJL*, 660, L43
- Offringa A.R., de Bruyn A.G., Biehl M., Zaroubi S., Bernardi G., Pandey V.N., 2010, *MNRAS*, 405, 155
- Offringa A.R., de Bruyn A.G., Zaroubi S., 2012, *MNRAS*, 422, 563
- Offringa A.R., et al., 2014, *MNRAS*, 444, 606
- Ogle P., Whysong D., Antonucci R., 2006, *ApJ*, 647, 161
- Ogle P.M., Cohen M.H., Miller J.S., Tran H.D., Fosbury R.A.E., Goodrich R.W., 1997, *ApJL*, 482, L37
- Okabe A., ed., 2000, *Spatial tessellations : concepts and applications of voronoi diagrams*
- Oliver S., et al., 2010, *MNRAS*, 405, 2279
- Osterbrock D.E., 1989, *Astrophysics of gaseous nebulae and active galactic nuclei*
- Owen F.N., Ledlow M.J., 1994, In Bicknell G.V., Dopita M.A., Quinn P.J., eds., *The Physics of Active Galaxies*, vol. 54 of *Astronomical Society of the Pacific Conference Series*, p. 319
- Özel F., Psaltis D., Narayan R., 2000, *ApJ*, 541, 234
- Padovani P., Giommi P., 1995, *MNRAS*, 277, 1477
- Page M.J., et al., 2012, *Nature*, 485, 213
- Pandey V.N., van Zwieten J.E., de Bruyn A.G., Nijboer R., 2009, In Saikia D.J., Green D.A., Gupta Y., Venturi T., eds., *The Low-Frequency Radio Universe*, vol. 407 of *Astronomical Society of the Pacific Conference Series*, p. 384
- Pâris I., et al., 2014, *A&A*, 563, A54
- Pascale E., et al., 2011, *MNRAS*, 415, 911
- Perley R.A., Napier P.J., Butler B.J., 2004, In Oschmann Jr. J.M., ed., *Ground-based Telescopes*, vol. 5489 of *Proc. SPIE*, pp. 784–795
- Peterson B.M., 1993, *PASP*, 105, 247

- Peterson B.M., 1997, *An Introduction to Active Galactic Nuclei*
- Pier E.A., Krolik J.H., 1992, *ApJ*, 401, 99
- Pier E.A., Krolik J.H., 1993, *ApJ*, 418, 673
- Poglitsch A., et al., 2010a, *A&A*, 518, L2
- Poglitsch A., et al., 2010b, *A&A*, 518, L2
- Price R., Duric N., 1992, *ApJ*, 401, 81
- Pudritz R.E., Hardcastle M.J., Gabuzda D.C., 2012, *Space Sci. Rev.*, 169, 27
- Punsly B., Zhang S., 2011, *ApJL*, 735, L3
- Quataert E., Gruzinov A., 2000, *ApJ*, 539, 809
- Ramos Almeida C., Tadhunter C.N., Inskip K.J., Morganti R., Holt J., Dicken D., 2011, *MNRAS*, 410, 1550
- Rawlings S., Eales S., Lacy M., 2001, *MNRAS*, 322, 523
- Reber G., 1944, *ApJ*, 100, 279
- Rees M.J., 1984, *ARA&A*, 22, 471
- Rees M.J., Netzer H., Ferland G.J., 1989, *ApJ*, 347, 640
- Rees N., 1990, *MNRAS*, 244, 233
- Reichard T.A., Heckman T.M., Rudnick G., Brinchmann J., Kauffmann G., Wild V., 2009, *ApJ*, 691, 1005
- Rengelink R.B., Tang Y., de Bruyn A.G., Miley G.K., Bremer M.N., Roettgering H.J.A., Bremer M.A.R., 1997, *A&AS*, 124
- Reuland M., Röttgering H., van Breugel W., De Breuck C., 2004, *MNRAS*, 353, 377
- Reynolds C.S., 2015, *ArXiv:1510.07638*
- Reynolds C.S., Fabian A.C., Celotti A., Rees M.J., 1996, *MNRAS*, 283, 873
- Rickard L.J., Harvey P.M., 1984, *AJ*, 89, 1520

- Riffel R.A., Storchi-Bergmann T., McGregor P.J., 2009, *ApJ*, 698, 1767
- Rigby E.E., Best P.N., Brookes M.H., Peacock J.A., Dunlop J.S., Röttgering H.J.A., Wall J.V., Ker L., 2011, *MNRAS*, 416, 1900
- Robson I., 1996, *Active galactic nuclei*
- Rosario D.J., Shields G.A., Taylor G.B., Salviander S., Smith K.L., 2010, *ApJ*, 716, 131
- Rosario D.J., Burtscher L., Davies R., Genzel R., Lutz D., Tacconi L.J., 2013, *ApJ*, 778, 94
- Rosario D.J., et al., 2012, *A&A*, 545, A45
- Röttgering H., et al., 2011, *Journal of Astrophysics and Astronomy*, 32, 557
- Röttgering H.J.A., et al., 2006, *ArXiv:0610596*
- Rovilos E., et al., 2012, *A&A*, 546, A58
- Runnoe J.C., Brotherton M.S., Shang Z., 2012a, *MNRAS*, 422, 478
- Runnoe J.C., Brotherton M.S., Shang Z., 2012b, *MNRAS*, 426, 2677
- Russell H.R., McNamara B.R., Edge A.C., Hogan M.T., Main R.A., Vantyghem A.N., 2013, *MNRAS*
- Rybicki G.B., Lightman A.P., 1979, *Radiative processes in astrophysics*
- Ryle M., Hewish A., 1960, *MNRAS*, 120, 220
- Ryle M., Smith F.G., Elsmore B., 1950, *MNRAS*, 110, 508
- Sabater J., Best P.N., Argudo-Fernández M., 2013, *MNRAS*, 430, 638
- Saikia D.J., Jamrozy M., Konar C., Nandi S., 2010, In *25th Texas Symposium on Relativistic Astrophysics*, p. 14
- Salim S., et al., 2007, *ApJS*, 173, 267
- Salpeter E.E., 1964, *ApJ*, 140, 796
- Sargent M.T., et al., 2010, *ApJL*, 714, L190

- Satyapal S., Dudik R.P., O'Halloran B., Gliozzi M., 2005, *ApJ*, 633, 86
- Schartmann M., Meisenheimer K., Camenzind M., Wolf S., Henning T., 2005, *A&A*, 437, 861
- Scheuer P.A.G., 1974, *MNRAS*, 166, 513
- Schilizzi R.T., 2005, In Gurvits L.I., Frey S., Rawlings S., eds., *EAS Publications Series*, vol. 15 of *EAS Publications Series*, pp. 445–463
- Schmidt M., 1963, *Nature*, 197, 1040
- Schmitt J.H.M.M., 1985, *ApJ*, 293, 178
- Serjeant S., Hatziminaoglou E., 2009, *MNRAS*, 397, 265
- Seyfert C.K., 1943, *ApJ*, 97, 28
- Shakeshaft J.R., Ryle M., Baldwin J.E., Elsmore B., Thomson J.H., 1955, *MmRAS*, 67, 106
- Shakura N.I., Sunyaev R.A., 1973, *A&A*, 24, 337
- Shao L., et al., 2010, *A&A*, 518, L26
- Shen Y., Ho L.C., 2014, *Nature*, 513, 210
- Shi Y., Rieke G.H., Ogle P., Jiang L., Diamond-Stanic A.M., 2009, *ApJ*, 703, 1107
- Shi Y., et al., 2005, *ApJ*, 629, 88
- Siebenmorgen R., Haas M., Krügel E., Schulz B., 2005, *A&A*, 436, L5
- Sijacki D., Springel V., Haehnelt M.G., 2009, *MNRAS*, 400, 100
- Silk J., Nusser A., 2010, *ApJ*, 725, 556
- Silk J., Rees M.J., 1998, *A&A*, 331, L1
- Silverman J.D., et al., 2009, *ApJ*, 696, 396
- Silverman J.D., et al., 2011, *ApJ*, 743, 2
- Simpson C., 1998, *MNRAS*, 297, L39

- Simpson C., et al., 2012, MNRAS, 421, 3060
- Smith D.J.B., et al., 2012a, MNRAS, 427, 703
- Smith D.J.B., et al., 2012b, MNRAS, 427, 703
- Smith D.J.B., et al., 2013, MNRAS, 436, 2435
- Smith D.J.B., et al., 2014, MNRAS, 445, 2232
- Smolčić V., 2009, ApJL, 699, L43
- Springel V., Di Matteo T., Hernquist L., 2005, MNRAS, 361, 776
- Stern D., et al., 2005, ApJ, 631, 163
- Stern D., et al., 2012, ApJ, 753, 30
- Stocke J.T., Morris S.L., Weymann R.J., Foltz C.B., 1992, ApJ, 396, 487
- Stone J.M., Pringle J.E., 2001, MNRAS, 322, 461
- Sun J., Shen Y., 2015, ApJL, 804, L15
- Tadhunter C., et al., 2011, MNRAS, 412, 960
- Tadhunter C.N., Morganti R., di Serego-Alighieri S., Fosbury R.A.E., Danziger I.J., 1993, MNRAS, 263, 999
- Takeuchi T.T., Buat V., Iglesias-Páramo J., Boselli A., Burgarella D., 2005, A&A, 432, 423
- Tasse C., Best P.N., Röttgering H., Le Borgne D., 2008, A&A, 490, 893
- Tasse C., van der Tol S., van Zwieten J., van Diepen G., Bhatnagar S., 2013, A&A, 553, A105
- Taylor G.B., 2007, Highlights of Astronomy, 14, 388
- Tchekhovskoy A., 2015, In Contopoulos I., Gabuzda D., Kylafis N., eds., The Formation and Disruption of Black Hole Jets, vol. 414 of Astrophysics and Space Science Library, p. 45
- Thacker R.J., MacMackin C., Wurster J., Hobbs A., 2014, MNRAS, 443, 1125

- Thomas D., Maraston C., Schawinski K., Sarzi M., Silk J., 2010, *MNRAS*, 404, 1775
- Thompson T.A., Quataert E., Murray N., 2005, *ApJ*, 630, 167
- Tingay S.J., et al., 2013, *PASA*, 30, e007
- Tregillis I.L., Jones T.W., Ryu D., Park C., 2002, *NewAR*, 46, 387
- Tremonti C.A., et al., 2004, *ApJ*, 613, 898
- Tristram K.R.W., et al., 2007, *A&A*, 474, 837
- Trouille L., Barger A.J., Tremonti C., 2011, *ApJ*, 742, 46
- Urry C.M., Padovani P., 1995, *PASP*, 107, 803
- van Breugel W., De Breuck C., Stanford S.A., Stern D., Röttgering H., Miley G., 1999, *ApJL*, 518, L61
- van der Kruit P.C., 1971, *A&A*, 15, 110
- van der Kruit P.C., 1973, *A&A*, 29, 263
- van Haarlem M.P., et al., 2013, *A&A*, 556, A2
- van Weeren R.J., et al., 2016, *ApJS*, 223, 2
- Veilleux S., Cecil G., Bland-Hawthorn J., 2005, *ARA&A*, 43, 769
- Veilleux S., et al., 2013, *ApJ*, 776, 27
- Virdee J.S., et al., 2013, *MNRAS*, 432, 609
- Visser A.E., Riley J.M., Roettgering H.J.A., Waldram E.M., 1995, *A&AS*, 110, 419
- Voelk H.J., 1989, *A&A*, 218, 67
- Wall J.V., Peacock J.A., 1985, *MNRAS*, 216, 173
- Weedman D., et al., 2006, *ApJ*, 653, 101
- Werner M.W., et al., 2004, *ApJS*, 154, 1
- Werner N., et al., 2014, *MNRAS*, 439, 2291
- Whysong D., Antonucci R., 2004, *ApJ*, 602, 116

- Wild V., Kauffmann G., Heckman T., Charlot S., Lemson G., Brinchmann J., Reichard T., Pasquali A., 2007, *MNRAS*, 381, 543
- Wild V., Heckman T., Charlot S., 2010, *MNRAS*, 405, 933
- Wilkins S.M., Trentham N., Hopkins A.M., 2008, *MNRAS*, 385, 687
- Willett K.W., et al., 2013, *MNRAS*, 435, 2835
- Williams W.L., Röttgering H.J.A., 2015, *MNRAS*, 450, 1538
- Williams W.L., et al., 2016, *MNRAS*
- Willott C.J., Rawlings S., Blundell K.M., Lacy M., 1998, *MNRAS*, 300, 625
- Willott C.J., Rawlings S., Blundell K.M., Lacy M., 1999, *MNRAS*, 309, 1017
- Willott C.J., Rawlings S., Blundell K.M., Lacy M., Hill G.J., Scott S.E., 2002, *MNRAS*, 335, 1120
- Willott C.J., Rawlings S., Jarvis M.J., Blundell K.M., 2003, *MNRAS*, 339, 173
- Wilson A.S., Colbert E.J.M., 1995, *ApJ*, 438, 62
- Worrall D.M., Birkinshaw M., Hardcastle M.J., 2001, *MNRAS*, 326, L7
- Wright E.L., et al., 2010a, *AJ*, 140, 1868
- Wright E.L., et al., 2010b, *AJ*, 140, 1868
- Wu X.B., Hao G., Jia Z., Zhang Y., Peng N., 2012, *AJ*, 144, 49
- Wu Y., Charmandaris V., Houck J.R., Bernard-Salas J., Leboutteiller V., Brandl B.R., Farrah D., 2008, *ApJ*, 676, 970
- Wurster J., Thacker R.J., 2013, *MNRAS*, 431, 2513
- Wykes S., et al., 2013, *A&A*, 558, A19
- York D.G., et al., 2000, *AJ*, 120, 1579
- Yu Q., Tremaine S., 2002, *MNRAS*, 335, 965
- Yuan F., Narayan R., 2014, *ARA&A*, 52, 529

Yuan F., Quataert E., Narayan R., 2003, *ApJ*, 598, 301

Yuan F., Quataert E., Narayan R., 2004, *ApJ*, 606, 894

Yun M.S., Reddy N.A., Condon J.J., 2001, *ApJ*, 554, 803

Zakamska N.L., et al., 2005, *AJ*, 129, 1212

Zakamska N.L., et al., 2016, *MNRAS*, 455, 4191

Zel'dovich Y.B., Rees I., 1964, *Sov. Phys. Dokl.*, 158, 811